The Dissertation Committee for Clinton Benjamin Morris Certifies that this is the approved version of the following Dissertation:

EXPLORATION AND VISUALIZATION OF DESIGN SPACES WITH APPLICATIONS TO NEGATIVE STIFFNESS METAMATERIALS

Committee:

Carolyn C. Seepersad, Supervisor

Michael R. Haberman

Richard Crawford

Jason Aughenbaugh

EXPLORATION AND VISUALIZATION OF DESIGN SPACES WITH APPLICATIONS TO NEGATIVE STIFFNESS METAMATERIALS

by

Clinton Benjamin Morris

Dissertation

Presented to the Faculty of the Graduate School of

The University of Texas at Austin

in Partial Fulfillment

of the Requirements

for the Degree of

Doctor of Philosophy

The University of Texas at Austin

August 2018

Acknowledgements

The achievement of this work is an accomplishment that does not belong to a single person. While it was written by myself, the influence and support of my mentors and peers is equally responsible for its completion. First, I would like to thank Dr. Carolyn Seepersad for her unwavering support and the example she set as an academic mentor. Her patience and attention to the well-being of her students is admirable. This work would also not exist without my family who has remained ever-present in my life, even though they are a thousand miles away. Specifically, I am grateful to my mom and dad for teaching me the importance of practicality and effort. My girlfriend, Ana, has been unbelievably patient through the late nights, long hours, and emotions that accompany graduate school and for that I am truly appreciative.

I would also like to thank my dissertation committee for reading this document and providing advice on what has been a fulfilling process. Specifically, I appreciate the passion that Dr. Haberman has instilled for a subject I never knew could be so rich with content and Dr. Crawford for his memorable classes that served as a reminder of the human aspects of engineering. Thank you to Dr. Aughenbaugh, as well, for his support and feedback on this work. I also would like to acknowledge support from the National Science Foundation under Grant No. CMMI -1435548, John Cormack for his acoustical expertise, David Debeau for his assistance in experimentation, and Aslan Alamdari, Sumanth Kashyap, and Dr. Jae-Won Choi at the University of Akron and Dr. Christopher Spadaccini at Lawrence Livermore National Laboratory for assistance with microstereolithography. I would also like to acknowledge Conner Sharpe and Tyler Wiest for their discussion of design methodology. Thank you to John Lange for his assistance with the SEM and Jordan Matthews and Tim Klatt for their past assistance in formulating the metamaterials example

problem. To everyone I have formed relationships with in graduate school as either a student, peer, lab mate, mentor, or simply a friend, I would like you to know how appreciative I am of your influence. Finally if you have not been mentioned but are reading this work, thank you.

Abstract

Exploration and Visualization of Design Spaces with Applications to Negative Stiffness Metamaterials

Clinton Benjamin Morris, Ph.D.

The University of Texas at Austin, 2018

Supervisor: Carolyn C. Seepersad

Engineering design problems are commonly hierarchical and multilevel which requires coordination between models at each scale. If the models are computationally expensive or highly nonlinear, such as many materials design applications, identification of an optimal design may be exceptionally difficult. Alternatives to optimization-based methods include set-based methods that classify and track sets or ensembles of high performance designs. By relaxing the requirement for an *optimal* design, it is often possible to identify promising, high performance regions of the design space efficiently. Bayesian network classifiers (BNCs) are such an approach that can identify these regions of promising designs in the presence of nonlinear relationships and mixed variables. When manufacturing the promising designs identified by the BNC approach, the intended design may not match the physical embodiment due to manufacturing variations. These variations may alter the performance of the design leading to unsatisfactory results and products. To facilitate selection of not only high performance but reliably manufacturable designs, a method for incorporating manufacturing variation, modeled as a joint probability distribution is presented for the BNC approach. The approach utilizes a dual classification

strategy that identifies regions of design that are likely to perform well within statistical confidence. These design regions can be high dimensional in which it becomes very difficult to identify and visualize clusters of promising designs. This leads to a lack of understanding of the design space. To enhance the designer's knowledge of the design space, this work presents a method, based on spectral clustering, that can identify high performance regions in a high dimensional space. Furthermore, a method for visualizing each individual design region is presented that is accomplished by incorporating t-Distributed Stochastic Neighbor Embedding. Through the accomplishment of these three tasks—incorporating manufacturing variation, clustering, and visualizing—a novel design methodology will be developed which will then be applied to identify satisfactory designs for a negative stiffness metamaterials design problem which will be manufactured and tested.

Table of Contents

List of Tables

List of Figures

Chapter 1: Introduction to Multilevel Materials

New material development and technologic advancement have historically benefited from a symbiotic relationship where progress in one field begets progress in the other. The history of metals development and new technology is an example of the intertwined nature of materials and technology. The first metals widely adopted for tool and weapon production were copper, tin, and their alloy, bronze. This prevalence was due to their relatively low melting temperatures allowing them to be easily extracted from ore in simple fires. Several cultures independently developed new furnaces capable of reaching sufficient temperatures to smelt iron which is the most abundant metal on earth. Iron and bronze have similar strengths and sharpening abilities, but the wide availability of iron allowed it to replace bronze [1].

Eventually, the Industrial Revolution led to the wide scale implementation of iron for new technology and infrastructure like tractors and railroads. Due to its high strength and durability, steel was viewed as a desirable replacement of iron for these applications [2]. Steel had previously been discovered long before the Industrial Revolution by adding manufactured charcoal to the furnaces used to produce iron, but it was not possible to produce large quantities of steel at low cost [1, 2]. Eventually, the Bessemer process was developed which exploits a unique furnace and oxygen injection process to develop low carbon steels that were readily manufacturable and inexpensive. The development of this new process and durable steel allowed for much of the innovation brought by the New Industrial Revolution, which eventually led to the modern technology currently being researched and implemented [2].

Prior to the 19th century, the time between material innovation and discovery took centuries to millennia [3]. This timeline is due to a generally inefficient approach where

significant resources and time were dedicated to physically developing new materials and processes. Rather than relying on rigorous theory and methods, materials development relied on expert knowledge and prediction of properties from empirical results. In the metallurgical example above, charcoal was not added to the furnaces with the intent of making steel; rather it was added to increase the temperature of the furnace and unexpectedly resulted in a higher quality material than iron [1]. It was not until scientists began analyzing the microstructure of the steel that they began to understand why steel exhibited its exceptional properties and began devising ways to improve the material. Process and material development began to accelerate due to the foundational knowledge of the material but there was still a heavy reliance on extensive physical experimentation and conjecture. This general methodology of educated exploratory experimentation has continued to be the norm for material production. Now with the introduction of new technology like high performance computing and advanced manufacturing techniques, the approach is being improved with computational modeling for designing of materials.

1.1 MULTILEVEL MATERIALS DESIGN

Computational resources have become increasingly powerful while significantly decreasing in cost allowing for higher fidelity material models [4]. These benefits have allowed for previously computationally intractable material models to be implemented for material property prediction without synthesizing the material. Computation is consistently being utilized to model material properties at each scale from the quantum scale to the product scale [5-8]. While the models may be well-suited at each length scale and describe the dominant physical phenomena well, the one of the largest difficulties in modern materials development is accurately portraying the dependency between scales within a manageable framework. How does the quantum level model relate to the atomic level

model which relates to the microstructure of the material which ultimately dictates the products performance? This question is at the core of current materials design.

The initial work in integrating multiple scales described by computational materials models focused on developing high-performance alloy steel. The high-performance alloy steel was viewed as a complex, hierarchical system where at the lowest level the processing of the steel influenced aspects of the mid-level microstructure which ultimately governed, at the highest level, the bulk material properties of the steel. Figure 1.1 provides the original system connectivity showing how processing affects the microstructure which yields the material properties [9].

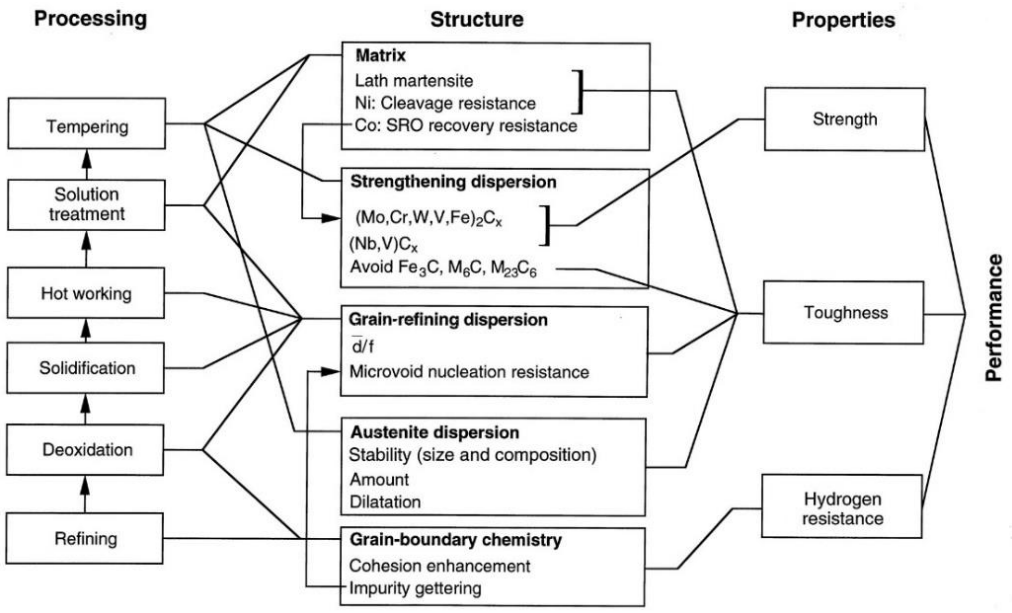

Figure 1.1: Illustration of the dependencies between processing, microstructure, and material properties of a high-performance alloy steel [9].

After establishing the dependencies among the process, microstructure, and material properties various models at each length scale were evaluated to determine how varying the processing parameters affects the microstructure. With the resultant

microstructure established, another set of models was evaluated to map the microstructure to the properties of the steel. The goal of developing the full material model was to identify a new, harder steel tailored to a specific application. Through the integrated modeling framework, processing parameters were identified that would result in a steel with the desired properties. Following identification, the steel was produced and shown to exhibit the desired properties. This approach drastically changed the way material synthesis can be approached [9]. Rather than perform expensive, iterative physical experiments to develop new materials, properties can be rigorously predicted computationally. Furthermore, computational modeling allows for accurate identification of inputs that result in the desired output.

The general strategy introduced by Olson formed the basis of multilevel materials design which can be divided into two essential categories: 1) forward modeling and 2) inverse modeling. Forward modeling predicts the outputs or performance variables given some inputs or design variables, which is demonstrated in the previous example by predicting the properties of the steel given processing conditions. Inverse modeling is identification of design variables given desired performance variables, which is analogous to identification of a previously unused processing route that results in a stronger steel. Figure 1.2 provides a simplified flowchart summarizing forward and inverse modeling.

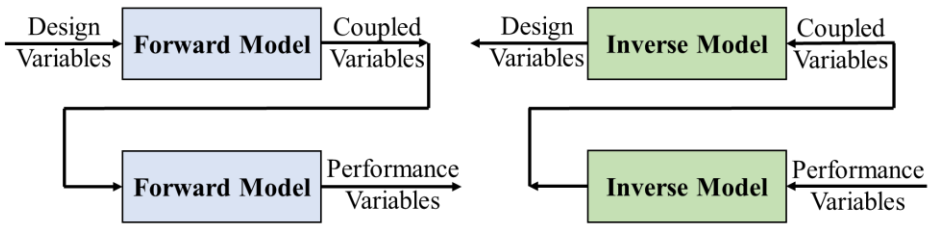

Figure 1.2: Flowcharts summarizing the nature of forward modeling and inverse modeling for a multilevel system.

The forward modeling approach introduced for materials design by Olson has since been applied to other metal alloys, ceramics, and composites. Olson utilized the strategy once again to predict the performance of a Nickel-based aeroturbine disk by using forward models to map processing to material properties. The identified processing parameters were applied, and a final part was produced that agreed with the computational results [10]. McDowell *et al.* computationally modeled the relationship between microstructure and fatigue life to predict how variability in microstructure affected fatigue performance. The results of the computational models were also validated by testing cast A356-T6 alloy samples [11]. The multiscale modeling of ceramics has been more focused on mapping interatomic structure to the molecular length scale [12, 13]. For example, Krishnamurthy *et al.* predicted the performance of cubic yttria-stabilized zirconia for various applications like thermals barrier coatings of turbine engines and resistive heating elements. The performance variable was oxygen diffusion into the cubic yttria-stabilized zirconia because oxygen diffusion lowers the material's conductivity and increases its thermal stability. From first principles, the activation energy for oxygen diffusion into a cubic sublattice was determined. The results were supplied to a Monte Carlo simulation of a larger lattice to determine how oxygen typically travels through the lattice. The results of the simulation were averaged to determine the self-diffusivity of the system which was compared to values in the literature [12].

Forward modeling of materials has largely been applied to composites, e.g., polymer composites [14, 15], fiber-reinforced composites [7], and metal-ceramic composites [16]. The typical approach for modeling composites relies on identifying a representative volume element (RVE) of the composite. An RVE is the smallest volume of the material that effectively captures the material properties of the bulk composite [17]. The RVE contains the typical microstructure of the composite whether it be the distribution

of nanoparticles within another polymer [14], carbon fibers embedded within a resin [7], or various grain orientations of a metal-ceramic mixture [16]. After identifying the material properties and interactions between the constituents of the RVE, some type of homogenization is performed on the RVE that predicts the effective material properties of the RVE. The effective material properties of the RVE are by definition the material properties of the composite. Figure 1.3 is provided to illustrate an RVE for a fiber-reinforced composite.

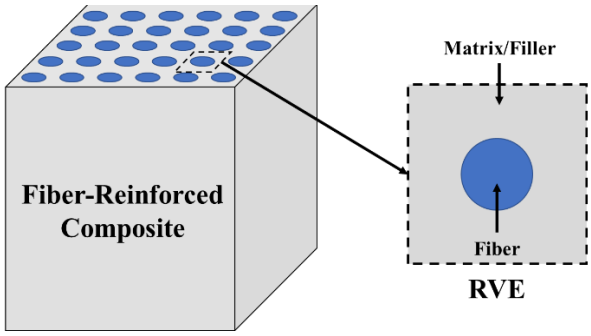

Figure 1.3: Illustration of an RVE for a fiber-reinforced composite that is utilized for multilevel modeling of composites.

While this forward modeling approach has proven effective, the designer's level of control over material structure has been limited by available processing technologies. With the introduction of additive manufacturing technologies, such as microstereolithography [18] or direct metal laser sintering [19], the micro- and meso-scale structures of larger parts can be finely controlled to dictate the bulk material properties. The new materials that derive their properties from the small-scale structure, rather than just their material composition are known as metamaterials. Examples of such mechanical metamaterials are lattice-based structures which can exhibit high stiffness to weight ratios, negative Poisson ratios, negative coefficients of thermal expansion, and negative stiffness

[20-23]. Figure 1.4 provides images of various lattice structures that exhibit the material properties previously discussed [24].

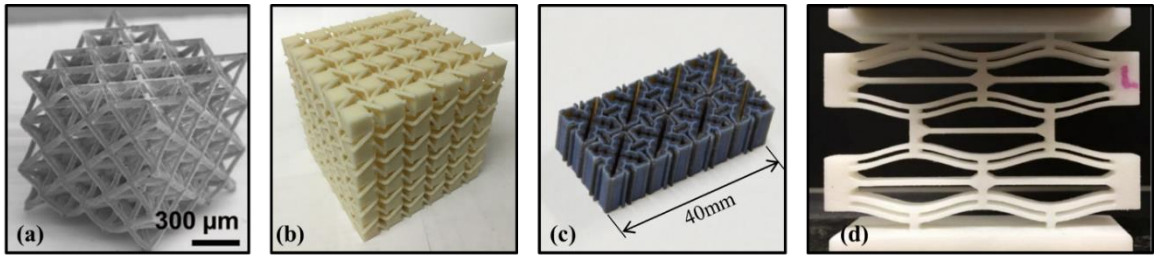

Figure 1.4: Lattice-structure based metamaterials that exhibit (a) extreme stiffness while being lightweight, (b) negative Poisson ratios, (c) negative coefficients of thermal expansion, and (d) negative stiffness [20-23].

The geometry and material properties of each cell, which can have micron-scale features, dictate the effective properties of the large-scale structure. While many of the previously identified mechanical metamaterials are lattice-based structures, mechanical metamaterials can be developed by embedding micro-scale structures within a homogenous medium such as the mechanical metamaterials that are the focus of this work [24].

Negative stiffness metamaterials are such non-lattice-based metamaterials that are composites formed when microscale NS inclusions are embedded within a ductile matrix material. They are of particular interest because NS metamaterials have the ability to dissipate significant amounts of dynamic energy while maintaining their effective stiffness when compared to the original matrix [25-27]. Due to their geometry, NS inclusions exhibit nonlinear and non-monotonic force-displacement behavior. During the "snap-through" regime of displacement, the inclusions require less applied force to displace further causing an apparent negative stiffness which is shown in Figure 1.4 [28]. When embedded in the matrix, the microstructural inclusions amplify local strains when a load is

applied because of their non-monotonic behavior. These localized strains increase the metamaterial's dynamic energy dissipation capacity compared to conventional materials [25-31]. Furthermore, through careful selection of inclusion design, the effective stiffness of the composite can be increased relative to the original matrix. Because these NS metamaterials can maintain and even increase their effective stiffness while drastically increasing their loss factor, they belong to a regime of materials that are not attainable through conventional manufacturing methods [32-34].

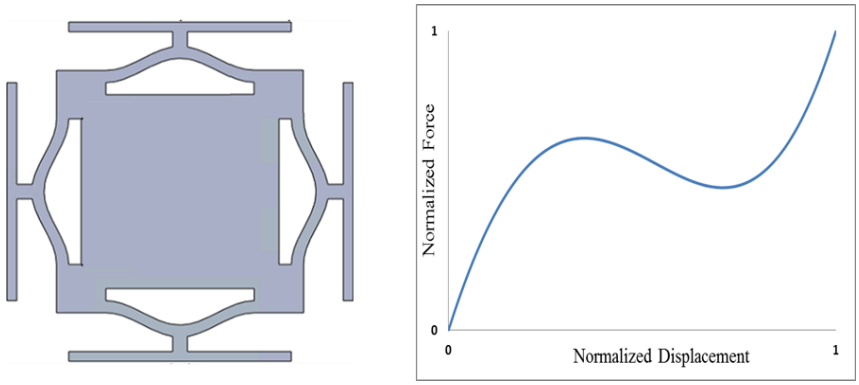

Figure 1.5: Illustration of a micro-scale negative stiffness inclusion (left) with typical normalized force-displacement curve of negative stiffness elements (right).

Following the general multilevel materials modeling approach introduced by Olson, the NS metamaterials are considered as a multilevel system consisting of three levels or length scales. Figure 1.6 provides an illustration and flowchart of the scales. The first and smallest scale known as the micro-scale contains material properties and lengths defining the inclusion which are on the order of microns to millimeters. The second scale, called the meso-scale, considers the composite material on length scales of millimeters to centimeters. The final and largest scale, which is on the order of centimeters to meters,

describes the properties of components. After establishing each of the levels, modeling can predict the performance of the NS metamaterial given the input designs.

Given a micro-scale design or the material and geometry of the inclusion a finite element-based homogenization model can determine the effective stiffness of the inclusion [35]. Then at the meso-scale level, a volume fraction and orientation distribution of the inclusions are supplied along with the material properties of the matrix material, so effective medium theory (EMT) modelling can determine the effective stiffness and loss factor of the composite material at the macro-scale [35].

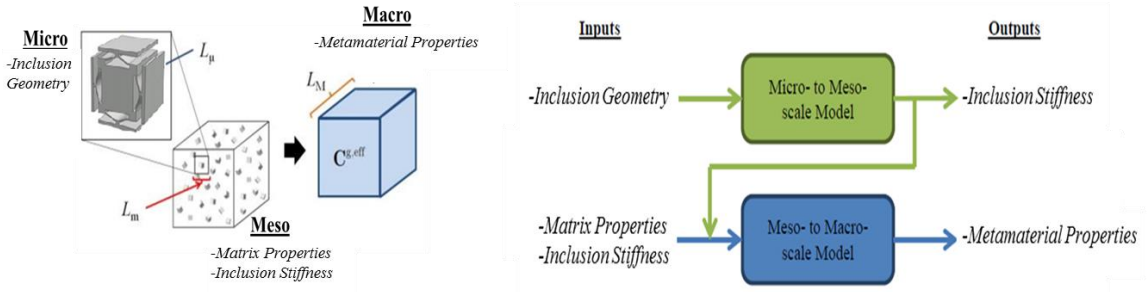

Figure 1.6: Illustration of each scale of the hierarchical materials design problem. Observe the different length scales and design/performance variables (left) and the flowchart depicting the connectivity and modeling needed to connect scales (right).

The forward modeling just described predicts the performance of the NS metamaterial given the inputs, but typically the inverse procedure is desired where candidate designs can be identified given a desired performance. Determining the inverse relationship for NS metamaterials as well as many of the other multilevel material systems previously described is rather difficult. The relationships between inputs and outputs can be highly nonlinear and nonunique (i.e., more than one input candidate design may lead to a specified output performance), and the inputs could be a mixture of discrete and

continuous variables complicating the relationship between inputs and outputs. Therefore significant effort has been devoted to developing inverse methods for multilevel materials design.

1.2 Inverse Methods for Multilevel Materials Design

Inverse methods for multilevel materials design seek to identify configurations of a material that yield the desired performance. Two distinct approaches exist for multilevel materials design: (1) point-based optimization and (2) set-based approaches. Point-based optimization seeks to identify the optimal design(s) given performance objectives and constraints. Since the method seeks to identify material designs that optimize some performance objective(s), there must be some objective function(s). Obtaining the objective function(s) is nontrivial due to the complex nature of multilevel materials modeling. For most material problems of interest, there is typically no simple, closed-form analytical relationship between design and performance variables. Therefore, as seen before, computational forward models are evaluated to map a design to its performance. Even with the growth of computational power, evaluation of certain computational models, such as complex finite element models, requires a large amount of computing time. For expensive computational models, it is typical to generate a metamodel, or a model of the computational model, that approximates the results of the computational model but in an efficient manner.

While there likely will be some decrease in forward modeling accuracy, metamodels allow for rapid discovery of results. Furthermore, metamodels create a functional relationship between design and performance variables, which enables evaluation and optimization of an objective function. As shown by Figure 1.1, though, there may be high degrees of dependency and connectivity among all the metamodels

resulting in a highly coupled optimization formulation. Methods like Analytical Target Cascading [36] and Concurrent Sub Space Optimization [37] have been proposed as effective approaches for materials design given suitable metamodels and an unchanging framework of variables.

These point-based optimization approaches still have several drawbacks that make them difficult to implement during materials development. The first drawback is the gradient-based nature of the strategies. Multilevel materials design problems commonly have mixed design variables, that is, design variables that are both discrete and continuous. Strategies like Concurrent Sub Space Optimization strategy can be modified to accept mixed variables with success, but not all optimization frameworks have been adapted. Also, complex materials design problems have nonlinear relationships between design variables and performance metrics for each forward model. These nonlinear relationships can be highly multimodal implying that even if a proper metamodel is supplied, a gradient-based approach may not identify the global optima. Rather, it could identify local minima even if multiple starting locations are supplied for sufficiently multimodal or high dimensional design spaces. Also, the nature of point-based optimization for complex systems requires a series of cascading, top-down optimizations which can be computationally expensive or even fail to converge to a solution. Performing optimization across levels for complex systems requires careful coordination and automation among the various models. Integrating multiple computational models can be rather difficult especially for bridging different commercial softwares or operating systems. Even if this integration is accomplished, convergence is never guaranteed when the gradient is required, especially if the optimization identifies an infeasible design to evaluate.

Another limitation of these methods is their flexibility to constraints. During the design process for multilevel materials design, there are typically multiple design teams

communicating. Unless the teams are communicating perfectly, there will be some amount of miscommunication initially that will need to be addressed during the design process. A typical miscommunication would be in the constraints of one of the forward models or levels. For optimization approaches, if the constraints change, the optimization must be rerun which can be a time-consuming effort. This could be compounded if it is an implicit constraint which would require even more time for an optimal solution to converge. In general, if all constraints are well-established and the relationships between design inputs and performance outputs are well-behaved, the point-based optimization approach is appropriate for multilevel materials design. Otherwise, other design approaches like the set-based approach, should be explored.

Introduced by Toyota, set-based concurrent engineering identifies sets of designs that meet specific performance requirements rather than identifying a single optimal design [38]. It provides a flexible, comprehensive design framework well-suited for multilevel materials design because there is no reliance on gradients for optimization. For example, a multilevel problem identical in structure to Figure 1.6 is shown in Figure 1.7 where micro-level design variables, $\boldsymbol{x}$, are the input to a micro-to meso-scale transition model, whose output variables, $\boldsymbol{y}$, are the input to a meso- to macro-scale transition model, which provides macro-scale performance parameters, $\boldsymbol{z}$, as output.

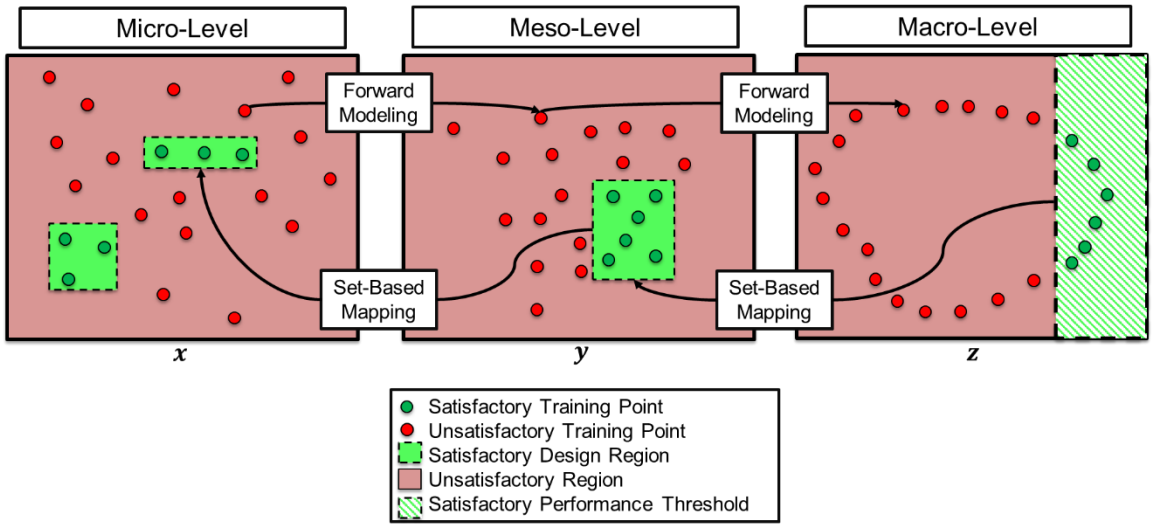

Figure 1.7: Simple illustration of the set-based approach being implemented to identify regions of the design space that are likely to meet a performance threshold for a multilevel materials design problem.

When the BNC approach is applied to this example, an initial set of simulations are then performed, called training points, which are represented by the points in Figure 1.7. Following generation of training points, performance requirements or thresholds are imposed at the macro-level by the designer to classify the performance of the training points at the macro-scale. The classification can then be traced or back-propagated to the associated design variable settings of the training points at the micro- and meso-levels. With the classified training points, some mapping technique (various techniques will be discussed) can be employed to classify each scale into continuous regions of satisfactory or unsatisfactory design.

For multilevel material design that involves multiple physical domains, the set-based approach is superior to the optimization based approach because it allows for decoupled design space exploration among teams. As shown in Figure 1.8, each team explores their respective design space to identify satisfactory design sets or regions for

their subsystem that meet performance requirements. Next, the satisfactory sets or regions are compared to identify intersecting regions of sets of design that satisfy the needs of all teams. From this smaller subset of possible designs, the "optimal" design can be selected and fabricated without the need to redesign to avoid violating design constraints.

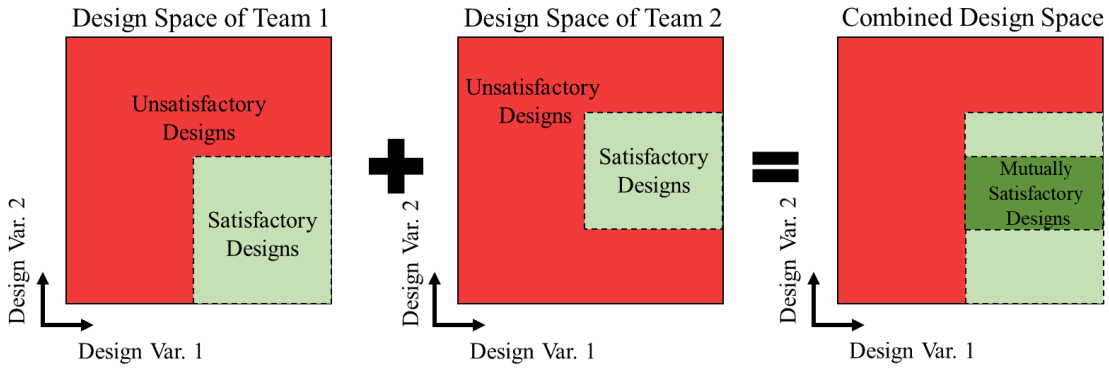

Figure 1.8: Illustration of set-based design identifying a mutually satisfactory design region.

The satisfactory design regions in Fig. 1.8 were determined by selecting an interval for each design variable that is acceptable for each team. Through this construction, the regions will necessarily be rectangular implying the region of intersection in which feasible designs lie for both teams must also be rectangular as well. For complex engineering systems, the set or region of designs that satisfy all design requirements may not lie in a rectangular region of the design space, so by restricting satisfactory regions to interval-based boundaries, feasible and possibly better designs may not be identified. This phenomenon is illustrated in Figure 1.9 where the true set of satisfactory designs occupies an arbitrarily shaped region of the design space, such that capturing it with intervals excludes many satisfactory designs.

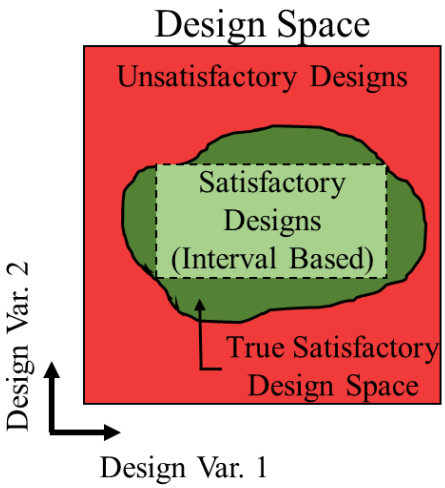

Figure 1.9: Illustration of interval method inaccurately determining the feasible designs.

The inability to capture non-rectangular, satisfactory design regions when using the interval method can lead to incorrect classification of designs. To improve classification accuracy, the true satisfactory region can be better approximated by introducing smaller subintervals of satisfactory designs. While effective, this method requires prior knowledge of the shape of the satisfactory space, which is the case when analytical equations relating the design variables to performance variables are known. Commonly, for complex design problems, these analytical equations and therefore boundaries between satisfactory and unsatisfactory designs are unknown. Therefore the question arises in these cases of how to identify the satisfactory design space.

By generating points or candidate designs in the design space and evaluating their performance, individual designs can be classified as satisfactory or not by whether or not they meet a performance criterion. If a sufficient number of points are evaluated, the boundary between satisfactory and unsatisfactory designs can be well approximated with subintervals, as shown in Figure 1.10.

Figure 1.10: Illustration of how sufficient evaluation design points can lead to accurate identification of satisfactory design region.

The drawback to implementing this method is the required resources to evaluate the performance of a sufficient number of points. Simulations can take hours and even days, so this interval-based method is not well-suited for design problems with time consuming simulations.

To accurately map complex, disjoint, irregularly shaped regions of interest in a multi-dimensional design space without the use of intervals, various approaches have been adopted. The Inductive Design Exploration Method (IDEM) creates flexible mappings of a multilevel design space and supports uncertainty analysis, but its exhaustive sampling strategy can be computationally expensive [39]. Malak and Paredis used support vector machines (SVM) to explore feasible design regions. [40]. Zeliff *et al.* utilized a Multi-Objective Genetic Algorithm (MOGA) modified by classifiers like random forest, kNN, and Naïve Bayesian classifiers to identify non-dominated solutions efficiently [41]. Chen and Fuge, recently developed a method for identifying feasible designs in the presence of implicit constraints by balancing exploration and exploitation with a Gaussian process-

based classifier [42]. While each of these methods have their advantages, drawbacks still exist like the discriminative nature of SVMs, the possible inaccuracies of the modified MOGA, or the computational expense of a Gaussian process with many training points.

Shahan and Seepersad adopted an approach based on Bayesian network classifiers (BNC) for mapping promising regions of a design space. The mappings captured the arbitrary shape of those promising regions resulting in substantially less classification error when compared to interval-based mappings [43]. Furthermore, the BNC approach is a generative method so it can be used for sequential sampling and remains computationally tractable with large numbers of training data. From an initial set of designs and their predicted performance, the BNC method leverages a stochastic, classification-based strategy to predict whether other designs are likely to meet performance thresholds. This allows design to be classified into sets of satisfactory or unsatisfactory designs.

The BNC approach is further discussed in Chapter 2 but Figure 1.11 is provided to introduce how the approach generates mappings of satisfactory and unsatisfactory design regions for a simple design problem. The design/input space, $\boldsymbol{x}$, can be mapped to the performance/output space, $\boldsymbol{y}$, through some forward model. After evaluating a series of designs to determine their performance, a performance threshold is set that classifies performance as satisfactory or unsatisfactory. This classification can be back-propagated to the design space to classify the previously evaluated designs as either satisfactory or unsatisfactory. Following the classification of the designs, the BNC approach generates the satisfactory and unsatisfactory design regions shown in Figure 1.11.

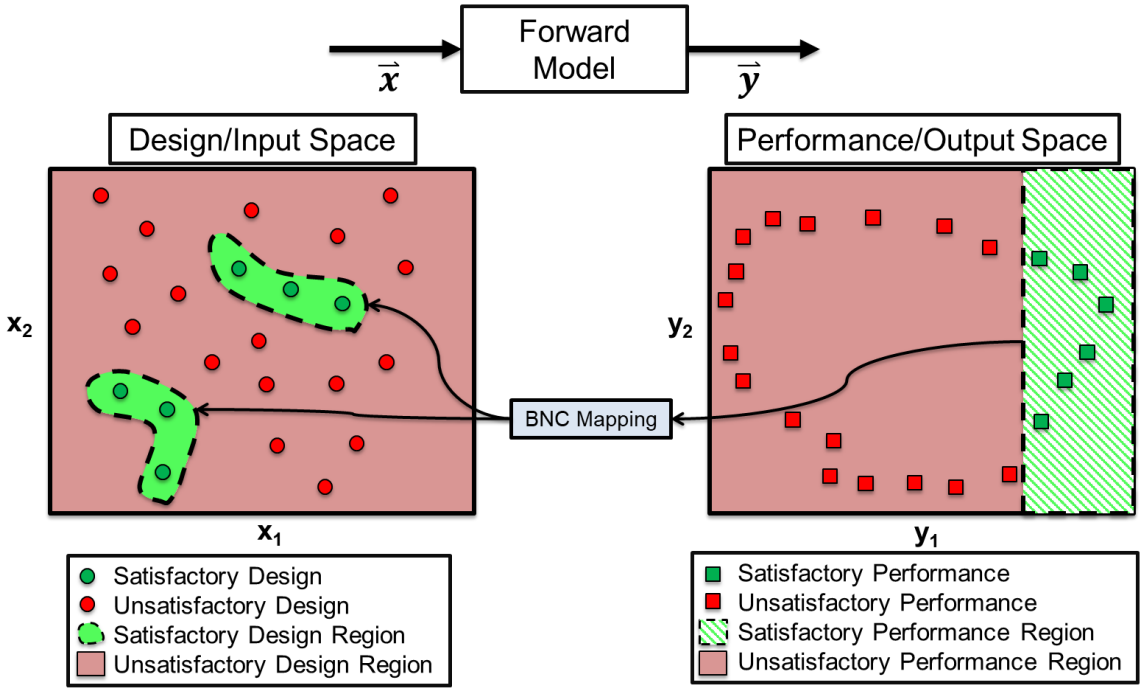

Figure 1.11: Illustration of the BNC approach used to identify irregularly shaped satisfactory design regions for a multilevel design problem.

As shown in Figure 1.11, multiple, disjoint satisfactory design regions with complex, nonrectangular boundaries can be captured by the BNC approach resulting in higher classification accuracy when compared to interval-based methods. Furthermore, the mappings provide an intuitive visualization of the design space facilitating information extraction for the user/designer. Due to its efficacy at classifying design spaces, the BNC approach was previously applied to a multilevel materials design problem to identify candidate designs [35]. The focus of this dissertation and research will be to expand the BNC approach for multilevel materials development by incorporating manufacturing variation information and providing mappings of the design space when more than three design variables are present.

Chapter 2: The Set-Based, BNC Approach for Material Design[1]

The BNC approach discussed in this chapter generates mappings of satisfactory and unsatisfactory design regions for multilevel, hierarchical design problems. The approach has been demonstrated on the materials design problem of interest, NS metamaterials, for classification of design spaces. To clarify the approach, this chapter first introduces the mathematical framework of the strategy in Section 2.1. Following the theoretical discussion, the previous application of the BNC approach for multilevel material design is introduced to document the current status of the approach. Areas of investigation for the BNC method are then identified in Section 2.2 to motivate the research tasks for this dissertation provided in Section 2.3.

2.1 The BNC Approach

As mentioned in Chapter 1, the BNC approach relies on first establishing forward models for a multilevel problem. Figure 1.10 illustrated a simple two-level design problem, but the BNC approach accommodates problems with additional levels. To provide a more comprehensive example, a three-level hierarchical problem is introduced. The lowest level or micro design space is described by the design variables, $\boldsymbol{x_{micro}}$, which are input to a forward model that outputs to the middle or meso space spanned by the coupled variables, $\boldsymbol{y_{meso}}$. The coupled, meso space variables can then be mapped by another forward model to the highest level performance space described by the performance variables, $\boldsymbol{z_{macro}}$. From an initial set of designs generated in the micro space, the forward models map the micro level designs to their evaluated performance in the macro level performance space.

[1] This chapter contains content published in J. Matthews, T. Klatt, C. Morris, C. C. Seepersad, M. R. Haberman and D. W. Shahan, "Hierarchical Design of Negative Stiffness Metamaterials Using a Bayesian Network Classifier," *Journal of Mechanical Design,* vol. 138, no. 4, pp. 1-12, 2016. Matthews, Morris, Seepersad, and Shahan contributed to the development and application of the BNC approach while Klatt and Haberman developed the forward models.

Figure 2.1 provides an illustration of how a sample of designs in the lowest level space can be propagated to their macro level performance. The set of evaluated designs and associated performance predictions are referred to as data in this work.

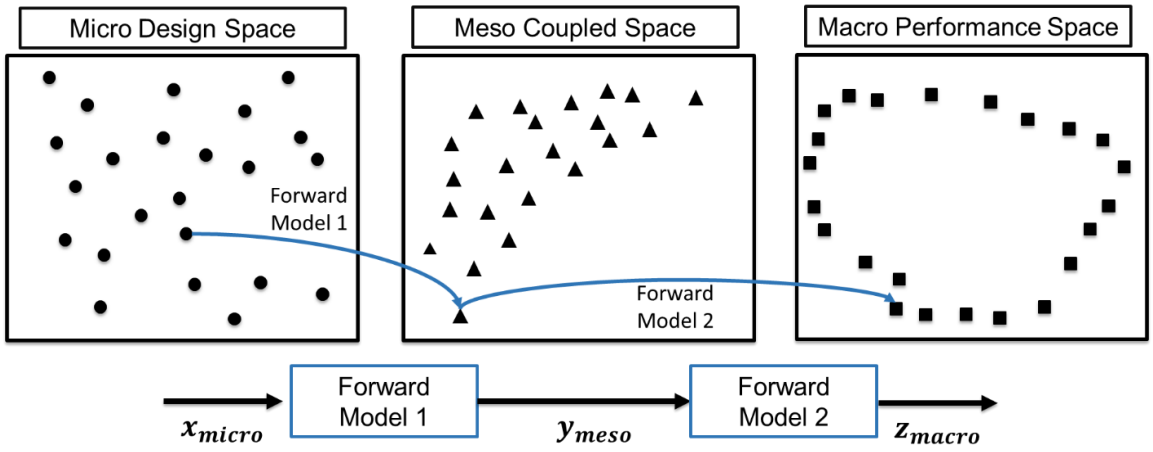

Figure 2.1: Forward modeling of designs to their respective performance for a three level hierarchical design problem.

After utilizing the forward models to determine the performance of a set of designs, performance thresholds are established in the highest (macro) level performance space. The performance thresholds define regions of the performance space that are desired or deemed satisfactory. With the performance thresholds selected, performance predictions can be classified as satisfactory or unsatisfactory if they are within or outside of the region defined by the performance thresholds, respectively. The classification at the highest performance level is back-propagated to the designs that yield that performance at the lower levels. Through this back-propagation strategy, designs at the lowest, micro-level can be classified as satisfactory or unsatisfactory. Figure 2.2 is provided to illustrate the back-propagation strategy and the classification of designs and performance predictions at each level of the example problem.

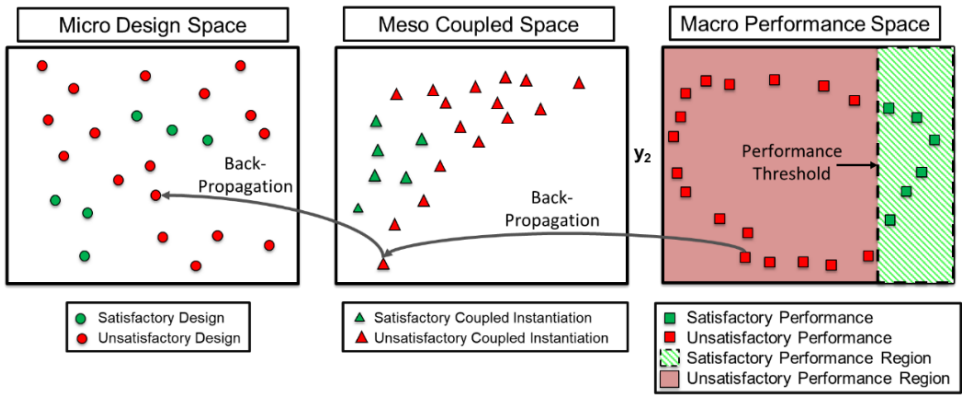

Figure 2.2: Classification of design and performance spaces based on a performance threshold at the highest level.

Following classification of candidate designs, mappings can be generated at each scale that predict the classification of new candidate designs that have not yet been evaluated. These mappings are generated by a Bayesian Network Classifier (BNC), which is a probabilistic algorithm that predicts the classification of designs [44-47]. In Figure 2.3, mappings are shown at each level of the design space that predict the classification of new designs for the simple example problem. The following section discusses how the mappings are generated from the known data points.

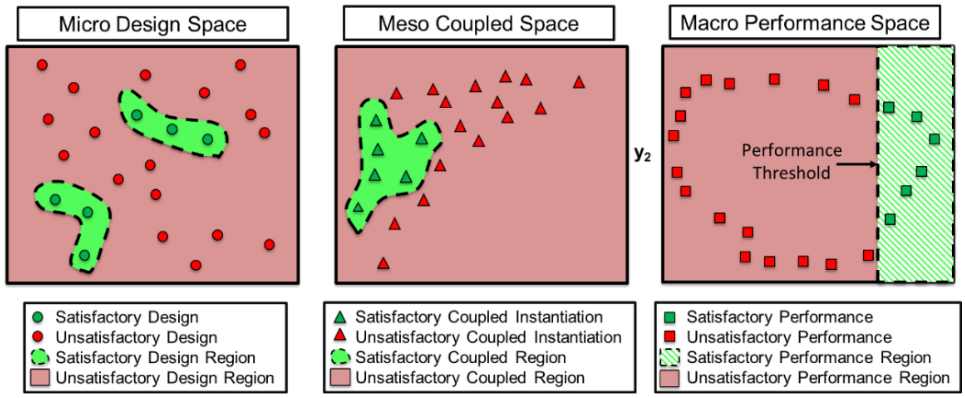

Figure 2.3: Illustration of mappings predicting the classification of candidate designs for a multilevel design problem.

To begin this discussion, the flowchart of Figure 2.4 is provided that explains the complete BNC approach for classifying the design space into regions of satisfactory and unsatisfactory designs. The flowchart serves as a reference to ensure the process is conveyed clearly.

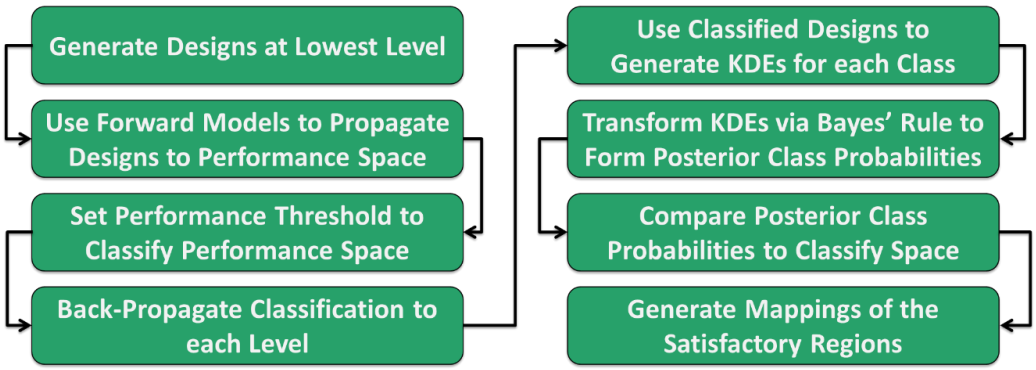

Figure 2.4: Flowchart illustrating the steps of the BNC approach used to map regions of satisfactory designs.

The left side of the flowchart shown in Figure 2.4 has been discussed in this section but the right hand side has yet to be discussed. Propagation of classifications is a trivial process but generating the mappings that partition design spaces is more difficult and can be accomplished with BNCs. BNCs are based on Bayesian statistics to generate probabilistic surfaces that predict the classification of designs, i.e., whether a design is satisfactory or unsatisfactory. Before the probabilistic classifier can be generated, the relationship between the design variables must be selected or determined. The relationships or conditional dependencies between design variables are naturally described by directed acyclic graphical models (DAGs) [48]. Nodes of the graph correspond to design variables and directed edges between nodes imply conditional dependence between variables.

Numerous graph structures exist to describe the dependencies of variables in design spaces, but there are two common graphs which are shown in Figure 2.5.

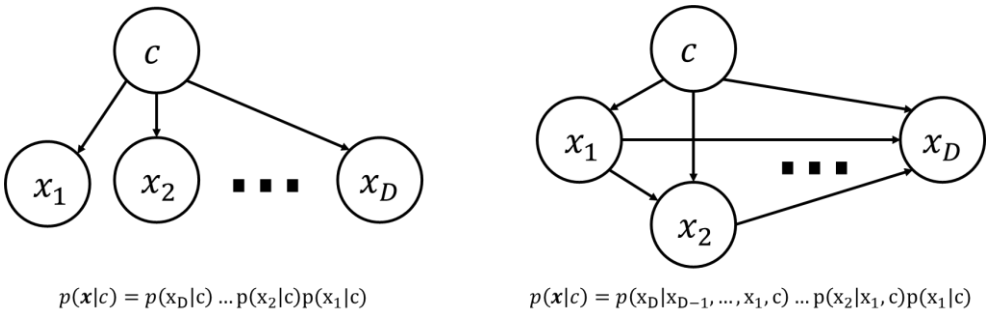

Figure 2.5: Directed acyclic graphical models describing a fully independent network (left) and a fully dependent network (right).

The first DAG describes a fully-independent or naïve network [44] in which the design variables are only conditionally dependent on the class. The second DAG describes a fully-dependent network in which there is a conditional dependency between each of the design variables as well as the class [49]. When one variable is conditionally dependent on another, the node at the beginning of the directed edge is named the parent node, and the terminal node is the child node. The conditional dependencies and DAGs provide a way of describing the class-conditional probability, $p(\boldsymbol{x}|c_l)$, of a candidate design, $\boldsymbol{x}$, for a class, c_l, in terms of the marginal distributions [47]. The class-conditional probability evaluates the probability of selecting a point given the class. In the context of multilevel design the class-conditional distribution is the probability of selecting a design given the specification of a satisfactory or unsatisfactory class.

A common way to determine the class-conditional probabilities is through kernel density estimates (KDE) [50-52]. To generate a KDE, a tunable Gaussian distribution is centered over each satisfactory training point in the design space. The individual Gaussian

distributions are aggregated into the KDE in the design space. Likewise, the same procedure is performed on the unsatisfactory design points to yield the KDE for the unsatisfactory class. Equation 2.1 provides the general form for how the distributions are aggregated for a class, c_l, based on the DAG that describes the dependencies.

$$p(\boldsymbol{x}|c_l) = \prod_{i=1}^{D} p(x_i|pa_i, c_l) = \prod_{i=1}^{D} \frac{1}{N_l} \sum_{j=1}^{N_l} \frac{\prod_{k=1}^{K} \mathcal{N}_k^j(pa_{i,k}, \hat{x}_k^j, \sigma_{k,l})}{\sum_{r=1}^{N_l} \prod_{s=1}^{K} \mathcal{N}_s^r(pa_i, \hat{x}_s^r, \sigma_{s,l})} \frac{1}{\sigma_{i,l}\sqrt{2\pi}} e^{\frac{\left(x_i - \hat{x}_i^j\right)^2}{2\sigma_{i,l}^2}} \quad (2.1)$$

$$where$$

$$\mathcal{N}_m^n(x_m, \hat{x}_m^n, \sigma_m) = \frac{1}{\sigma_m\sqrt{2\pi}} e^{-\frac{(x_m - \hat{x}_m^n)^2}{2\sigma_m^2}}$$

In Equation 2.1, $\boldsymbol{x}$ is the candidate design of interest, $\hat{\boldsymbol{x}}^j$ is j^{th} training point, $\sigma_{i,l}$ is the bandwidth of the Gaussian distribution for the i^{th} dimension of a D-dimensional design space, pa_i is the set of parent variables for the i^{th} dimension, and N_l is the number of training points for class, l.

The form of Equation 2.1 is dependent on the network structure of the design variables or the conditional dependencies. Choosing the correct network structure has been shown to increase the ultimate classification accuracy with fewer training points but *a priori* knowledge of the network structure is typically unknown. Previous work by Sharpe *et al.* focused on uncovering the underlying structure of the network dependencies by using a genetic algorithm that encodes the network dependency [53]. The cross-validation classification accuracy is used as the fitness function to determine which network structures "survive" and "mate" resulting in an approach that has shown significant promise for obtaining an accurate network structure. A simpler but possibly more inaccurate approach is to assume that the network is either naïve or fully-dependent. Equation 2.1 simplifies to

Equations 2.2 and 2.3 when the relationships are assumed to be fully independent or dependent, respectively.

$$p(\boldsymbol{x}|c_l) = \prod_{i=1}^{D} \frac{1}{N_l} \sum_{j=1}^{N_l} \frac{1}{\sigma_{i,k}\sqrt{2\pi}} e^{\left(-\frac{\left(x_i - x_i^j\right)^2}{2\sigma_{i,k}^2}\right)} \tag{2.2}$$

$$p(\boldsymbol{x}|c_k) = \frac{1}{N_l} \sum_{j=1}^{N_l} \prod_{i=1}^{D} \frac{1}{\sigma_{i,k}\sqrt{2\pi}} e^{\left(-\frac{\left(x_i - x_i^j\right)^2}{2\sigma_{i,k}^2}\right)} \tag{2.3}$$

There are advantages and disadvantages to both network structures in regards to the time required to calculate the KDE and the accuracy of the classification. The fully-dependent KDE, given enough training data, will approach the true classification distribution, but the computation time scales with the product of the number of training points and dimensions. The fully-independent KDE has variable accuracy but much less computational expense that scales only with the number of points [54].

To clarify how a KDE is generated, an illustration of a KDE being formed in a one dimensional space is provided by Figure 2.6.

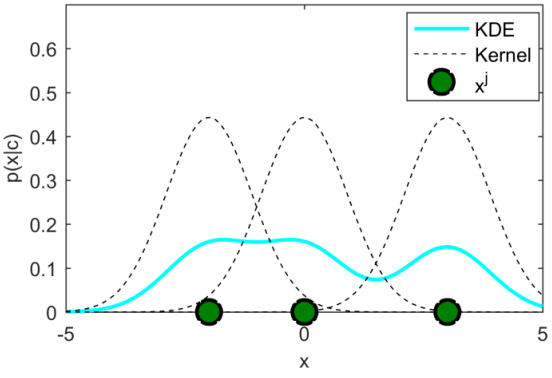

Figure 2.6: Illustration of a kernel density estimate being formed in 1D space.

In Figure 2.6, the training points are indicated by the green circles and a tunable Gaussian distribution is centered on each point which are shown by the dotted lines. Then the distributions are summed and normalized resulting in the KDE shown by the turquoise line.

Given a set of classified designs and an assumed network structure, Equation 2.1 generates two non-parametric class-conditional probability functions that can be evaluated for any arbitrary design. This class-conditional probability predicts the probability of selecting a design given a satisfactory or unsatisfactory class, but the goal of classification is to assign a class for each candidate design. To obtain this classification, Bayes' theorem is leveraged to generate the posterior class probabilities, $(c_l|\boldsymbol{x})$. The posterior class probability estimates the probability that a candidate design belongs to a specific class. To determine its values, a prior probability of a class, $p(c_l)$, is required, but it is typically unknown. For this work it is assumed to be equal to the proportion of training points in the class. Equation 2.4 provides the relationship between the prior probability, class-conditional probability, posterior class probability, and evidence, $p(\boldsymbol{x})$, via Bayes' theorem.

$$p(c_l|\boldsymbol{x}) = \frac{p(c_l)p(\boldsymbol{x}|c_l)}{p(\boldsymbol{x})} = \frac{p(c_l)p(\boldsymbol{x}|c_l)}{\sum_{l=1}^{2} p(\boldsymbol{x}|c_l)p(c_l)} \tag{2.4}$$

The goal of the BNC approach is to determine the likelihood a design is satisfactory or not. Therefore, the posterior class probabilities for different classes can be compared to classify a specific candidate design, as shown in Equation 2.5.

$$\boldsymbol{x} \in c_1 \; if \; p(c_1|\boldsymbol{x}) \; > p(c_2|\boldsymbol{x}) \tag{2.5}$$

Equation 2.4 can be substituted into Equation 2.5 to yield Equation 2.6

$$\boldsymbol{x} \in c_1 \; if \; \frac{p(c_1)p(\boldsymbol{x}|c_1)}{\sum_{l=1}^{2} p(\boldsymbol{x}|c_l)p(c_l)} > \frac{p(c_2)p(\boldsymbol{x}|c_2)}{\sum_{l=1}^{2} p(\boldsymbol{x}|c_l)p(c_l)} \tag{2.6}$$

Since the denominator of Equation 2.6 is only zero in degenerative cases, Equation 2.6 can be manipulated to yield Equations 2.7 and 2.8:

$$\boldsymbol{x} \in c_1 \; if \; p(c_1)p(\boldsymbol{x}|c_1) - p(c_2)p(\boldsymbol{x}|c_2) > 0 \tag{2.7}$$

$$\boldsymbol{x} \in c_2 \; if \; p(c_1)p(\boldsymbol{x}|c_1) - p(c_2)p(\boldsymbol{x}|c_2) < 0 \tag{2.8}$$

Equations 2.7 and 2.8 provide a method for classifying candidate designs with only the prior distributions and class-conditional probabilities, which can be generated with KDEs.

Figure 2.7 illustrates how the posterior class probabilities are generated from two-dimensional candidate designs that are classified as either satisfactory or unsatisfactory. The decision boundary is defined by designs with equivalent posterior probabilities for both classes. The posterior class probabilities are then compared via Equation 2.7 and Equation 2.8 to produce Figure 2.8 where the design space has been partitioned into satisfactory and unsatisfactory regions.

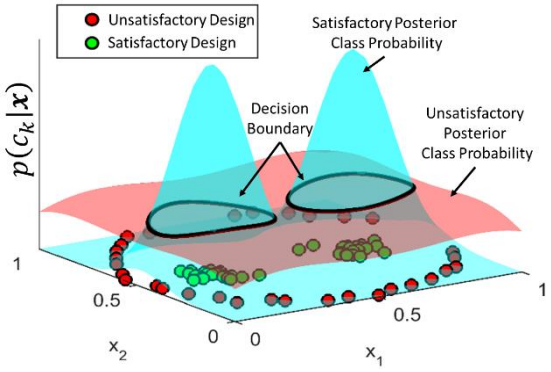

Figure 2.7: Classified satisfactory (green) and unsatisfactory (red) training data generates posterior class probabilities.

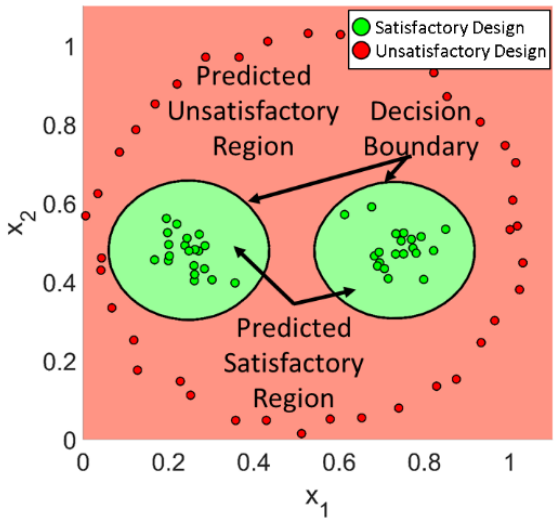

Figure 2.8: Comparing the posterior class probabilities identifies regions of satisfactory or unsatisfactory designs.

2.2 Applications and Limitations of the BNC Approach

Matthews *et al.* [35] adopted the BNC approach for the design of NS metamaterials, which was introduced in Section 1.2. The NS metamaterials design problem was decomposed into three distinct length scales: (1) micro-scale for inclusion design, (2) meso-scale to describe the embedding of the inclusions in a host matrix, and (3) macro-scale to describe the effective properties of the metamaterial. Various inclusion designs

were generated and modeled to predict macro-scale performance. Following modeling, a performance threshold was established at the macro-scale, requiring a certain amount of damping in the metamaterial so performance could be classified and back-propagated to the micro-scale. With the resulting sets of satisfactory and unsatisfactory designs, the BNC approach could be applied. A mapping of the satisfactory design regions was developed through the BNC approach with the results shown in Figure 2.9. The macro-scale performance space is also provided with performance threshold indicated by the shaded region on the right side of the figure.

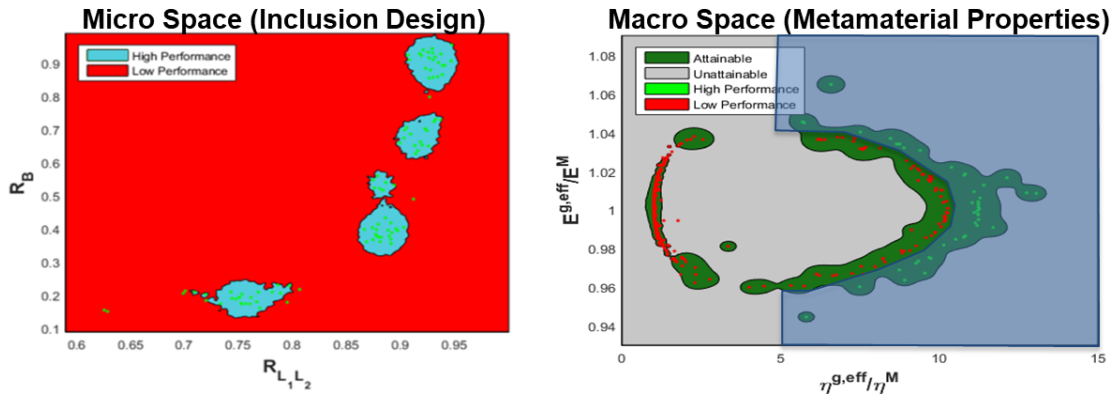

Figure 2.9: Illustration of the BNC approach mapping regions of satisfactory (blue) and unsatisfactory designs (red) in a micro-scale design space (left) of a multilevel materials design problem. A performance threshold was set in the macro-scale performance space (right), as indicated by the shaded region, so the BNC approach could be applied to generate the design space mapping.

The previous work on the design of NS metamaterials effectively identified promising regions of the micro-scale design space with complex, nonrectangular boundaries that could be explored for metamaterial development. Several unsolved challenges remain, however, to apply the BNC approach effectively to this design problem. Specifically, the manufacturing of the inclusions has some degree of variance such that the

nominal dimensions and material properties of the inclusion do not match the physical product precisely. To manufacture the NS inclusions, microstereolithography, a relatively new additive manufacturing technology, must be utilized, and the precision and material properties are not well understood. There may be a large amount of variation in the proposed dimensions or material properties. This variation could be further complicated if the material properties and dimensional accuracy are dependent. Therefore, one of the challenges for developing NS metamaterials is identifying designs that will perform reliably when manufactured.

The simplest but most time consuming method for resolving this challenge would be to identify a satisfactory design, manufacture the design, and measure performance. While this brute-force approach may result in the eventual identification of a reliable inclusion design a more sophisticated approach could be explored for identifying reliably manufacturable designs. The manufacturing variation could be measured and modeled by some probabilistic distribution so it can be incorporated into the BNC approach allowing for reliably manufacturable and satisfactory designs to be identified. This identification would cause only the most reliable designs to be manufactured reducing the time of production for a viable product.

The second challenge that must be addressed for the design of NS metamaterials is to expand the number of variables used to describe the inclusions. The NS inclusions were initially described by only two dimensionless ratios that partially determined their geometry. This dimension reduction restricted the design space, so that a wide variety of inclusions that could be produced were not being explored. To better explore the design space, more design variables must be included such as the material properties. Also, the dimensionless ratios should be omitted in favor of the absolute geometric parametrization of the inclusions for more intuitive interpretations of the design space. By including more

than three design variables, the ability to simply visualize the design space mappings shown in Figure 2.9 is lost. Visual mappings provide intangible insight into the physics of the problem and relationships between design variables. For nonlinear problems such as NS metamaterials viewing the structure of the design region that leads to satisfactory performance can provide insights into the problem that could not have been obtained by any other means. To continue to present these intuitive mappings when more than three variables are present, a visualization framework specific to the BNC approach must be developed.

To address this challenge the proposed general workflow shown in Figure 2.10 will be adopted.

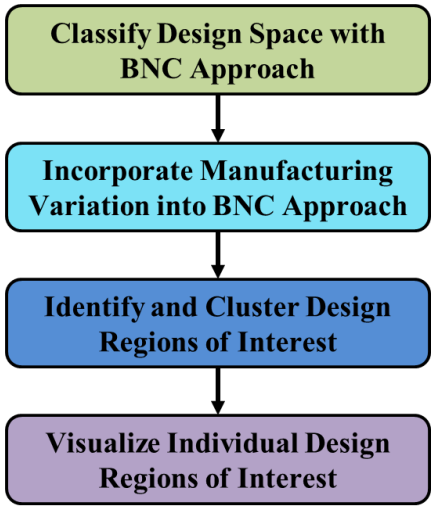

Figure 2.10: Flowchart of proposed visualization methodology for the BNC approach.

The method uses the BNC approach to classify a high-dimensional design space into satisfactory and unsatisfactory regions. Furthermore, by incorporating manufacturing variation, design regions that are not only satisfactory but reliably manufacturable can be identified. There may be multiple, disjoint regions, so a spectral clustering-based method

is utilized to identify individual regions or clusters of promising designs. Following identification of the clusters, a dimension reduction/visualization technique is used to visualize each individual region. Observation of the topology, structure, and number of satisfactory regions may elucidate hidden, nonlinear relationships between variables that otherwise would have remained explored. Clustering and visualization, though, are not simple tasks, and a vast body of literature exists for various methods that have problem-dependent strengths and weakness. Accordingly, this work proposes a framework to systematically inform the designer of the quality of a visualization approach for the problem of interest. It also introduces a visualization approach that has not been applied within the design automation community. It works well for this problem, but it may not be superior for all applications.

The research requirements for augmenting the BNC approach for materials design can be summarized by Table 2.1.

Table 2.1: Research tasks of this work.

1	Incorporate manufacturing variation inherent to production into the BNC approach.
2	Provide the designer with an effective and appropriate clustering method for identification of design regions of interest in a high dimensional design space.
3	Provide the designer with an effective and appropriate visualization technique to visualize each cluster/region in a high dimensional design space.
4	Apply the new design tool to manufacture and evaluate a NS metamaterial.

2.3 Research Objectives

By augmenting the BNC approach, this work will develop a design tool that addresses two limitations of the approach and leads to the central thesis of this work:

The Bayesian Network Classifier approach can be expanded by incorporating manufacturing variation to generate satisfactory and reliably manufacturable designs. Furthermore, by introducing a visualization methodology to the approach, regions of interest in a high dimensional design space can identified and visually interpreted for increased insight into the problem. By applying this augmented approach to complex, hierarchical systems, manufacturable designs can be easily identified allowing for rapid fabrication of satisfactory products.

To accomplish the thesis of this work, the methodology for incorporating manufacturing variation into the BNC approach will be introduced in Chapter 3. Following the flowchart from Figure 2.10, the identification of design regions through clustering will be discussed in Chapter 4. In Chapter 4, variations of spectral clustering will be compared and applied to demonstrate their efficacy for problem-dependent scenarios. An introduction and discussion of visualization techniques for cluster/region visualization follows in Chapter 5. A novel metric for visualization evaluation will be introduced, which allows designers to select the most appropriate visualization technique. Furthermore, a recently developed visualization technique will be utilized for design space exploration. Whereas in Chapters 3-5, the desired design tool will be developed, Chapter 6 will fully develop the NS metamaterial problem and apply the complete BNC design tool to visualize reliably manufacturable regions and identify a design of interest for manufacturing. Chapter 7 will provide details of how the selected design was manufactured and integrated into a NS metamaterial, so it could be mechanically tested to evaluate its performance. Finally, in Chapter 8, future avenues of work for the design of NS metamaterials through the BNC approach are discussed.

Chapter 3: Incorporating Manufacturing Variation into the BNC Approach

To accomplish the first task of incorporating manufacturing variation into the BNC approach, the role of manufacturing variation in design must be discussed. Therefore Section 3.1 discusses approaches for describing and incorporating manufacturing variation into various design approaches. Section 3.2 describes the approach selected for this work, which is representing manufacturing variation with multivariate joint probability distributions [55-57]. After describing the benefits of using multivariate joint probability distributions for modeling manufacturing variation, the strategy for incorporating the distributions into the BNC approach is outlined in Section 3.3. The proposed approach invokes a dual classification strategy in which candidate designs are classified first according to the candidate design's performance capabilities and then according to the likelihood that the candidate design provides satisfactory performance after manufacturing variability is considered. Finally, the implications of the proposed approach are discussed in Section 3.4.

3.1 Designing with Variation

In engineering design there are two different categories of variation: (1) epistemic variation, which arises from insufficient information, and (2) aleatory variability, which is the irreducible variability that cannot be eliminated from a system [58]. Typically, epistemic uncertainty is described by Evidence Theory [59] or Possibility Theory [60], whereas aleatory variability is described with probability distributions or intervals. Epistemic variation is of significant interest to the design community because it is inherent to all computational models including forward models and metamodels. One source of epistemic variation is the precision of the machine, which limits the numerical accuracy of

computational models. Secondly, models are based on assumptions, which are commonly known as approximations. If the assumptions are improved to better align with the true system, the accuracy of the model increases, but the model itself likely becomes more complex. Significant research has been conducted to identify robust designs when epistemic uncertainty is considered. These methods include but are not limited to Random/Fuzzy Continuous Discrete Variables Design Optimization (RFCDV-DO) [61], Possibility-Based Robust Design [62], Modified Bayesian Kriging Modeling (MBKG) [63], and Extended Expected Improvement Bayesian Global Optimization (EEI BGO) [64]. These approaches, though, are typically applicable to single-level optimization problems; whereas, the focus of this work is multilevel set-based approaches and incorporating aleatory variation.

Aleatory variation cannot be eliminated and is simply inherent to any physical system. The variation in geometry of a part or the variation in material properties are both examples of aleatory variation. This variation inherently exists due to entropy, implying manufacturing variation is an example of aleatory variation. It should be noted that all variation is intrinsically epistemic because if sufficient information is known about a system it can be eliminated. Therefore aleatory variation is typically thought of as the uncertainty that would require too many resources to eliminate, implying a degree of subjectivity to the definition. For the purposes of this research, however, the manufacturing variation is assumed to be aleatory which is an approach adopted by other works.

Manufacturing variation is not the only source of aleatory variation. For example, common design variables for systems, such as input force, voltage, or current may vary due to uncontrollable causes. This variation has driven the classification of design variables to be either deterministic or stochastic, such that deterministic design variables do not vary and stochastic variables exhibit aleatory variation. There have been efforts to incorporate

stochastic variables into design frameworks. Specifically, this work is focused on approaches that incorporate stochastic variables that arise due to manufacturing variation. Some of these frameworks, like those described previously, are single-level optimization based approaches. Examples include the work of Yu and Ishii [65] who developed an optimization strategy to design a robust molded helical gear with the minimum peak-to-peak transmission error (PPTE). The approach reformulated the objective function to include the variation in the design variables. This single-objective reformulation required determination of second order derivatives for the objective function which could become computationally prohibitive. It also assumed, for simplification, the stochastic variables were normally distributed which may not always be true. Ahmad *et al.* [66] performed a multi-objective optimization approach to design a 6 degree of freedom haptic device that was insensitive to manufacturing variation. The approach leveraged a genetic algorithm to optimize a weighted sum of performance indices. A robustness constraint was then imposed within the optimization formulation to ensure robust designs are identified.

These approaches effectively identified designs for the desired problems but, as stated earlier, they were for single-level optimization frameworks. The single-level optimization framework as well as assumptions of normality for the stochastic variation severally limit their applicability to multilevel materials design. As a result of the limitations of the previous approaches, other strategies have been developed for multilevel design. Typical multidisciplinary design optimization approaches (MDO) approaches have been modified to incorporate aleatory variation. Examples include Collaborative Optimization, Concurrent Subspace Optimization, and Analytical Target Cascading [67-70]. As discussed in Section 1.2, though, point-based optimization approaches can be infeasible for mixed variable design, computationally expensive, or slow to converge making them less desirable for materials design applications. Therefore, the remainder of

this section will provide a detailed discussion of the progression of incorporating manufacturing variation and aleatory variation into set-based design approaches.

The set-based approach was first modified by Finch and Ward to account for stochastic design variables [68]. The approach built on the initial set-based design work of Ward but expanded the approach by introducing the concept of constraint satisfaction problems (CSP) for set-based variables. This expansion allowed stochastic variables to be introduced to the set-based approach although the stochastic variables were described by intervals rather than probabilistic distributions. By defining causal relationships between variables and providing constraint-based quantified relationships, Finch's approach could eliminate infeasible designs through the Bounding Set Theorem and the Interval Propagation Theorem. This approach was developed to sort through catalogs of parts with known specifications and variations to identify the most reliable configuration of products given a performance interval. To apply the approach, analytical relationships between design variables and performance parameters were essential; furthermore, the approach suffered when the complexity of the problem increased due to the computational requirements needed to sort through designs for elimination.

Building on the work of Finch and Ward, various researchers expanded the set-based approach to assist in concept selection when both epistemic and aleatory variation are present [69-71]. Rekuc *et al.* developed an approach that modeled imprecision or variation through probability bounds analysis (PBA). PBA are natural ways of describing the uncertainty in concept generation when design requirements are nebulous. Rather than provide a single distribution with a single mean and standard deviation to describe the variability of a stochastic variable, it provides an interval on the mean and standard deviations to indicate a higher level of uncertainty. The PBA approach facilitated the use of distributions to describe the performance of set of designs to be propagated. The decision

maker (DM) could then eliminate sets of designs based on their single-valued performance by using interval dominance, maximality, and E-admissibility criterion [69]. This approach was expanded by Malak *et al.* to incorporate multiple objectives. This approach was shown useful for concept selection using the set-based approach but suffered from computational expense when sorting through designs for concept generation. Furthermore, if the forward modeling of candidate designs is computationally expensive, this approach would not be viable. Similar research has been conducted to utilize the set-based approach for concept generation, but these approaches have not been developed for multilevel frameworks [70]. The only method known to the author that incorporates aleatory variation into multi-level design using a set-based approach is the modified Inductive Design Exploration Method (IDEM), which also considers epistemic variation [72].

IDEM was introduced in Chapter 1 as a multilevel, set-based approach that was leveraged for materials design. The approach, originally developed by Choi *et al.* [73], was furthered by Sinha *et al.* [74] to incorporate numerous sources of variation including both aleatory and epistemic variation. The adapted approach closely follows the initial IDEM approach of discretizing the design space into an n-dimensional grid where the points of intersection are evaluated with a forward model. Following sampling, points are classified by whether they meet performance criteria, and if a point does meet the criteria, a Gaussian kernel is centered on the point. This step is followed by a summation over the entire space to generate a classification metamodel. From this point, the approach was augmented to incorporate variation, which allows for an upper bounding and lower bounding model to be fit to the data by assuming normal variation of the design variables. With the upper bound and lower bound known, a metric known as the hyperdimensional error margin index (HD_EMI) is utilized to indicate the reliability of a design relative to constraints and performance metrics. Using this approach, mappings of robust regions of the design space

can be generated, but it still relies on a large number of training points due to its required evaluation of all points on the grid. Therefore, for computationally expensive forward models the approach is not truly feasible for developing accurate mappings of the design space.

From this literature review, it is apparent that challenges must be addressed for incorporating manufacturing variation into a multilevel design framework. First, no computationally efficient set-based approached exists that incorporates manufacturing variation into the design framework. This dissertation provides a strategy for doing so that is more computationally efficient than current methods. Second, many of the approaches have been limited to modeling manufacturing or aleatory variation as distributed normally or uniformly (by intervals). This dissertation demonstrates that arbitrary, non-parametric distributions can be compiled to model manufacturing variation more flexibly, so it can be incorporated into the BNC approach. The following section discusses the various models that can be used for modeling manufacturing variation in the BNC approach.

3.2 MODELING MANUFACTURING VARIATION WITH MULTIVARIATE JOINT PROBABILITY DISTRIBUTIONS

An intended design likely differs from its as-built counterpart in measurable ways. Furthermore, if the same design were manufactured numerous times, a range of characteristics could be measured and eventually modelled. The variation in characteristics may be dependent not only on the manufacturing process but also on the design being manufactured. For example, a certain design may be manufacturable by a CNC machine, but another design may require a metal additive manufacturing system to produce. These systems induce different variations in the as-built designs, implying that the model chosen to represent manufacturing variation should reflect this dependency. To model these

complex manufacturing variations, multivariate joint probability density functions are utilized because they represent the probability that each of several design variables assume specific values (i.e., they are capable of capturing design variable interdependencies), and they can model manufacturing-induced variation in a very general way, without necessarily assuming a functional form. Furthermore, they can be built from KDEs and integrated straightforwardly into the BNC approach for multilevel design.

A continuous multivariate joint probability density function, $f(x_1, \dots, x_n)$, is used to calculate the joint probability of occurrence of multiple variables, $x_1, \dots, x_n$. A continuous multivariate joint probability density function must satisfy the conditions specified by Equations (3.1-3.3) [75]:

1. The probability of any particular occurrence $(x_1, \dots, x_n)$ must be greater than or equal to zero.

$$f(x_1, \dots, x_n) \geq 0 \tag{3.1}$$

2. The entire hyper-volume of the distribution must be equal to 1

$$\int_{-\infty}^{\infty} \dots \int_{-\infty}^{\infty} f(x_1, \dots, x_n)\, dx_1 \dots dx_n = 1 \tag{3.2}$$

3. The probability that continuous random variables, $X_1, \dots, X_n$, lie in a region, ϕ, is equal to the hyper-volume of the joint probability density function bounded by the region.

$$P[(X_1, \dots, X_n) \in \phi] = \int_{\phi} f(x_1, \dots, x_n) dx_1 \dots dx_n \tag{3.3}$$

These properties provide the most general description of a multivariate joint density function, and they provide significant freedom for selecting an appropriate distribution to model the manufacturing variation. A pivotal detail regarding these 3 conditions is that no

restriction has been imposed on the independence of the individual variables. This feature is important when considering manufacturing variability because the probability distribution of a design variable may be conditional on the value of another design variable; i.e., the variables may require a joint distribution for dependent, rather than independent, variables. Whether the variables can be considered independent or dependent when formulating a joint probability distribution could differ from problem to problem and variable to variable, so strategies for implementing both cases are discussed below.

The simplest multivariate joint probability distributions are those in which the design variables are independent. Independence can be defined by the multivariate joint probability distribution and the marginal distributions. A marginal distribution, $g_i(x_i)$, is the univariate probability distribution of a random variable, x_i, and is defined in terms of the multivariate joint probability distribution, $f(x_1, \dots, x_n)$, by Equation (3.4) [75].

$$g_i(x_i) = \int_{-\infty}^{\infty} \dots \int_{-\infty}^{\infty} f(x_1, \dots, x_n) \frac{dx_1 \dots dx_n}{dx_i} \tag{3.4}$$

The random variables $x_1, \dots, x_n$ are considered independent if Equation (3.5) is true [28]

$$f(x_1, \dots, x_n) = g_1(x_1) \dots g_n(x_n) \tag{3.5}$$

For a given manufacturing process *and* design it is difficult to determine definitively whether this independence relation is true. To confirm independence, the designer must have exact knowledge of $f(x_1, \dots, x_n)$, which he or she likely does not possess. Therefore, it is the task of the designer to decide whether the manufacturing variation can be characterized by independent variables. Empirical results can corroborate

the decision, but they could be resource intensive to gather. If independence cannot be assumed or proven, dependence must be assumed.

After independence or dependence is determined, a multivariate joint probability distribution can be generated to model empirical manufacturing data. There are many parametric distributions that can be leveraged for this purpose. These multivariate joint probability distributions include normal, lognormal, gamma, and uniform distributions as well as many others. An advantage of using these parametric distributions is that many of them, such as normal and lognormal distributions, can be parameterized for both dependent and independent variables. Unfortunately, many of the standard parametric distributions rely on linear dependencies between variables, which do not capture nonlinear dependencies. For example, in the bivariate normal distribution [75]:

$$p(\vec{\boldsymbol{x}}) = \frac{1}{2\pi}|\Sigma|^{-\frac{1}{2}} \exp\left(-\frac{1}{2}(\vec{\boldsymbol{x}} - \vec{\boldsymbol{\mu}})^T \Sigma^{-1}(\vec{\boldsymbol{x}} - \vec{\boldsymbol{\mu}})\right) \tag{3.6}$$

$$where$$

$$\vec{\boldsymbol{x}} = \begin{bmatrix} x_1 \\ x_2 \end{bmatrix}, \vec{\boldsymbol{\mu}} = \begin{bmatrix} \mu_1 \\ \mu_2 \end{bmatrix}, \& \ \Sigma = \begin{bmatrix} \sigma_1^2 & \rho\sigma_1\sigma_2 \\ \rho\sigma_1\sigma_2 & \sigma_2^2 \end{bmatrix}$$

The covariance matrix, **Σ,** is parameterized by a constant correlation coefficient ρ, which implies that x_1 and x_2 are linearly dependent. Due to this assumption of linear dependence, parametric distributions may not be suitable for modeling manufacturing variation. Furthermore, using parametric distributions also implies that the designer has some knowledge of the manufacturing variation and that it neatly follows the chosen parametric distribution, which may not be the case. For these reasons an alternative approach for modeling the manufacturing variation is utilized here.

An alternative approach is to use KDEs to build a multivariate joint probability distribution from empirical manufacturing data. To form a KDE an assumed joint

probability distribution is centered on each manufacturing data point. The distributions are aggregated over all the data points to form a new joint probability distribution. Typically, a multivariate independent Gaussian probability distribution is centered at each data point, but any distribution can be used. In this paper, a Gaussian probability distribution is used. If there are N manufacturing data points, $\vec{\boldsymbol{x}}^{i=1\ldots N}$, each with D dimensions, Equation 3.7 demonstrates how the KDE is calculated. The value of σ influences the coverage of the Gaussian probability distribution [51].

$$p(\vec{\boldsymbol{x}}) = \frac{1}{N}\sum_{i=1}^{N}\prod_{j=1}^{D}\frac{1}{\sqrt{2\pi}\sigma_j}\mathrm{e}^{\frac{\left(x_j - x_j^i\right)^2}{2\sigma_j^2}} \tag{3.7}$$

This equation yields the dependent multivariate joint probability distribution based only on the manufacturing data supplied. It should be noted that even though the form of the KDE assumes dependence it can still be used for manufacturing variation data based on independent variables.

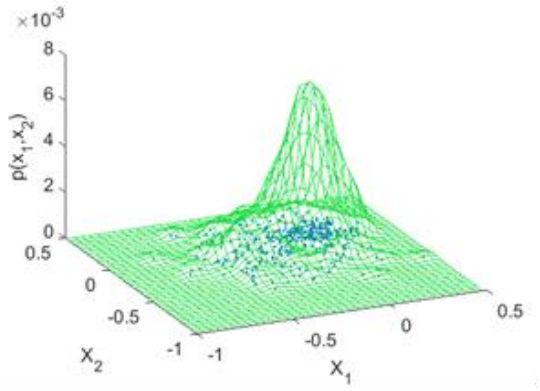

Figure 3.1: Kernel density estimate from random distribution of bivariate data.

Figure 3.1 illustrates a KDE generated from bivariate data points. The points are intended to represent repeated manufactured instantiations of a single design, such that one can begin to see the extent of the manufacturing variation. We can see that regions with a higher density of points have a larger joint probability than more sparse regions. One of the major advantages of utilizing a KDE is that it can encapsulate the linear and nonlinear dependencies between variables but requires no *a priori* knowledge of a parametric function that might accurately model the manufacturing variation. A drawback to this method is that it inherently relies on the availability of sufficient manufacturing data.

For nonparametric distributions, it may be unclear whether sufficient data has been collected to converge to a single distribution. Therefore, this work proposes using a strategy provided by the flowchart of Figure 3.2 to determine whether sufficient manufacturing variation data has been collected.

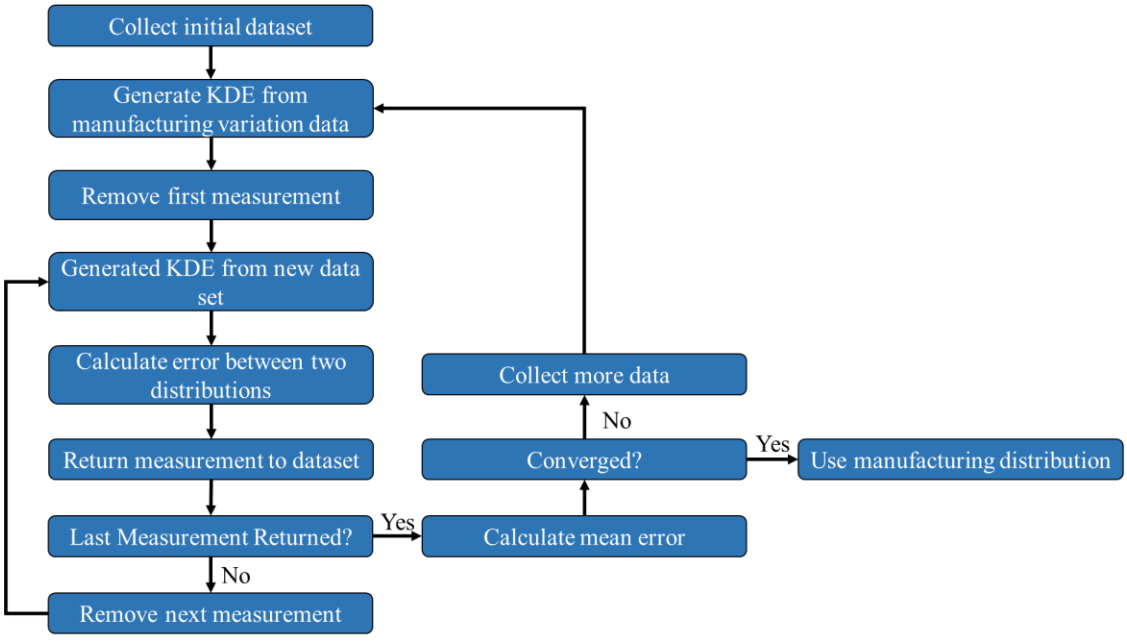

Figure 3.2: Flowchart describing a method for determining whether sufficient manufacturing variation data has been selected to generate a stable KDE.

First, the nonparametric manufacturing variation distribution, $p_0(\vec{\boldsymbol{x}})$, is generated by the KDE of Equation (3.7) using the entire manufacturing variation data set. Next, the k^{th} measurement is omitted from the manufacturing variation data set and a secondary KDE, $p_k(\vec{\boldsymbol{x}})$, given by Equation (3.8), is generated using the remaining measurements.

$$p_k(\vec{\boldsymbol{x}}) = \frac{1}{N-1} \sum_{i=1, i\neq k}^{N} \prod_{j=1}^{D} \frac{1}{\sqrt{2\pi}\sigma_j} \mathrm{e}^{\frac{\left(x_j - x_j^i\right)^2}{2\sigma_j^2}} \tag{3.8}$$

The square of the difference between the original KDE distribution and the second distribution is computed and integrated over the domain, Ω, to yield a scalar value describing the error between the two distributions. The omitted k^{th} point is returned to the data set and the next measurement is then removed so the previously described procedure can be repeated to yield a new error. Once every point in the data set has been removed, the mean error, $\bar{\epsilon}$, can be computed by Equation (3.9).

$$\bar{\epsilon} = \frac{1}{N} \sum_{k=1}^{N} \int_{\Omega} \left(p_k(\vec{\boldsymbol{x}}) - p_0(\vec{\boldsymbol{x}})\right)^2 d\Omega \tag{3.9}$$

If this value is sufficiently close to zero or appears to be converging with diminishing returns as additional data points are compiled, it can be assumed that enough manufacturing variation data has been obtained and the resulting distribution has converged to a stable distribution. Otherwise, more manufacturing variation data should be obtained and the convergence testing procedure repeated. To demonstrate how the error converges to zero as more points are collected, the example distribution shown in Figure

3.3a was used to draw samples. Then the procedure given in Figure 3.2 was followed to produce the plot in Figure 3.3b that shows the mean error as a function of sample size.

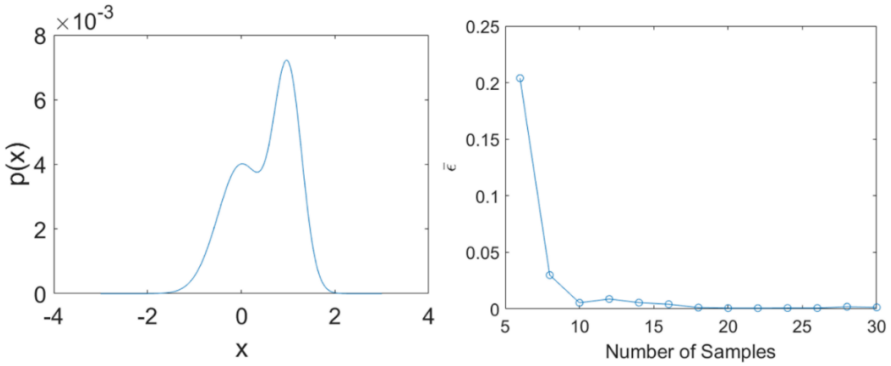

Figure 3.3: Example 1D manufacturing variation (a) where an increasing number of samples were drawn. The mean error using the omission strategy was calculated as a function of the number of points sampled (b).

With the process discussed previously, the manufacturing variation associated with a specific design can be modeled by a multivariate joint probability distribution and incorporated into the set-based BNC approach to determine the satisfactory and reliably manufacturable regions of the design space.

3.3 Strategy to Incorporate Manufacturing Variation into the BNC approach

The BNC approach for design exploration is augmented to enable identification of designs that are reliably manufacturable. In this paper, a candidate design is considered reliably manufacturable if the likelihood that a manufactured part performs satisfactorily exceeds a specified threshold; this threshold is called the reliability threshold. Figure 3.4 provides a broad overview of the work flow of the augmented method. First, the BNC approach classifies or partitions the design space into satisfactory and unsatisfactory regions, based on specified performance thresholds. In the next step, the satisfactory region

is further classified using quantitative models of manufacturing variability to identify candidate designs that are likely to perform well, even when manufacturing variability is taken into account. Following this secondary classification, the constricted design space is mapped to the performance space to identify performance capabilities that are achievable reliably, given the inherent variability in the manufacturing process.

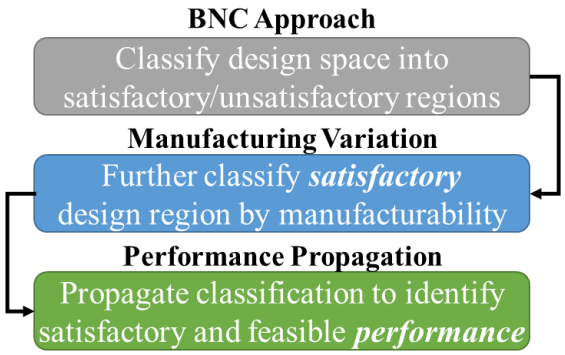

Figure 3.4: Flowchart illustrating the workflow of incorporating manufacturing variability in the BNC approach.

The procedure for classifying designs according to manufacturing reliability is outlined in Figure 3.5. This secondary classification is accomplished by first selecting one of the training points or designs classified as satisfactory. Next, a Monte Carlo sampling method based on the multivariate manufacturing distribution is performed *for each satisfactory design*. The set of sampled designs are classified by the BNC approach as satisfactory or unsatisfactory, and the proportion of the samples classified as satisfactory is determined. If this proportion of satisfactory points meets a designer's specification for the reliability threshold, T_{rel}, the training point is classified as reliably manufacturable. Otherwise the training point is classified as unreliably manufacturable. This process is repeated until all of the satisfactory training points have been reclassified. Furthermore, the

manufacturability classifications of the training points in the design space can be propagated to the performance space to identify performance regions that are reliably attainable as discussed in Section 6.3.

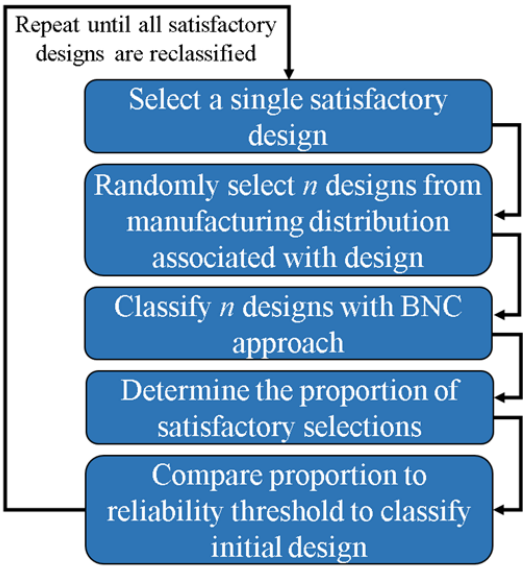

Figure 3.5: Flowchart describing classification scheme for incorporating manufacturing variation.

The procedure for classifying design points based on their manufacturability also has a geometric interpretation. By performing a Monte Carlo sampling of the manufacturing distribution and determining the proportion of satisfactory designs, the volume/hypervolume of the manufacturing distribution bounded by the BNC decision boundary is approximated. Figure provides an illustration of the volume of the manufacturing variation bounded by the BNC decision boundary of the satisfactory design region.

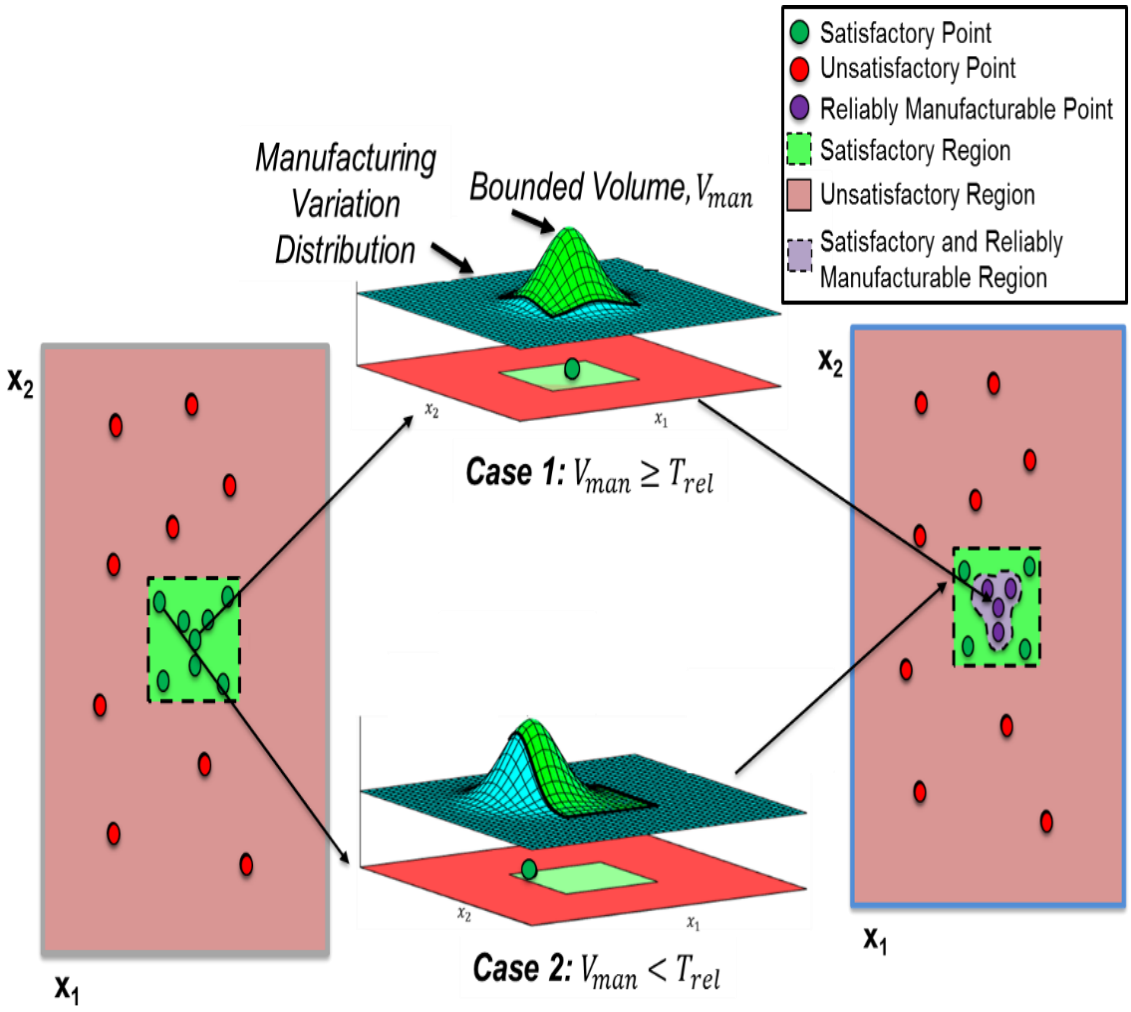

Figure 3.6: Illustration of the geometric interpretation of the relationship between the manufacturing variation and BNC satisfactory region. The manufacturing variation distribution is formed via Monte Carlo sampling from the multivariate manufacturing distribution centered on the candidate point. If the hypervolume of the manufacturing distribution bounded by the BNC decision boundary is greater than a manufacturability threshold specified by the designer, the candidate point is considered reliably manufacturable.

If this bounded volume is greater than or equal to the reliability threshold, then the design point is reliably manufacturable. Increasing the reliability threshold requires the decision boundary to encompass more of the manufacturing variation if a point is to be

considered reliably manufacturable; therefore, as the reliability threshold is increased, fewer designs are classified as reliably manufacturable—a result that matches intuition. As the reliability threshold approaches 100%, the number of points classified as reliably manufacturable approaches a minimum set size. Therefore, a certain amount of leniency from the designer may be required to ensure that some of the designs are identified as reliably manufacturable. A major advantage of the proposed classification method for incorporating manufacturing variation is that it requires very few computational resources to classify points as reliably manufacturable because the Monte Carlo samples are evaluated with the Bayesian network classifier rather than the forward models. For computationally expensive simulations, the Bayesian network classification can be orders of magnitude faster than simulation.

After classification of the designs by manufacturability, two new sets of designs can be created, those that are satisfactory *and* reliably attainable and those that are not. With these two sets of designs, the BNC approach can once again be applied to create design space mappings. Two KDEs can be generated for each set of designs which are transformed by Bayes' rule to produce posterior class probabilities. By comparing the probabilities, regions of satisfactory *and* reliably manufacturable designs can be mapped. Figure 3.7 presents an image of a design space that has been partitioned into three different regions of unsatisfactory designs, satisfactory designs, and satisfactory and reliably manufacturable designs, which are indicated by red, green, and purple respectively.

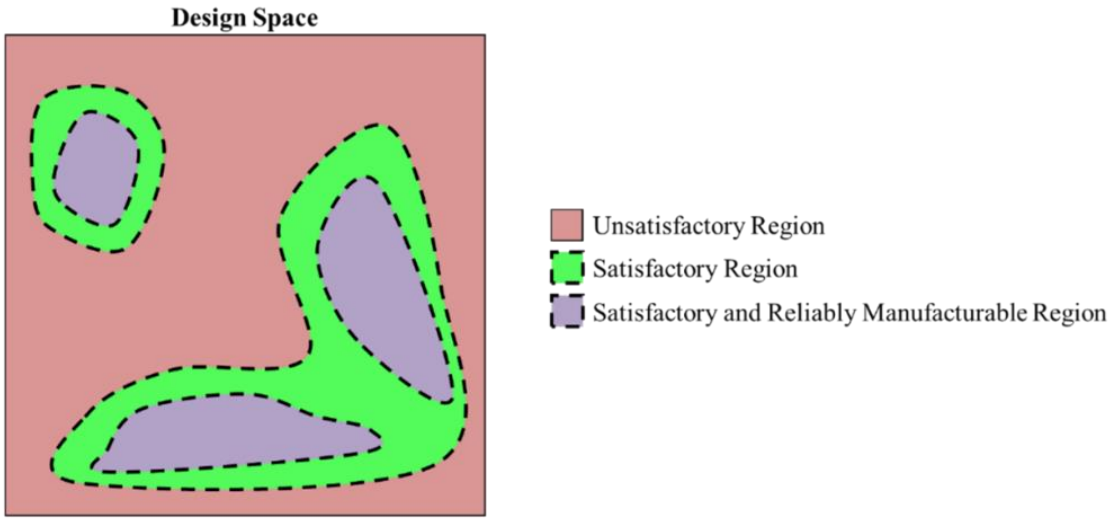

Figure 3.7: Design space that has been classified by manufacturability so regions of unsatisfactory (red), satisfactory (green), and satisfactory *and* reliably manufacturable (purple) design can be mapped with the BNC approach.

After mapping the design space, the final task of the flowchart of Figure 3.4 can be accomplished, namely, reclassifying the highest level performance space by manufacturability. This task is accomplished by forward propagating the design space classification to its associated performance space. This classification once again generates two sets of training points: (1) performance that is satisfactory *and* reliably attainable when the system is manufactured and (2) performance that is either not satisfactory or not reliably attainable after manufacturing. Once the performance training points have been classified, the BNC approach can be applied to the performance space to partition the space into the two classes of regions just discussed. The visual flowchart in Figure 3.8 is provided to illustrate the entire approach for integrating manufacturing variation into the BNC approach to generate intuitive mappings of the design and performance space.

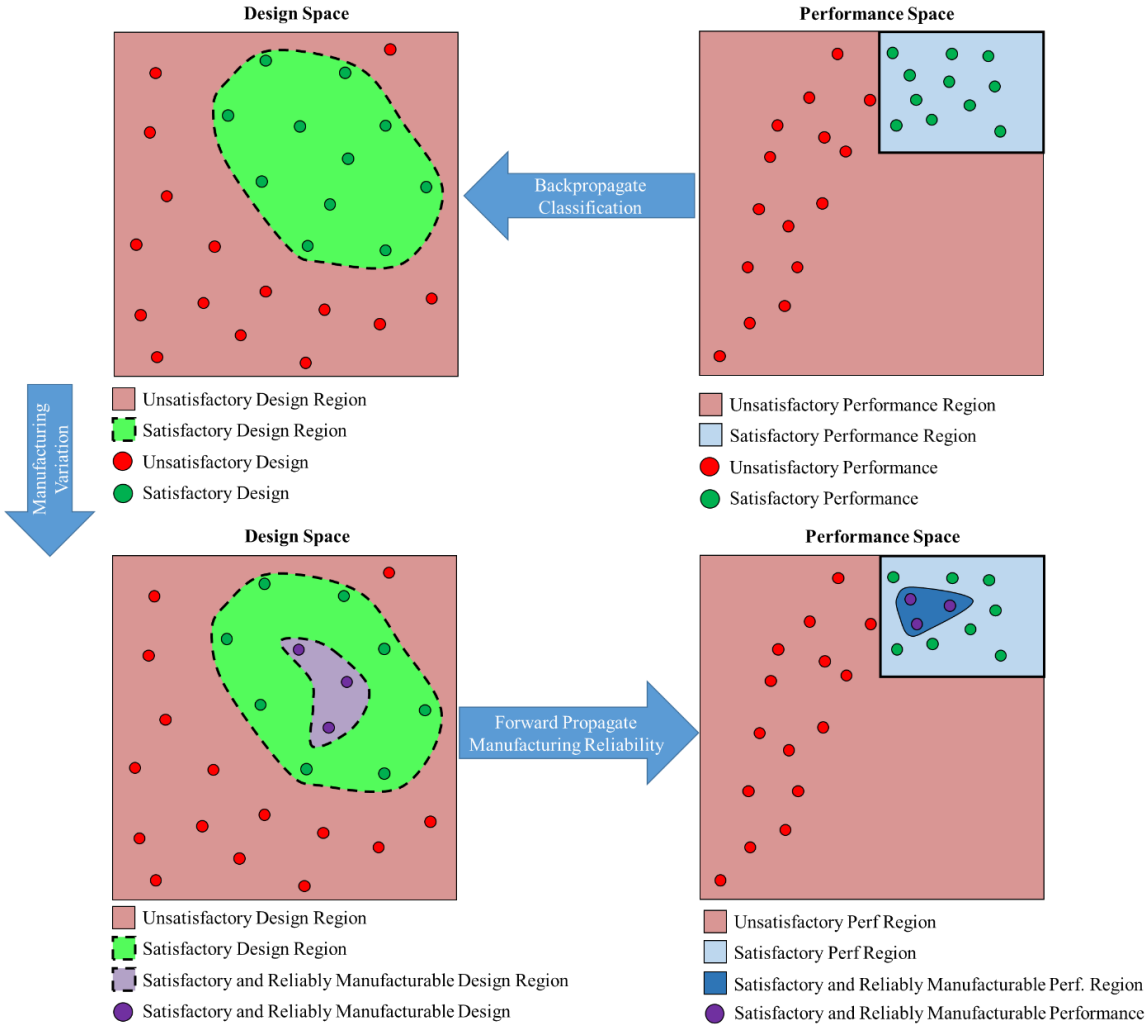

Figure 3.8: Visual flowchart illustrating the incorporation of manufacturing variation in the BNC approach. First, the performance space is classified by a performance threshold (top right). The classification is backpropagated to the design space where the BNC approach is leveraged to generate regions of satisfactory and unsatisfactory designs (top left). Next, manufacturing variation further classifies the design space allowing for regions of satisfactory and reliably manufacturable designs to be generated (bottom left). Finally, the classification is forward propagated to the performance space so regions of reliably attainable performance can be determined (bottom left).

3.4 DISCUSSION

In this chapter, a strategy for incorporating manufacturing variation into the BNC approach was introduced. First, a review of previous strategies for incorporating manufacturing variation into design approaches was provided. Most of the approaches focused on finding robust designs within an optimization framework, but due to the multilevel, nonlinear, and often discrete nature of materials design and the desire to identify sets of promising designs, these approaches were not appropriate. Therefore, previous attempts to incorporate aleatory variation into set-based design approaches were discussed. Many of the approaches utilized the set-based approach for single-level design problems, limiting their utility for materials design. The most relevant approach that accounted for stochastic variables, IDEM, proved to be too computationally expensive to implement for materials design problems with complex forward models. These limitations of previous approaches motivated the development of the set-based approach with manufacturing variation.

To model manufacturing variation, general multivariate joint probability distributions are preferable for their flexibility. These distributions can capture variable dependencies and encompass a wide variety of distributions including nonparametric distributions. Many approaches do not consider or incorporate nonparametric distributions into their design frameworks because they add significant computational cost. With the strategy proposed here, nonparametric distributions have the same computational expense as parametric distributions. The largest difficulty for nonparametric distributions, though, is obtaining enough manufacturing variation data to generate the distributions. To ensure an appropriate dataset had been obtained to accurately model the variation, a root mean squared error approach was introduced that allows the designer to set a threshold for convergence of the distribution.

After selecting a model for manufacturing variation, the strategy for incorporating variation into the BNC approach was provided. First, the original BNC approach was implemented, in which the performance space is classified by a performance threshold allowing the classification to be backpropagated to the design space. Then, a classifier was trained in the design space so arbitrary candidate designs could be classified. A Monte Carlo based approach was used to sample from manufacturing distributions associated with each satisfactory candidate design, and the samples were classified using the newly generated classifier. If a reliability threshold was met, the design was further classified as reliably manufacturable allowing a secondary classifier to be trained to predict reliably manufacturable designs. Finally, the reliably manufacturable design space classification could be forward propagated to the performance space so regions of reliably attainable performance could be obtained. Because reliability was determined using the BNC approach, the method does not suffer from typical computational complexity issues. The classifier is relatively efficient to use, so a Monte Carlo based approach can be leveraged. This approach allowed a broader family of distributions to be used rather than the typical normal or uniform distributions.

These new mappings of reliably manufacturable regions are not easily visualized, however, when the number of design variables exceeds three. Therefore, the following chapter discusses the first step of developing a visualization technique for the BNC approach, which is clustering.

Chapter 4: Identifying Satisfactory Design Regions with Clustering

The BNC approach, introduced in Chapter 2, was furthered to incorporate manufacturing variation in Chapter 3. The approach now classifies design spaces into regions of satisfactory *and* reliably manufacturable designs and unsatisfactory *or* unreliably manufacturable designs. Previously, mappings of the design space were produced to convey information regarding the topology of the regions, but displaying these mappings relied on the design space being low-dimensional with no more than three design variables. As discussed in Chapter 2, the design space is naturally described by much more than three variables. To explore a high-dimensional design space (more than three design variables) with the BNC approach and visualize the regions, a mapping technique more sophisticated than Cartesian plotting must be implemented.

In design automation, visualization methods, which will be further discussed in Chapter 5, can be divided into two general categories: 1) simultaneous mapping of design and performance space and 2) mapping only the design space. Some examples of the first category of methods are Cityplot[76], Visual Design Steering [77], and the ARL Trade Space Visualizer [78]. Examples in the second category are Interactive Multi-Scale Nested Clustering and Aggregation [79] and the method introduced by Chen, *et al*. [80]. This work proposes a visualization strategy within the latter category, and a two-part strategy to visualize the regions of interest classified by the BNC approach is employed. The first task is identification of the number of non-connected regions of interest in the design space, which is followed by the second task of visualizing each region individually. The term "regions of interest" is used to indicate that the proposed visualization approach can be applied to the satisfactory design regions determined by the original BNC approach or satisfactory *and* reliably manufacturable regions identified by the augmented BNC

approach discussed in Chapter 3. To accomplish the first task of visualizing—identification of design regions—clustering will be employed.

Clustering is a general term in the machine learning community describing the unsupervised grouping of data by some type of similarity metric [81]. A vast number of clustering algorithms exist in the literature, but this work describes the most fundamental clustering techniques in Section 4.1. This review of techniques motivates the selection of the clustering technique used in this work, spectral clustering, which is presented in Section 4.2. Once the mathematical theory of spectral clustering is introduced, three different implementations of spectral clustering for identification of design regions are introduced in Sections 4.3-4.5. The three different techniques vary in complexity of implementation, accuracy, computational expense, and degree of automation, which provides the designer with choices that perform better for certain problems. These tradeoffs are demonstrated on example datasets in Section 4.6 to clarify the strengths and weaknesses of the approaches. The goal of the demonstrations is to illustrate how the tradeoffs can be balanced during design exploration to ensure the best clustering and visualization for the present application. Following demonstration, a brief discussion of the approaches is provided to motivate the following chapter on visualization of each identified cluster. The visualization approach will use a modified implementation t-Distributed Stochastic Neighbor Embedding (t-SNE) that optimizes the quality of the visualization to retain both the global and local structure of the clusters

4.1 Review of Clustering Techniques

The first step in developing the visualization methodology proposed in this work is to identify the number of high performance regions in the design space. In three or fewer dimensions, identification is a simple task because the designer can easily plot the data and

visually identify the regions. In higher dimensional spaces, though, this is not possible, so a computational method of identifying regions or clusters must be employed.

A general definition of clustering is to partition a given set of data points into groups that are as similar as possible [81]. This definition can be recast depending on the domain and proposed method used to partition the data, but in general, all methods are essentially trying to accomplish this goal. Identifying higher dimensional clusters of data has been explored in numerous fields including biology, image processing, and text identification [81]. A vast amount of literature exists in these fields for identifying clusters for various types of data including categorical, discrete, and continuous. Due to this large amount of literature, it is difficult to complete an exhaustive review of all methods used to identify clusters, but a brief review of common methods to identify clusters in the mechanical design community is provided next.

Methods like K-means [82], Fuzzy C-Means [83], and Gaussian Mixture modeling [84] cluster data via similar techniques. Through an iterative process that begins with a user-defined initial seeding of centroids or centers of normal distributions, each method uses a distance metric to determine to which centroid group or normal distribution each point belongs. With each iteration, the location of the centroids or centers is updated until the algorithm converges. The differences between the methods lie in whether hard or soft clustering is used and whether the covariance matrix of the normal distribution is varied. While these methods are known to produce viable clusters for many datasets, they typically require an initial guess of the number of clusters and are prone to local minimum convergence rather than global. They also do not perform well unless the data clusters follow a Gaussian distribution [81, 47].

Hierarchical Clustering Algorithms [85] do not require an initial guess of the number of clusters to build hierarchical structures of clusters. Agglomerative hierarchical

algorithms begin at the bottom level of the hierarchy with each data point as a data cluster and merge two clusters at a time until all data points are grouped in one cluster. Divisive hierarchical algorithms begin with all data points in one cluster and iteratively split the data into clusters until each data point belongs to its own cluster. With hierarchical algorithms, the partitioning can be illustrated using a dendrogram which shows how the data is partitioned at each level. The simplicity and deterministic nature of hierarchical clusters makes them attractive in many fields but determining which of the branches of the dendrogram is the correct clustering is still ambiguous, which makes them less attractive for the needs of this work.

Self-organizing maps (SOM) [86], are another commonly used method for identifying clusters. They are simultaneous clustering and visualization techniques in which the goal is to construct an artificial neural network in which the nodes attempt to capture the behavior of the data through an associated vector weight on the node. Through an iterative process, the number of clusters can be determined, and the original *n*-dimensional space is mapped to a 2D space in which different clusters are identifiable. While this method is promising for determining clusters, the number of clusters identified can be erroneous, and the 2D mappings can struggle to capture the high dimensional topology of the original space. Dependencies between variables are lost, and only the approximate "size" of the clusters is obtained. Research has been performed by Richardson *et al.* [87] to obtain more meaningful measures from the data, but the inability to map the original data in an intuitive way is a significant disadvantage of SOMs for the present application.

Grid-based clustering algorithms can be used to determine the underlying structure of the data by partitioning the data space into a finite number of cells and then calculating the density of each cell. From this information, regions of high density can be explored and

probed further to understand the space. Grid-based clustering algorithms are used primarily for their simplicity but do not handle non-uniform data or data with large variations in their structure well. Also, they can fail if the dimensionality becomes too high because the number of cells can grow exponentially with dimensionality. Research has been performed to improve the efficacy of the grid-based method through adaptive grid refinement and axis-shifted grid clustering, but much of the utility in the method is in obtaining an initial understanding of the space rather than detailed information [88].

Spectral Clustering [89] is a promising method of clustering that requires no assumptions of the shapes of clusters and does not need an initial seeding of the number of clusters. Unlike many of the other methods discussed and used in the design automation community [76, 78-95], it does not need to perform iterations to determine the number of clusters. It is deterministic and typically only requires the user to input a similarity graph of the data points [96-98]. The drawback of spectral clustering is the computational expense of the method because it typically requires calculation of eigenvalues and vectors [97]. As long as the number of data points is not prohibitively large, the unmodified method is capable of identifying irregularly shaped clusters accurately and efficiently. This ability to determine an unknown number of clusters of unknown and relatively arbitrary structure makes spectral clustering an attractive candidate for this proposed clustering method. Therefore, it will serve as the main framework for identifying clusters in this visualization framework.

Spectral clustering has been used previously to identify regions of interest in a design space. Chen, *et al.* proposed a visualization scheme in which sets or groupings of designs were automatically identified through spectral clustering, so they could be visualized by learning the low dimensional embedding of the clusters [80]. The results of this method were promising for uncovering semantic attributes of the design space, but the

clustering method became computationally intractable for large numbers of candidate designs. Therefore, the proposed implementations of spectral clustering for identification of design regions introduced in this work attempts to alleviate the computational expense introduced by the work of Chen *et al.*

4.2 SPECTRAL CLUSTERING

Graph theory forms the basis for spectral clustering [89]. At the core of graph theory is the graph, G, composed of nodes, V, which are connected by weighted edges, E. Figure 4.1 provides an example graph structure in which the weighted edge between nodes, V_i and V_j is given by, w_{ij}.

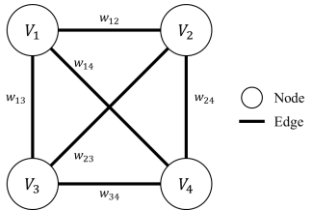

Figure 4.1: Example graph structure with four nodes connected by 6 edges.

Given such a graph, an adjacency and degree matrix, A and D, respectively, can be constructed to unambiguously describe the complete structure and connectivity of the graph[99]. Equations 4.1 and 4.2 describe how the adjacency and degree matrices are determined from a given graph structure.

$$A_{ij} = \begin{cases} w_{ij} & if\ i \neq j \\ 0 & if\ i = j \end{cases} \tag{4.1}$$

$$D_{ij} = \begin{cases} \sum_{j=1}^{n} w_{ij} & if\ i = j \\ 0 & if\ i \neq j \end{cases} \tag{4.2}$$

For a graph with n nodes, the adjacency and degree matrix are n by n symmetric matrices that indicate the connectivity of nodes. Rows and columns are associated with each node and entries correspond to the weights between nodes. The degree matrix is a diagonal matrix that contains information about the degree of each vertex—that is, the sum of the edge weights at a node. To further clarify how to calculate the adjacency and degree matrices another example graph structure is provided by Figure 4.2 where the values of the weighted edges are specified. From the graph, both adjacency and degree matrices are determined to clarify their calculation

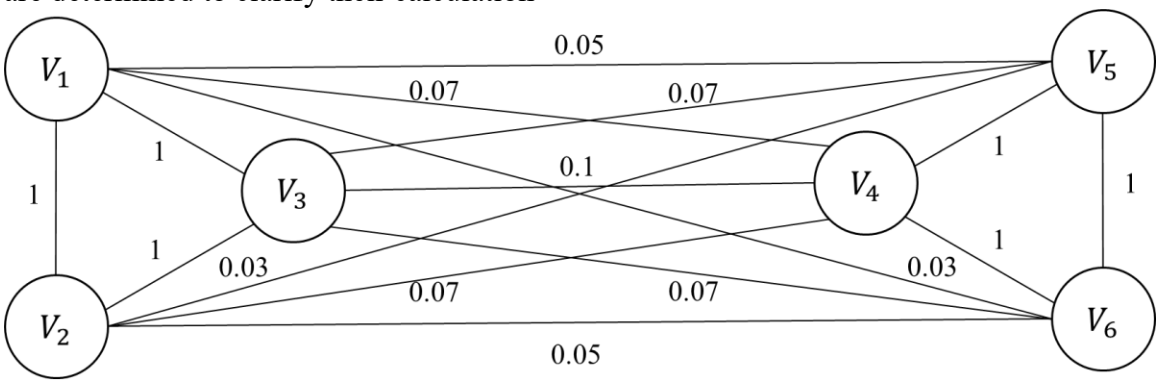

$$A = \begin{bmatrix} 0 & 1 & 1 & 0.07 & 0.05 & 0.03 \\ 1 & 0 & 1 & 0.07 & 0.03 & 0.05 \\ 1 & 1 & 0 & 0.1 & 0.07 & 0.07 \\ 0.07 & 0.07 & 0.1 & 0 & 1 & 1 \\ 0.05 & 0.03 & 0.07 & 1 & 0 & 1 \\ 0.03 & 0.05 & 0.07 & 1 & 1 & 0 \end{bmatrix} \quad D = \begin{bmatrix} 2.15 & 0 & 0 & 0 & 0 & 0 \\ 0 & 2.15 & 0 & 0 & 0 & 0 \\ 0 & 0 & 2.24 & 0 & 0 & 0 \\ 0 & 0 & 0 & 2.24 & 0 & 0 \\ 0 & 0 & 0 & 0 & 2.15 & 0 \\ 0 & 0 & 0 & 0 & 0 & 2.15 \end{bmatrix}$$

Figure 4.2: An example graph structure with associate adjacency matrix (A) and degree matrix (D).

Once the adjacency and degree matrices have been determined, the Laplacian matrix, L, can be determined by simply subtracting the adjacency matrix from the degree matrix. With all three of the matrices determined the normalized Laplacian matrix can be formed by Equation 4.3.

$$L_{norm} = D^{-\frac{1}{2}} L \, D^{-\frac{1}{2}} = I - D^{-\frac{1}{2}} A \, D^{-\frac{1}{2}} \tag{4.3}$$

Using the example graph of Figure 4.2, the normalized Laplacian matrix is provided by Figure 4.3.

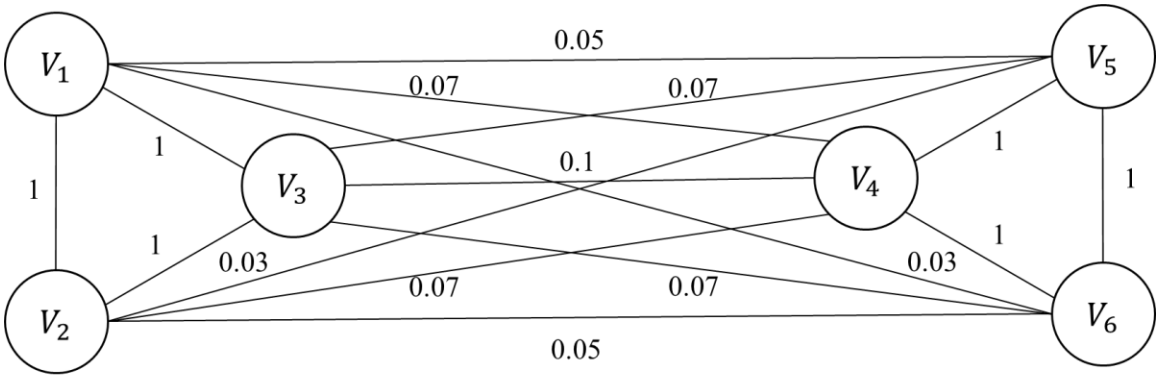

$$L_{norm} = \begin{bmatrix} 1 & -0.465 & -0.456 & -0.032 & -0.023 & -0.014 \\ -0.465 & 1 & -0.456 & -0.032 & -0.014 & -0.023 \\ -0.456 & -0.456 & 1 & -0.045 & -0.032 & -0.032 \\ -0.032 & -0.032 & -0.045 & 1 & -0.456 & -0.456 \\ -0.023 & -0.014 & -0.032 & -0.456 & 1 & -0.465 \\ -0.014 & -0.023 & -0.032 & -0.456 & -0.456 & 1 \end{bmatrix}$$

Figure 4.3: Normalized Laplacian determined from the shown graph.

The eigenvectors and eigenvalues of the normalized Laplacian correspond to solutions of an optimization problem seeking to partition the associated graph. The graph is partitioned by removing weights between adjacent nodes to form clusters. The goal is to maximize the sum of the weights within clusters while minimizing the sum of the weights removed. The entries of the eigenvectors of the Laplacian associated with the first k eigenvalues can be used to partition the nodes into k clusters satisfying the stated optimization problem. This partitioning via the eigenvectors associated with the first k eigenvalues is accomplished through the following algorithm developed by Ng *et al.* [100]

- Compute the first k eigenvectors $\boldsymbol{v_1}, \ldots, \boldsymbol{v_k}$ of L_{norm}.
- Define $V \epsilon \mathbb{R}^{nxk}$ to be the matrix containing the vectors first k eigenvectors $\boldsymbol{v_1}, \ldots, \boldsymbol{v_k}$ as columns.
- Form U by normalizing V so the rows are normalized to 1.
- For $i = 1, \ldots n$, let $\boldsymbol{y_i} \epsilon \mathbb{R}^k$ be the vector corresponding to the i^{th} row of U.
- Cluster the points $\boldsymbol{y_i}$ with k-means algorithm into clusters $C_1^y, \ldots, C_k^y$.
- Output clusters of nodes, $C_1^V, \ldots, C_k^V$ with $C_i^V = \{V_j \, \forall \, j \big| \, \boldsymbol{y_j} \epsilon \, C_i^y\}$

Once again referencing the example graph of Figure 4.2, the previous procedure was performed step by step to produce the results provided in the flowchart of Figure 4.4 for an example with k = 2. The procedure culminates in the clustering of the graph structure into two nonconnected clusters that maximize the edge weights within clusters while minimizing the sum of the weights eliminated.

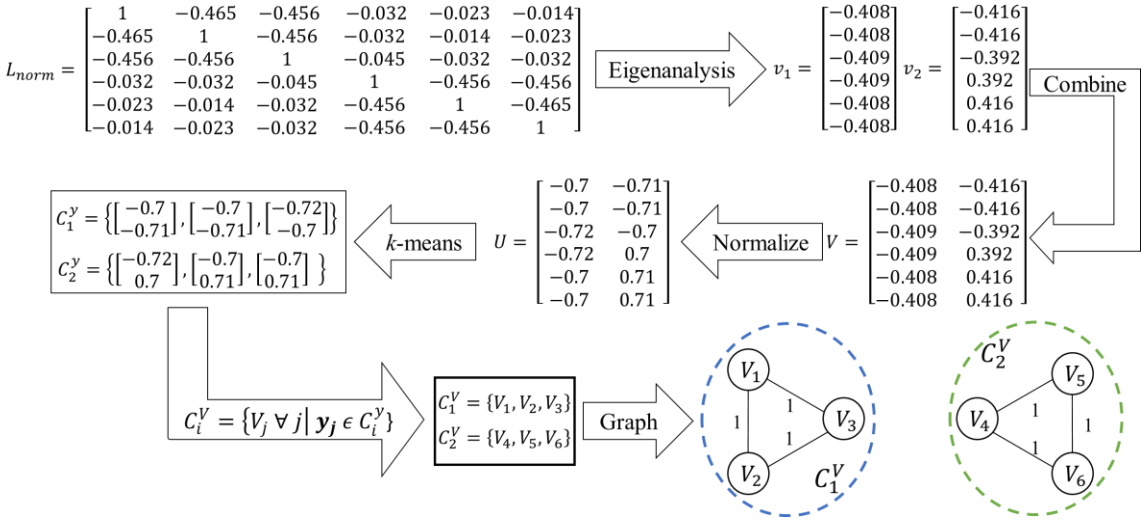

Figure 4.4: Flowchart of the procedure for clustering the simple example graph.

With the general procedure of spectral clustering discussed, the next step is to clarify the connection between graph theory/spectral clustering and the identification of satisfactory design regions classified by the BNC approach.

To perform spectral clustering to identify design regions, nodes and weighted edges must be defined within the framework of the BNC approach. It is natural to define the nodes of the graph as the set of all points on the decision boundaries of the satisfactory design regions or the satisfactory *and* reliably manufacturable regions. By selecting points on the decision boundary, the topology can be conveyed with fewer points. For example, if all of the satisfactory points lie within a sphere, it would be sufficient to visualize only points on the surface of the sphere to understand the topology.

The decision boundary, theoretically, contains an infinite number of points making it infeasible to form the required matrices for spectral clustering. Furthermore, the decision boundaries are formed by nonparametric distributions subject to a machine's numerical precision limits, so obtaining points that are precisely on the decision boundaries is difficult. Therefore, the requirements are relaxed, so nodes of interest are the set of n randomly sampled points sufficiently close to the decision boundaries. To generate this set of n points the design space is randomly sampled, so the BNC can classify the designs. If a randomly sampled design's posterior probability is sufficiently close to zero, the point is considered a node for spectral clustering, where sufficiently close is designer-defined. This procedure results in the value of n being crucial for accurate clustering. If n is not sufficiently large, designs on each of the decision boundaries may not be obtained but if n is too large, the calculation of the eigenvectors may be impossible. This is because the computation time for calculating eigenvectors scales with $O(n^3)$ [101]. Therefore, the value of n can affect how spectral clustering should be implemented in regards to how the

weighted edges are determined as well as the method used to calculate the eigenvalues/eigenvectors.

Various versions of spectral clustering have been developed that attempt to alleviate the computational expense of determining the eigenvectors by balancing accuracy, computational complexity, implementation complexity, and degree of automation. This work has identified three candidate spectral clustering-based techniques with various strengths and weaknesses with regards to the four criteria: accuracy, computational complexity, implementation complexity, and ability to be automated. The first method discussed in Section 4.3 is ε-neighborhood spectral clustering [102]. It is the simplest method to implement while still being highly accurate, offers reduced but still exponential computational complexity, and requires user feedback. The second proposed method, self-tuning spectral clustering (STSC) [96], discussed in Section 4.4, is moderately complex to implement, highly accurate, and fully automated but suffers from the worst possible computation time. Finally, the last method introduced in Section 4.5 is the Nyström modified self-tuning spectral clustering approach [103] that is fully automated with linear computation time, but it can be inaccurate at times and complex to implement. Each of these three approaches is summarized in Table 4.1 with respect to the four listed criteria.

Table 4.1: Table summarizing the strengths and weaknesses of the three proposed spectral clustering based techniques.

Method	Accuracy	Computational Complexity	Implementation Complexity	Degree of Automation
ε-neighborhood Spectral Clustering	High	$O(n^{2.5})$	Low	Low
Self-Tuning Spectral Clustering	High	$O(n^3)$	Moderate	High
Nyström Modified	Moderate	$O(n)$	High	High

STSC				

The remainder of this chapter discusses the three proposed strategies for identifying satisfactory design regions and compares the benefits and costs of each method on example problems. Following demonstration of each approach, the Nyström modified STSC approach will be identified as the most suitable technique to identify design regions of interest. Its selection is largely due to its generally accuracy while being exceptionally efficient when the number of data points is large.

4.3 ε-NEIGHBORHOOD SPECTRAL CLUSTERING

There are numerous methods for determining the weights between nodes which can impact the computational expense of determining the eigenvalues/eigenvectors. While numerous methods exist for determining the weights, the most common approaches relate the weights to the distance between nodes. Closer points in the Cartesian space are assigned larger weights between the associated nodes. Other approaches use a binary classification where the weight between two nodes is either one or zero if the distance between the associated points, d_{ij}, is within a distance threshold, ε. Such methods are known as ε-neighborhood spectral clustering and the adjacency matrix weights are given by Equation 4.4.

$$w_{ij} = \begin{cases} 1 \; if \; d_{ij} \leq \varepsilon \\ 0 \; if \; d_{ij} > \varepsilon \end{cases} \tag{4.4}$$

The degree, Laplacian, and normalized Laplacian are identical to the forms discussed previously, but the binary weighting of the edges results in desirable properties of the eigenvectors/values. If a graph has clusters such that no nodes of one cluster are

adjacent to another cluster there will be a multiplicity of the zero eigenvalue of the Laplacian matrix of the number of distinct clusters, due to how the Laplacian is formed. The sum of the values in each row must sum to zero, therefore a vector of ones is automatically an eigenvector for all Laplacian matrices. If there are k distinct clusters, through similar logic, there will be k eigenvalues equal to zero. The entries of the k eigenvectors associated with the zero eigenvalue will have entries that are either 0 or 1. Using the point indexing scheme to form the Laplacian, the original dataset can be partitioned by observing the index of the nonzero values of the eigenvectors. In other words, the entries of the basis of the null space of the Laplacian partition the graph into clusters, and the number of clusters is the rank deficiency of the Laplacian matrix.

When using the ε-neighborhood method, only the null space must be calculated which has a computation time lower bound of $O(n^{2.5})$ [104]. When dealing with large datasets, this reduction in computational time is important. If an appropriate graph is created, the ε-neighborhood method will allow us to identify regions of the design space that lead to high performance. The graph must describe the data points of the high-performance design region by connecting points of the same cluster but not those of different clusters. With the proper graph, the Laplacian matrix can be used to partition the dataset by determining the null space as described earlier. The difficulty of this method lies in obtaining a meaningful graph structure that accurately connects points of the same cluster. The methodology of determining the correct graph structure is discussed in the following section.

Figure 4.5 illustrates the effect of identifying the correct ε value, so an erroneous number of clusters is not identified. Selecting the proper ε is important because if it is too large, points in different clusters will be connected which would lead to multiple distinct clusters being collapsed into a single cluster. If ε is too small, points in the same cluster

may not be connected, and too many clusters will be identified. Therefore, an appropriate ε must be selected in order to accurately identify the correct number of clusters. When working with high-dimensional data, it may not be clear how to choose the appropriate ε.

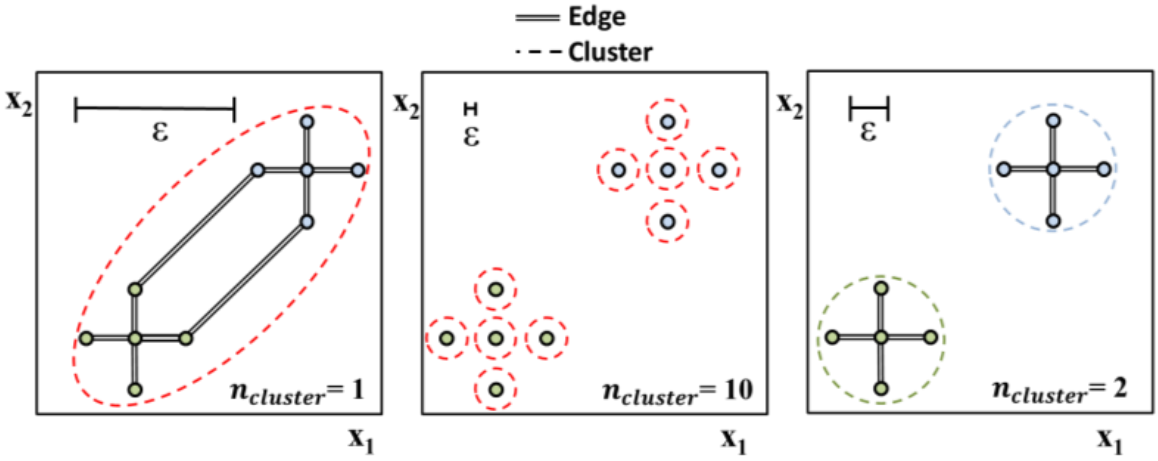

Figure 4.5: The same set of data points in a 2D Cartesian space yield a different number of clusters if the value of ε is not carefully chosen.

To determine a suitable ε, multiple methods can be used. One proposed method is derived from grid-based search methods and aims to be a quick and easy way to determine an acceptable ε value. To accomplish this, the normalized design space is discretized into a variable number of bins. Each bin is searched and the number of points in each bin is recorded. Using the bins containing points, a normalized kernel density estimate is generated. The process is repeated over a range of bin sizes from very coarse to very fine. The goal of this method is to find a characteristic distribution shape that indicates an appropriate bin size has been found. This bin size should be indicative of the correct value of ε. While this method was very computationally efficient, the results were not accurate for identifying the correct ε value. We did not find a probability distribution that was

indicative of the correct ε value being chosen. The problem became even more difficult as the dimensionality increased.

A second method for identifying clusters can be explored that shares some similarities to the previous method but is more accurate at identifying an acceptable value of ε. Like the previous binning method, the space is normalized, and the maximum distance between adjacent points is varied. For each value of ε, the number of clusters is determined and plotted against the inverse of ε. We anticipate a standard behavior with this method as shown in Figure 8. At very small values of ε the number of clusters identified will approach the number of points in the space. Then as ε increases over some range the correct or nearly correct number of clusters should be identified. Finally as ε approaches unity, the number of clusters identified will be one. Note that in Figure 4.6 the vertical axis is $\ln(n_{identify}/n_{true})$, in which $n_{identify}$ and n_{true} are the number of clusters identified by the ε value and the true number of clusters, respectively; the log scale is used because the number of points can vastly exceed the number of clusters. If the y-axis has a value of zero, or $\ln(1)$, the correct number of clusters has been identified. We should note that the true number of clusters, in general, is not known so datasets with an unknown number of clusters cannot be normalized in this way but the general shape should remain true.

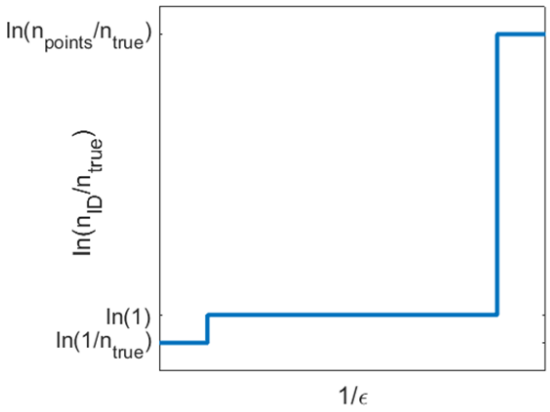

Figure 4.6: Normalized log plot illustrating the expected number of clusters to be identified when varying the value of ε.

In Section 4.6 it will be demonstrated that the ε-neighborhood spectral clustering approach can be used to identify the number of clusters or decision boundaries for an example test set, but the method requires the designer to set the ε heuristic as part of the process. Furthermore, the computational expense of the method, while still better than standard spectral clustering, will scale exponentially with the number of designs classified on the decision boundary. Motivated largely by the lack of automation, a different spectral clustering based method, self-tuning spectral clustering, is explored in Sections 4.4 and 4.5 because it can identify the correct number of clusters or decision boundaries without the need for a sensitive heuristic although it does result in a higher computational expense.

4.4 Self-Tuning Spectral Clustering

Self-Tuning Spectral Clustering (STSC) was initially developed to automatically identify clusters of objects within images but the approach can be easily expanded to identify regions in a high dimensional design space [96]. The approach has two attractive features where the first is the approach can effectively cluster even if the density of points in a region is higher or lower than others. Secondly, the approach was developed to automatically determine the number of clusters that best partitions the graph structure. The insensitivity to point density is largely due to how the weights between nodes is determined with local tuning parameters. Specifically, the weights, w_{ij}, between two nodes, V_i and V_j, separated by a distance, d_{ij} is determined with the Gaussian kernel with local tuning parameter σ_i and σ_j shown in Equation 4.5 [96].

$$w_{ij} = \exp\left(\frac{-d_{ij}^2}{\sigma_i \sigma_j}\right) \tag{4.5}$$

The local tuning parameters σ_i and σ_j are determined by exploiting the local structure of the graph around the two nodes of interest. The initial work completed on STSC showed that σ_i and σ_j should be set to be equivalent to the distance to the 7th closest point to V_i and V_j although the results indicate that other values can be used [96]. These local tuning parameters encode information about the local structure where the tuning parameter will be smaller (larger) in regions with high (low) densities of points. This allows for a scalar weight to better represent the structure of the high dimensional data. With this approach, Equation 4.5 can generate the adjacency matrix, degree matrix, and normalized Laplacian describing a set of designs. Once again, the eigenvectors and eigenvalues of the normalized Laplacian formed with these weights correspond to solutions of the optimization problem seeking to partition the associated graph but how the approach automatically identifies the number of clusters needs to be defined.

To accomplish this automatic selection, the original paper on STSC proposed a quality metric for determining the correct number of clusters [96]. It was based on finding a rotation matrix, R, of the eigenvectors associated with the first k eigenvalues that best aligns the vectors with the original coordinate system. The better the eigenvectors are aligned with the original coordinate system, the better the graph is clustered. By minimizing a scalar value, known as the quality, Q, that describes how well the eigenvectors and original coordinate bases are aligned, the number of partitions can be selected. To determine the quality of k clusters of n points, Equation 4.6 [96] is provided where the matrix, Z, is generated by rotating the matrix of k eigenvectors, X_k, by R to best align the eigenvectors with the original coordinate system—that is, $Z = RX_k$, and the normalizing value, $M_j = \max_i Z_{ij}$.

$$Q = \sum_{i=1}^{n} \sum_{j=1}^{k} \frac{Z_{ij}^2}{M_j^2} \tag{4.6}$$

For more information regarding the details of self-tuning spectral clustering the reader is directed towards the original paper [96]. By using STSC, the correct number of clusters can be identified accurately but for graphs with a large number of nodes the computational expense is large, $O(n^3)$. The method requires the computation of each eigenvalue of the matrix. When dealing with large datasets, this computational time can be significant. Therefore, the Nyström Method is introduced as a final clustering approach that can approximate the eigenvalues and eigenvectors of the Laplacian without the computational expense.

4.5 NYSTRÖM MODIFIED SELF-TUNING SPECTRAL CLUSTERING

The Nyström method is based on a classical method for the solution of the integral eigenvalue problem that was adapted to approximate the eigenvectors and eigenvalues of the Laplacian matrix [103]. The method takes a sample of *m* nodes from the graph to approximate the structure of the graph. Then the solution of the subset of nodes is extrapolated to determine the solution of the entire graph structure. The major advantage of this method is that the computational expense, for a given sample size, grows linearly with the number of nodes in the graph.

The Nyström Method approximates the eigenvectors of the Laplacian using the following procedure with more details provided by Fowlkes *et al.* [103]. First, a random sample of *m* nodes is drawn from the initial graph with *n* nodes, in which $m \ll n$. To approximate the affinity matrix, *A*, of the entire graph a secondary square adjacency matrix, *M*, is formed between only the *m* randomly sampled points. Another rectangular adjacency

matrix, *N*, is formed between the *m* randomly sampled points and the *n-m* remaining points. Finally, the affinity matrix, *C*, between the *n-m* remaining points can be formed. Therefore, the exact affinity matrix, *A*, can be represented by Equation 4.7.

$$A = \begin{bmatrix} M & N \\ N^T & C \end{bmatrix} \tag{4.7}$$

With this representation of the affinity matrix, the matrix, *S* can be defined as $S = M + M^{-1/2}NN^TM^{-1/2}$ in which *S* can be diagonalized by $S = U_S\Lambda_S U_S^T$. The columns of the *m x m* matrix, U_S, are the eigenvectors of the associated eigenvalues that form the diagonal of Λ_S. Finally, it can be shown that the first *m* eigenvectors of *A* and subsequently the eigenvectors of L_{norm} can be approximated by the matrix V_{Nyst} given by Equation 4.8.

$$V_{Nyst} = \begin{bmatrix} M \\ N^T \end{bmatrix} M^{-\frac{1}{2}} U_S \Lambda_S^{-\frac{1}{2}} \tag{4.8}$$

The form of Equation 4.8 shows that any inversions or diagonalization procedures are performed on *m x m* matrices rather than the original *n x n* affinity matrix. Inversion or diagonalization procedures have a cubic computational complexity for hard drive storage and a quadratic complexity for memory. Therefore, by only performing the complex computations on the *m x m* matrices the computational expense of self-tuning spectral clustering is greatly reduced. For a given sample size *m*, any additional computational expense scales linearly with the number of nodes, *n,* due to the multiplication of the matrix *N* in the computation of V_{Nyst}. The calculation of the eigenvalues and vectors is only an approximation, though, so it is possible for the approach to be inaccurate when identifying clusters and design regions.

With each of the three different approaches introduced, the following section will highlight the strengths and weaknesses of each method on synthetic datasets.

4.6 Comparison of Approaches

The three spectral clustering-based approaches were claimed to have varying levels of accuracy, computational complexity, implementation accuracy, and degrees of automation. This section seeks to clarify the claims previously made with regards to each criterion and summarized by Table 4.1. First, the ε-neighborhood spectral clustering approach is applied to demonstrate that it can effectively and accurately cluster high dimensional datasets. Determining the correct number of clusters requires the designer input, though, so it will be shown that the approach is not automated. Following demonstration of the ε-neighborhood spectral clustering approach, self-tuning spectral clustering will be compared to the Nyström modified STSC approach with a high dimensional dataset. The results confirm that STSC is highly accurate for clustering, but requires significant computational time, which can be alleviated by incorporating the Nyström method with an accuracy tradeoff.

To demonstrate the ε-neighborhood spectral clustering approach, ten datasets of normalized, ten-dimensional data were pseudo-randomly generated. Each dataset consisted of at least one but no more than three clusters in the shape of each of the following structures: a hypersphere, a hyperellipsoid, and a hyperspherical shell. Figure 4.7 demonstrates the 2 dimensional analogs of each structure. It should be noted that the clusters represent the interior and not just the boundary of each structure. The hyperspherical shell was chosen to test the spectral clustering based method because it is difficult to accurately identify with methods such as k-means and Gaussian Mixture models [81]. The design regions obtained by the BNC approach will likely have irregular and

nonlinear boundaries so the efficacy of spectral clustering with identification of complex shapes must be demonstrated.

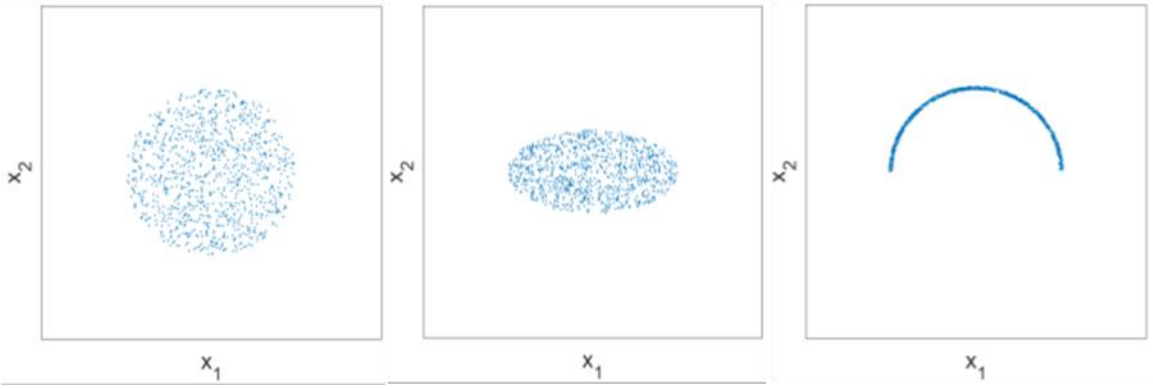

Figure 4.7: Illustration of the 2D analogs of the three cluster structures used to generate higher dimensional data.

The size and location of the hypersphere, hyperellipsoid, and hyperspherical shell are given respectively by Eqs. 4.9-11 [105].

$$\frac{1}{r^2}(\vec{\boldsymbol{x}} - \vec{\boldsymbol{c}})^T(\vec{\boldsymbol{x}} - \vec{\boldsymbol{c}}) \leq \mathbf{1} \tag{4.9}$$

$$(\vec{\boldsymbol{x}} - \vec{\boldsymbol{c}})^T\boldsymbol{\Sigma}^2(\vec{\boldsymbol{x}} - \vec{\boldsymbol{c}}) \leq \mathbf{1}\frac{1}{r^2}(\vec{\boldsymbol{x}} - \vec{\boldsymbol{c}})^T(\vec{\boldsymbol{x}} - \vec{\boldsymbol{c}}) \leq \mathbf{1} \tag{4.10}$$

$$(r+\epsilon)^2 \geq (\vec{\boldsymbol{x}} - \vec{\boldsymbol{c}})^T(\vec{\boldsymbol{x}} - \vec{\boldsymbol{c}}) \geq (r+\epsilon)^2 \text{ where } x_n \geq c_n \tag{4.11}$$

In Equation 4.9, $\vec{\boldsymbol{x}}$, is an *n*-dimensional spatial vector, *r* is the radius of the hypersphere and $\vec{\boldsymbol{c}}$ is the location of the center of the hypersphere. Equation 4.10 is identical to Equation 4.9 except a diagonal matrix $\boldsymbol{\Sigma}$ is used in which each entry of the diagonal corresponds to the inverse of the semi-major axis of the corresponding dimension ($\boldsymbol{\Sigma_{ii}} =$

$1/\sigma_i$). Equation 4.11 describes the region bounded by two distinct boundaries. The first boundary is the region between two hyperspheres centered at $\vec{\boldsymbol{c}}$ whose radii are $r + \epsilon$ and $r - \epsilon$ where $\epsilon \ll r$. The second boundary, which bounds the first region from below, is a hyperplane corresponding to $x_n = c_n$ where x_n is the last dimension of the spatial vector $\vec{\boldsymbol{x}}$ and c_n is the last entry of $\vec{\boldsymbol{c}}$.

As Equations. 4.9-11 show, each shape can be randomly generated by arbitrarily choosing the various parameters described above. For hyperspheres, the center, $\vec{\boldsymbol{c}}$, and radius, *r*, must be selected. For hyperellipsoids, the center, $\vec{\boldsymbol{c}}$, and various semi-major axes lengths, σ_i, must be chosen. Finally, for the hyperspherical shells, the center, $\vec{\boldsymbol{c}}$, radius, *r*, and shell gap, ϵ, must be chosen as well. When generating each of the 10 datasets the parameters were uniformly and randomly chosen from the ranges described in Table 4.2. Also by using Equations 4.12-14 the volumes of each region were calculated to ensure the regions had a similar point density [106]. For Equations 4.12-14, Γ, is the Gamma function which is an extension of the factorial function.

Table 4.2: Range of parameters used to generate higher dimensional clusters.

	Hypersphere		*Hyperellipsoid*		*Hyperspherical Shell*		
	$\vec{c}$	*r*	$\vec{c}$	σ_i	$\vec{c}$	*r*	ϵ
Min	*0.2*	*0.1*	*0.2*	*0.05*	*.15*	*.1*	*0.01*
Max	*0.8*	*0.2*	*0.8*	*0.2*	*.85*	*.2*	*0.03*

$$V_{hypsph} = \frac{\pi^{\frac{D}{2}}}{\Gamma\left(\frac{\mathrm{D}}{2}+1\right)} r^D \tag{4.12}$$

$$V_{hypell} = \frac{\pi^{\frac{D}{2}}}{\Gamma\left(\frac{\mathrm{D}}{2}+1\right)} \prod \sigma_i \tag{4.13}$$

$$V_{hypshell} = \frac{\pi^{\frac{D}{2}}}{2\Gamma\left(\frac{\mathrm{D}}{2}+1\right)}[(r+\epsilon)^D - (r-\epsilon)^D \tag{4.14}$$

Table 4.3 shows the number of each structure generated when constructing each random dataset.

Table 4.3: Number of hyperspheres, hyperellipsoids, and hyperspherical shells in each cluster.

	Hypersphere	***Hyperellipsoid***	***Hyperspherical Shell***	***Total***
Dataset 1	1	1	3	5
Dataset 2	3	3	1	7
Dataset 3	3	3	2	8
Dataset 4	2	1	3	6
Dataset 5	3	3	1	7
Dataset 6	1	3	1	5
Dataset 7	3	2	1	6
Dataset 8	2	3	1	6
Dataset 9	1	2	3	6
Dataset 10	2	2	2	6

After generating the 10 datasets, the value of ε was varied from 0.06 to 1 in 50 equal increments. For each value of ε, spectral clustering was performed on each dataset and the multiplicity of the zero eigenvalue of the Laplacian was determined which indicated the number of clusters. It should be noted that Matlab 2016 was used to calculate the eigenvectors associated with the zero eigenvalue; it uses singular value decomposition (SVD) to calculate the null space. The computational complexity of such an operation scales cubically with the number of points rather than according to a theoretical lower bound of $O(n^{2.5})$. The results of the ε-neighborhood sweep algorithm are presented in Figure 4.8 where each colored line indicates a different dataset. Figure 4.8 shows that the method accurately determines the number of clusters for a wide range of ε values. It can

also be seen that the behavior of this method mirrors what was hypothesized from Figure 4.6. When the value of ε is too large, the method only identifies one cluster, but when the value of ε is too small, the number of clusters identified drastically increases. This sharp increase in the number of clusters is a strong indicator that the value of ε should be increased. There is also a large bandwidth of ε values for which the correct number of clusters is identified.

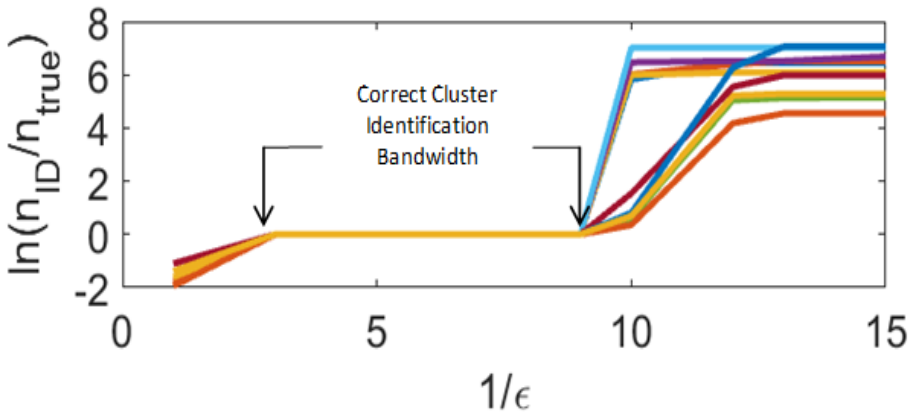

Figure 4.8: Normalized log plot showing the number of clusters identified when varying the value of ε for 10 different sets of 10 dimensional data.

The approach, though, still requires a user to make a somewhat arbitrary decision regarding the true number of clusters based on empirical evidence. For engineering applications the correct value of ε may not be as clear, motivating a rigorous, deterministic approach for selection of clusters. Furthermore the approach, when implemented in Matlab 2016, requires cubic computational time, so other approaches should be studied. STSC solves the issue of determining the correct number of clusters but still suffers from large computation times. This issue can be solved by incorporating the Nyström method, as demonstrated in the remainder of this section.

To validate the STSC and the Nyström modified STSC approach a series of studies were performed on synthetic datasets generated in a 10-dimensional space. The datasets consisted of 3 clusters of data: (1) points on the hypersurface of a 10-dimensional hypercube, (2) points on the hypersurface of a 10-dimensional sphere, and (3) points on a 10-dimensional line. Figure 4.9 provides a 3-dimensional analog of the design space generated in 10-dimensions. The points of each dataset were selected to be on the surfaces of the geometric shapes or along curves to approximate the decision boundaries of a design space.

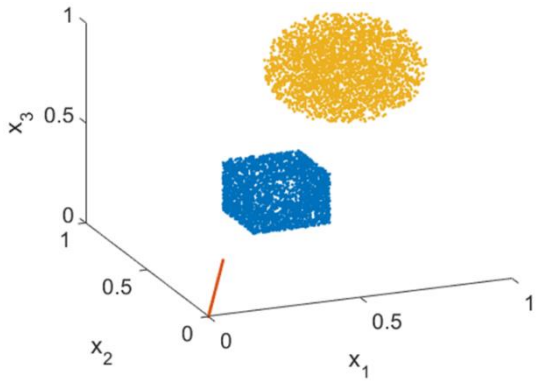

Figure 4.9: 3D representation of the 10D design space used to validate the augmented spectral clustering method.

First, a study was performed to investigate the accuracy of the Nyström modified STSC method and its computational expense relative to the original STSC method. In this study, the 10-dimensional analog of each shape shown in Figure 4.9 was generated in a common 10-dimensional space, resulting in three clusters. The clusters were generated by randomly sampling *n* points within the domain of each high-dimensional shape. Specifically, *n* points on the surface of a 10D hypercube were randomly sample, *n* points on the surface of a 10D hypersphere were randomly sampled, and *n* points on a 10D line

were randomly sampled. The value of n was increased from 1,000 to 5,000 in 1,000 point increments resulting in five different datasets each containing three clusters and $3n$ points. For each dataset of $3n$ points, the original STSC was performed once, and the Nyström modified STSC was performed 10 times to investigate the consistency of the results. The execution time was recorded as well as the number of clusters identified. When using the Nyström modified STSC approach, 1,000 random samples were used to approximate the space and the local tuning parameters were equal to the distance to the 7^{th} closest point for each point of interest.

Results of the study using an Intel Core i7-7700 CPU at 3.60GHz with 16GB of RAM are shown in Figure 4.10, which documents the computational time for each clustering method as a function of the total number of training points. Due to the random sampling required of the Nyström modified STSC method, the mean and standard deviation of the computational time were calculated over the 10 evaluations of each dataset. The standard deviation never exceeded 2% of the mean, implying consistent computational times. The mean computation time for each dataset is plotted in Figure 4.10.

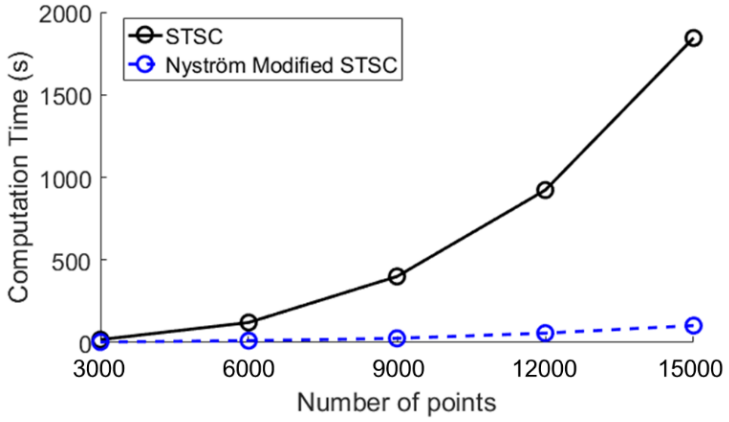

Figure 4.10: Plot comparing the computation time as a function of the number of points clustered for both methods.

Figure 4.10 illustrates that the computational time scales approximately linearly with the total number of designs for the augmented approach while the original approach scales exponentially.

While Figure 4.10 illustrates the computational efficiency of the Nyström modified STSC approach, its accuracy still needs to be investigated. The original STSC method always identifies the correct number of clusters but the Nyström modified STSC approach does not. The accuracy of the method for this study is documented in Table 4.4. For each of the five datasets, the mode of the number of clusters identified by the 10 evaluations of the Nyström modified STSC approach corresponds to the correct number of clusters. As shown in the final column of Table 4.4, among the 10 evaluations of the method, it correctly identified 3 clusters at least 60% of the time, regardless of the number of sampled points. However, to identify the number of clusters accurately, the mode must be extracted from repeated sampling and analysis.

Table 4.4: Accuracy of Nyström modified STSC approach for various numbers of points.

Number of Points, $3n$	Mode of number. of clusters identified (Nyström modified STSC)	Accuracy
3000	3	90%
6000	3	80%
9000	3	80%
12000	3	60%
15000	3	60%

The reduced computational expense of the method, allows the algorithm to be implemented rapidly numerous times to determine the most likely number of clusters based on the mode. For example, the Nyström modified STSC approach required about 18 times less computational expense than the standard STSC approach for the dataset containing

15,000 points. Furthermore, the mode of the number of clusters identified for the 10 evaluations for each set of points was always the correct value of 3.

To illustrate this point, another dataset was generated in a similar manner as before. 1,000 points were drawn from each of the three 10D shapes to generate a dataset with three clusters and 3,000 points. The Nyström modified STSC approach was applied to the dataset 100 times where 500 random samples were drawn and the previously specified local tuning parameter settings were used. Figure 4.11 presents a histogram showing the number of clusters identified for each iteration.

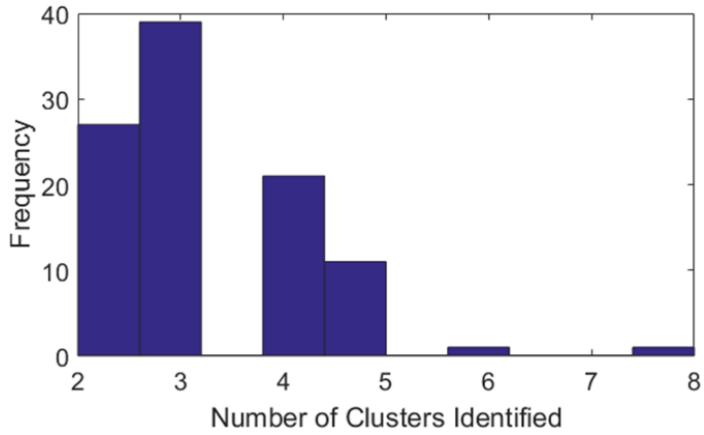

Figure 4.11: Histogram of the number of cluster identified by the Nyström modified STSC approach.

Figure 4.11 also corroborates that the Nyström modified STSC approach can suffer from inaccuracy but can be used to identify the correct number of clusters. The general accuracy of the Nyström modified STSC approach improves as the number of points sampled approaches the number of points in the original set. Therefore, a secondary study was performed to determine whether a general rule could be proposed regarding the number of sample points required to reliably determine the correct number of clusters.

For the second study, five datasets were generated that each contained three clusters and 3*n* points where *n* varied for each dataset. The first cluster of each dataset consisted of *n* points drawn from the surface of the 10D hypercube. The second cluster of each dataset consisted of *n* points drawn from the surface of the 10D hypersphere, and the third cluster of each dataset consisted of *n* points drawn from the 10D line. The value of *n* was varied between 100 and 3200 at five equal increments on a logarithmic scale to generate the five datasets with 3*n* points. For each of the five datasets, the Nyström modified STSC approach was implemented 10 times for four different random sample sizes. The random sample sizes were chosen to be 10%, 20%, 30%, and 40% of the total set size of each dataset. In summary, for each of the 5 datasets, the Nyström modified STSC approach was applied 40 times and for each implementation the number of clusters identified was recorded. Table 4.5 presents the results of this study showing the accuracy or the percentage of the implementations of the Nyström modified STSC approach that identified the correct number of clusters for each dataset and sample size.

Table 4.5: Matrix showing the accuracy of the proposed clustering method. The orginal number of points is varied while the ratio of the sample size to the original number of points is varied as well.

		Ratio of Sample Size to Number of Points			
		0.1	0.2	0.3	0.4
Number of Points	300	10%	40%	30%	100%
	720	70%	90%	100%	90%
	1680	90%	60%	70%	90%
	3990	50%	80%	100	90%
	9600	30%	100%	100%	100%

Table 4.5 demonstrates that for the synthetic problem posed, if the sample size is 40% of the original dataset, accurate results are achieved in general. Also, the method seems to perform better for larger data sets, even if as few as 20% of the points are sampled. With a larger data set, more information on the clusters is available, allowing for a high certainty in the results. Also, the dimensionality of the problem may be important; in a space with fewer dimensions, better accuracy may be achievable with fewer points. There was an anomalous result in accuracy for a sample size that is 10% of the total sample size of 1680 points. The accuracy was much higher than expected, although the reason for this increased accuracy is unclear, which indicates more than ten implementations of the approach may need to be done for the percentages to converge.

A final study was performed on a more challenging synthetic dataset. The datasets consisted of 9 clusters: (1) points on the hypersurface of three different 15-dimensional hypercubes, (2) points on the hypersurface of three different 15-dimensional spheres, and (3) points on three different 15-dimensional lines. Each cluster contained 1,000 points resulting in a dataset with 9,000 total points. Following generation, the Nyström modified STSC approach was applied to the dataset 20 times where only 1,000 points were randomly sampled. A histogram showing the results of the study is provided by Figure 4.12.

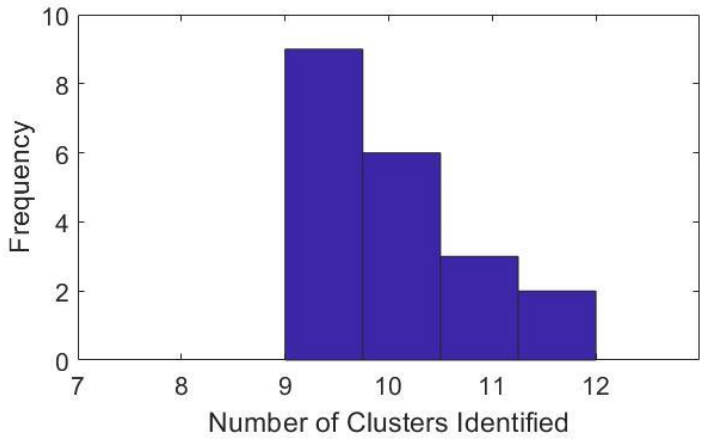

Figure 4.12: Histogram of the number of clusters identified by the Nyström modified STSC for a 15D dataset consisting of 9 clusters.

Figure 4.12 corroborates the previous results that the Nyström modified STSC approach in general identified the correct number of clusters while the original STSC approach was always accurate but required a large computation time.

4.7 DISCUSSION

The first task in the proposed visualization strategy was to identify the number of clusters or design regions of interest in a high dimensional design space. Spectral clustering was identified as a potential method for identification of the regions due to its ability to cluster irregularly shaped regions and its deterministic approach. A major limitation of the approach, though, is the computational expense of performing an eigenanalysis with computational complexity that nominally scales cubically with the number of point being clustered. In high-dimensional design spaces, it is pivotal to sample sufficient numbers of points to ensure all decision boundaries are represented, which may limit the applicability of spectral clustering. Therefore, three different approaches were introduced that balance

difference aspects of spectral clustering such as the accuracy, computational complexity, degree of automation, and ease of implementation.

Ease of implementation is a somewhat subjective criteria but was still considered in this work because the intent of this chapter was to introduce spectral clustering to designers who may not be exposed to the algorithms presented. By commenting on the ease of implementation designers who seek to use the proposed visualization strategy can consider the amount of commitment needed to implement the algorithm. The ranking in ease of implementation was based mostly on the author's experience in developing the algorithms for Matlab as well as for the identification of satisfactory design regions.

To objectively evaluate the other three criteria for each clustering method a series of tests was performed on synthetic datasets that demonstrated the results summarized in Table 4.1. The ε-neighborhood spectral clustering approach was accurate for identifying clusters but relied on an empirically-based decision to determine the correct number of clusters. STSC avoided the subjectivity in determining the correct number of clusters by formulating an optimization problem that accurately identified the best number of clusters, but it suffered from computationally complexity. Finally, after augmenting STSC with the Nyström approach the calculation of the eigenvalues and eigenvectors could be approximated to greatly reduce computational expense. While the method was not always accurate, the mode of the number of clusters tended toward the correct value when the method was implemented multiple times, so for sufficiently large datasets, the modified approach could be run multiple times to determine the most likely clustering result. The approach is so much more efficient than STSC that it is a viable alternative to STSC. Therefore, it is used throughout the rest of this work, although any of the other methods could have been used for the identification of design regions

While the Nyström approach appears to be the most appropriate for identifying and eventually visualizing clusters in the high dimensional regions classified for NS metamaterials, the other approaches may be more suitable for other designers or problems. From this comparison of various spectral clustering techniques, information is now available to assist designers in determining the most appropriate clustering technique for identifying design regions in a high dimensional design space. Regardless of what method is selected, the design regions classified by the BNC approach can now be identified with the ultimate goal of visualizing each region. Therefore, the following section will discuss how these regions identified by the BNC approach can be visualized using various visualization techniques. In particular, t-Distributed Stochastic Neighbor Embedding will be introduced as a viable method for obtaining high quality visualization of the identified design regions

Chapter 5: Visualizing Satisfactory Design Regions

After identifying the number of distinct design regions of interest with a spectral clustering-based approach, the final step of the visualization framework is to produce a visual mapping of each region. Much like clustering, numerous different approaches have been studied for visualizing high dimensional data structures. Many of these visualization approaches have been adapted to assist in design exploration, so they will be discussed in Section 5.1. Following the review of visualization strategies in design exploration, two of the more promising algorithms, Kernel Principal Component Analysis (KPCA) [107] and t-Distributed Stochastic Neighbor Embedding (t-SNE) [108], will be discussed in more detail in Section 5.2 as proposed strategies for visualizing the regions identified through the BNC approach. KPCA [80] has been used previously to visualize design spaces, but t-SNE has yet to be used in that capacity.

While two visualization algorithms will be examined in depth, there are still many other visualization approaches available to designers, so determining which approach to select can still be a challenge, especially to designers unfamiliar with visualization. KPCA and t-SNE, like all visualization approaches, have advantages and disadvantages for visualizing design spaces so knowing *a priori* which approach to select is typically impossible. To help identify the most suitable visualization, general metrics such as continuity and trustworthiness have been developed and utilized in tandem [109]. These metrics, along with geodesic distance inconsistency (GDI) [80], are discussed in Section 5.3, but they can overestimate the quality of a visualization or do not allow for sufficient gradation in quality. Therefore, this work proposes a new, single metric called preservation that attempts to avoid some of the shortcomings of the other metrics as discussed in Section 5.3. Following introduction of preservation, the metric will be compared to the previous

metrics for clusters of varying visualization difficulty in Section 5.4. Following exploration of the metric, a procedure for using preservation to automatically select the heuristics of the visualization techniques will be introduced in Section 5.5. The approach will be demonstrated on sample datasets. Not only will the approach be introduced but the quality of visualizing each cluster will be compared to the quality of visualizing the entire dataset. This will provide insight into the tradeoffs between visualizing the entire design space versus individual clusters. Following validation of the metric and approach, the results will be discussed in Section 5.6 which will be followed by application of the proposed visualization in Chapter 6.

5.1 Review of Visualization Techniques

This review of visualization techniques is divided into two topics. The first topic is general visualization and dimension reduction techniques while the second topic is the application of the visualization techniques for design exploration. A complete review of all visualization techniques available across all disciplines would be too lengthy for inclusion. Rather this review will provide a general overview of various visualization techniques that can be categorized based on their similarities. The reader is encouraged to see the reviews provided by van der Maaten *et al*. [110] or Liu *et al*. [111] if they are interested in obtaining further information. In general, the terms dimension reduction and visualization will be used interchangeably even though they are distinct areas of focus. This work assumes any use of dimension reduction is intended to visualize.

Referencing the categorization by van der Maaten [110], visualization or dimension reduction techniques can be generalized into a taxonomy of two different families: (1) convex techniques or (2) nonconvex techniques. A convex technique minimizes a convex objective function to uncover the low dimensional structure of a high dimensional data set

while a nonconvex technique optimizes a nonconvex objective function. Figure 5.1 provides the taxonomy of dimension reduction techniques as proposed by van der Maaten [110].

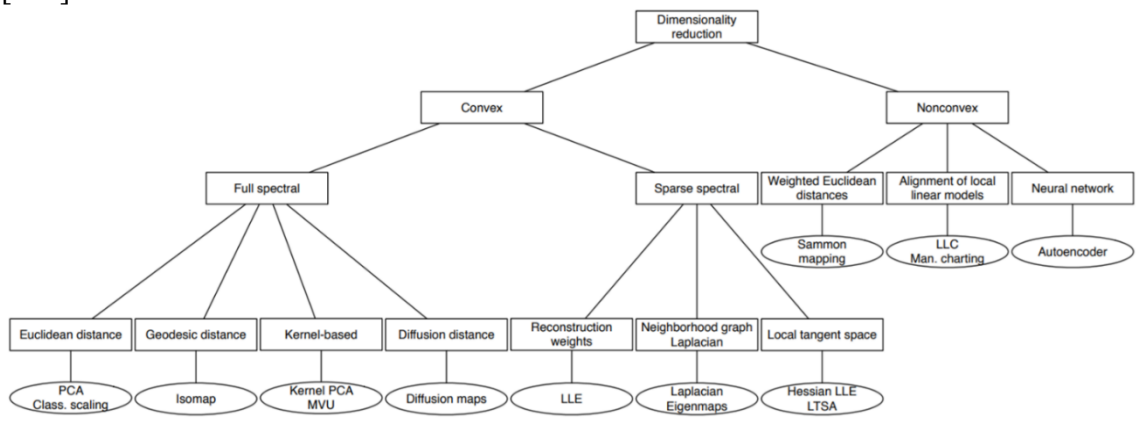

Figure 5.1: Taxonomy of dimensionality reduction techniques [110].

As shown by Figure 5.1, these families can be subdivided further into various other classes of techniques. These include, for the convex class of reduction, techniques that typically rely on spectral analysis to solve the convex objective functions. These spectral techniques are either full spectral or sparse spectral depending on the formulation of the objective function. Full spectral techniques contain the common Principal Components Analysis (PCA) [112] that uses the eigendecomposition of a high dimensional data set to determine the orthogonal vectors, or principal components, along which most of the variation in the data occurs. By projecting the data into the space spanned by three or less of the principal components the data can be visualized. PCA is just one example of a full spectral technique but others include Isomap [113], Maximum Variance Unfolding [114], and Kernel PCA [107] which will be discussed further. One of the limitations of these full spectral approaches is that the computational expense of calculating eigenvalues and eigenvectors scales cubically with the number of points in the dataset [110].

The other member of the convex family of dimension reduction techniques is sparse spectral techniques. The reason these techniques are considered sparse is because they do not consider the global structure of the dataset; rather, they solve a sparse or generalized eigenproblem that considers the local structure of the data. For example, one such sparse technique is local tangents spaces approximation (LTSA) [115] which projects local manifolds into low dimensional spaces based on the behavior of the tangent at a point. It then stitches these local tangent spaces together to produce a low dimensional approximation of the space. More simply, it looks at the local curvature and structure of a high dimensional dataset and attempts to find a low dimensional plane that approximates the surface at each point. Other similar approaches are Local Linear Embeddings (LLE) [116], Laplacian Eigenmaps [117], and Hessian LLE [118]. These approaches have found success in many fields, but they commonly collapse regions of high dimensional data into points or rescale the axes to distort the topography [110].

The other family of dimension reduction approaches, nonconvex techniques, is far more general than convex techniques. Various approaches of dimension reduction can be classified as nonconvex, and much of the current research on visualization is focused on nonconvex techniques. Nonconvex techniques have typically been avoided because of the existence of local minima which can be troublesome for gradient-based strategies. If gradient-based strategies cannot be used, more computationally intensive search approaches must be used to seek the global minima. With the increase in computational power and RAM, search approaches for global minima are becoming less prohibitive. Furthermore, research indicates that while the global optima of a nonconvex approach may not be discovered, the formulation of the objective function and constraints yield better visualization results for suboptimal solutions than convex approaches yield for optimal solutions.

Some examples of nonconvex approaches are Sammon Mappings [119], Locally Linear Coordination [120], Manifold Charting [121], t-Distributed Stochastic Neighbor Embedding (t-SNE) [108] and Multilayer Autoencoder [122]. Multilayer autoencoders are becoming especially popular for visualization because they are based on neural networks that are popular across dozens of fields including the design automation community. This work, though, does not employ such neural network based approaches for visualization because they can require extensive resources for training the networks and are highly blackbox which leads to a lack of intuition about the visualization for the designer. One of the goals is to implement a visualization approach that can run on a typical desktop system rather than a supercomputing cluster. Therefore, another nonconvex approach that should be considered is t-SNE, a recently developed visualization approach with less computational expense. Further information about the approach and its suitability for design space visualization is discussed in Section 5.2

Various other visualization techniques exist such as topological splines [123] and other charting approaches [124], but for the sake of brevity the remainder of this section will focus on the implementation of the dimension reduction and visualization techniques that have been applied for design exploration.

Many of the methods available for visualizing high-dimensional spaces focus on visualizing how the variables in the design space influence the performance. This is usually in the context of an optimization problem. It should be noted that our method of relating the design space to the performance space is a set-based method that does not seek to optimize performance subject to constraints. Nonetheless, a review of such methods is essential to determine if any of the approaches can be adapted to visualize design regions of interest and adapt visualization methods in the optimization domain for our purposes.

Cloud Visualization (CVis) [125] is an optimization visualization tool for making effective decisions throughout the design and optimization process by matching the data in both the performance (output) space and the design (input) space for comparisons. The performance space shows the variables with the greatest influence on a design. The performance space can also display the solution relative to multiple objectives instead of just a single objective. CVis is limited to viewing three design variables at a time, requiring the designer to use multiple plots to show all of the design variables, which can lead to confusion.

Visual design steering [77] allows designers to interact with the optimization algorithm throughout the optimization process. Using a "rank and reduce" method, visual design steering determines the impact of design variables on the objective function. Then, through graph morphing the n-dimensional design space can be visualized in a three-dimensional space where each of the three axes is a variable responsible for the most change in performance. Slider bars, where the remaining variables can be modified, update the 3D graph. Again, this method is limited to plot only three variables per plot.

Hyper-radial visualization (HRV) developed by Chiu et al. views the interactions of multiple objectives of an optimization problem [126]. By grouping the multiple objectives together, the interactions can be visualized in a two-dimensional (2-D) space. A notion deemed the utopia point, is defined as the point where both manufactured objectives are minimized and is represented at the origin. A radial projection is then constructed around the utopia point where each radius has an equal overall objective value, and therefore every point located on that radius has an identical objective value. The two-dimensional visualization allows for simple interpretation of the data but has limited ability to interface with individual design variables as the focus is on the objective values.

Stump *et al*. developed the Applied Research Laboratory (ARL) Trade Space Visualizer (ATSV) to focus on displaying trade spaces or tradeoffs within the design space [78]. The visualization techniques applied in ATSV include but are not limited to scatter plots, glyph plots, and parallel coordinates, which are not unique techniques. A unique contribution of this work is visualizing uncertainty in the design variables but this visualization technique still suffers from the inability to visualize more than three design variables at a time.

Many other methods are concerned with showing the interplay of design spaces with performance space for optimizing problems, including commercially available packages such as Isight, VizQL, and Sportfire. For the sake of brevity only methods that can be used to visualize the design space separately from the performance or objective space will be discussed.

Self-organizing maps (SOM) [86] discussed previously have been used to identify and visualize clusters in the design space. Cityplot [76] is a method that attempts to do so. It can visualize a sample of an arbitrary (continuous or combinatorial) design space and the corresponding single or multidimensional objective space simultaneously. Essentially a superposition of a dimensionally reduced representation of the design decisions and bar plots representing the multiple criteria of the objective space, Cityplot can provide explicit information on the relationships between the design decisions and the design criteria. Cityplot can present decision settings in different parts of the space and reveal information on the decision criteria mapping, such as sensitivity, smoothness, and key decisions that result in particular criteria values. By focusing Cityplot on the Pareto frontier, Cityplot can reveal tradeoffs and Pareto optimal design families without prior assumptions on the structure of either. A drawback of this method is that it commonly splits similar clusters into multiple clusters and distributes them across the space being visualized. To avoid

undesirable cluster separation the approach requires careful initialization that is not possible generally.

Another recent visualization strategy that has been discussed previously is the work of Chen *et al.* [80] that has focused on visualizing the low dimensional embedding of a high dimensional design space to uncover semantic attributes. The approach first used the original spectral clustering approach to identify clusters of designs that had already been termed feasible. Following identification of clusters Chen *et al.* visualized the clusters to determine if semantic relationships could be uncovered. The three approaches used were principle component analysis (PCA) [112], Kernal PCA [107], and stacked denoising autoencoders (SdA) [127] which is a neural network-based approach. They compared the quality of each visualization using two metrics which provided insights into two aspects of visualization although selection of the various tuning parameters of the visualization algorithms was not explained.

The first metric, reconstruction, determined the accuracy of the inverse mapping from low dimensional design space to the original space. This metric was of interest to the authors because the feasible design boundary was unknown, and the researchers wanted to be sure designs identified in the low dimensional space were reasonable in the high dimensional space. Reconstruction is of less interest in this dissertation because the design boundaries have been well-defined and the BNC approach can identify the feasible decision boundary easily.

The second metric evaluated the quality of the visualization with respect to structural preservation of the low dimensional mapping. The metric, known as the geodesic distance inconsistency (GDI), which is discussed further in Section 5.2, provided useful information regarding the quality of the visualization but comes at a high computational expense that can be prohibitive when the data set is large. Furthermore, the geodesic

distance is the quantity being optimized for certain visualization techniques such as Isomap and LTSA so using this as the quality metric naturally favors such visualization approaches.

The work by Chen *et al.* provided a framework for visualization and introduced algorithms that are the state of the art for visualization in the field of design. The work helped to form the structure of the visualization approach adopted in this work and led to the identification of areas of improvement. As such it will be referenced extensively in this work to provide a datum for current visualization algorithms for design exploration. This dissertation introduces a new metric for evaluating the preservation of design space structure. Before introducing the metric, the visualization strategies used in this work are introduced, including a new approach, t-SNE, that has yet to be utilized for design exploration.

5.2 Introduction to Dimension Reduction and Visualization Techniques

As previously introduced, various forms of dimension reduction techniques are available to designers to aid in visualizing high dimensional datasets. This work will focus on two particular approaches: Kernel Principal Components Analysis (KPCA) and t-Distributed Stochastic Neighborhood Embedding (t-SNE). KPCA has been explored by other researches for design space exploration while t-SNE, to the best knowledge of the author, has not been employed. The first approach, KPCA, is a convex based approach while t-SNE is a nonconvex based approach. The remainder of this section provides the mathematical theory describing both approaches and provides insight into how these approaches can be tuned to affect their performance.

5.2.1 KERNEL PRINCIPAL COMPONENT ANALYSIS

Much of KPCA [107] is similar to the original PCA but there are some key similarities and differences between the two approaches. Both approaches rely on eigenanalysis to project a high-dimensional dataset into a low-dimensional space but KPCA performs a nonlinear projection whereas PCA performs a linear projection into a low-dimensional space. Because KPCA performs a nonlinear embedding, it commonly captures the structure of nonlinear high dimensional datasets better. KPCA accomplishes this by exploiting a kernel trick to produce the nonlinear projection.

To begin the discussion of KPCA, consider a datapoint, $\boldsymbol{x_j} \epsilon \mathbb{R}^D$, that is in a high dimensional dataset, for example, points on the boundary of a satisfactory design region. Next consider some unknown function $f(\boldsymbol{x_j})$ that maps $\boldsymbol{x_j}$ **to** some feature space, $F \epsilon \mathbb{R}^M$ where $M \gg D$. The covariance of the mapped points, $\Sigma_f \epsilon \mathbb{R}^{MXM}$ can be determined by Equation 5.1.

$$\Sigma_f = \frac{1}{N} \sum_{j=1}^{N} f(\boldsymbol{x_j}) f(\boldsymbol{x_j})^T \tag{5.1}$$

The scalar eigenvalues, λ_p and the eigenvectors, $\boldsymbol{\phi_p} \epsilon \mathbb{R}^m$, must satisfy Equation 5.2.

$$\Sigma_f \boldsymbol{\phi_p} = \lambda_p \boldsymbol{\phi_p} \tag{5.2}$$

It is worth noting at this point that the eigenvectors of the covariance are the principal components of the mapped data in the feature space. Since the high dimensional mapping is unknown the vectors cannot be directly calculated using this form. Therefore, the following discussion describes how these principal components can be determined

without knowing the mapping. Equation 5.1 can be substituted into Equation 5.2 and manipulated with the properties of transposes to yield Equation 5.3.

$$\left[\frac{1}{N}\sum_{j=1}^{N} f(\boldsymbol{x_j})f(\boldsymbol{x_j})^T\right]\boldsymbol{\phi_p} = \frac{1}{N}\sum_{j=1}^{N}\left[f(\boldsymbol{x_j})\left[f(\boldsymbol{x_j})^T\boldsymbol{\phi_p}\right]\right]^{T^T}$$

$$= \frac{1}{N}\sum_{j=1}^{N}\left[\left[f(\boldsymbol{x_j})^T\boldsymbol{\phi_p}\right]^T f(\boldsymbol{x_j})^T\right]^T$$

$$= \frac{1}{N}\sum_{j=1}^{N}\left[[\boldsymbol{\phi_p^T} f(\boldsymbol{x_j})]f(\boldsymbol{x_j})^T\right]^T = \frac{1}{N}\sum_{j=1}^{N} f(\boldsymbol{x_j})[\boldsymbol{\phi_p} \cdot f(\boldsymbol{x_j})] = \lambda_p\boldsymbol{\phi_p} \qquad (5.3)$$

With the form presented in Equation 5.3, $\boldsymbol{\phi_p}$ can be determined implicitly by Equation 5.4 which further shows that $\boldsymbol{\phi_p}$ is a linear combination of the mapped datapoints.

$$\boldsymbol{\phi_p} = \frac{1}{\lambda_p N}\sum_{j=1}^{N}(f(\boldsymbol{x_j})\cdot\boldsymbol{\phi_p})f(\boldsymbol{x_j}) = \sum_{j=1}^{N} a_j^{(p)} f(\boldsymbol{x_j}) \qquad (5.4)$$

The coefficients of the linear combination, $a_j^{(p)}$, are given by Equation 5.5

$$a_j^{(p)} = \frac{1}{\lambda_p N}\, f(\boldsymbol{x_j})\cdot\boldsymbol{\phi_p} \qquad (5.5)$$

Next, we will define the kernel function, κ, by Equation 5.6 which results in Equation 5.7 after left multiplying Equation 5.4 by $f(\boldsymbol{x_i})^T$

$$\kappa(\boldsymbol{x_i}, \boldsymbol{x_j}) = f(\boldsymbol{x_i})\cdot f(\boldsymbol{x_j}) \qquad (5.6)$$

$$f(\boldsymbol{x_i}) \cdot \boldsymbol{\phi_p} = \sum_{j=1}^{N} a_j^{(p)} f(\boldsymbol{x_i}) \cdot f(\boldsymbol{x_j}) = \sum_{j=1}^{N} a_j^{(p)} \kappa(\boldsymbol{x_i}, \boldsymbol{x_j}) \tag{5.7}$$

Note that Equation 5.7 provides the projection of the mapped data into its principal components, so if the kernel function is known and the coefficient values are determined, the projection can be obtained without knowing the original mapping function, $f(\boldsymbol{x_i})$. To obtain these desired quantities some steps must first be taken. By multiplying Equation 5.5 by $\lambda_p N$ and substituting the result into Equation 5.7, the result shown in Equation 5.8 can be determined.

$$a_j^{(p)} \lambda_p N = \sum_{j=1}^{N} a_j^{(p)} \kappa(\boldsymbol{x_i}, \boldsymbol{x_j}) \tag{5.8}$$

Next the kernel matrix, $\mathrm{K} \epsilon \mathbb{R}^{MXM}$, and coefficient vector, $\boldsymbol{a^{(p)}}$, can be defined by Equation 5.9 and 5.10, respectively, which allow Equation 5.8 to be recast as a matrix equation given by Equation 5.11.

$$\mathrm{K}_{ij} = \kappa(\boldsymbol{x_i}, \boldsymbol{x_j}) \tag{5.9}$$

$$\boldsymbol{a^{(p)}} = \left[a_1^{(p)}, \ldots, a_N^{(p)}\right]^T \tag{5.10}$$

$$\lambda_p N \boldsymbol{a^{(p)}} = \mathrm{K} \boldsymbol{a^{(p)}} \tag{5.11}$$

Equation 5.11 is actually an eigenvalue problem where $\boldsymbol{a^{(p)}}$ are the eigenvectors of K, which have implications for calculating the projection of the mapped data into its principal components. First, the coefficients, $\boldsymbol{a_j^{(p)}}$, can be determined by calculating the eigenvectors of the kernel matrix. Second, the eigenvalues are proportional to the

eigenvalues of the original covariance matrix from Equation 5.1. With the eigendecomposition of the kernel matrix, the projection, $f(\boldsymbol{x_i}) \cdot \boldsymbol{\phi_p}$, of the mapped data into its principal components can be determined by Equation 5.7. By selecting the eigenvectors associated with the largest eigenvalues, the components responsible for the most variance in the mapped data can be determined, which allows features of the original data to be extracted.

One task still remains to perform KPCA. What should the kernel function be? Based on the formulation just discussed, the only restriction on the kernel is that its associated kernel matrix must be positive semidefinite (PSD). One of the most common kernel functions and the one selected in this work is the Gaussian kernel defined by Equation 5.12.

$$\kappa(\boldsymbol{x_i}, \boldsymbol{x_j}) = \exp\left(-\frac{\left\|\boldsymbol{x_i} - \boldsymbol{x_j}\right\|_2}{2\sigma^2}\right) \tag{5.12}$$

The tuning parameter σ can be varied to control the influence of the kernel for large and small distances. As a result, the projections determined by the approach are sensitive to the values selected for this parameter. Current research has utilized cross validation to automatically select the value of the tuning parameter, but cross validation for approaches based on PCA are not straightforward. As a result, an approach must be proposed to determine the best tuning parameter. This approach is the focus of the new metric introduced in the next section, but first, a second dimension reduction technique and visualization approach, t-SNE, is discussed.

5.2.2 t-Distributed Stochastic Neighbor Embedding

The nonconvex visualization approach, t-SNE, [108] has been gaining popularity for visualization due to its effective and efficient results. It is able to balance retaining both global and local structures of high dimensional data sets. To the best knowledge of the authors, this approach has yet to be implemented to visualize design spaces, so part of the focus of this work is to introduce a novel visualization method that can accompany a novel implementation approach. The formulation of t-SNE is largely based on the original stochastic neighbor embedding (SNE) approach but modifies the algorithm slightly to achieve significantly better visualizations. Therefore the discussion on t-SNE begins with a discussion of the original SNE.

SNE begins by defining a high dimensional datapoint, $\boldsymbol{x_i}$, that can be transformed to a low-dimensional point, $\boldsymbol{y_i}$ through a mapping. The set of all high dimensional points, $\boldsymbol{X}$, contains N points and is mapped to the low-dimensional set, $\boldsymbol{Y}$. To determine this mapping, a stochastic approach is used. The high-dimensional pairwise distance between two points in the set, $\boldsymbol{X}$, is converted to a conditional probability, $p_{j|i}$ that represents the similarity of two points, $\boldsymbol{x_i}$ and $\boldsymbol{x_j}$ in the high dimensional space. The conditional probability is given by Equation 5.13 where $p_{i|i} \equiv 0$ and σ_i is a local tuning parameter.

$$p_{j|i} = exp\left(\frac{\left\|\boldsymbol{x_i} - \boldsymbol{x_j}\right\|_2^2}{2\sigma_i^2}\right)\left(\sum_{k\neq i}^{N} exp\left(-\frac{\|\boldsymbol{x_i} - \boldsymbol{x_k}\|_2}{2\sigma_i^2}\right)\right)^{-1} \tag{5.13}$$

Similarly, a conditional probability in the low-dimensional space, $q_{j|i}$, can be defined by Equation 5.14 that relates the pairwise Euclidian distance between the low-dimensional mapped points $\boldsymbol{y_i}$ and $\boldsymbol{y_j}$.

$$q_{j|i} = \exp\left(\left\|\boldsymbol{y_i} - \boldsymbol{y_j}\right\|_2^2\right)\left(\sum_{k\neq i}^{N} \exp\left(\left\|\boldsymbol{y_i} - \boldsymbol{y_j}\right\|_2^2\right)\right)^{-1} \tag{5.14}$$

Note that the tuning parameter has been eliminated in the low-dimensional conditional probability because, as will be seen later, it will not affect the results of the visualization. With this conditional probability formulation, SNE considers mappings to be of high quality if the mismatch between $p_{j|i}$ and $q_{j|i}$ is low with $p_{j|i} = q_{j|i}$ representing a perfect mapping. To quantify the level of mismatch over all the points, the Kullback-Leibler divergence measure is used which is provided by Equation 5.15. The cost function, C, is the objective that SNE attempts to minimize through a momentum-based gradient descent algorithm to help avoid local minima that likely exist.

$$C = \sum_{i=1}^{N}\sum_{j=1}^{N} p_{j|i} \log\frac{p_{j|i}}{q_{j|i}} \tag{5.15}$$

The form of the cost functions leads to a nonsymmetric penalization of mappings. For example, points that are close in the high-dimensional space (large $p_{j|i}$) that are mapped far apart in the low-dimensional space (small $q_{j|i}$) are penalized more severely than points that are far away in a high dimensional space (small $p_{j|i}$) but mapped closely in a low-dimensional space (large $q_{j|i}$). With this structure SNE focuses on preserving local structure rather than global structure. Furthermore, the formulation causes points that are close to each other in the high dimensional space to be condensed at the center of the low dimensional space. Commonly, if multiple clusters are being visualized, they tend to condense to one region.

The t-SNE approach builds on the SNE approach but modifies the formulation to balance both global and local structure to produce better mappings of regions and multiple clusters. The first modification t-SNE makes is to use joint probability rather than conditional probabilities to describe the similarity of two points. This is done to decrease the computation time required to calculate the gradient of the cost function by reducing the number of terms in the gradient function [108]. The joint probabilities are not the standard probabilities one would expect given the initial formulation of SNE. Rather, they each have their own form. First, the joint probability describing the similarity of high dimensional points, p_{ji}, is the weighted average of the conditional probabilities given by Equations 5.13, as documented in Equation 5.16.

$$p_{ij} = \frac{p_{j|i} + p_{i|j}}{2N} \tag{5.16}$$

The joint probability describing the similarity of low dimensional points, q_{ji}, is now described by the student t-distribution with one degree of freedom due to its heavy-tailed nature. Heavy-tailed means that the tails of the distribution are not bounded by negative exponential distributions. Equation 5.17 provides the form of the low-dimensional joint distribution.

$$q_{ji} = \frac{\left(1 + \left\|\boldsymbol{y_i} - \boldsymbol{y_j}\right\|_2^2\right)^{-1}}{\sum_{k \neq l}(1 + \|\boldsymbol{y_k} - \boldsymbol{y_l}\|_2^2)^{-1}} \tag{5.17}$$

The use of the heavy-tailed distribution has some attractive features compared to the light-tailed normal distribution used for the original SNE approach. First, it allows moderate separation in the high dimensional space to be modeled more faithfully by larger

distances in the low dimensional spaces because there is more "probabilistic mass" distributed into the tails. Second, for large pairwise distances in the low dimensional space, the t-distribution approximates an inverse square law. This allows for better separation of clusters when visualizing multiple clusters while still balancing local structure within clusters well; much in the same way that the gravitational force on a planet varies with its structure but the interactions between planets assumes they are point masses.

With the joint probabilities at each scale established for the t-SNE approach, the cost function given by Equation 5.18 must be defined so the optimization strategy can be discussed. As discussed previously, the Kullback-Leibler divergence measure is used, but the joint probabilities are compared instead of the conditional probabilities.

$$C = \sum_{i=1}^{N} \sum_{j=1}^{N} p_{ji} \log \frac{p_{ji}}{q_{ji}} \tag{5.18}$$

By taking the partial derivative of the cost function with respect to a mapped point $\boldsymbol{y_i}$, the real benefits of the approach can begin to be uncovered. The derivative is provided by Equation 5.19 which is then used to generate Figure 5.2 [108] that plots the gradient values as a function of the high dimensional distance between two point, $\left\|\boldsymbol{x_i} - \boldsymbol{x_j}\right\|_2$, and the low dimensional distances between the two mapped points, $\left\|\boldsymbol{y_i} - \boldsymbol{y_j}\right\|_2$.

$$\frac{\delta C}{\delta y_i} = \sum (p_{ij} - qij)(y_i - y_j) \left(1 + \left\|\boldsymbol{y_i} - \boldsymbol{y_j}\right\|_2^2\right)^2 \tag{5.19}$$

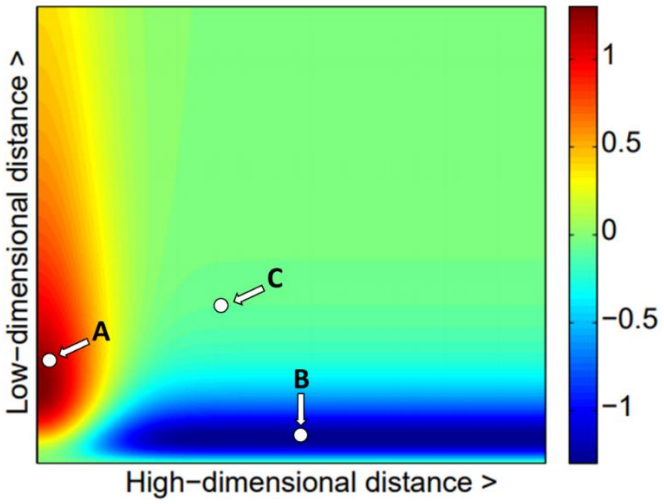

Figure 5.2: Value of the gradient for the t-SNE approach as a function of the mapped separation and original separation of two points. Marker A indicates mapped points that will be attracted in the mapped space, Marker B indicates mapped points that will be repelled in the mapped space, and Marker C indicates mapped points that have no attraction or repulsion [108].

A negative gradient value indicates a “force” that will attempt to repel the points driving them farther apart, a positive value will try to drive points closer together, and a zero value will keep the points stationary. Three Markers, A, B, and C are specified on Figure 5.2 to highlight the strengths of the approach. First, Marker A indicates mapped points that are far apart in the low dimensional space but are close in the high dimensional space. The gradient indicates that these points should be driven together which matches intuition. In opposition to Marker A is Marker B that indicated two points that are close in the low dimensional space but far apart in the high dimensional space. The gradient is negative which drives them apart in the low dimensional space. Finally Marker C indicates two points that have approximately equivalent distances in both spaces and the gradient is zero implying there will be no force to drive them apart.

The final aspect of the t-SNE approach is the tuning parameter. The tuning parameter, σ_i, of the conditional probabilities used for the high dimensional data must be set. To set its value, another heuristic is introduced called the perplexity, $Perp$, which is related to the tuning parameter by Equations 5.20 and 5.21.

$$Perp = 2^{H(p_{j|i})} \tag{5.20}$$

where

$$H(p_{j|i}) = \sum_{j=1}^{N} p_{j|i} \log_2 p_{j|i} \tag{5.21}$$

Effectively, the perplexity is the continuous analog of neighborhood selection. If a value of perplexity is selected, the value of σ_i will be selected at each point to have the same neighborhood effect at each point, but the selection of the perplexity value is still required. The original paper recommended a perplexity value of approximately 50 as robust to change, but this work demonstrates that this is not necessarily true.

KPCA and t-SNE both require a certain level of tuning to obtain quality visualizations. A quality visualization varies in definition depending on which approach is used because both approaches seek to minimize a different objective. In general, different visualization approaches optimize different objective functions. To be able to compare the quality of visualization, metrics must be developed that are impartial to the approach being used. This is not a simple task but this work proposes a new metric—preservation—that attempts to combine the best features of other metrics while eliminating some of their shortcomings. Secondly, the proposed metric, to the best of the author's knowledge, has not been implemented in other dimension reduction techniques, so it is less likely to be

biased towards specific techniques. Section 5.3 reviews previous metrics and introduces the new metric and a framework for utilizing it.

5.3 Evaluating the Quality of Visualizations

The vast number of visualization and dimension reduction techniques make it difficult to select which approach is best to use. While this work proposes using t-SNE to visualize satisfactory design regions identified by the BNC approach, there may be another approach developed in the future that outperforms t-SNE. But what does it mean for a visualization to outperform another visualization technique? Saying one is better than the other is quite subjective, so there have been attempts to quantify the quality of a visualization. The two most common metrics used to objectively measure the quality of a visualization are trustworthiness and continuity, which are typically used together [109].

Informally, trustworthiness quantifies how many points mapped closely in the low-dimensional space are not close in the high-dimensional space while continuity quantifies how many points that are close in the high-dimensional space are not mapped closely in the low-dimensional space. To formally provide a definition of each metric some terms need to be defined. First, N, is the total number of points being visualized and k is the number of points defined to be in the neighborhood of a point, i.e., the k closest points. Next, $r(i,j)$ is the rank order in terms of distance for the j^{th} point relative to the i^{th} point in the high-dimensional space and $\hat{r}(i,j)$ is the rank order in terms of distance for the j^{th} point relative to the i^{th} point in the low-dimensional space. Finally the set, $U_k(i)$, is the set of points that are in the k-nearest neighborhood (kNN) of the i^{th} point in the low-dimensional space but not in the high-dimensional space and $V_k(i)$, is the set of points that are in the k-nearest neighborhood of the i^{th} point in the high-dimensional space but not in the low-dimensional space. To clarify the definitions of the sets $U_k(i)$ and $V_k(i)$, Figure

5.3 is a Venn diagram where the red region represents points that are in the kNN of the i^{th} point in the original, high dimensional space and the blue region represents mapped points that are in the kNN of the mapped i^{th} point.

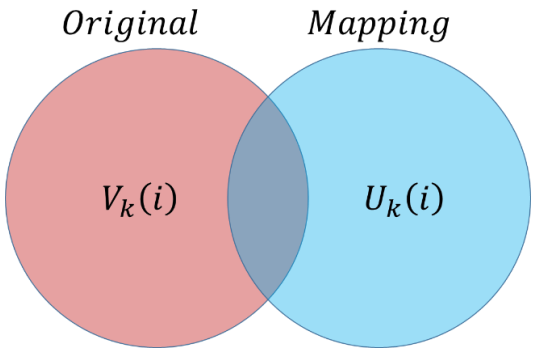

Figure 5.3: Venn diagram clarifying the definition of the two sets, $U_k(i)$ and $V_k(i)$, in terms of the mappings and original space.

The overlapping region represents points that are in the kNN of the original space and in the mapped space. The non-overlapping red region, or $U_k(i)$, affects trustworthiness. The nonoverlapping blue region, $V_k(i)$, affects continuity.

With these terms established, trustworthiness, $T(k)$, and continuity, $C(k)$, can be provided by Equations 5.22 and 5.23. Notice that both metrics are dependent on the neighborhood size.

$$T(k) = 1 - \frac{2}{Nk(2N - 3k - 1)} \sum_{i=1}^{N} \sum_{j \in U_k(i)} (r(i,j) - k) \tag{5.22}$$

$$C(k) = 1 - \frac{2}{Nk(2N - 3k - 1)} \sum_{i=1}^{N} \sum_{j \in V_k(i)} (\hat{r}(i,j) - k) \tag{5.23}$$

Both metrics are bounded between 0 and 1 where a perfect mapping will have a trustworthiness and continuity of 1 and a low-quality mapping will be lower. It is important to note though, that a mapping need not be perfect to have a continuity and trustworthiness of 1. This is because these metrics are not concerned with the exact distances separating points, rather with the rank ordering of the distances. This distinction was made intentionally, so the metric could be used for categorical problems. By using only a rank ordering, non-perfect mappings can cause the metric to be falsely high for continuous spaces.

To elucidate how the metrics can overestimate the quality of a mapping a simple example is provided. Consider a set of points in $\mathbb{R}^2$ that are initially in the L-shaped configuration shown in Figure 5.4.

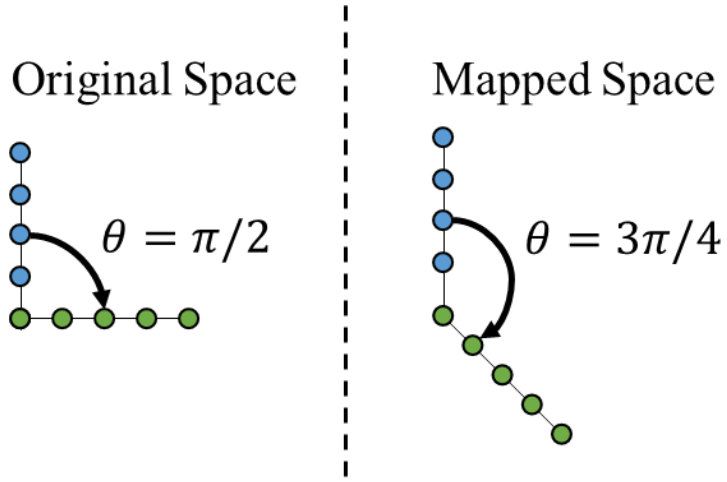

Figure 5.4: Example data set where the original dataset (left) can be mapped to the dataset (right) by varying the angle, θ.

Define the angle, θ, to be the angle between the two lengths of the L-shaped structure. Initially $\theta = \pi/2$, and a mapping is defined that simply varies θ within the interval $[0,2\pi]$. Figure 5.5 also provides a specific mapping of the original space where the

angle between arms, $\theta = 3\pi/4$. For each value of θ in the interval, the continuity and trustworthiness between the resultant mapping and original space were determined. Four different values of the neighborhood size were considered, $k = 5$, 10, 25, and 50, for the dataset where $N = 100$. The results of the various mappings are shown in Figure 5.5 where the horizontal axis is the angle of rotation in radians and the vertical axes are the metrics used.

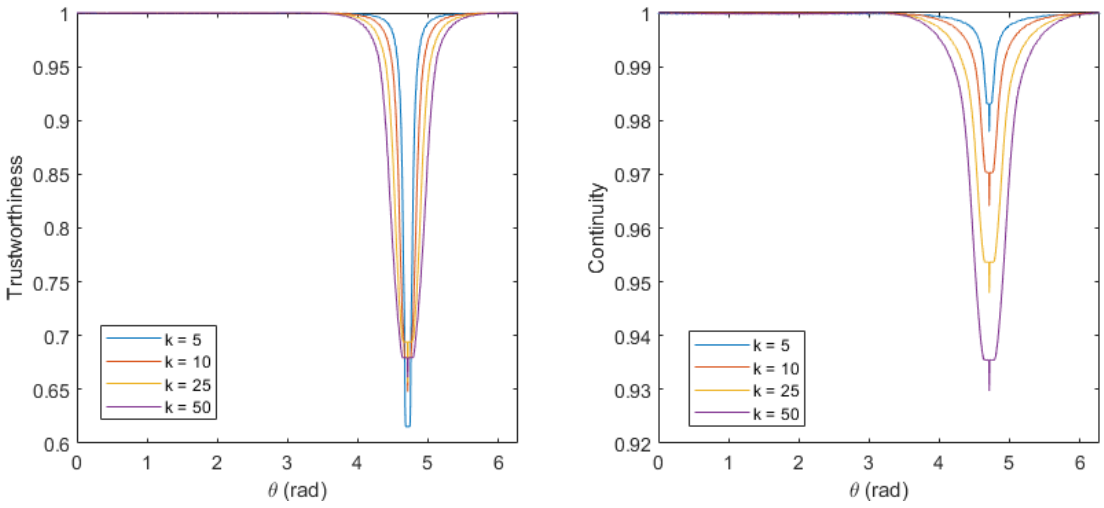

Figure 5.5: Trustworthiness (left) and continuity (right) as a function of θ for the L-Shaped example structure.

As stated previously, a value of 1 for continuity and trustworthiness should indicate a perfect mapping, but this is not the case. A few select mappings with continuity and trustworthiness metrics simultaneously equal to 1 are provided in Figure 5.6 for $k = 10$.

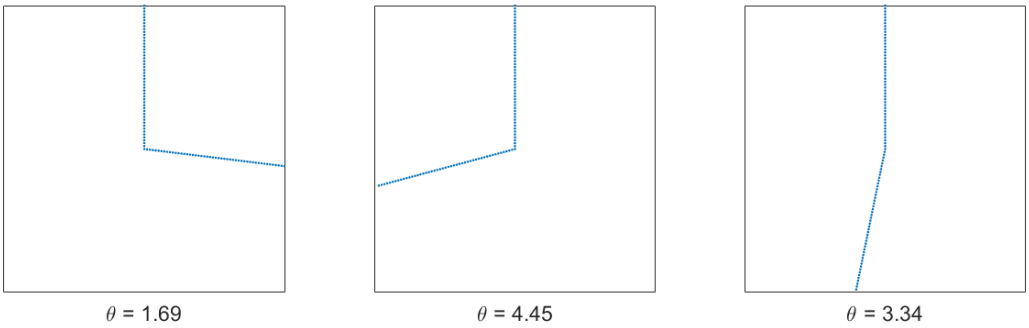

Figure 5.6: Selected mappings in which the trustworthiness and continuity metrics are both 1.

Within rotational symmetry, the only perfect mapping should be at odd integer intervals of $\pi/2$, that is $\pi/2, 3\pi/2, 5\pi/2, ...$, but as indicated in the plots of Figure 5.6, continuity and trustworthiness are simultaneously 1 for nonperfect mappings. This outcome is due to the rank ordering of distances, rather than the consideration of their continuous values in the metrics. Even through various rotations, the ranks of the k^{th} closest points remain the same because, generally, points are closest to other points on the same line segment. If the whole line is rotated, then the rank ordering of distances will be largely unchanged.

Another metric that has been used is the geodesic distance inconsistency (GDI) which was proposed by Chen *et al* [80]. in their work on visualizing design spaces. The metric was used to evaluate the quality of three different dimension reduction/visualization techniques, PCA, KPCA, and stacked denoising autoencoder (SdA). The metric is first determined by creating a graph in the high-dimensional space where the edge weights are the pairwise distances between the kNN points. The approach utilizes a technique, based on LTSA, that determines the number of kNN to use in the graph to preserve the local structure. With the graph created, the minimum geodesic distance between points can be calculated. The geodesic distance is a path dependent distance on a graph that is equivalent

to the sum of the edge weights traveled to get from one node to another. Therefore the minimum geodesic distance is the minimum sum of edge weights to travel from one node to the other. Figure 5.7 provides an image of 4 points in $\mathbb{R}^2$ that were used to determine a graph structure that allows for the minimum geodesic distance matrix, D_G, to be determined.

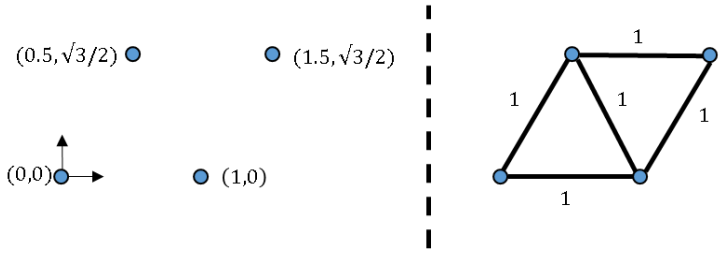

Figure 5.7: Four points in the original Cartesian space (left) that are converted into a graph (right) where the edge weights are based on the distance to the kNN ($k = 1$).

With the geodesic distance matrix determined, the low dimensional mapping is considered in a similar manner. Instead of creating a graph, the pairwise Euclidian distance between low dimensional points that are connected in the high dimensional space are calculated and placed in a similarity matrix, D_E. Figure 5.8 provides the associated similarity matrix for the same structure as Figure 5.7.

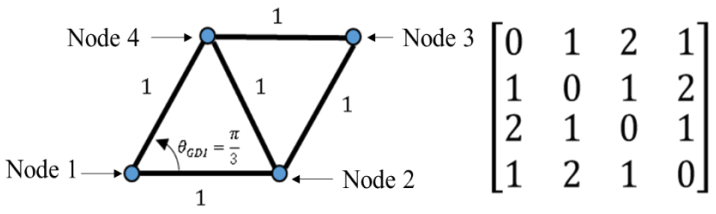

Figure 5.8: The associated similarity matrix for the shown graph structure in which the indices of the matrix, i and j, correspond to the geodesic distance between the i^{th} and j^{th} point.

With the similarity and geodesic distance matrix determined, they are reshaped into the vectors, $\boldsymbol{d_E}$ sand $\boldsymbol{d_G}$ respectively. The GDI can be determined by Equation 5.24 where $\rho(\boldsymbol{d_G}, \boldsymbol{d_E})$ is the Pearson Correlation Coefficient.

$$GDI = 1 - \rho(\boldsymbol{d_G}, \boldsymbol{d_E})^2 \tag{5.24}$$

The GDI is measuring the correlation between the similarity and geodesic matrices, such that high correlation implies the geodesic distances and Euclidian distances increase and decrease linearly with each other. In contrast to trustworthiness and continuity, a low GDI indicates a quality visualization, therefore to be consistent, this work will consider only the correlation term of Equation 5.23 to compare the metrics on the same scale.

While the GDI metric does not fall into the same pitfalls as trustworthiness and continuity, it can lead to erroneous results. To demonstrate, consider the points and graph structure shown in Figure 5.8. Consider the case when the angle, $\theta_{GDI} = \pi/3$, to form a regular rhombus and the edge weights are all 1. Note that node 1 and 3 are not connected because a kNN value of 1 is used. Similar to the previous example with the L-Shaped structure, a mapping varies the angle, θ_{GDI}, in the range $[0, \pi/2]$. The GDI was determined for each angle and a plot showing the value of GDI as a function of θ_{GDI} is provided by Figure 5.9. The structure that maximizes GDI is plotted.

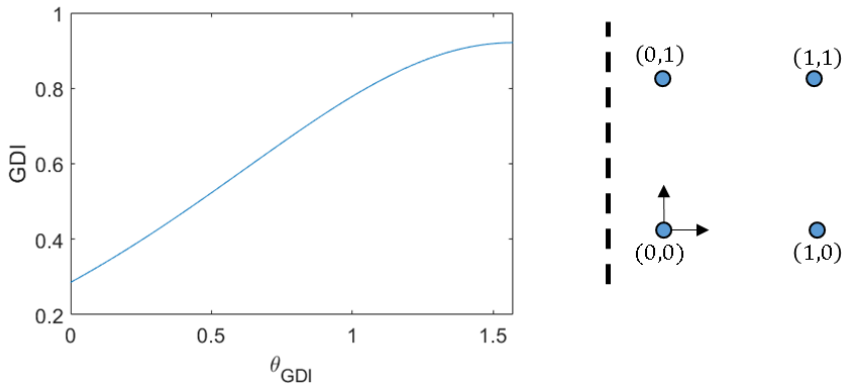

Figure 5.9: Plot of GDI as a function of θ_{GDI} for the example sheared square (left) with identified mapping that maximizes the correlation (right).

Interestingly, the results show that the mapping favors the square shaped structure and not the original structure. This can be explained by comparing the plots shown in Figure 5.10 where $\boldsymbol{d_G}$ is plotted against $\boldsymbol{d_E}$ for both mappings.

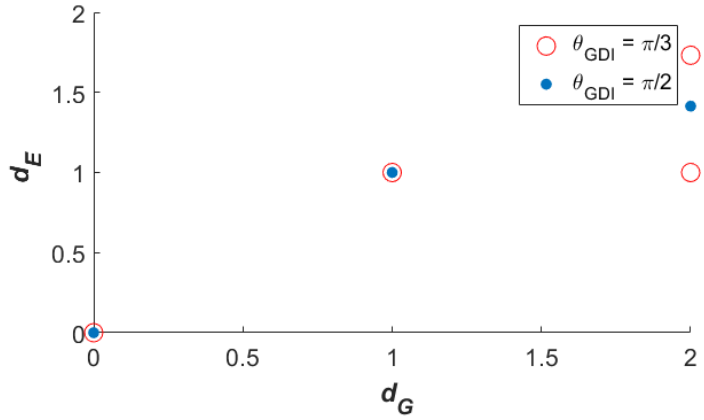

Figure 5.10: $\boldsymbol{d_G}$ plotted against $\boldsymbol{d_E}$ for the angle of the original mapping (red) and the angle identified as the best mapping (blue)

The red dots indicate the mapping where $\theta_{GDI} = \pi/3$, and the blue dots indicate the mapping where $\theta_{GDI} = \pi/2$. The correlation is higher for the square mapping because the distance between diagonal points in the Cartesian space is equal. This leads to the

erroneous conclusion that the square structure is a better mapping when the original mapping is clearly better. If the original graph structure connected both diagonals (Nodes 2 to 4), different results would be achieved, but they would still indicate the best mapping is not the original mapping.

The GDI metric also is biased towards selecting methods such as LTSA and LLE as the best visualization because these dimension reduction/visualization techniques minimize an objective function that is related to the GDI metric. The GDI metric was based on these methods, so it will naturally be biased to select these methods. Therefore, a metric that preserves distances well, conserves the rank ordering of the neighborhood, and is less biased for selection of specific visualization methods should be used. This work proposes such a metric. While slightly more complex to explain than the other metrics, it is hypothesized that the metric, which is called preservation in this work, provides more insight into the quality of the visualization.

The proposed metric combines aspects of the previous metrics that lead to preferable evaluation of visualizations. Much of the formulation of preservation, P, is also borrowed from spectral clustering due to its ability to balance both local and global structure. At a high level, the metric generates a kernel matrix on the original cluster in the high-dimensional space, K^O, and a kernel matrix on the mapped cluster in the low-dimensional space, K^M, that can be compared to measure the quality of the dimension/reduction and associated visualization. To generate the high-dimensional kernel matrix for a cluster, Equation 5.25 is provided, which has a similar form to the kernel used for STSC.

$$K_{ij}^0(k) = \exp\left(-\frac{d^2(\boldsymbol{x_i}, \boldsymbol{x_j})}{\sigma_i^O(k)\sigma_j^O(k)}\right) \tag{5.25}$$

The value of the i^{th} and j^{th} component of the kernel matrix is related to the Euclidian distance, d, between the points $\boldsymbol{x_i}$ and $\boldsymbol{x_j}$ via a self-tuning Gaussian. The smoothing parameters, $\sigma_i^O(k)$ and $\sigma_j^O(k)$, are provided by Equation 5.26 in which the dummy variable, l, is used to represent the l^{th} point of interest, $\boldsymbol{x_l^k}$ is the k^{th} closest point to point $\boldsymbol{x_l}$.

$$\sigma_l^O(k) = d\left(\boldsymbol{x_l}, \boldsymbol{x_l^k}\right) \tag{5.26}$$

Secondly, to generate the low-dimensional kernel matrix for the mapped cluster, Equation 5.27 is provided in a similar form to the kernel used for STSC, as well.

$$K_{ij}^M(k) = \exp\left(-\frac{d^2\left(\boldsymbol{y_i}, \boldsymbol{y_j}\right)}{\sigma_i^M(k)\sigma_j^M(k)}\right) \tag{5.27}$$

The value of the i^{th} and j^{th} component of the kernel matrix is related to the Euclidian distance, d, between the mapped points $\boldsymbol{y_i}$ and $\boldsymbol{y_j}$, which correspond to the original points $\boldsymbol{x_i}$ and $\boldsymbol{x_j}$. The smoothing parameters, $\sigma_i^M(k)$ and $\sigma_j^M(k)$, have a slightly different form than their high-dimensional counterpart, as provided by Equation 5.28.

$$\sigma_l^M(k) = d\left(\boldsymbol{y_l}, \tilde{\boldsymbol{y}}_l^{\boldsymbol{k}}\right) \tag{5.28}$$

Once again, the dummy variable, l, is used to represent the l^{th} mapped point of interest, $\boldsymbol{x_l}$, and the subtle, but important difference, lies in the definition of $\tilde{\boldsymbol{y}}_l^{\boldsymbol{k}}$. Unlike in previous formulations, it is *not* the k^{th} closest point to point $\boldsymbol{y_l}$, rather it is the k^{th} closest point k^{th}in the original space, $\boldsymbol{x_l^k}$.

Finally, with the two kernel matrices defined, the preservation, $P(k)$, can be determined via Equation 5.29 where $\|X\|_F$ is the Frobenius norm of a matrix.

$$P(k) = 1 - \frac{1}{2}\left\| \frac{K^O}{\|K^O\|_F} - \frac{K^M}{\|K^M\|_F} \right\|_F \tag{5.29}$$

Preservation, which is bounded between [0, 1] by the Cauchy-Schwartz inequality, provides information regarding the mismatch between each weighted pairwise distance across spaces. If the two kernels are equivalent, implying all distances are conserved, then the difference is the zero matrix with Frobenius norm 0 leading to a preservation of 1. The structure of preservation has features that should allow it to be a more reliable measure of visualization quality. By setting the tuning parameters in the low dimensional space based on the mapping of the k^{th} closest points in the high dimensional space, mappings that preserve distance *and* ordering of points are favored. Rather than prefer one or the other as is the case for the other metrics, they were combined into one single metric. Also all elements in the kernels contribute to preservation ensuring that points that are initially far away need to be far away and are penalized for being close. With preservation introduced, it should be compared to the other metrics to ensure it is at least competitive for providing the quality of dimension reduction/visualization techniques. Therefore Section 5.5 will compare the metrics on various datasets to explore the behavior of the metric.

5.4 Validation of Preservation for Cluster Visualization

To first demonstrate the accuracy of the metric it is applied to the example problems where trust and continuity were inaccurate. The same procedure for mapping the L-Shaped structure is followed as before but the metric used is preservation. As shown in Figure 5.11

the preservation metric only has a value of 1 at the increments of theta initially identified as the best values, odd integer multiples of $\pi/2$.

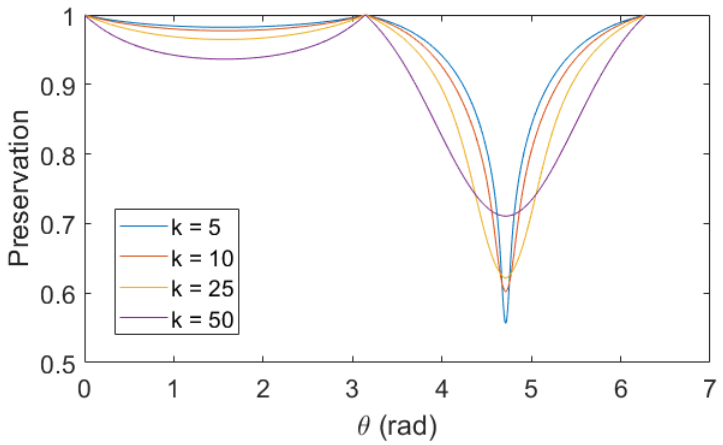

Figure 5.11: New metric, preservation, as a function of θ for the L-Shaped example structure.

Next, the metric is demonstrated on the example where GDI was not successful as well. Figure 5.12 provides the values of preservation for the various values of θ_{GDI} used where once again the metric identified the best mapping.

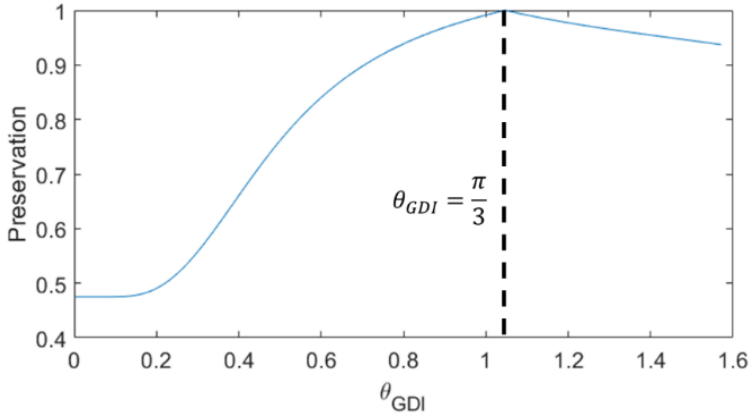

Figure 5.12: Preservation as a function of θ_{GDI} for the sheared square example problem.

These example problems, however, may be biased to favor the preservation approach so more complex examples are needed to validate the approach.

Five different clusters, each consisting of 243 points, were generated in a 24-Dimensional space: (1) a spiral or swiss roll, (2) a cross, (3) a multimodal surface (4) a hyperspherical shell, and (5) a complex parametric geometry. Each of the first 3 clusters lies on a 2-dimensional manifold so images are provided of the structure in $\mathbb{R}^3$ in Figure 5.13 (note that more than 243 points are shown to help clarify the structures).

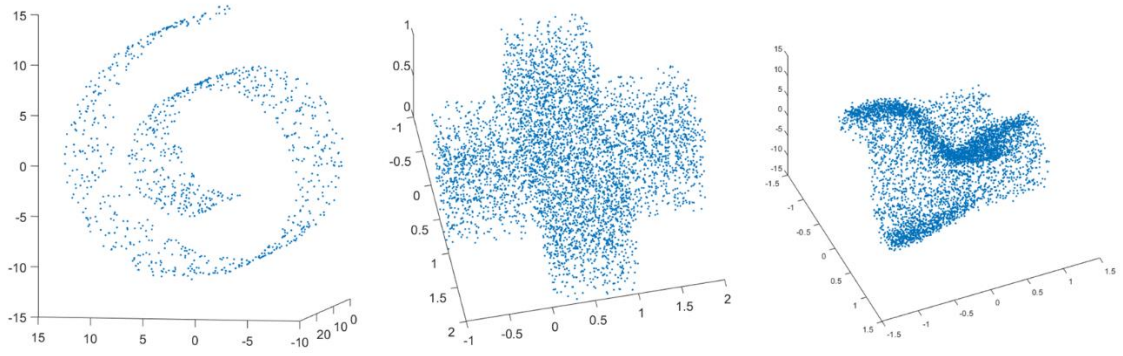

Figure 5.13: 3-Dimensional projection of the first three clusters, swiss roll (left), cross (center), and twin peaks (right), that were embedded in a 24-Dimensional Space

The hypersphereical shell and complex parametric geometry are described after discussion of the first three clusters.

The clusters shown in Figure 5.13 were selected because of their varying degree of difficulty to visualize even though they lie on a low dimensional manifold. First, the swiss roll, $\boldsymbol{x_{swiss}}$, is described by Equation 5.30 in which $\boldsymbol{e_i}$ is the i^{th} dimension in the 24-dimensional space; t and h are parametric variables; and $\boldsymbol{\epsilon_{noise}} \in \mathbb{R}^{24}$ is normally distributed noise centered at 0 with standard deviation 0.05.

$$\boldsymbol{x_{swiss}}(t,h) = t\cos(t)\boldsymbol{e_1} + h\boldsymbol{e_2} + t\sin(t)\boldsymbol{e_3} + \boldsymbol{\epsilon_{noise}} \tag{5.30}$$

$$where$$

$$t \in \left[\frac{3\pi}{2}, \frac{9\pi}{2}\right] \; and \; h \in [0,30]$$

This shape was selected because both global and local structure must be balanced to visualize it accurately. Since it spirals, points can be close based on absolute Euclidian distance, but if you must travel between them on the manifold, the points are far away due to the necessary path. This requires the visualization technique to be sophisticated enough to balance the global and local preservation.

The second shape or cross, $\boldsymbol{x_{cross}}$, which is given by Equation 5.31, was selected because of its sharp corners and abrupt transitions in directions along the outer surface. Furthermore, the BNC approach has identified similarly shaped regions for the NS metamaterials application previously, so it appeared to be a shape of interest.

$$\boldsymbol{x_{cross}} = \boldsymbol{R}_1 \cup \boldsymbol{R_2} \tag{5.31}$$

$$where$$

$$\boldsymbol{R_1} = l_1\boldsymbol{e_4} + l_2\boldsymbol{e_5} + l_2\boldsymbol{e_6} + \boldsymbol{\epsilon_{noise}}, \boldsymbol{R_2} = l_2\boldsymbol{e_4} + l_1\boldsymbol{e_5} + l_2\boldsymbol{e_6} + \boldsymbol{\epsilon_{noise}},$$

$$l_1 \in [-1,2], and \; l_2 \in [0,1]$$

The multimodal surface, or twin peaks, $\boldsymbol{x_{twin}}$, is given by the parametric Equation 5.32. This is a standard visualization structure that was selected due to its complex surface geometry. The BNC approach likely produces multimodal surfaces such as the twin peaks surface so it is desirable to see how these visualizations fare with such geometries.

$$\boldsymbol{x_{twin}} = t_1\boldsymbol{e_7} + t_2\boldsymbol{e_8} + 10sin(\pi t_1)tanh(3t_2)\boldsymbol{e_9} + \boldsymbol{\epsilon_{noise}} \tag{5.32}$$

$$where$$

$$t_1 \in [-1,1], and\ t_2 \in [-1,1]$$

Since the first three structures lie on low dimensional manifolds, whatever technique is used to visualize them in $\mathbb{R}^3$ should indicate a metric score that is nearly 1, if not 1.

The next cluster is a 5-Dimensional hyperspherical shell, $\boldsymbol{x_{sphere}}$, which can be described by Equation 5.33 and the five parameters, t_1, t_2, t_3, t_4, and t_5.

$$\boldsymbol{x_{sphere}} = t_1\boldsymbol{e_{10}} + t_2\boldsymbol{e_{11}} + t_3\boldsymbol{e_{12}} + t_4\boldsymbol{e_{13}} + t_5\boldsymbol{e_{14}} + \boldsymbol{\epsilon_{noise}} \tag{5.33}$$

$$where$$

$$t_1^2 + t_2^2 + t_3^2 + t_4^2 + t_5^2 = 1$$

By visualizing the relatively simple high-dimensional hypersherical shell, the quality of the visualization approaches can be compared. It is anticipated that the quality metrics will be lower than 1 but not substantially lower than 1 for the hyperspherical shell because it cannot be truly visualized in 3-dimensions.

The final cluster to be used for comparisons of metrics is the difficult shape described by Equation 5.34 with parameters, t_1, t_2, t_3, t_4, and t_5. This shape was selected due to its complex geometry and its difficulty for visualization in lower dimensions.

$$\boldsymbol{x_{difficult}} = \cos(t_1)\boldsymbol{e_{15}} + \tanh(3t_2)\boldsymbol{e_{16}} + (t_1 + t_3)\boldsymbol{e_{17}} + \cdots$$
$$t_4 sin(t_2)\boldsymbol{e_{18}} + t_5\cos(t_2)\boldsymbol{e_{20}} + (\mathrm{t}_4 + t_5)\boldsymbol{e_{21}} + \cdots$$
$$t_2\boldsymbol{e_{22}} + t_3 t_4\boldsymbol{e_{23}} + t_1\boldsymbol{e_{24}} + \boldsymbol{\epsilon_{noise}} \quad (5.34)$$

$$where$$

$$t_i \in [0,2\pi]$$

It is anticipated that for such visualizations the metrics should not be able to attain a value close to 1 because it is too complex for significant feature visualization.

For each of the first three clusters described by Equations 5.30-5.32, KPCA and TSNE were performed for a variety of heuristics. KPCA was performed where the tuning parameter of the Gaussian kernel, σ, was varied at 250 equal increments between the interval [0.001, 15] and the perplexity of t-SNE was varied at 243 equal increments between the interval [1, 243]. For each resultant dimension reduction/visualization, the trustworthiness, continuity, GDI, and preservation metrics were evaluated. Also, for trustworthiness, continuity, and preservation the kNN value was set to four different values, [12, 24, 36, and 48] which correspond to flooring 5%, 10%, 15%, and 20% of the number of points in each cluster respectively. The results of the KPCA study for the first 3 clusters (swiss roll, cross, and twin peaks) are presented in Figure 5.14(a,b, and c) in which the value of the kernel tuning parameter is plotted against the various metrics. The different kNN values are also indicated where applicable. Figure 5.15(a,b, and c) provides a similar plot but for the t-SNE visualization.

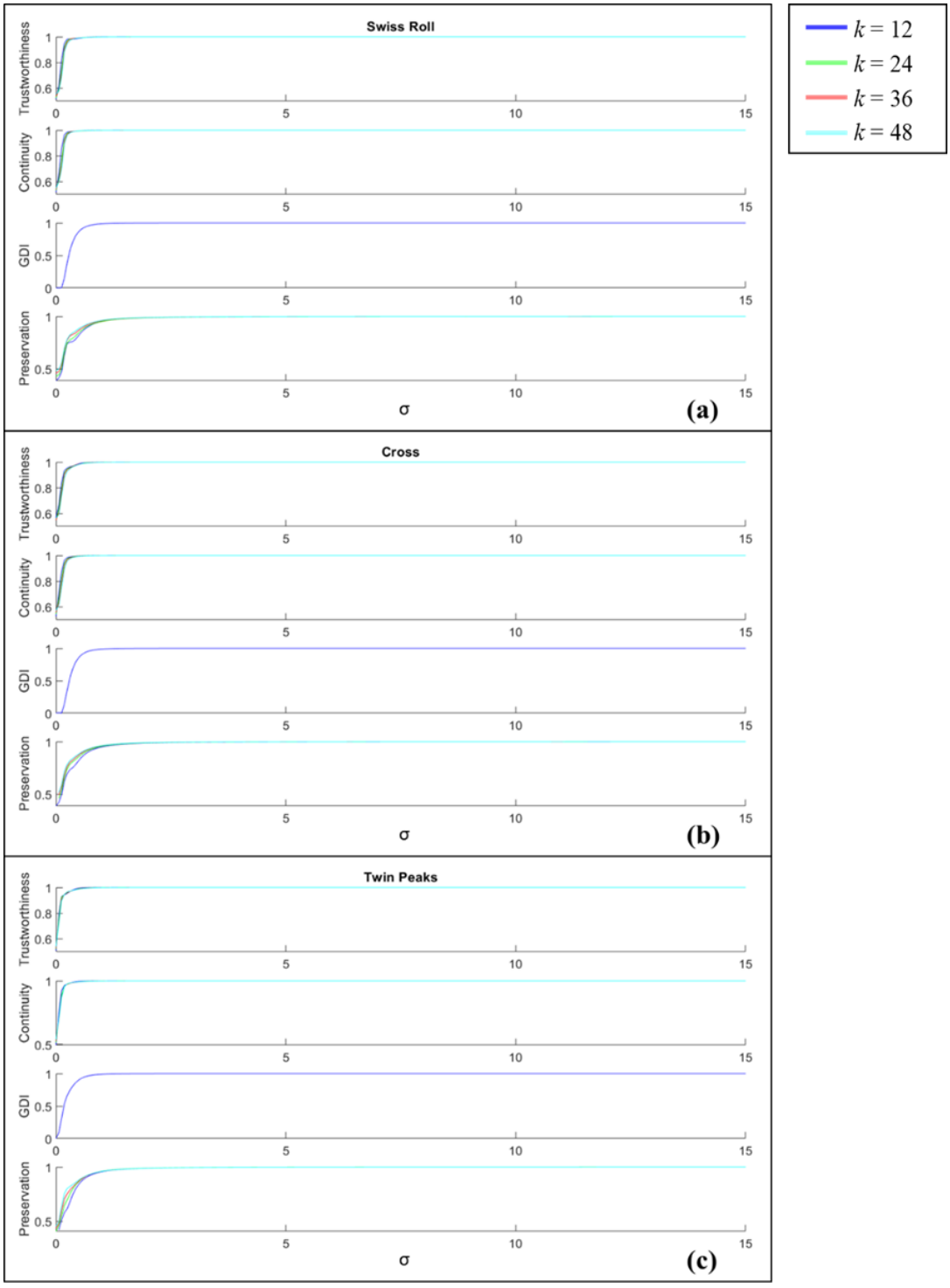

Figure 5.14: Results of metric comparison study for the KPCA dimension reduction for the (a) swiss roll, (b) cross, and (c) twin peaks.

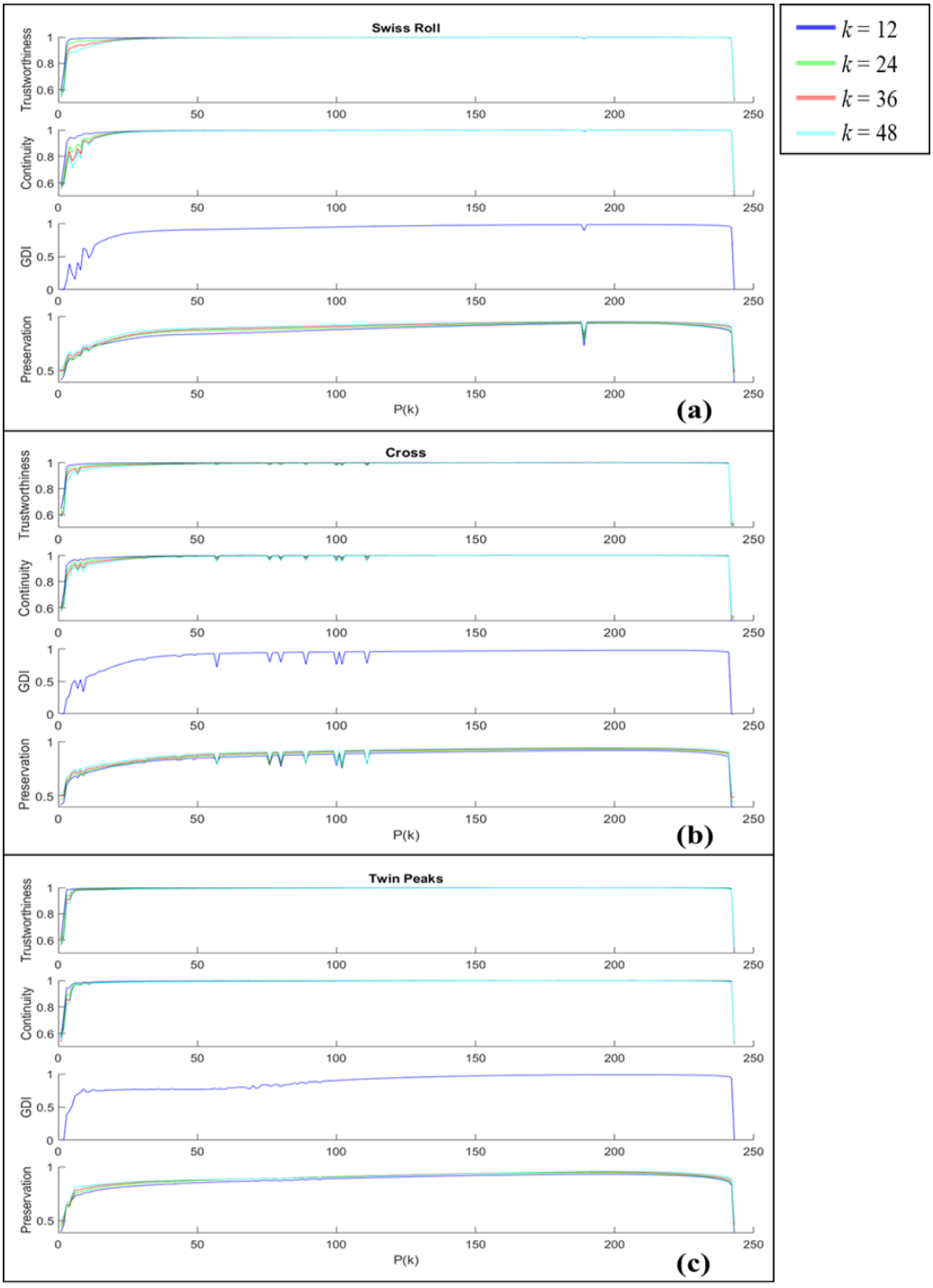

Figure 5.15: Results of metric comparison study for the t-SNE dimension reduction for the (a) swiss roll, (b) cross, and (c) twin peaks.

Figure 5.14 and Figure 5.15 indicates that preservation provides similar results to GDI for both visualizations. Also, as expected, the metrics indicate that the dimension reduction/visualization techniques do an excellent job at extracting the low dimensional structure of the 3 clusters. It appears, as observed previously, that trustworthiness and continuity overestimate the quality of dimension reduction because they are concerned more with the rank ordering of the distances rather than their actual values. The maximum values of the trustworthiness and continuity metrics are indicative of high quality visualizations but even the inferior visualizations have high trustworthiness and continuity. Tables 5.1 and 5.2 provide information about the heuristic values for KPCA and t-SNE that lead to the best metric results.

Table 5.1: Tuning parameter values resulting in the highest value of each metric for each cluster for various kNN where applicable.

	Trustworthiness				Continuity			
	k=12	*k=24*	*k=36*	*k=48*	*k=12*	*k=24*	*k=36*	*k=48*
Swiss Roll	15	15	15	15	15	15	15	15
Cross	15	15	15	15	15	15	15	15
Twin Peak	15	15	15	15	15	15	15	15

	GDI	Preservation			
	NA	*k=12*	*k=24*	*k=36*	*k=48*
Swiss Roll	15	15	15	15	15
Cross	15	15	15	15	15
Twin Peak	15	15	15	15	15

Table 5.2: Perplexity values resulting in the highest value of each metric for each cluster for various kNN where applicable.

	Trustworthiness				Continuity			
	k=12	*k=24*	*k=36*	*k=48*	*k=12*	*k=24*	*k=36*	*k=48*
Swiss Roll	201	191	190	191	201	195	193	190
Cross	188	191	190	198	198	201	191	196
Twin Peak	203	200	208	193	196	192	197	193

	GDI	Preservation			
	NA	*k=12*	*k=24*	*k=36*	*k=48*
Swiss Roll	205	201	198	198	197
Cross	214	200	200	197	203
Twin Peak	205	194	190	193	199

The best visualization results were inspected, as well, to confirm that the visualization that achieved the maximum value for each metric matched the original structure. Another result of the study is that the value of kNN does affect the value of preservation but does not affect the shape of the plots or the maximum metric values significantly, indicating a robustness to the kNN, which is promising. It is proposed that a kNN of 5% of the number of points in a cluster be used to ensure a conservative value of preservation is obtained since the value increases with kNN. This trend is likely due to the reduced importance of conserving local distances with a larger neighborhood value.

When comparing the two visualization approaches for these three structures, it appears that t-SNE has a single perplexity value that leads to the highest quality visualization for preservation and GDI. For the same metrics, KPCA is relatively insensitive to the heuristic value once a certain minimum tuning value is achieved. This appears to indicate that KPCA may be the superior choice of technique for visualizing these clusters that lie on low dimensional manifolds. The results shown in Figure 5.15 also indicate a spike for the swiss roll cluster at a single perplexity value for all metrics, which

is much more exaggerated for GDI and preservation. Therefore, the visualization achieved at this perplexity value of 189 is presented in Figure 5.16 to gain some insight.

Note that the axes of the mappings resulting from t-SNE are nonlinear transformations of the original axes so they will be indicated in general by b_i. Even though the same axes labels, b_i, are used for each mapping shown in this work, they not truly the same axes across different visualization. This implies the results of one t-SNE visualization cannot be simply plotted in the same axes as another t-SNE visualization. Structure can be compared between visualizations but simply plotting one visualization in the space generated by another mapping is misleading. Furthermore, the nonlinear aces make physical interpretation of each axis unclear and this will be addressed in Chapter 6.

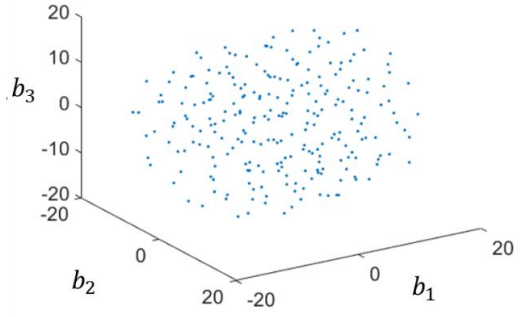

Figure 5.16: Visualization of the swiss roll produced by t-SNE for the anomalous preservation value of 0.785 at a perplexity value of 189

The visualization shows that the nonconvex formulation of t-SNE resulted in a visualization that did not converge to an accurate visualization given the max number of iterations. This is a promising result of the preservation metric. It highlighted the anomalous point very clearly and led to investigation of the results. The other metrics were less sensitive to the nonconvergent result, but it was highly apparent for preservation.

The clusters that lie on a high dimensional manifold (hyperspherical shell and difficult geometry) were subjected to a similar study where the heuristics and the kNN were varied for each technique. The results for the KPCA and t-SNE studies are provided in Figures 5.17 and 5.18, respectively, for the hypersherical shell (a) and the difficult geometry described by Equation 5.33 (b).

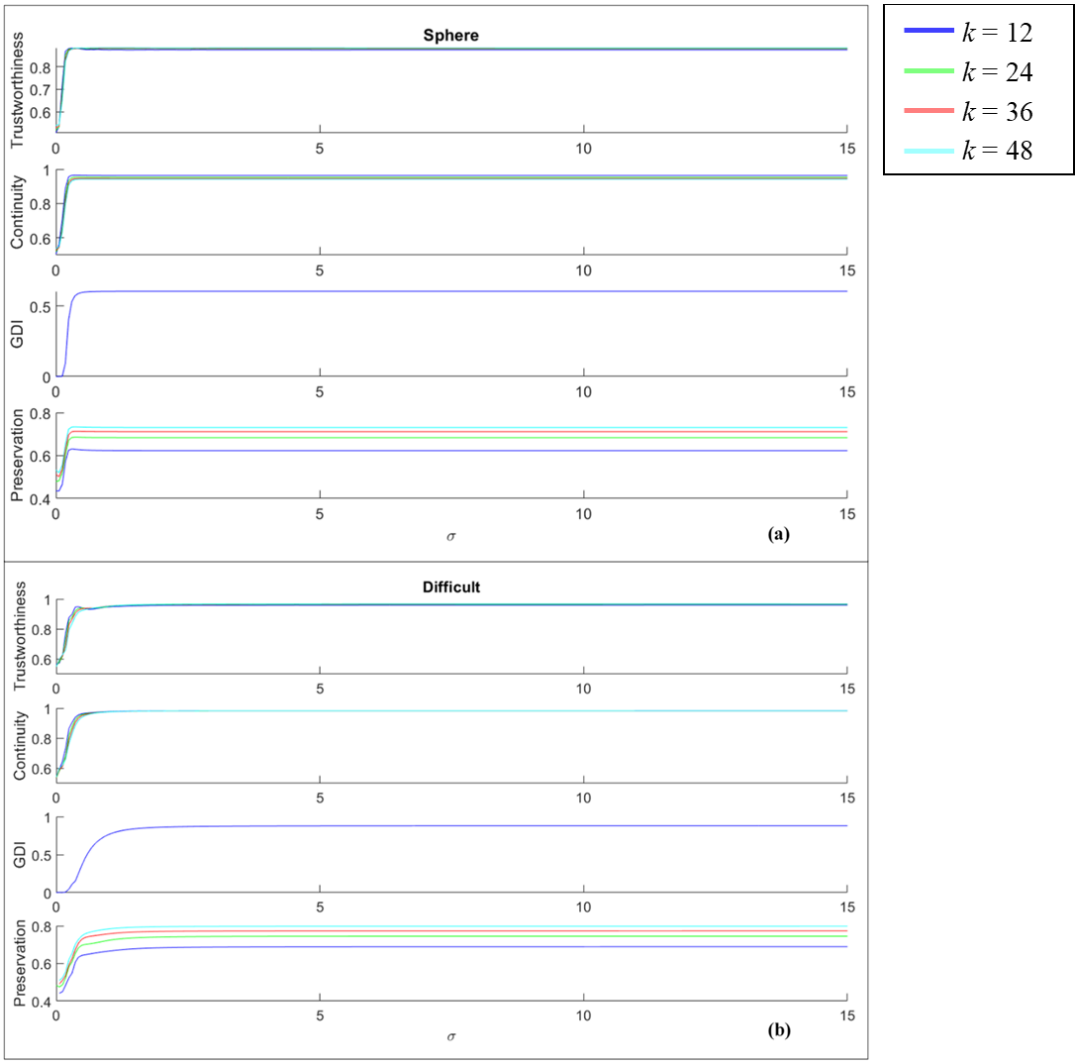

Figure 5.17: Results of metric comparison study for the KPCA dimension reduction for the (a) hyperspherical shell and (b) difficult geometry described by Equation 5.33.

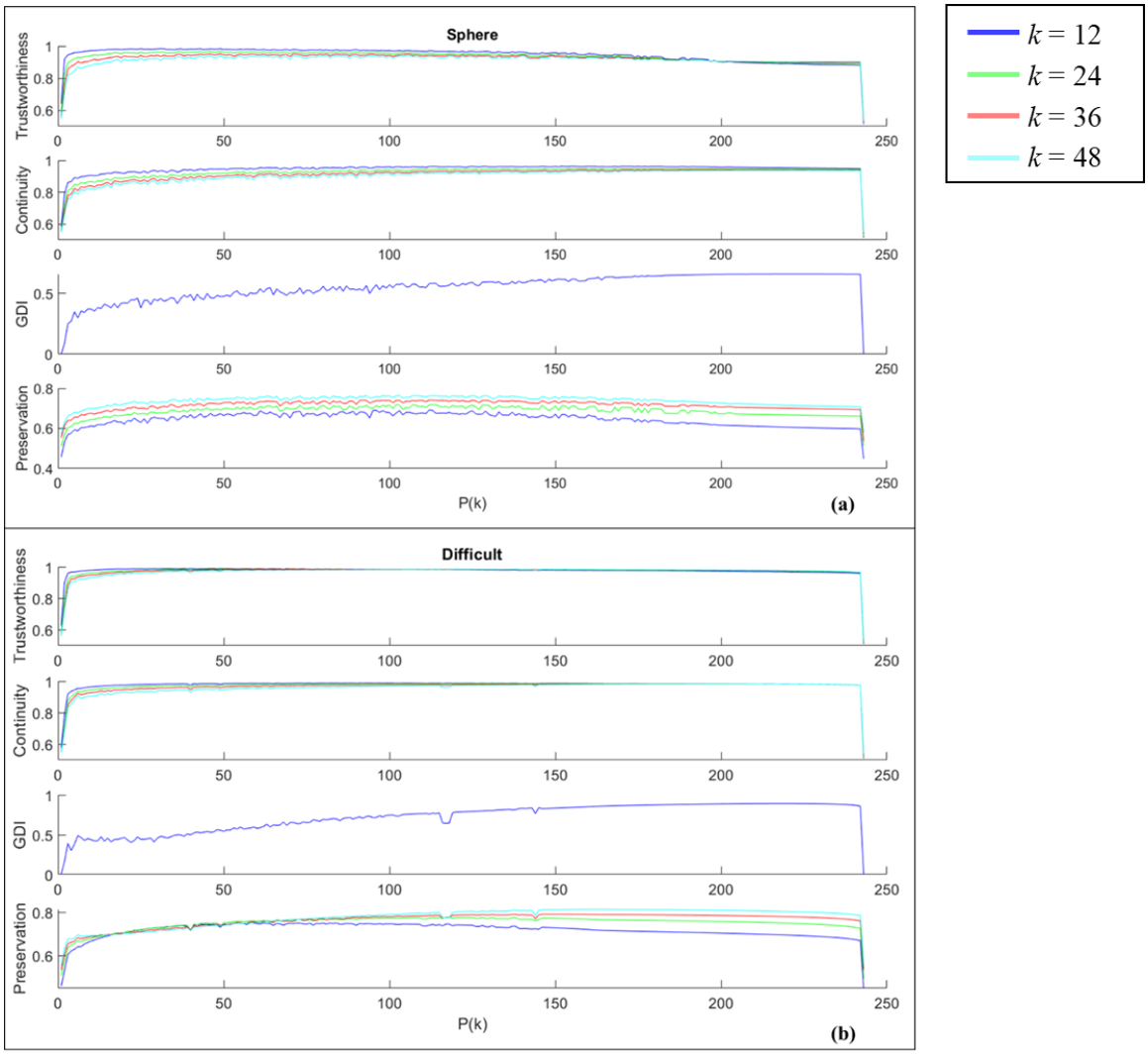

Figure 5.18: Results of metric comparison study for the t-SNE dimension reduction for the (a) hyperspherical shell and (b) difficult geometry described by Equation 5.33.

The visualization of the hyperspherical shell led to surprisingly low preservation and GDI values while the continuity and trustworthiness values were high once again. These two metrics are high due to their consideration of only the rank ordering of distances. Typical visualization approaches preserve local distances reasonable well so the set of the k-closest points in the in the high dimensional space is likely similar to the set of the k-

closest points in the low dimensional space. The exact order may not be conserved, such as the second closest point in the original space may not be the second closest in the mapped space but it will likely still be in the k-closest neighborhood. This will drive the sets U_k and V_k to be small and thus the trustworthiness and continuity to be large. This is why even relatively poor representations that do not preserve structure, but do preserve distance, also perform well for these two metrics.

Due to the above reasons, the remainder of this section will focus on GDI and preservation because they appear to be the superior metrics. For KPCA, both the GDI and preservation plots for both clusters followed similar trends. The main difference was in the TSNE visualizations where the metrics diverged in behavior for both clusters. The best results are summarized for each cluster visualized by t-SNE in Table 5.3 and Table 5.4 where the former table provides the best value of the metric and the latter provides the perplexity that achieves the best metric value.

Table 5.3: Maximum preservation and GDI values c for each cluster for various kNN where applicable.

	GDI	Preservation			
		k=12	*k=24*	*k=36*	*k=48*
Hypersphere	0.66	0.69	0.72	0.74	0.76
Difficult	0.89	0.75	0.78	0.79	0.81

Table 5.4: Perplexity values resulting in the highest value of each metric for each cluster for various kNN where applicable.

	GDI	Preservation			
		k=12	*k=24*	*k=36*	*k=48*
Hypersphere	223	112	113	112	103
Difficult	219	58	117	146	160

For various kNN values, the preservation metric indicates a relatively consistent choice of the best perplexity values for the hypersphere, but those values do not match the value identified based on the GDI. Furthermore, the value of the best perplexity varies with the value of kNN when preservation is used as the metric for the difficult geometry. The value of the preservation is consistent, but the perplexity that attains the best preservation varies. To see if the visualizations are significantly different, Figure 5.19 is provided.

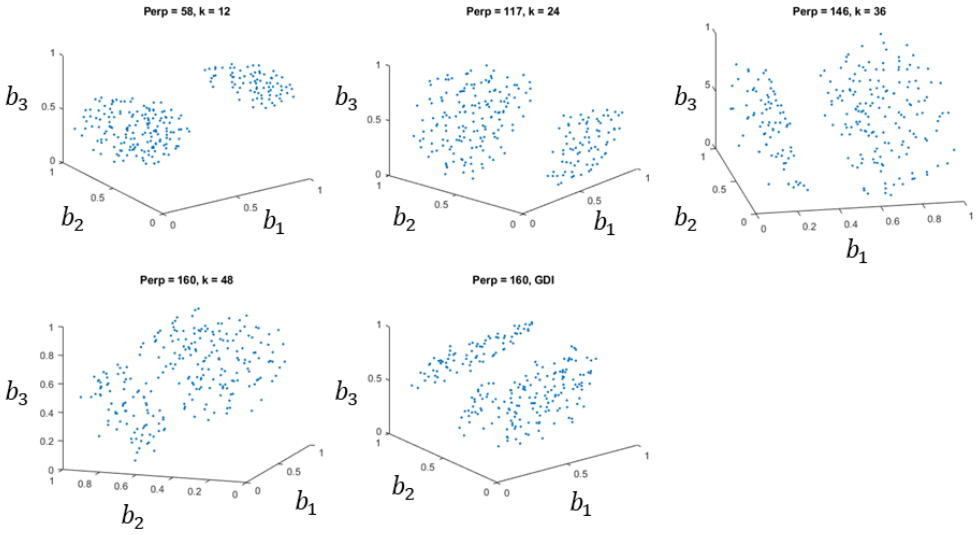

Figure 5.19: Visualizations of the difficult structure determined by t-SNE for the perplexity values that lead to the best preservation results for a variety of kNN values.

The visualization of the difficult geometry is created for each of the perplexity values shown in Table 5.4. For comparison, the best visualization identified by GDI is provided. As shown by Figure 5.19, the visualizations are not significantly different in structure even though they have varying perplexity values. There are two possible options depending on which metric is trusted. Based on GDI, the visualizations identified by preservation are inferior to visualization determined by the GDI. Based on preservation,

the visualizations are all effectively equivalent. This result seems more reasonable based on the 5 mappings shown in Figure 5.19 that are all similar. While additional studies should be performed, the results indicate that the preservation metric provides a truer measurement of the quality of the visualization.

To further compare preservation and GDI a real dataset was obtained from the UC Irvine Machine Learning archive. The name of the dataset is the Block Classification [128], in which pages of various documents have been segmented into blocks that are either text, horizontal lines, graphics, vertical lines, or a picture. The dataset contains 10 integer or continuous variables that describe the 5473 different blocks in which the total number of each class is given by Table 5.5. The data was selected due to its high dimensionality and assigned classifiers, which provided a simplistic approach for separating the data into clusters. The t-SNE visualization requires the data be numeric to determine the distances between points, which is another reason this dataset was selected.

Table 5.5: Number of points in each class of different types of block

Text	Horiz. Line	Graphic	Vert. Line	Picture
4915	329	28	88	115

Since the classification of each block was known, the data was trivially divided into 5 different clusters. The moderately sized clusters associated with horizontal lines, vertical lines, and pictures were then visualized by both KPCA and t-SNE for various heuristic values and for each heuristic, the preservation and GDI values were determined. The tuning parameter for KPCA was varied in the same manner as before with 250 equal increments on the interval [0.0001, 15] while the perplexity of t-SNE was varied at increments of 1 on the interval of 1 to the number of points in the cluster. For this study, only the kNN of 5% of the total number of points in the clusters was used. The results of the KPCA study are

shown in Figure 5.20, and the results of the t-SNE study are shown in Figure 5.21 in which the respective heuristics of KPCA and t-SNE are plotted against the preservation and GDI.

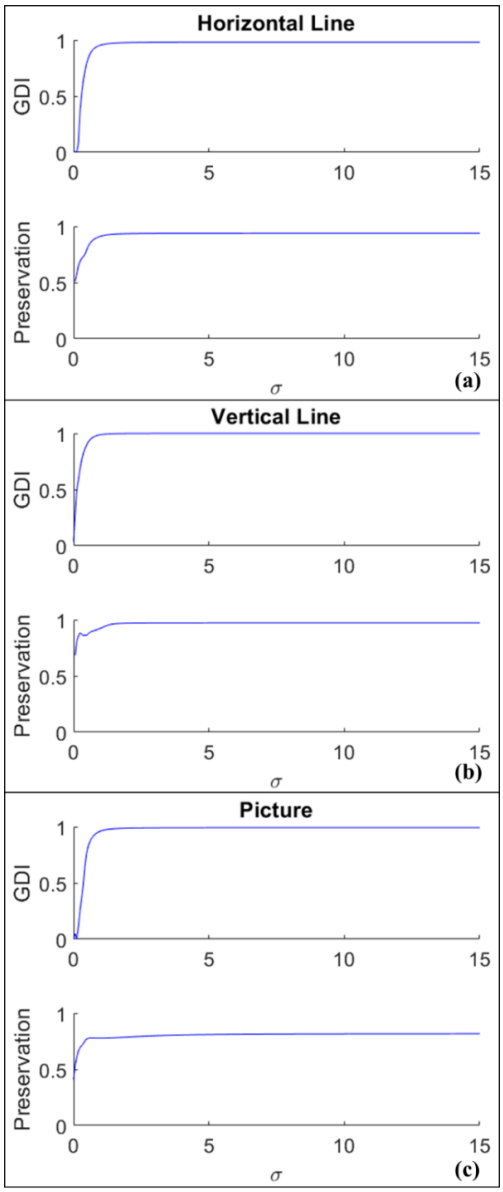

Figure 5.20: Preservation and GDI as function of $\boldsymbol{\sigma}$ for visualizations produced by KPCA for three clusters associated with blocks that are (a) horizontal line, (b) vertical lines, and (c) pictures.

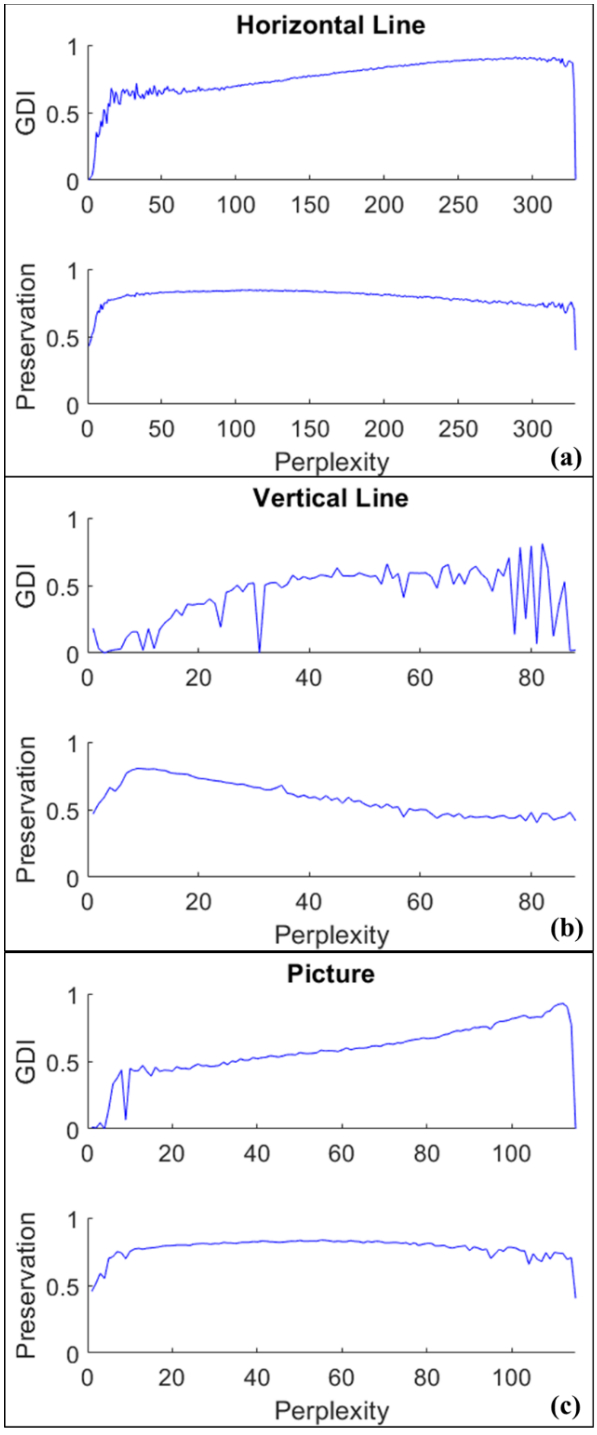

Figure 5.21: Preservation and GDI as function of perplexity for visualizations produced by t-SNE for three clusters associated with blocks that are (a) horizontal line, (b) vertical lines, and (c) pictures.

Interestingly, the metrics seem to agree when KPCA is used as the visualization strategy since similar behavior is seen in Figure 5.20 across metrics. The quality for both metrics is exceptionally high so the results are investigated further by performing a PCA analysis on each cluster. It was found that at least 95% of the variance in each cluster could be explained by three components. This implies that the clusters were likely linearly embedded in a low-dimensional space and extremely well suited for KPCA. The results become strange when t-SNE is used for dimension reduction because the results disagree between the two metrics. The author hypothesizes that the source of these discrepancies is the formulation of the metrics. The mappings of t-SNE are attempting to balance global and local structure nonlinearly which may be producing a strange mapping if the original structures are linear. Since GDI uses the Pearson Correlation Coefficient between the mapped distance and geodesic distances this could mean a single outlier point could greatly skew the correlation coefficient.

Furthermore, most of the points are separated by moderate distances so any mismatch between extreme distances for the mapped and original space causes the correlation to decrease. While the preservation would detect the outliers, it may not be as greatly affected by it. The mappings generated by the best perplexity identified by each metric were visually inspected and compared to the KPCA mapping. Once again, there did not appear to be any major discrepancies in the structure of the visualizations. This strengthens the argument that there may be outlier points skewing the results for GDI. While these points are mapped incorrectly, the goal of this approach was to visualize the structure of clusters and it appear the preservation metric allows for an accurate measure of structure preservation.

From these studies, it appears that the new metric introduced in this work, preservation, performs at least as well as GDI and better than trustworthiness and

continuity. There may be special cases in which there is a discrepancy. It can provide the designer with a reasonable absolute value that indicates the quality of a dimension reduction/visualization. Furthermore, it is not based on any other visualization strategy, so it should not be ased towards any visualization technique although further work should be performed with more datasets to fully compare the metrics. This work serves as an introduction to the metric, and it is assumed that sufficient results have been provided to motivate the use of preservation in this work to develop a strategy to select an appropriate visualization technique when visualizing high dimensional design regions.

5.5 A Strategy for Automatically Visualizing Cluster with Preservation

The previous section discussed a heuristic sweep to compare metrics that determined the quality of visualizations. It was shown that preservation performed at least as well as the GDI metric while providing a high level of gradation in values when compared to metrics like trustworthiness and continuity. With this validation, preservation will be used to select the proper heuristic for a visualization without performing a heuristic sweep. In order to accomplish this task, Bayesian optimization will be leveraged to maximize preservation as a function of the heuristic associated with the visualization technique.

Whether a desired visualization technique has been selected or not, the following strategy allows designers to efficiently select the proper heuristic for the desired visualization technique. Since t-SNE has not been used previously in a design framework, it will be used as the example visualization technique in this strategy. The visualization strategy, t-SNE, has shown promise for visualizing design regions, but one of the drawbacks to the approach is that it can be computationally expensive for large numbers of points in a cluster. Therefore, a perplexity sweep to determine the best preservation value

may not be feasible. This motivates the use of Bayesian optimization to identify the perplexity value that leads to the minimum preservation.

As seen before on the Block Classification dataset, the preservation metric value as a function of perplexity is rather multimodal with various local minima. Typical gradient descent algorithms would not fair well with such functions, so a more robust optimization approach is required. Bayesian optimization, while typically unable to identify the exact global maxima, can identify nearly optimal values and is less sensitive to local minima. It accomplishes this by stochastically balancing exploration and exploitation of the input variables to find the global optimum. It simultaneously looks for the global optimum while ensuring regions of uncertain behavior have been explored by maximizing the expected improvement of a Gaussian process model. For further information regarding Bayesian optimization the reader is referred to [129].

The objective function for the Bayesian optimization strategy is simply the preservation metric value, and the input variable is the perplexity. Using the built-in Bayesian optimization tool, an algorithm was implemented in Matlab to maximize the preservation of a t-SNE visualization. The algorithm is described by the flowchart in Figure 5.22.

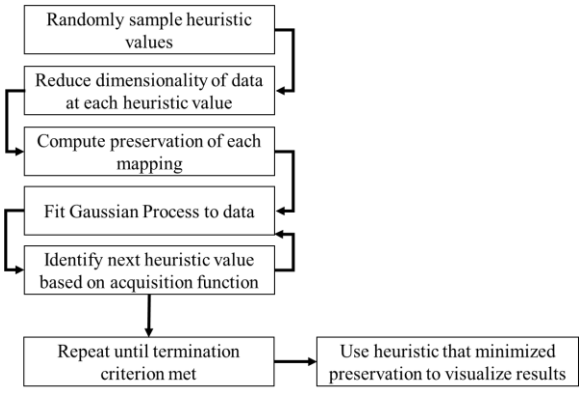

Figure 5.22: Flowchart summarizing the Bayesian optimization approach for visualization of clusters.

Note that the visualization technique need not be t-SNE, it could be KPCA, Sammon Mapping, or LTSA, which all require specification of heuristics that affect the quality of the visualization. First, a set of random heuristic values (perplexity) are selected and the desired dimension reduction/visualization technique (t-SNE) is performed using each heuristic. The preservation is determined for each of the mappings determined by the initial seeding of heuristics. This allows a Gaussian process model to be fit to the data. Next, the heuristic that maximizes the expected improvement of the Gaussian process model is identified from the acquisition function and is used to map the high dimensional dataset. The preservation is calculated once again for the most recent mapping, allowing the Gaussian process model to be updated and a new heuristic to be identified that maximizes the expected improvement. This approach is repeated until either a maximum number of iterations is reached or the algorithm converges to a global solution. In this work, an iteration limit of 100 is used.

To demonstrate the Bayesian optimization approach on a real dataset that contains a cluster with a large number of points and high dimensions, the Block Classification dataset was used once again. The first class of blocks, text, contains 4913 different instances that causes the t-SNE technique to be rather slow so performing a heuristic sweep would be typically be infeasible on a desktop computer. Therefore the Bayesian optimization based strategy was used to automatically select the best perplexity for visualizing the data based on preservation. Figure 5.23 shows the maximum preservation metric value identified for each iteration of the Bayesian optimization algorithm.

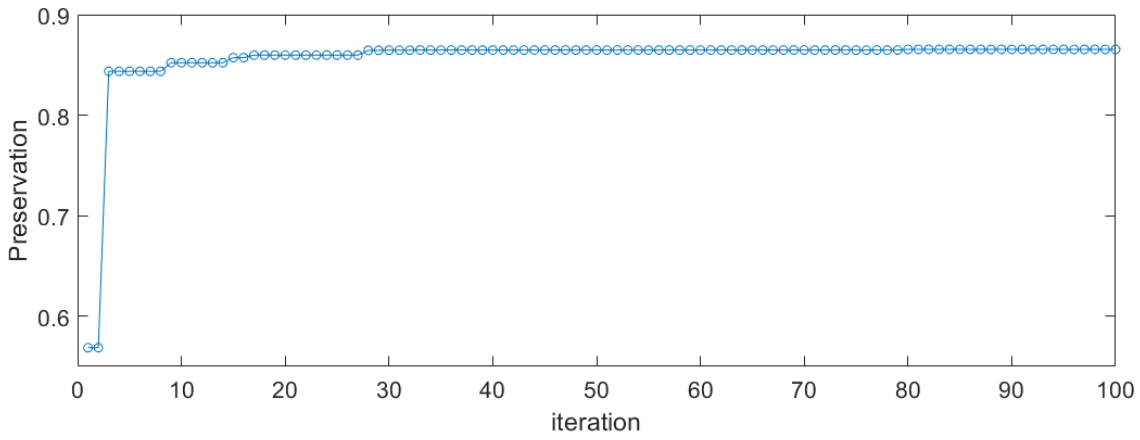

Figure 5.23: Plot of the maximum preservation for each iteration of the Bayesian optimization strategy.

Note that the maximum value does not increase every iteration because it is exploring unknown values of perplexity to ensure that no global maxima are missed. The average evaluation time per t-SNE mapping was 25.6 and the best perplexity value identified was 1869. The results strongly indicate that the Bayesian optimization approach identifies satisfactory perplexity values rapidly and requires fewer iterations than the heuristic sweep approach, which would typically be infeasible given the required computation time.

To confirm that the optimal, or near optimal, perplexity value had been determined through the Bayesian approach, the heuristic sweep was actually performed on the dataset. If the sweep were naively performed, the computation time would exceed a month, therefore parallel computing was implemented which allowed the sweep to be performed in a week. After performing the sweep, the optimal perplexity of 1832 and preservation of 0.87 were obtained which are similar to the results obtained by the Bayesian optimization approach. It should be noted, that t-SNE is a stochastic approach which is sensitive to the initial implementation; the same input parameters can lead to slightly different results.

Therefore, slight variations in the optimal perplexity and preservation are expected between different runs.

At this point, a complete visualization strategy, as proposed in Figure 2.10, has been developed and demonstrated on both synthetic and real datasets. The approach identifies each cluster with a spectral clustering based method then uses a Bayesian optimization-based approach to identify the heuristic of a visualization technique that maximizes a newly introduced metric, preservation. One of the key assumptions of the approach is that visualizing individual clusters provides better visualizations than globally visualizing the design space. To test this assumption another study is performed using a modified version of the toy dataset.

A new dataset consisted only of the swiss roll, sphere, and difficult geometry cluster. The dataset was still in a 24-dimensional space and consisted of 243 points per cluster. Next, each cluster was visualized with the Bayesian optimization augmented t-SNE where preservation was the objective. Table 5.6 provides the best preservation value and associated perplexity for each cluster that was visualized.

Table 5.6: Summary of visualization of individual clusters in a 24-Dimensional Space.

	Max Preservation	Perplexity
Swiss Roll	0.94	194
Sphere	0.72	116
Difficult	0.78	118

Then the entire dataset (all 3 clusters) were visualized simultaneously using a similar Bayesian optimization approach with t-SNE as the visualization and a modified version of preservation, P_{mod} as the metric. This modified version of preservation is given by Equation 5.33 in which the j^{th} point belonging to the i^{th} cluster, C_i, is denoted by $\boldsymbol{x_j^i}$

and the associated mapping is $\boldsymbol{y_j^i}$. The total number of clusters is given by N_C and the total number of points is N_{tot}. The kNN of each cluster, k_i, is 5% of the number of points in the cluster to ensure consistent results.

$$P_{mod} = 1/N_{tot} \sum_{i=1}^{N_C} N_i P_i(k_i) \tag{5.33}$$

$$where$$

$$P_i = \quad 1 - \frac{1}{2} \left\| \frac{K_i^O}{\|K_i^O\|_F} - \frac{K_i^M}{\|K_i^M\|_F} \right\|_F$$

$$where$$

$$K_{jl}^O = \exp\left(-\frac{d^2(\boldsymbol{x_j^i}, \boldsymbol{x_l^i})}{\sigma_j^O(k_i)\sigma_l^O(k_i)} \right) and\ K_{jl}^M = \exp\left(-\frac{d^2(\boldsymbol{x_j^i}, \boldsymbol{x_l^i})}{\sigma_j^M(k_i)\sigma_l^M(k_i)} \right)$$

The form of Equation 5.33 ensures the pairwise distance is calculated only between points within the same cluster, so if the dimension reduction technique poorly separates the cluster, it will result in a low preservation. Another view of the metric is that it is the weighted average of the preservation of each cluster, C_i, by the number of points in a cluster, N_i. Note that the metric given by Equation 5.33 requires *a priori* knowledge of the number of clusters and the cluster membership of each point which is known from the spectral clustering based approach.

This modified preservation was maximized using the Bayesian optimization approach and t-SNE. Next, the individual preservation values for the each cluster visualization was averaged using a weighted average just as before. The results are summarized in Table 5.7.

Table 5.7: Summary of visualization of individual clusters and entire 24-Dimensional space.

Mean Preservation (Individual Visualization)	Preservation (Global Visualization)
0.815	0.80

As can be seen from Table 5.7, visualizing each cluster individually leads to better results in terms of preservation. This is likely due to multiple perplexity values being tuned to each cluster rather than one perplexity value attempting to visualize all clusters. The main advantage of using the full space, though, is that the relationship between clusters can be understood. Therefore, rather than visualizing each cluster individually, it is proposed that a complimentary visualization be performed of the entire space so the relationship between clusters can be understood. The individual mapping provides higher fidelity mappings that can be used to better understand the structure of each region.

5.6 DISCUSSION

This chapter introduced a strategy for visualizing each cluster of a design space. The preferred visualization strategy in this work is a new technique, t-SNE, that provides quality mappings of individual clusters as well as superior mappings of multiple clusters when compared to other techniques. To measure the quality of the visualizations, a new metric, preservation, was introduced and validated on both synthetic and real data. It was shown that the metric performed at least as well as GDI and was superior to trustworthiness and continuity. Preservation and t-SNE were then integrated into a Bayesian optimization strategy to automatically select the heuristics of a visualization. The approach can be used for any visualization technique but importantly allows the designer to efficiently compare the quality of various visualization if it is unclear which technique should be used. Finally the new metric was used to support the hypothesis that visualization of each cluster

individually results in better visualization quality than if the whole space were visualized. It was also stated that using the global and local visualizations in tandem could lead to significant insight. With the complete visualization strategy and incorporation of manufacturing variation strategy introduced, the augmented BNC approach can be applied to the design of NS metamaterials

Chapter 6: Application to NS Metamaterials

With the methodology established for incorporating manufacturing variation into the BNC approach and visualizing the classified regions, the approach will be applied to identify and visualize regions of reliably manufacturable designs for a NS metamaterial. In Section 6.1 the forward modeling for the design of NS metamaterials is discussed, so the augmented BNC approach can be applied to identify reliably manufacturable inclusion designs. To identify these designs, the manufacturing variation of a microstereolithography system, which is used to produce the NS inclusion, is quantified and discussed in Section 6.2. Following collection of the manufacturing data, the modified BNC approach is applied to the NS metamaterials design problem in Section 6.3 to visualize multiple regions of the design space that are reliably manufacturable and to study the effects of changing the reliability threshold. Finally, the results are discussed in Section 6.4 where a final design is selected for manufacturing.

6.1 NS METAMATERIALS

NS metamaterials derive their exceptional capabilities by exploiting microstructural mechanisms to realize macroscale performance advantages [29]. One particular structure of interest is the NS inclusion illustrated in Figure 6.1 that derives it NS behavior from curved beams. When the curved beams are subjected to a transverse loading, they exhibit nonlinear or snap-through stress-strain behavior indicative of NS. By embedding low volume fractions of NS inclusions within a viscoelastic material, composites or NS metamaterials with exceptional effective damping and little to no loss in strength can be obtained [32]

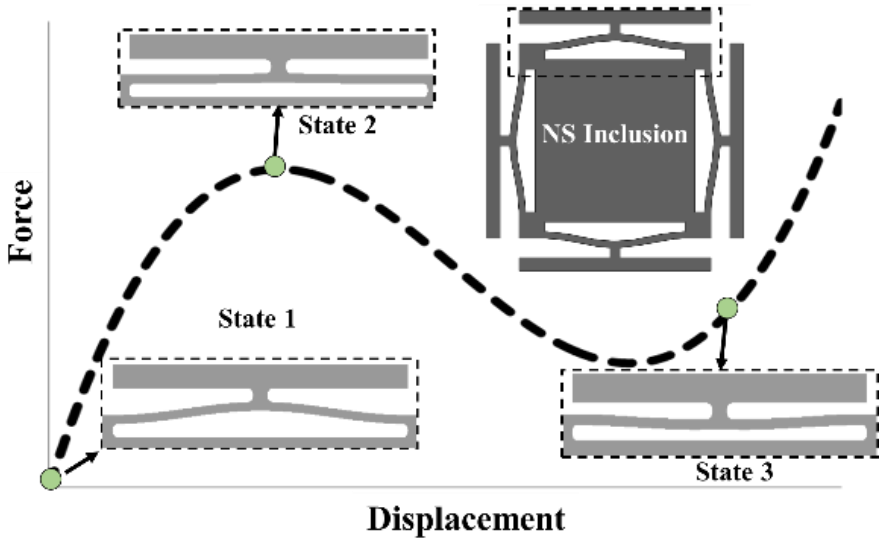

Figure 6.1: Proposed geometry for a NS inclusion (top right) with associated force-displacement curve for a loaded beam.

To manufacture a NS metamaterial with the desired effective properties, an appropriate inclusion geometry must be designed, and a viscoelastic matrix must be properly selected. Identification of the appropriate geometry and complementary viscoelastic matrix is a nontrivial multilevel design problem. Figure 6.2 provides an illustration and Figure 6.3 provides flowchart describing the multilevel design of the NS metamaterials.

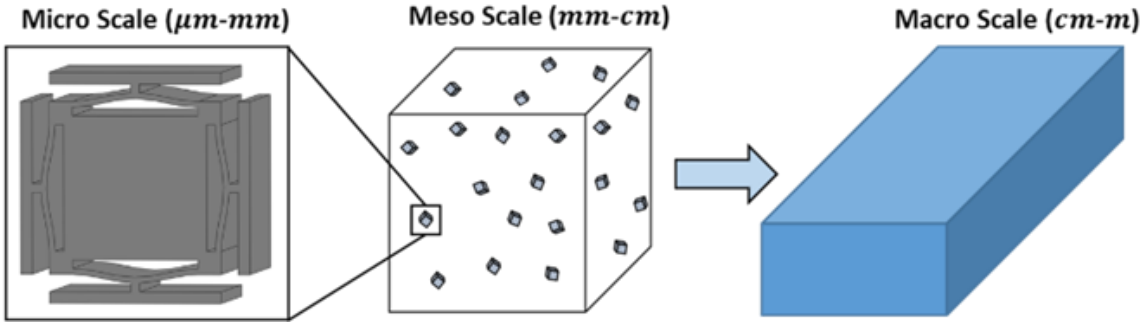

Figure 6.2: Schematic illustrating the multilevel nature of the design of negative stiffness metamaterials.

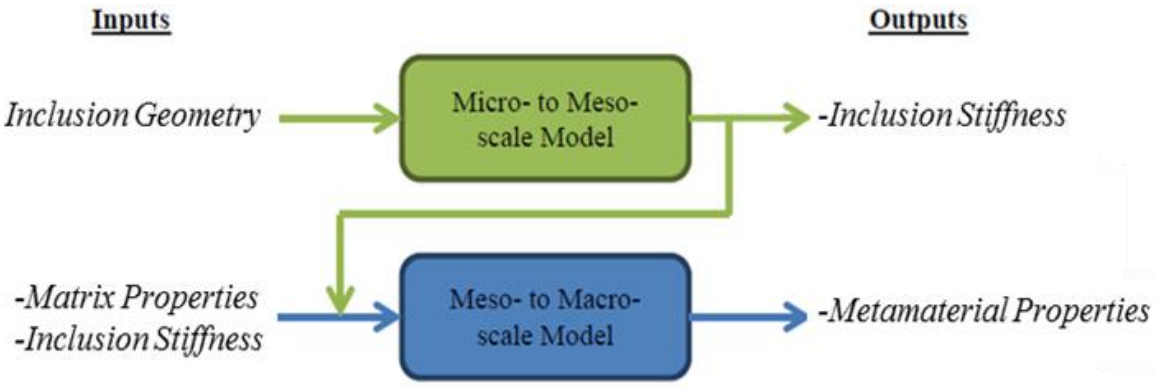

Figure 6.3: Flowchart illustrating the connectivity of the design and performance spaces/

In the first design space, or micro-scale, the geometry and material properties of the inclusion are determined to provide the effective stiffness tensor of the inclusion. The second scale, or the meso-scale, is simultaneously a design and performance space, or a coupled space, in which the stiffness tensor of the inclusion, volume fraction of inclusions, and viscoelastic matrix properties are supplied to determine the effective composite properties at the macro-scale. To model the relationship between each design and performance space, two models—the micro-to-meso and meso-to-macro—were previously developed.

The micro-to-meso model is a finite element, direct energy based homogenization method that relates the NS inclusion properties to its nonlinear, strain-dependent stiffness tensor, $\mathcal{C}^{NL}$ [130]. In general, the direct energy method treats a structure of interest, in this case a NS inclusion, as a representative volume elements (RVE) in which various displacement, u_i, can be prescribed to the boundaries of the RVE to determine different elements of the nonlinear stiffness tensor, $\mathcal{C}^{NL}$. As the prescribed displacements are incrementally applied using FEA, the strain energy, $U^{elastic}$, of the RVE is recorded. Then,

the incremental displacements can be converted to strains, E_{ij}, so Equation 6.1 can be used to relate the strain energy and strains to the nonlinear stiffness tensor.

$$C_{ijkl}^{NL} = \frac{\partial^2 U^{elastic}(\underset{\sim}{E})}{\partial E_{ij} \partial E_{kl}} \tag{6.1}$$

Various prescribed loading configurations simplify Equation 6.1 that allows each element of the nonlinear stiffness tensor to be calculated straightforwardly. Figure 6.4 provides an example displacement configuration for a NS inclusion which allows for the C_{1111}^{NL} element or C_{11}^{NL}element of the Voigt stiffness matrix to be determined via Equation 6.2.

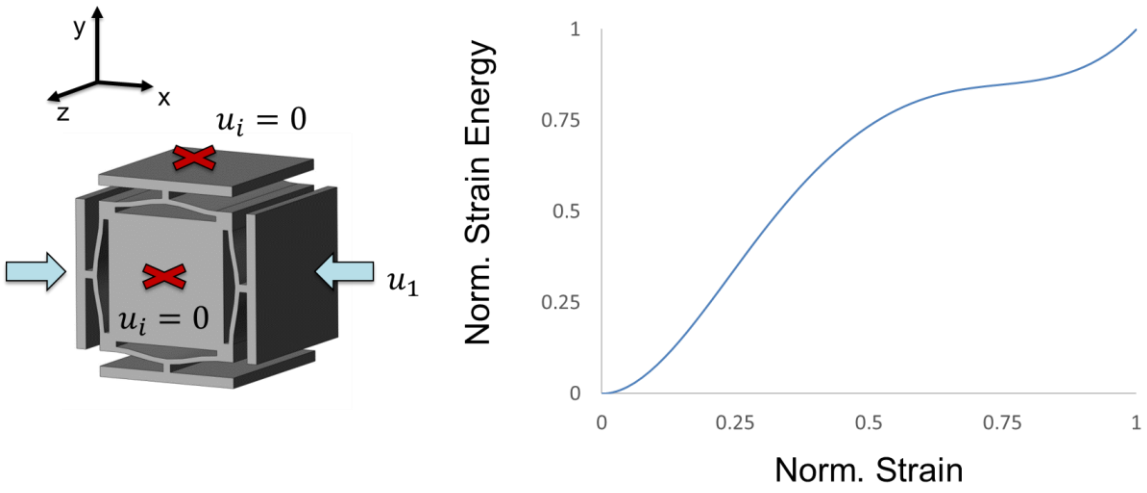

Figure 6.4: Prescribed displacements for inclusion (left) to determine the $\boldsymbol{C_{11}^{NL}}$ element of the stiffness tensor that can be derived from the strain energy plot shown (right).

The strain dependent volume of the RVE, $V(\underset{\sim}{E})$, must be recorded, as well, and the strain, E, is simply the ratio of the prescribed displacement and length in the x direction of the RVE.

$$C_{11}^{NL} = \frac{1}{V(\underset{\sim}{E})} \frac{\partial^2 U^{elastic}(\underset{\sim}{E})}{\partial E^2} \tag{6.2}$$

In Figure 6.4 it is assumed that there is symmetry about the xy, xz, and yz faces of the inclusion for both the geometry and the prescribed loading, which results in the nonlinear elastic strain energy also included in Figure 6.4. Note that for linearly elastic materials, the strain energy as a function of the strain will be quadratic, but due to the nonlinearity of the NS beams, the strain energy shown in Figure 6.4is non-quadratic. For further discussion of the theory of the direct energy method and the various prescribed displacement conditions used to generate the full nonlinear stiffness tensor, see Klatt and Haberman [32].

With the stiffness tensor obtained with the micro-to-meso model, the meso-to-macro model based on effective medium theory (EMT) can be used to relate the inclusion stiffness tensor, volume fraction, and matrix properties to the dynamic material properties of the composite/metamaterial [131]. The approach determines the strain field around the embedded inclusions due to a macroscopically applied load to the metamaterial. Then the approach performs a homogenization of the material to determine the material properties of the bulk composite based on the weighted volumetric average of the localized stress and strain fields. To obtain the desired metamaterial properties, it must be assumed that the inclusions are prestrained initially while embedded in the polymer matrix so that they are in the negative stiffness regime. Not only does the EMT model assume that the inclusions

have been prestrained, it also assumes that all disturbance to the metamaterial are small such that the negative stiffness of the inclusion is locally linear. Typically, the value of the storage modulus of the polymer should be approximately equal in magnitude to the negative stiffness of the inclusion to obtain the desired metamaterial properties. Once again, for more information regarding the forward models, the reader is directed to the work of Klatt and Haberman [32].

To better define the multilevel design problem, design variables and performance parameters must be defined. Table 6.1 summarizes the list of variables and parameters in each level of the multilevel design space, and some of the variables are illustrated in Figure 6.5. This work expands on previous work that required the dimensionality of the design space to be less than three for ease of visualization [132]. Previously, at the micro-scale, the beam thickness, t, apex height, h, and Young's modulus of the NS inclusion, E_{inc} , were varied while the beam length, L, and beam separation, W, were fixed. In this work, a fourth variable is introduced, which is the ratio of beam prestrain, d, to the apex height h, so $r_d = d/h$. The beams are prestrained in compression, and the geometry of the beams bounds r_d on the interval between zero and two. By introducing a fourth variable, the design space is no longer simple to visualize. At the meso-scale the inclusion stiffness tensor, C^{Inc}, is supplied by the micro-to-meso model, the inclusion volume fraction, v_f, is held constant, and the matrix storage modulus, E_m, and loss factor, η_m, are fixed to approximately match the material properties of a polyurethane elastomer [133]. Finally, the variables describing the macro-scale performance space are the effective storage modulus, E_c^{eff}, normalized by the storage modulus of the matrix, E_m', and the loss factor, η_c^{eff}, of the composite, normalized by the loss factor of the matrix, η_m.

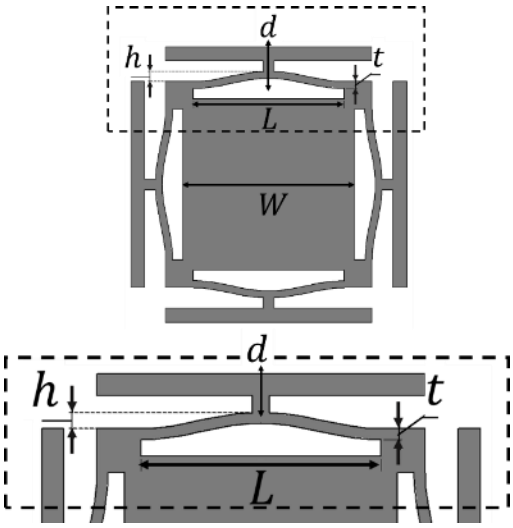

Figure 6.5: Variables describing the NS inclusion geometry.

Table 6.1: List of variables for each level of the design space and ranges or fixed values for each variable.

	Variable	Design Variable	Perf. Variable	Defined Range
Micro-to-Meso	h	Yes	No	[25,110]μm
	t	Yes	No	[25,75]μm
	E^{inc}	Yes	No	[0.52,0.79]GPa
	L	Yes	No	1.3mm
	W	Yes	No	1.6mm
	r_d	Yes	No	[0,2]
	C^{inc}	No	Yes	*NA*
Meso-to-Macro	C^{inc}	Yes	No	*NA*
	E'_m	Yes	No	1.25MPa
	η_m	Yes	No	0.1
	v_f	Yes	No	2%
	E_c^{eff}/E'_m	No	Yes	NA
	η_c^{eff}/η_m	No	Yes	NA

The assigned values and ranges at the micro-scale are selected to be consistent with two microstereolithography systems. Microstereolithography systems were chosen to manufacture the NS inclusion because they can produce the micron-sized features required for the NS inclusions. The first microstereolithography system uses a photopolymer with

a Young's modulus between 0.60 and 0.66 GPa while the second system's photopolymer has a Young's modulus between 0.72 and 0.77 GPa.

With the variables and parameters defined, the BNC approach is applied to the NS metamaterials design problem to identify regions of the design space likely to lead to satisfactory performance. First, a Halton sequence was generated in the micro-scale design space to obtain 5000 micro-scale designs that satisfied an initial set of constraints that ensure that 1) the geometries are physically realizable and 2) the beams do not exceed the yield criteria established in Qui *et al.*[28]. The micro-scale designs are evaluated in the micro-to-meso model to obtain the effective stiffness tensor of the inclusion at the meso-scale. Then, for each NS inclusion design, 20 different initial beam displacements are randomly selected resulting in 5,000 different NS inclusion designs with 100,000 different stiffness tensors.

After determining the stiffness tensor of each inclusion, the meso-to-macro model is employed to determine the dynamic properties of the metamaterial. A performance threshold is set at the macro-scale, requiring the effective loss factor of the NS metamaterial to be at least 4 times the loss factor of the polymer matrix. This classification is propagated to the micro-scale design space. Following classification by the macro-scale performance, the micro-scale is further classified to reflect available inclusion material properties. To be considered satisfactory, micro-scale designs must have a Young's modulus within the bounds documented in Table 6.1. This classification based on modulus is forward propagated to the meso and macro-scales. The fully classified macro-scale space is shown in Figure 6.6 where the performance has been classified by the performance threshold and modulus restriction.

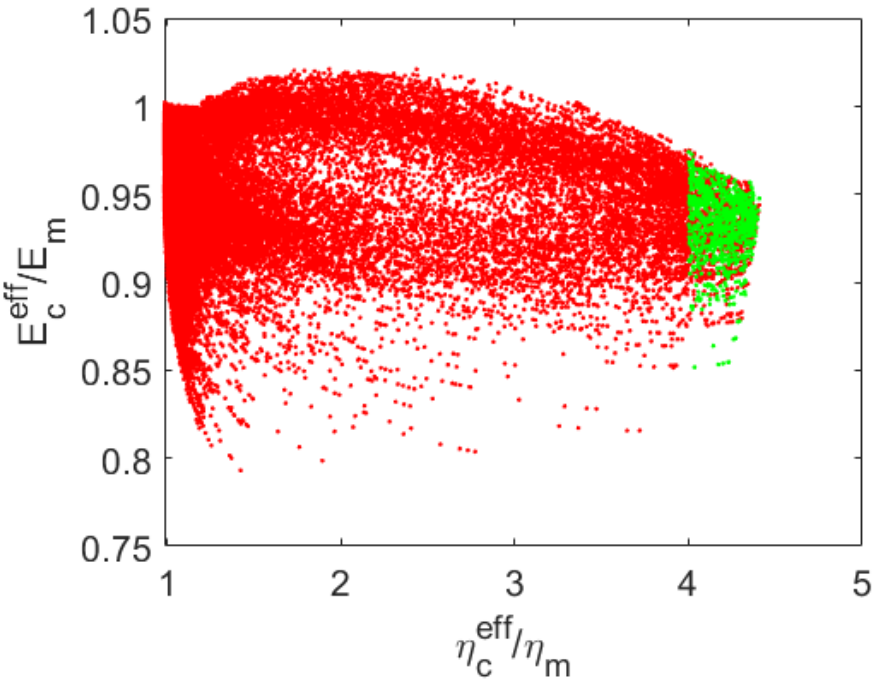

Figure 6.6: Classification of the macro-scale performance space. Satisfactory designs are provided in green and unsatisfactory points are red.

Following classification, the BNC classifier can be trained to identify the decision boundaries of the satisfactory design space(s). To determine the required number of training points for accurate classification, the number of training points was varied. The same number of satisfactory and unsatisfactory training points were selected to train the classifier to avoid an imbalanced classifier. A fixed heuristic for each class was used for each set of training points following the heuristic rule proposed by Sharpe *et al.,* [53]. The receiver operating curve (ROC) and area under curve (AUC) were determined for 1000 test points in each class. This procedure was repeated 20 times to evaluate not only the mean but also the variation in classification accuracy as a function of the number of training points. Figure 6.7 presents the results of the training.

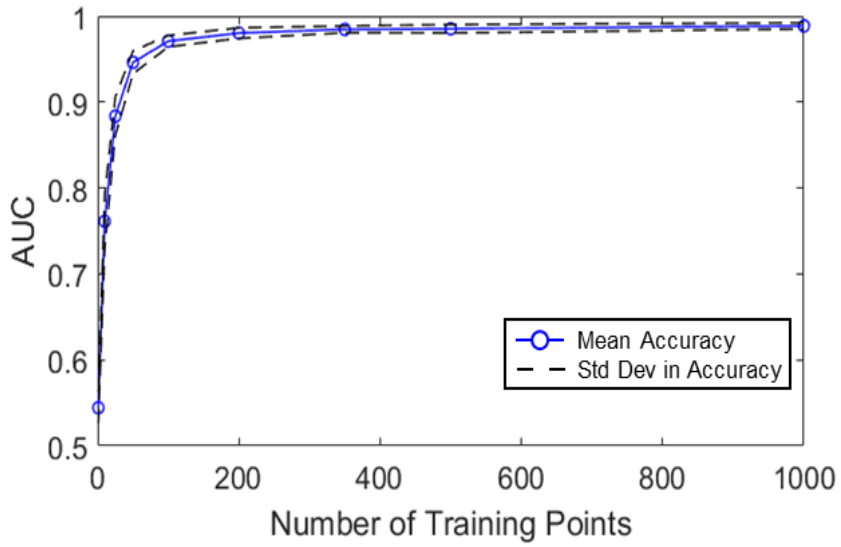

Figure 6.7: AUC as a function of the number of training points used for the classifier.

Figure 6.7 illustrates that the classification accuracy is excellent even for a relatively small number of training points. To ensure high levels of accuracy, 1000 designs were selected to train each classifier. At this point, the typical BNC approach has been applied to classify the design space into satisfactory and unsatisfactory regions, but in order to design for manufacturing variation, more information is required. Specifically, the manufacturing variation of a microstereolithography system that can produce the inclusions must be obtained. Obtaining this data is the focus of the next section.

6.2 Quantifying Manufacturing Variation from a Microstereolithography System

Microstereolithography systems are capable of producing structures with micron-sized features, so they are suitable for manufacturing the NS inclusions. They produce parts layer by layer by activating/deactivating each pixel of a Digital Micromirror Device (DMD) so that the correct image is formed when a UV light source reflects off the device. Then, through a series of optics, the light image is greatly reduced in size and focused on

the top of a build stage at the surface of a volume of liquid photopolymer. A thin layer of the photopolymer solidifies on the build plate that matches the light image. Once the layer has solidified the build stage moves downward, the liquid polymer flows over the part to form another layer, and the build process is repeated to form the final parts.

Like all additive manufacturing (AM) systems, the material properties and geometry of parts produced by a microstereolithography system are not identical to the intended, as-designed values [134, 135]. Therefore, the microstereolithography systems used in this work must be characterized. One of the difficulties of characterizing microstereolithography systems is that there are no standardized parts or procedures for quantifying material properties or resolutions. Therefore, this work required the development of two different metrology parts which were then fabricated by microstereolithography systems for part characterization. The first metrology part enabled measurement of the storage modulus of the photopolymerized polymer, and the other metrology part helped determine the geometric variation of an NS beam. While this work requires measurement of the manufacturing variation via sample metrology parts, future work may no longer require it. As mentioned earlier, characterization of AM systems is a topic of significant research interest [136-141]. As information from these characterization and metrology studies becomes available, designers can begin to reference the available data to quickly design for variation. However, this type of data on manufacturing accuracy and variation is not currently available for microstereolithography.

The development of metrology parts for material property determination is hindered by the build envelope of a microstereolithography system, which is prohibitively small for fabricating parts for standard tensile testing procedures. Other testing methods such as micro indentation or dynamic mechanical analysis (DMA) were also unavailable for testing. Therefore, to measure the storage modulus of the polymer, the vibrational

response of the polymer was measured. Four cylindrical rods with the nominal dimensions provided in Table 6.2 were produced, and each rod was subjected to an experimental procedure, which is depicted in Figure 6.8, to determine the storage modulus.

Table 6.2: Nominal design values for metrology parts used to characterize a microstereolithography system.

Cylindrical Metrology Rod	
Diameter	2.00 mm
Length	12.55 mm
Inclusion Metrology	
Apex Height, h	70.25 μm
Beam Thickness, t	50 μm
Beam Length, L	1.3 mm
Beam Separation, W	1.6 mm

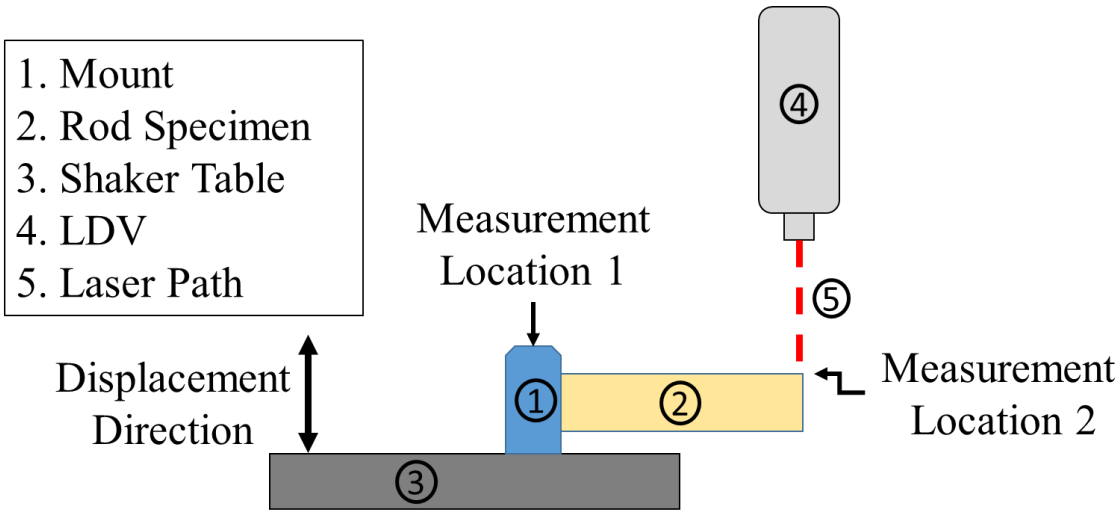

Figure 6.8: Schematic of configuration used to determine the material properties of microstereolithography rod.

Each rod produced by the first microstereolithography system was cantilevered from a shaker table that was excited with a logarithmic frequency sweep from 1 Hz to 4500 Hz over 120 s. A laser Doppler vibrometer (LDV) measured the tip velocity of the rod as

well as the base velocity of the rod during the sweep. By computing the magnitude of the transfer function between the tip velocity and base velocity in the frequency domain, $|H|$, the natural frequency, f_n, was determined. The natural frequency is the frequency that maximizes the magnitude of the transfer function. After determining the natural frequency of each rod, the distance from the tip of the rod to the base, l_r, density of the rod, ρ_r, cross-sectional area, A, and area moment of inertia, I, were measured to obtain the storage modulus by Equation 6.3 [142].

$$E' = \left(\frac{2\pi f_{\mathrm{n}}}{3.52}\right)^2 \frac{A\rho_r l_r^4}{I} \tag{6.3}$$

The above procedure was performed four times for each of the rods for a total of 16 measurements of the storage modulus. Figure 6.9 illustrates the transfer function obtained for one of the rods as a function of frequency for one of the measurements.

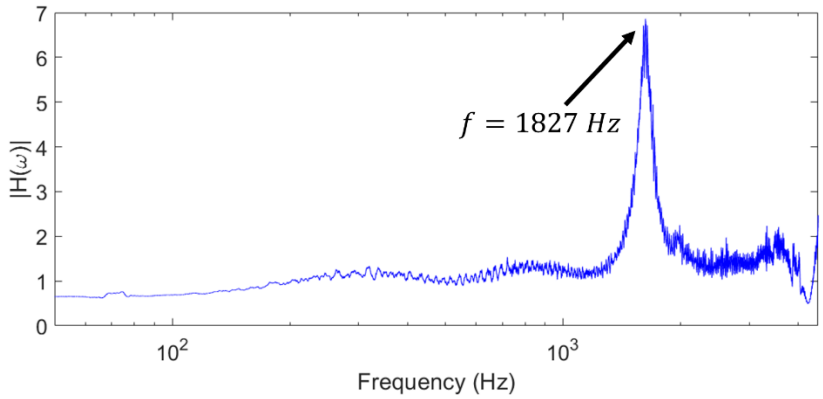

Figure 6.9: Results of frequency sweep for rod produced by microstereolithography.

After determining the storage modulus for each of the 16 measurements, the distribution of storage moduli results was assumed to be normal, and the mean and standard

deviation of the data was computed. The mean storage modulus is 0.67 GPa and the standard deviation is 32.1 MPa. The assumption of normality was confirmed by the Kolmogorov-Smirnov test at a 5% significance level [143].

To determine the geometric variation in the thickness of NS beams produced by the microstereolithography systems, a batch of 140 inclusions was manufactured with the geometry provided in Table 6.2. A scanning electron microscope (SEM) was used to image the parts, but the size of the build plate required further post-processing because it was too large for the SEM. It was desired that the inclusions remain on the build plate to avoid disturbing the parts, so wire electron discharge machining (EDM) was used to cut the build plate into smaller pieces that would fit inside the SEM while minimizing the impact on the inclusions. After subdividing the build plate, each inclusion was inspected using an optical microscope to determine whether the parts were damaged. Microstereolithography is a rather new manufacturing method, so the quality of the parts varied drastically such that some inclusions resolved well while others were damaged or included severe defects in their topology. The damaged or topologically inaccurate inclusions were eliminated from the inclusion population resulting in only 18 inclusions that resolved properly.

The 18 inclusions that passed the initial screening process were sputtered with 250 Å of gold and imaged with an SEM to determine the beam thickness and apex height. Figure 6.10 illustrates two images of the NS inclusion magnified with the SEM: one shows the entire inclusion and the other shows a magnified view of one of the beams. After obtaining the various SEM images of the inclusion, a script was developed that allowed the authors to select points on the outer perimeter of each beam. With these selected points, an interpolating, cubic spline was generated for both the top and bottom boundaries that approximated the curvature of the beam. To determine the beam thickness, the normal distance between the two curves was calculated at various points on the curves and then

scaled by the legend to convert the units to microns. Figure 6.11 provides an illustration of the fitted cubic splines overlaid on the original image with associated curve normals. After calculating the thickness of the beam at various locations, the average beam thickness was calculated and recorded.

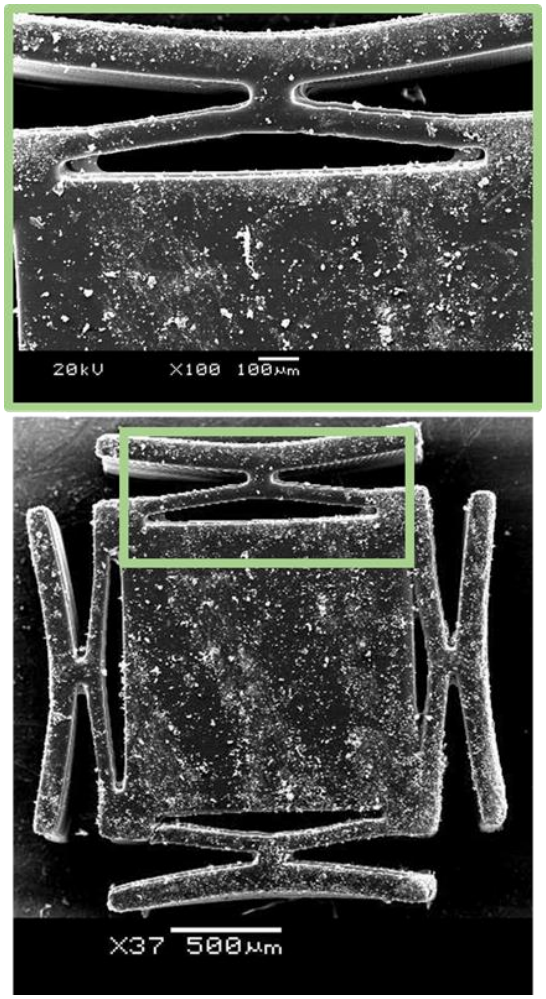

Figure 6.10: SEM images of a NS inclusion (top) and magnified view of one of the measured beams (bottom).

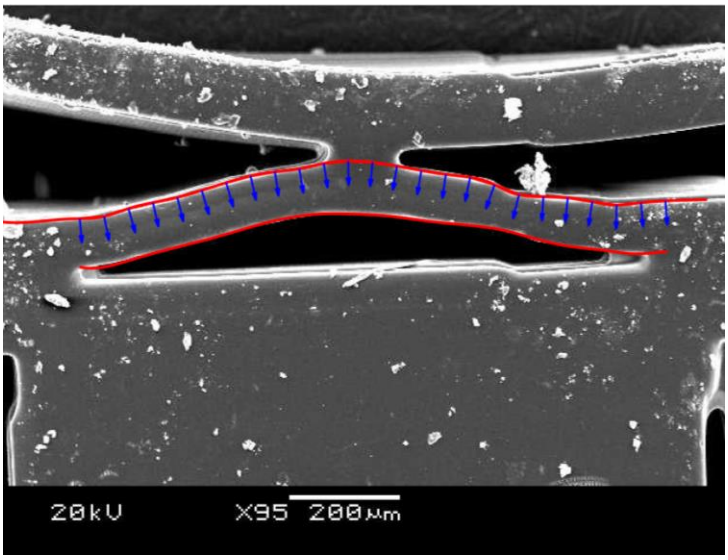

Figure 6.11: Illustration of a cubic spline fit to the boundary of a NS beam. Arrows indicate the normal direction used to measure beam thickness.

With the same pair of cubic splines, the apex height was measured relative to two datums for the top and bottom spline resulting in four measurements of the apex height per beam. These datums are shown in Figure 6.12.

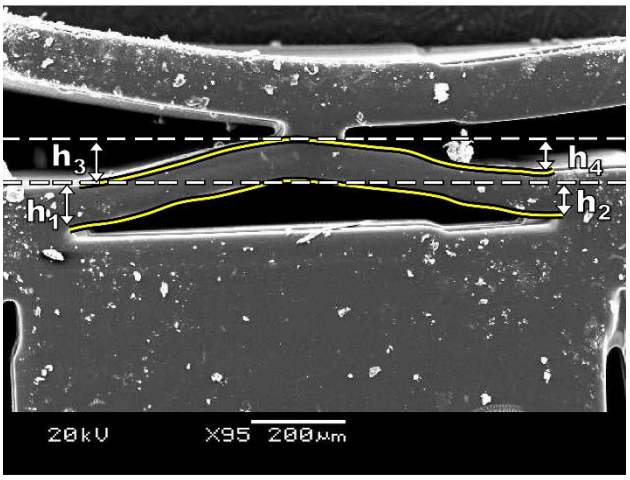

Figure 6.12: Illustration of a cubic spline fit to the boundary of a NS beam along with datums for determining the apex height of the beam.

The first datum for each spline measured the difference between the height of the left-most point on the spline and the point with the maximum height on the spline while the second measurement compared the maximum height to the right-most point. Using both splines and each of the two measurement per spline, four measurements were obtained and averaged to determine the mean apex height, h_3, of each beam. This method was employed to try to eliminate any bias introduced by variations in the beam thickness along the length of the beam.

Using this procedure, the beam thickness and apex heights were measured, allowing the kernel density estimator of Equation 6.3 to be generated to approximate the distribution of measurements, as shown by the contour map of Figure 6.13. Rather than modeling the variation in beam thickness and apex height with a standard Gaussian model, it was modeled using a KDE to demonstrate how the methodology for incorporating manufacturing variation can easily handle non-parametric distributions.

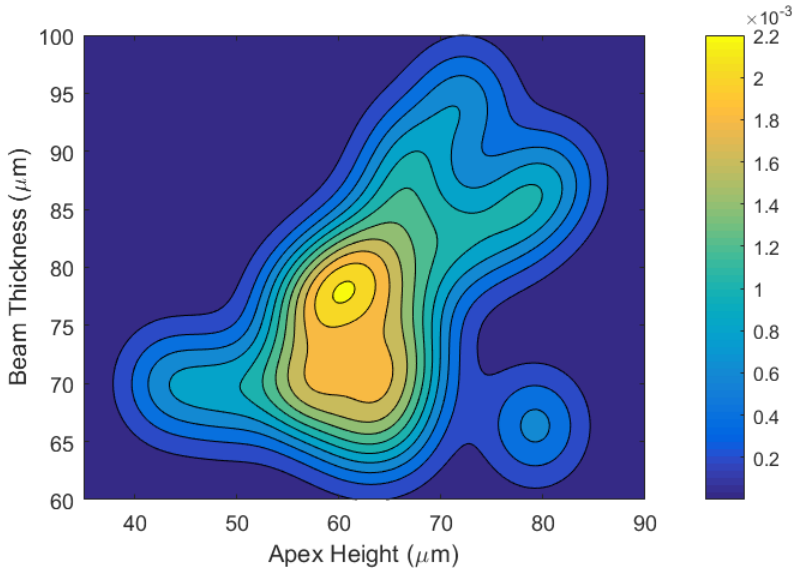

Figure 6.13: KDE generated from beam thickness measurements.

There are a few things to note about this distribution. First, the mean of the distribution is biased from the nominal values provided in Table 6.2. This bias is corrected by shifting the distribution so that the mean values are equivalent to the nominal values. Second, there appears to be some dependence between the beam thickness and apex height. The larger the beam thickness the larger the apex height. The authors hypothesize that this relationship may be caused by the post processing method that removes any residual resin. A mixture of isopropyl alcohol, a surfactant, and water is used to remove any trapped, uncured resin from the inclusions, but this process seams to warp the beams and cause them to bend inward reducing the apex height. It is hypothesized that with larger beam thickness, the warping effects are reduced implying a higher residual stress within the beams.

To ensure that enough measurements were obtained, the convergence test discussed in Chapter 3 was applied to the collected thickness data. Figure 6.14 presents the mean error as a function of the number of samples measured.

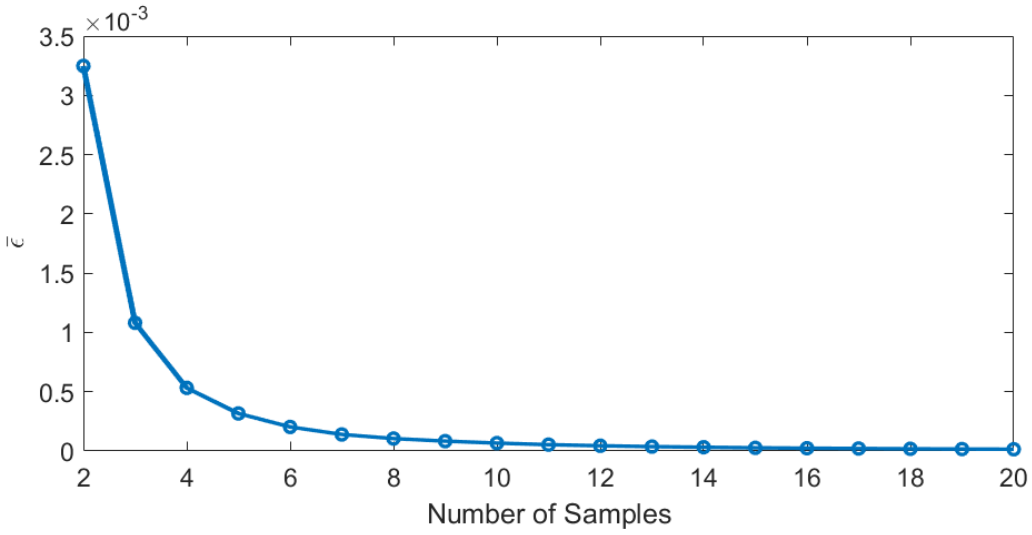

Figure 6.14: Plot illustrating that sufficient samples have been obtained for thickness and apex height measurements to converge to a stable thickness variation distribution.

The plot of Figure 6.14 indicates that the manufacturing variation distribution generated by the KDE converged to a stable distribution after 10 samples if an average error of 1E-4 between samples sizes is desired. Therefore, there is a high level of confidence in the distribution determined using 20 samples, implying that it can be used to model the manufacturing variation. While a number of beam thickness measurements were taken, a major limitation was that only one inclusion geometry was used for the measurements. As a result, only one nominal beam thickness was produced. To better characterize the system, different beam geometries should be produced and measured. A preliminary study of the effects of different geometries will be discussed in Chapter 8.

Since all of the measurements were based on a beam with as-designed thickness of 50 microns, the multivariate distribution was shifted for beams with different as-designed thickness. The distribution was shifted linearly by the difference between the intended beam thickness of the design and 50 microns.

6.3 Incorporating Manufacturing Variation

After forming the multivariate joint distribution for each design point using the data previously collected, the methodology described in Figure 3.5 was applied to identify designs that meet performance thresholds for the NS metamaterials design problem even when subjected to manufacturing variability; these designs are defined as reliably manufacturable. Throughout this section, it is assumed that the manufacturing variation associated with the Young's modulus is independent of the manufacturing variation describing the dependent beam thickness and apex height. [51].

After developing the classifier in the micro-scale design space, manufacturing variation was incorporated into the BNC approach using the procedure described in Chapter 3. First, for each design or training point classified as satisfactory, a Monte Carlo

sampling method was performed on its associated manufacturing distribution. The percentage of randomly sampled designs classified as satisfactory was determined and compared to the reliability threshold for classification. If the percentage of sampled, satisfactory designs exceeded the reliability threshold the point was classified as reliably manufacturable. Following classification of the designs by manufacturing reliability, another classifier was trained and tuned with the same leave-one-out procedure utilized previously. This classifier predicts whether a design is likely to perform satisfactorily and be reliably manufacturable. This procedure was repeated for a variety of reliability thresholds ranging from 10% to 30% at 10 even intervals.

Previously, it was hypothesized that as the reliability threshold increased, the number of available designs should decrease until the null set is reached. To quantify the effect of the reliability threshold on the size of the reliably manufacturable regions, a secondary study was performed. This study determined the volume of the regions bounded by the reliably manufacturable decision boundary, V_{man}, for the same variety of reliability thresholds. First, the space was normalized so that each design variable was bounded from 0 to 1. Following normalization, a Monte Carlo based sampling method was employed to approximate the volume of the reliably manufacturable region. 1,000,000 random samples of the design space were drawn and classified by the manufacturability classifier. The percentage of reliably manufacturable designs was then evaluated to approximate the volume of the reliably manufacturable region. This calculation was also performed on the initial satisfactory design region to determine its volume, V_0. This allowed the ratios between the volumes of the reliably manufacturable regions to be compared to the volume of the original design space. The results of this study are shown in Table 6.3 for a variety of reliability thresholds.

Table 6.3: Effect of increasing the reliability threshold on the normalized volume of the reliably manufacturable region of the micro-scale design space.

Reliability Threshold	V_{man}/V_0
0.1	1
0.122	1
0.144	0.994
0.167	0.991
0.189	0.991
0.211	0.956
0.233	0.900
0.256	0.840
0.278	0.768
0.3	0.653

Table 6.3 illustrates that the relationship between the reliability threshold and the change in volume of the reliably manufacturable regions is nonlinear. Small changes in the reliability threshold can yield large changes in the volume while large changes in the threshold can yield small changes in the volume. These volume reductions in the reliably manufacturable design regions imply that fewer designs are available for selection. A limited design space may lead to a limited range of possible performance capabilities, as well, so the impact of the reliability threshold on the performance space must be studied.

Initially, the macro-scale performance space was classified according to whether it met pre-specified performance requirements or not. Specifically, the original macro-scale performance space was classified so that satisfactory performance required the ratio between the loss factor of the composite and the loss factor of the base matrix to exceed four and that the Young's modulus be in some range. It is also possible to use the BNC approach to map the attainable portion of the macro-scale performance space, defined as the combinations of macro-scale performance parameters that are attainable with the micro- and meso-scale designs evaluated so far. Following classification a Bayesian

network classifier was trained and tuned by a leave-one-out strategy in which 50% of the unsatisfactory performance points were randomly omitted. This allowed for the classification of the entire attainable performance space shown in Figure 6.15 in which the classifier maps the attainable regions of the macro-scale performance space.

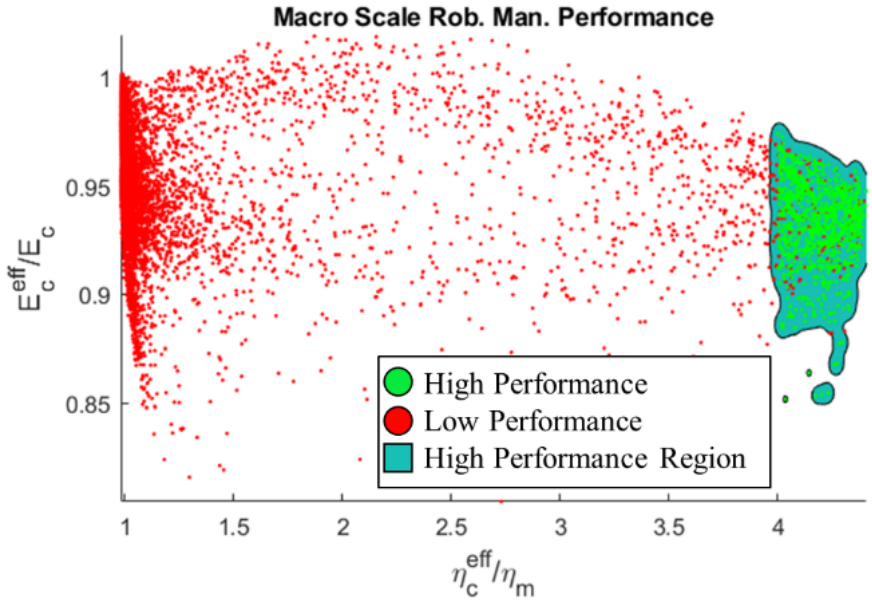

Figure 6.15: Mappings of the performance space predicting satisfactory and attainable performance for the highlighted performance requirement.

The mapping in Figure 6.16, however, does not contain any information regarding manufacturing reliability. With the implementation of manufacturing reliability, the macro-scale performance space must be revisited to determine if a portion of that space is both satisfactory and reliably attainable. Reliably attainable means that the combination of macro-scale performance parameters can be attained by a reliably manufacturable micro-scale design. First, the micro-scale design space is classified by the reliably manufacturable criteria. Then, the reliably manufacturable classification is forward propagated to the macro-scale performance space. This classification identifies performance that is not only

satisfactory but also likely to be reliably attainable. Following classification of the macro-scale performance space, a classifier can be generated to map likely regions of satisfactory and reliably attainable performance.

To better understand how the reliability threshold affects the size of the satisfactory and reliably attainable performance regions, a variety of reliability thresholds were selected and the general procedure described above was performed to obtain satisfactory and reliably attainable performance regions for each reliability threshold. Using a Monte Carlo sampling method, the area of each satisfactory and reliably attainable performance region, A_{sat}, was determined for each reliability threshold. The areas of the satisfactory and reliably attainable regions were compared to the area of the original satisfactory performance region, A_0. Table 6.4 presents the results of this study in which the reliability threshold is shown with the associated ratio of the area of the satisfactory and reliably attainable region to the area of the satisfactory region.

Table 6.4: Effect of increasing the manufacturing reliability threshold on the normalized area of the reliably attainable region of the macro-scale performance space .

Reliability Threshold	A_{man}/A_0
0.1	1
0.122	1
0.144	1
0.167	1
0.189	0.999
0.211	0.930
0.233	0.929
0.256	0.939
0.278	0.801
0.3	0.760

Table 6.4 corroborates the notion that increasing the value of the reliability threshold simultaneously decreases the size of the reliably manufacturable design space

and the satisfactory and reliably attainable performance space. The results also demonstrate that as manufacturing variation is taken into account, certain performance levels are no longer attainable. This information about the performance space is especially important for coupled variables. In a multilevel design space, incorporating manufacturing variation causes the satisfactory and reliably attainable performance region for a coupled variable to shrink. This constrains the available candidate designs for the coupled variable, which may limit performance at the highest level of interest.

To further understand the impact of incorporating manufacturing variation on both the micro-scale design space and macro-scale performance, five NS inclusion designs were identified of which three should meet the performance requirements with 25.6% reliability and the other two should not. The geometries and material properties of the identified inclusions are provided in Table 6.5 as well as the performance predicted from the forward models. The interval bounds of the reliably manufacturing regions identified by the augmented BNC approach are also included to provide some preliminary information on the topology of the design space. The design regions will eventually be visualized in Section 6.4.

Table 6.5: Properties of three NS inclusions identified to be reliably manufacturable and two inclusions that were originally satisfactory but not reliably manufacturable for a reliability threshold of 25.6%. The nominal performance of the design is included as well.

	Reliably Manufacturable ($T_{rel} = 0.256$)				Unreliably Manufacturable ($T_{rel} = 0.256$)	
	Design 1	Design 2	Design 3	Range	Design 1	Design 2
h (μm)	90	91	88	[86, 92]	104	85
t (μm)	52	54	52	[38, 57]	36	46
E^{inc} (GPa)	0.61	0.61	0.63	[0.53, 0.75]	0.76	0.72
r_d	1.23	1.43	1.15	[0.94,1.67]	1.29	0.93
E_C^{eff}/E'_m	0.96	0.97	0.95		0.85	0.94
η_c^{eff}/η_m	4.04	4.00	4.3129		4.23	4.12

Following the identification of the designs, the expected performance of the identified inclusions after manufacturing was desired as well. The BNC approach cannot provide this information because it is a classification technique and not a regression technique. It can predict if a manufactured design can perform satisfactorily but it does not predict the precise performance. Therefore, to predict the range in performance of the manufactured inclusions a basic regression approach was performed

.A Monte Carlo based approach was used in which 5000 designs were sampled from the manufacturing variation distributions of the five identified inclusions. For each of the randomly sampled designs, the closest training point, whether satisfactory or unsatisfactory, was identified and its associated macro-scale performance recorded. Due to the high density of training points, it is assumed that the training point closest to a sampled

point should predict its performance reasonably well. For each inclusion, the range corresponding to the top 25.6% of performance values was recorded. This range should correspond closely to the best performance of 25.6% of the manufactured inclusions. The results of the expected performance are documented in Table 6.6.

Table 6.6: Range in effective loss factor relative to the matrix material for the top 25.6% of manufactured designs based on five nominal designs.

	Reliably Manufacturable ($T_{rel} = 0.256$)			Unreliably Manufacturable ($T_{rel} = 0.256$)	
	Design 1	Design 2	Design 3	Design 1	Design 2
Top 25.6% of (η_c^{eff} / η_m)	[4.02, 4.33]	[4.00, 4.40]	[4.00, 4.37]	[1.67, 4.33]	[3.37, 4.19]

The three designs identified to be reliably manufacturable by the augmented BNC approach are expected to perform above the required threshold of $\eta_c^{eff} / \eta_m = 4$ at least 25.6% of the time following manufacturing based on the basic regression employed. Furthermore, the designs identified as unreliably manufacturable did not perform satisfactorily frequently enough. Unreliable Design 2, fell only slightly below the required performance threshold of $\eta_c^{eff} / \eta_m = 4$, but the performance of unreliable Design 1 fell by more than a factor of two. This insight is pivotal to why incorporating manufacturing variation is necessary for designing such metamaterials produced by AM. It assists the designer identify not only satisfactory designs but those that will not degrade in performance when manufactured.

6.4 Visualization of Design Regions

Following the procedure described in the previous leads to the generation of various mappings but the dimensionality of the design space prevents the results from being shown

without further work. Therefore, the proposed visualization approach was applied to each of the classified design spaces for each reliability threshold. First, 2000 points were identified that were on or near the decision boundary of the satisfactory and reliably manufacturable design regions. A point was considered near the decision boundary if the magnitude of its associated posterior class determinant was less than 0.05. This threshold was arbitrarily selected and smaller values could be used to obtain points even closer to the decision boundary but there will be an increase in computation time to discover appropriate points. Future work could investigate ways of uncovering points on the decision boundary possibly based on Bayesian optimization. After obtaining points on the decision boundary, the Nyström STSC method was performed (*m = 300)* to identify the number of clusters in each micro-scale design space. The most common number of clusters identified for each mapping is shown in Table 6.7. Normal STSC was also performed on the datasets to corroborate the results which are also shown in Table 6.7.

Table 6.7: Results of the clustering approaches for a variety of reliability thresholds to compare the accuracy of the Nyström method.

Reliability Threshold	Nyström STSC	STSC
0.1	2	2
0.122	2	2
0.144	2	2
0.167	2	2
0.189	2	2
0.211	2	2
0.233	2	2
0.256	2	2
0.278	2	2
0.3	2	2

It appears that, in general, the clustering methods identify the same number of clusters, i.e., two clusters. The identification of two clusters makes intuitive sense because two different materials were being considered.

Following identification of the design regions using the Nyström modified STSC, the Bayesian optimization modified t-SNE approach was applied to each of the mappings in which preservation was the objective function, k was 5% of the number of elements in a cluster, and 100 iterations were performed. Each cluster was visualized, but the entire design space was also visualized for each reliability threshold. Table 6.8 provides the various optimal preservation and perplexity values for each visualization.

Table 6.8: Optimal visualization parameters for t-SNE visualization of design space identified by Bayesian optimization scheme.

	Cluster 1		Cluster 2		Full Data	
Reliability Threshold	Perp.	*P(k)*	Perp.	*P(k)*	Perp.	*P(k)*
0.1	1119	0.899	792	0.902	1200	0.882
0.122	803	0.902	1126	0.899	1177	0.891
0.144	802	0.902	1116	0.900	1205	0.900
0.167	814	0.902	1107	0.900	1175	0.886
0.189	1093	0.899	793	0.902	1159	0.901
0.211	1203	0.917	531	0.916	1193	0.915
0.233	1247	0.922	516	0.918	1002	0.896
0.256	1209	0.908	723	0.902	1231	0.903
0.278	1243	0.920	405	0.911	1183	0.899
0.3	433	0.895	88	0.897	384	0.876

Based on the preservation values it appears that the visualizations are high quality and that, in general, local visualizations are superior to global variations.

To view one of the mappings, Figure 6.16 shows the associated visualized mappings of the design space and each cluster when the reliability threshold was 0.256. The different colors in Figure 6.16 are simply used to distinguish the clusters.

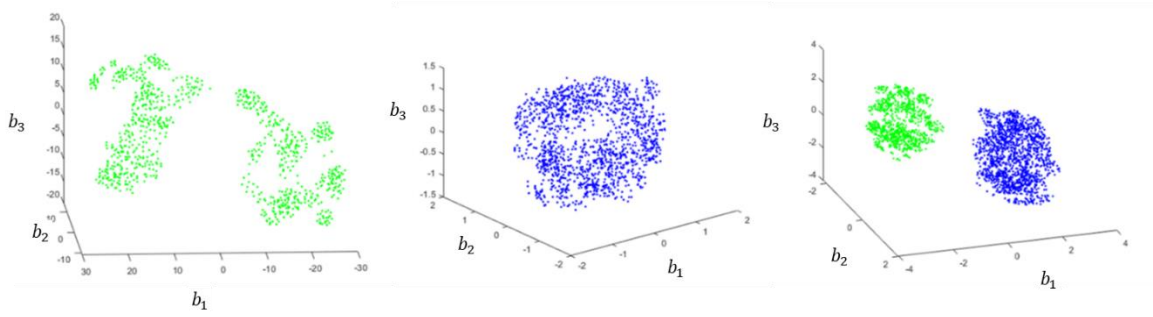

Figure 6.16: Visualization of each cluster (left and middle) and entire design space (right) for a reliability threshold of 25.6%.

From the global mapping it is clear that there are two clusters in this space, and the local mappings provide high resolution visualizations of each cluster. The structure of the design regions are also quite strange in which the green cluster has a narrowing and the blue cluster has a hole within it. Due to the nonlinear nature of the mappings, it is unclear how the different topologies correspond to physical geometries. Furthermore, for the global mapping it is unclear if the different clusters correspond to different material properties. To help explain what the structures physically represent, the visualization approach was augmented to allow the designer to select points in each mapping which will then cause an image of the associated inclusion to populate another figure. Furthermore, the color of the inclusion indicates the material properties of its base material. A gradient of color from green to blue is used in which blue indicates a lower Young's modulus and green indicates a higher Young's modulus. The value of each of the design variables is also provided for each cluster which allows the designer to see how designs vary across the structures or design spaces. Figure 6.16 provides snapshots of the tool illustrating that points on Cluster 1 have higher Young's moduli than Cluster 2.

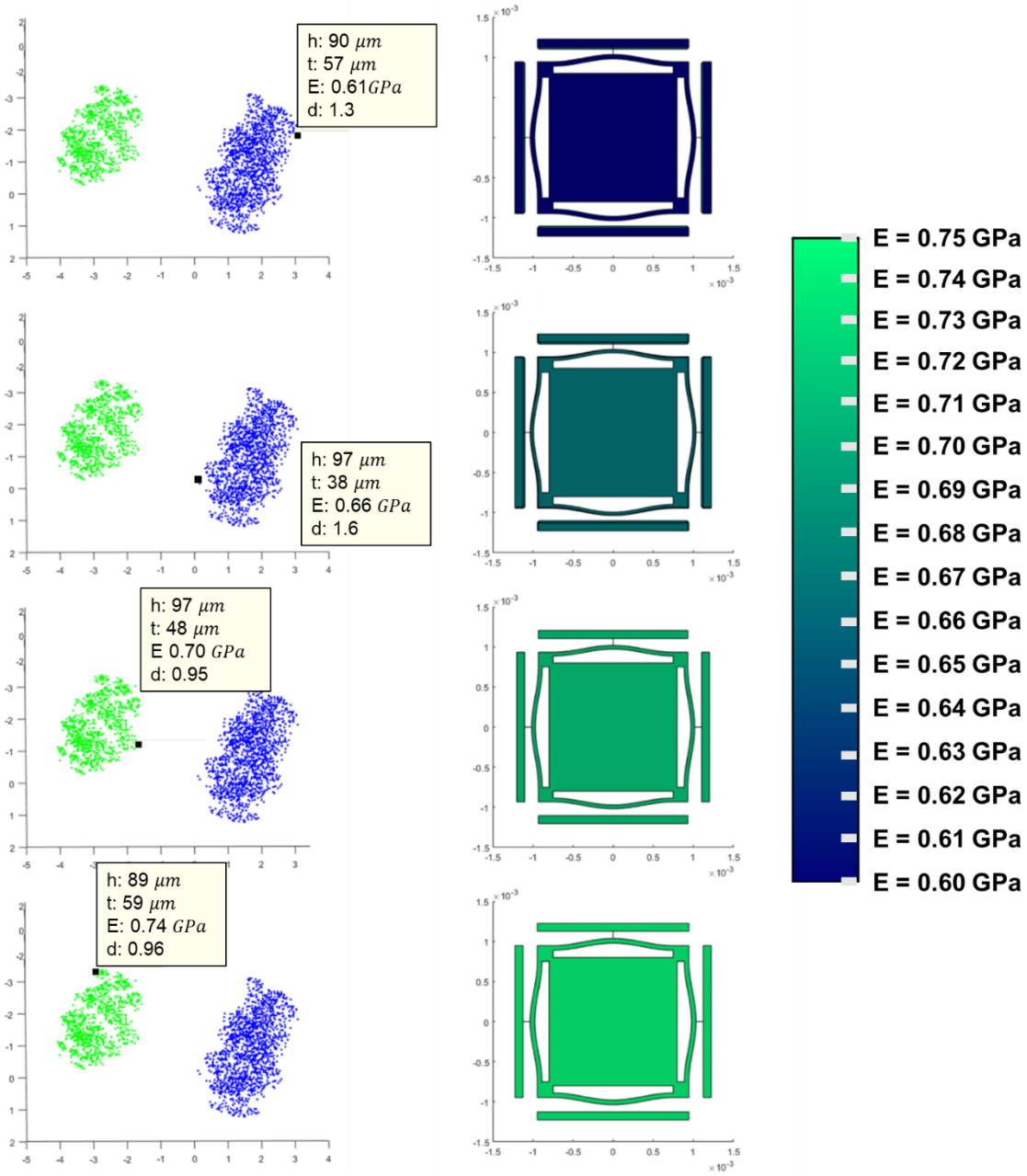

Figure 6.17: Snapshot of the visualization tool used to clarify how designs vary across nonlinear mappings.

Figure 6.17 corroborates the notion that the clusters are primarily separated by their Young's modulus due to the color of the inclusion in each cluster. Even more interestingly,

the points that are closest to the other cluster have a more similar blue green color. The points farthest from each other are the most different in color.

To further explore the quality of the visualizations and attempt to interpret the axes determined by the t-SNE approach, a PCA of both clusters and the entire design space was performed. Figure 6.18 presents the results of the clusters and design space projected into the space spanned by the first three principal components. The results of the t-SNE visualization are also shown for the same regions of interest below the associated PCA analysis for comparison.

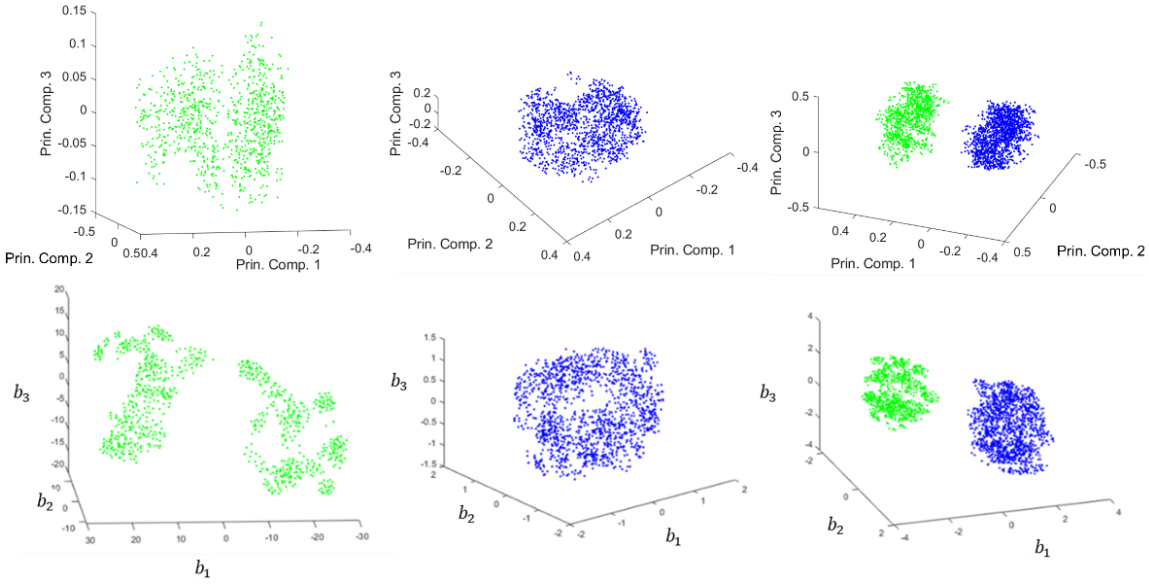

Figure 6.18: Visualizations of each cluster (left and middle) and entire design space (right) for a reliability threshold of 25.6% using PCA (top) compared to t-SNE visualizations (bottom).

In general, it appears the t-SNE visualization and the PCA visualization are similar in structure although the first cluster of Figure 6.18 shows some slight differences. The tightening of the region towards the center is more dramatic for the t-SNE visualization although the exact reason for the emphasis in that region is unclear. The approach may be

balancing the local and global structure of the cluster and emphasizing the separation of the furthest points in the cluster.

Interestingly, for the regions shown in Figure 6.18 that were identified by PCA, at least 95% of the variation of each structure can be explained by only three components. For the individual clusters, the first three principal components are nearly the original axes associated with beam thickness, initial displacement, and Young's modulus, respectively. This implies the variance in beam height is low for the reliably manufacturable designs, which is corroborated by Table 6.7. For the full design space, the first three principal components align with the original axes associated with the Young's modulus, beam thickness, and initial displacement, respectively. Once again, beam height has low variance but now the Young's modulus exhibits the most variance which confirms the expectation that clusters are separated by material properties.

It is tempting to conclude that the each axis of the t-SNE visualization is associated with the principal components but this is not necessarily true. The axes of the t-SNE visualization are not aligned with the PCA axes, that is, the clusters are rotated relative to each other. They have similar structures but they are not in the same space so further work could investigate alignment of the visualization to gain insight into the nature of the t-SNE axes. This may not be always possible because other design problems may have more variables responsible for the variance so they cannot be projected into a low-dimensional space with PCA while retaining structure. The formulation of the NS metamaterials problem proposed in this work only utilized four design variables but even more could be added that would likely impact the variance of the design space making the analysis just performed more difficult. The t-SNE visualization approach though has been shown to align well with the resulting visualization of PCA for this NS metamaterials design problem.

6.5 DISCUSSION

After proposing a strategy for incorporating manufacturing variation into the BNC approach and visualizing the resulting design regions, the approach was successfully demonstrated on a NS metamaterials design problem. The visualizations of the design space provided some insight into the topology of the design space and reliably manufacturable regions. Specifically there are two disconnected regions of the design space that appear to have very unique topologies when considering manufacturing variation. The main limitation of the visualization approach is that it is a nonlinear mapping, so the meaning of the axes is unclear. Future work could investigate clarifying the meaning of the axes, although this may not always be feasible. To help explain the structure of the visualized regions, a complimentary tool was developed that provided an image of an inclusion design. This helped clarify low resolution information regarding the separation of clusters, but did not assist strongly in finding relationships between design variables. Therefore, future work should investigate methods increasing the interoperability of the axes.

With a validated method for incorporating manufacturing variation and visualizing the results introduced, a final application of the augmented BNC approach was performed where the reliability was increased to 50% to determine a design for manufacturing. At this reliability threshold, only 16 training points were classified as reliably manufacturable. One such design was identified whose properties are given in Table 6.9

Table 6.9: Properties of three NS inclusions identified to be reliably manufacturable.

	Initial Inclusion Geometry	Final Inclusion Geometry
Apex Height, h	71.4 μm	143 μm
Beam Thickness, t	51 μm	102 μm
Young's Modulus, E_{Inc}	0.65 GPa	0.65 GPa
Initial displacement, r_d	1.48	1.48
Beam Length, L	1.3 mm	2.6 mm
Beam Separation, W	1.6 mm	3.2 mm

The small amount of designs available when only a 50% reliability threshold is used is telling of the high variation of AM processes. Since the reliability threshold of 50% is quite low, the entire geometry of the inclusion was doubled and slightly modified to improve the likelihood of producing a viable design. This geometry is also provided in Table 6.9. It is thought that by doubling the size of the inclusion the reliability will also increase dramatically. The doubling in size should not affect the inclusion's stiffness tensor, but when embedding the inclusion, a larger volume will require more matrix material. When classifiying designs as reliably manufacturable, the same manufacturing variation distribution was used for each design. If this assumption of constant variation is true, doubling the size of the inclusion should approximately double the chances of success because the variation is relatively half as small compared to the design dimensions. This assumption should certainly be investigated, but assuming it is true, there is a higher chance of success by doubling the size.

At this point of the paper, the first three tasks have been accomplished and a design approach has been developed. Therefore the final task of this work is to manufacture the metamaterial to test its properties. The following Chapter discusses the procedure for manufacturing and testing a NS metamaterial.

Chapter 7: Manufacturing and Testing of NS Metamaterials

With a final inclusion design identified, the next task is to manufacture and test a NS metamaterial. The main difficulty of this task is to identify a manufacturing and testing approach that is feasible in terms of time and resources. To begin manufacturing the metamaterial, a suitable matrix for embedding the inclusions must be identified. As noted by Klatt and Haberman [32], the positive stiffness of the matrix must be approximately equal to the negative stiffness of the inclusion to obtain desired metamaterial properties. Therefore, the meso-to-macro model utilized a material with a storage modulus of 1.25 MPa and a loss factor of 0.1, which approximately describes some commonly available elastomers.

Elastomers, like all plastics, are viscoelastic due to their molecular structure in which long chains of molecules are entangled in amorphous, noncrystalline structures. The molecular structure is sensitive to loading conditions and temperatures resulting in material properties that are dependent on application and environment. In particular, the frequency of the input loading results in different material properties such as the storage modulus and loss factor. As a result, specific polymers may be applicable only in a small window of applied frequencies, initial loading conditions, and temperatures. Considering these factors, a possible matrix material was identified. The material is a polyurethane known as Clear Flex 30 manufactured by Smooth-On Inc. A similar polyurethane, Clear Flex 75, which is no longer available, was characterized by Van Ekeren *et al.* [144] for armor applications and shown to have material properties at room temperature close to the storage and loss factor modeled with EMT in Chapter 6. Therefore, Clear Flex 30 was selected as the matrix within which to embed the inclusions, although the precise properties of Clear Flex 30 were unknown at the time.

Various approaches exist for characterizing the storage and loss modulus of viscoelastic materials but the most common approach is the use of a dynamic mechanical analyzer (DMA). The DMA is a commercially available device that can be used to determine the dynamic modulus of viscoelastic materials by providing a time-dependent load to a specimen (usually sinusoidally varying) in a temperature-controlled environment and measuring the response of the part to the load [145]. After sweeping through various temperatures and frequencies, the results can then be used to determine the dynamic modulus of the material for an even wider range of frequencies and temperatures using the principle of time-temperature superposition [146].

While Clear Flex 30 would be well suited for a DMA, the equipment was not available so an experimental apparatus described in Section 7.1 was developed to not only quantify the material properties of both the polyurethane elastomer and the NS metamaterial but also to prestrain the materials. Prestraining the materials is essential because the embedded inclusion must be displaced to a critical regime to activate the exceptional properties of the metamaterials. Determination of the material properties, requires a forward model which is developed in Section 7.2 that predicts the performance of the experimental apparatus and materials. This discussion is followed by a description of the manufacturing method adopted to embed the inclusions in Section 7.3 The manufactured materials are tested and evaluated with the experimental measurements to determine the material properties of the specimens in Section 7.4 and these results are discussed in Section 7.5.

7.1 Characterization of Matrix and NS Metamaterial

The performance of a NS metamaterial is highly dependent on the prestrain imparted to the embedded inclusion. Since the inclusions will be embedded initially in a

stress-free state (discussed in Section 7.3), an external force or prescribed displacement must be supplied to the metamaterial to strain the inclusion. Therefore, the testing apparatus must allow the prescribed stress or displacement of the metamaterial to be varied in a controllable manner. Furthermore, the material properties (storage modulus and loss factor) of the NS metamaterial must be compared to those of the original matrix to determine if any advantages have been gained by embedding inclusions. Those material properties must also be compared to the properties of a matrix with voids in place of the inclusions, to determine whether the lack of polyurethane was the cause of any change in material properties. This motivates the characterization of three different materials: (1) the original matrix, (2) the original matrix with voids equal in size to the inclusions, and (3) the matrix with the embedded inclusions. The experimental setups are illustrated in Figure 7.1.

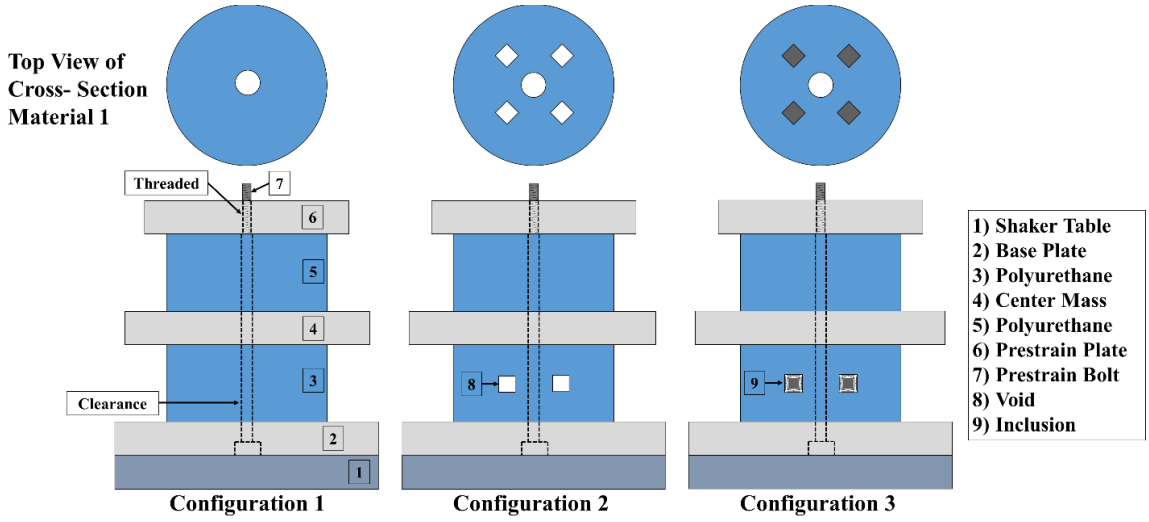

Figure 7.1: Experimental configuration used to measure the material properties of the polyurethane (left), voided polyurethane (middle), and NS metamaterial (right). All configurations are axially symmetric and the cross sectional view of the bottom polymer is provided for clarity.

As shown in Figure 7.1, three similar experimental configurations are utilized to compare the properties of the various material systems of interests. All of the configurations are axially symmetric and mounted to a shaker that excites the system. Rigidly mounted to the shaker table is a metallic plate with a rotationally constrained steel bolt mounted to it. The bolt travels through the axis of the entire system. Above the base plate is the material of interest with the cross section shown in Figure 7.1. There is a clearance hole in the center of the material of interest that allows the central rod to travel through the material without interfering. Above the material of interest is a central mass of aluminum and a pure polyurethane material that each have the same sized clearance hole as the material of interest. Finally, on top of each configuration is an aluminum plate that is centrally threaded, which allows it to be tightened to precisely prescribe the prestrain for the material system.

The goal of such a setup is to excite the system via a frequency sweep of the shaker table to measure the response of the central mass. An accelerometer measures the acceleration of the central mass while a second accelerometer measures the acceleration of the base plate. The frequency response of the central mass can be compared to the input, or base response, to determine the material properties of the material of interest.

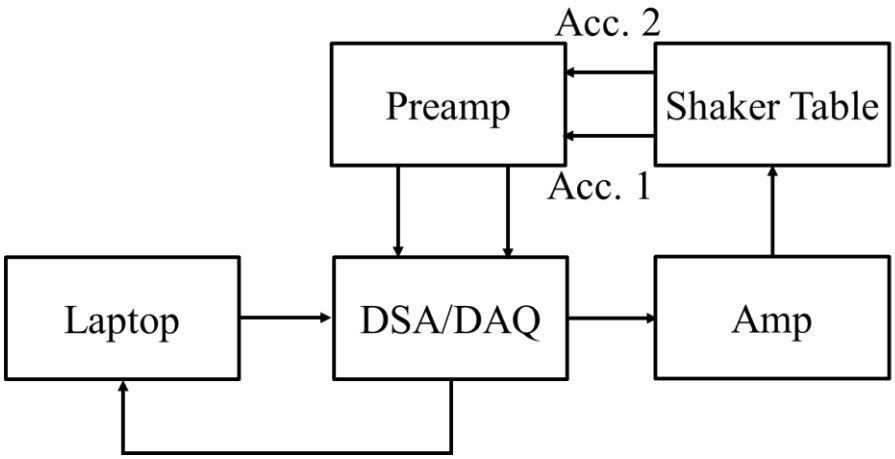

Figure 7.2: Schematic of signal generation and collection configuration used for the material characterization experiments

The data collection system is outlined in Figure 7.2. A laptop with SignalCalc 240 software generates the desired frequency sweep or chirp profile and supplies it to the Data Physics Quattro Dynamic Signal Analyzer (DSA). The output from the DSA which is simultaneously a data acquisition device (DAQ) is amplified by the Crown XT 4000 amp, which drives the Labworks Inc. ET-139 shaker table. While the shaker table is driven, the two accelerometers (33B30 manufactured by PCB Piezotronics) record the acceleration of the base and central mass. This signal is supplied to a preamp within the DAQ which allows the DAQ to send the data to the laptop, where software evaluates the transfer function between the shaker table and the two accelerometers. Figure 7.3 provides a labeled image of the experimental apparatus.

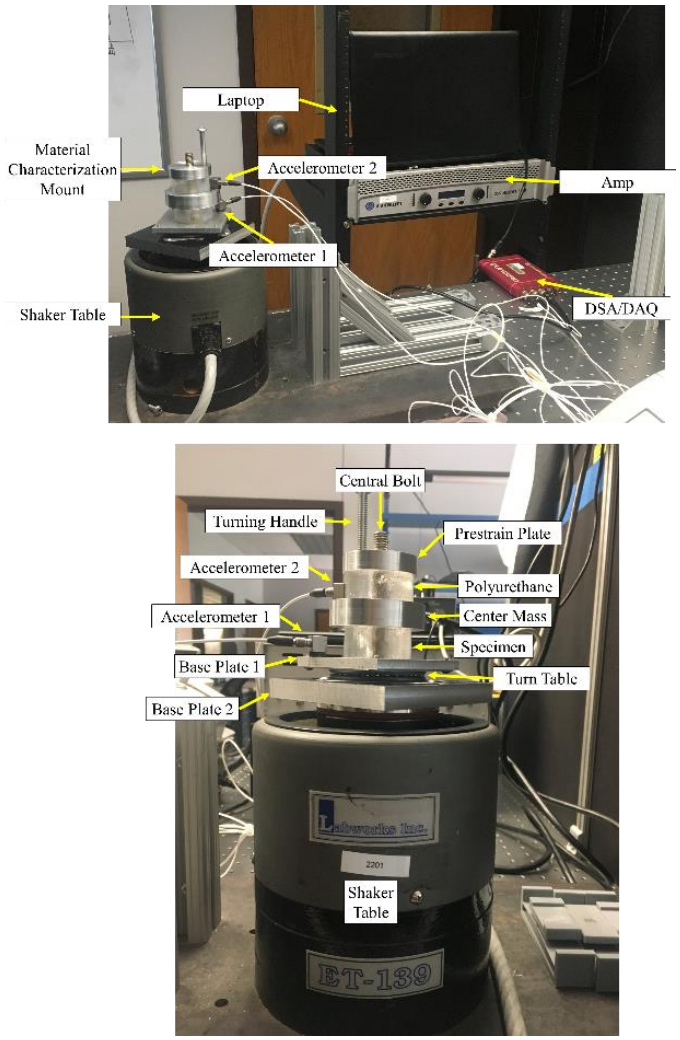

Figure 7.3: Experimental setup used to characterize materials (top) and image of the mounted shaker table with specimen to be analyzed (bottom).

It should be noted that the material characterization mount in Figure 7.3 has been slightly modified relative to the schematic shown in Figure 7.1. An additional base plate and turntable have been added to the system to prevent the prestrain plate from applying a torque to the material. The entire material system can rotate with the prestrain plate to prevent unnecessary stresses from forming. The reference accelerometer, denoted Accelerometer 1, is placed on the Base Plate 1 to ensure any vibrations related to the

turntable have a minimal impact on the results. If the accelerometer were placed on Base Plate 2, the transfer function between the center mass and the plate may be noisy due to the tolerances of the bearings in the turntable.

This system configuration allows for the magnitude and phase of the transfer function between the two accelerometer signals to be recorded. This is known as a transmissibility measurement, and it can be used to characterize the overall response of the heterogeneous materials between Base Plate 1 and the center mass. At low frequencies, this system is a single degree of freedom (DOF) damped mass-spring oscillator. Figure 7.4 provides representative results of a frequency sweep from 1-600 Hz for this type of test. The magnitude and phase of the transfer function, T, is a function of the input frequency, f, and one clearly observes a transmissibility approaching unity with in-phase motion of the baseplate and center mass in the low frequency limit as well as a lumped parameter resonance peak, indicative of a damped single DOF system.

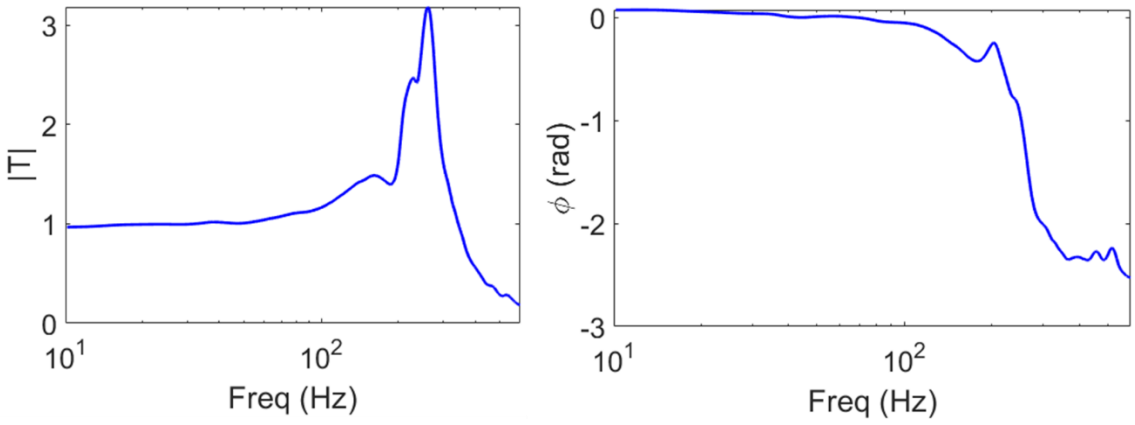

Figure 7.4: Representative results of a transmissibility test with the magnitude (left) and phase (right) of the acceleration transfer function between the baseplate and center mas as a function of frequency.

For an idealized single DOF system, the magnitude of the transfer function should attain a single maxima but the transmissibility test, shown in Figure 7.4, indicates multiple maxima. These peaks are likely due to other components of the system vibrating. For an ideal system, Base Plate 1 and the prestrain plate should be rigidly attached so the magnitude of the transfer function between each component should be unity. To determine if Base Plate1 and the prestrain plate are moving in unison, the magnitude of the transfer function, H_0, was measured between the two components which is shown in Figure 7.5. This measurement was taken to determine if there are any vibrations being induced in the system that could affect the movement of the central mass. Therefore, the magnitude of the transfer function between the central mass and base plate is also shown in Figure 7.5.

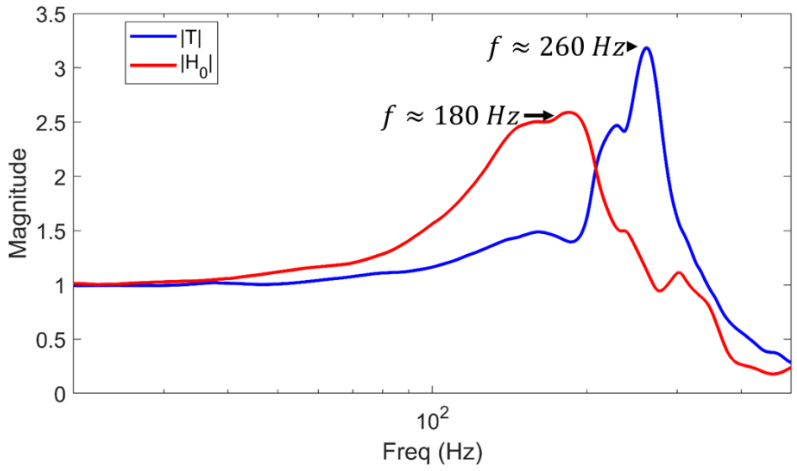

Figure 7.5: Magnitude of the transfer function between the prestrain plate and Base Plate 1 (red) compared to $|T|$.

As can be seen in Figure 7.5, $|H_0|$ indicates that there is a resonance between Base Plate 1 and the prestrain plate at approximately 180 Hz. This resonance affects the motion of the central mass and is contributing to the multi-modality of $|T|$ as indicated by the secondary peak at the natural frequency of H_0. This undesired resonance, though,

attenuates before the resonance of the central mass allowing the resonance of the central mass to be clearly defined. While the system will be treated as a single DOF system for the modeling discussed in Section 7.2, special considerations will be made to account for the undesired resonances when extracting material properties.

7.2 Modeling of Experimental Apparatus

Analytical models relate the material properties to the measured signal. In this work, the testing apparatus is modeled as a single DOF system, as shown in Figure 7.6. More complex models could be used to describe the dynamics of the system, but the single DOF model is assumed to be accurate enough for sufficiently low frequencies, where higher order modes and wave motion effects can be ignored. In particular, it is assumed that Base Plate 1 and the prestrain plate are rigidly attached, which as shown in Section 7.1, is not necessarily true.

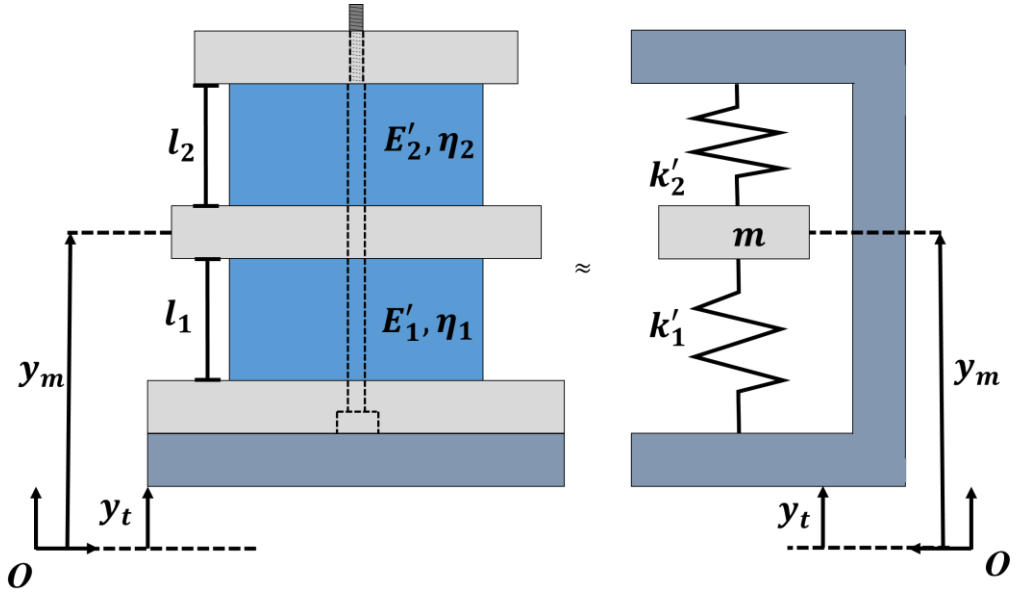

Figure 7.6: Simplified single (DOF) model of the experimental setup.

In Figure 7.6, the input displacement of the shaker table, y_t, and output displacement, y_m, of the mass are the desired values to be measured for material property characterization. Technically, the acceleration is measured but it will be shown that this does not matter for determination of the material properties. Throughout the discussion, the subscript, 1, corresponds to the material of interest and the subscript, 2, corresponds to the top block of polyurethane. Therefore, the storage modulus and loss factor of the material of interest are given by E'_1 and η_1, while the storage modulus and loss factor of the polyurethane block are E'_2 and η_2. The two complex springs of the single DOF system, k'_1 and k'_2, can be related to the material properties and geometry of the materials by Equation 7.1 in which l is the initial height of the materials and A is the cross-sectional area of the materials.

$$k'_i = \frac{E'_i(1+\eta_i j)A}{l} \tag{7.1}$$

Note the use of the complex number, j, that is associated with the loss of the material. For the remainder of the discussion, the displacements to the system are assumed to be small, such that the material properties are constant and the cross-sectional area does not change when excited. As posed, Equation 7.1 need not assume that the modulus is frequency-independent, just that the perturbations are small. Following establishment of the spring stiffnesses, the equation of motion can be determined, as documented in Equation 7.2 in which m is the total mass of the specimen combined with the aluminum center mass and the top polyurethane block.

$$m\ddot{y}_m = (k'_1 + k'_2)(y_t - y_m) \tag{7.2}$$

Gravity is ignored because it is simply a bias for the eventual transfer function. The Laplace transform of Equation 7.2 is represented by Equation 7.3, assuming that the system begins from rest.

$$ms^2 Y_m(s) = (k_1' + k_2')\big(Y_t(s) - Y_m(s)\big) \tag{7.3}$$

Substituting Equation 7.1 into Equation 7.3, assuming the geometry is the same for both materials, and collecting like terms, results in Equation 7.4.

$$Y_m\left[ms^2 + \frac{A}{l}(E'_1 + E_2') + \frac{A}{l}(E_1'\eta_1 + E_2'\eta_2)j\right] = Y_t\left[\frac{A}{l}(E'_1 + E_2') + \frac{A}{l}(E_1'\eta_1 + E_2'\eta_2)j\right] \tag{7.4}$$

Equation 7.4 can rearranged to yield the transfer function in Equation 7.5 where c_1 and c_2 are given by Equations 7.6 and 7.7, respectively.

$$\frac{Y_m(s)}{Y_t(s)} = \frac{c_1 + c_2 j}{s^2 + c_1 + c_2 j} \tag{7.5}$$

where

$$c_1 = \frac{A}{ml}(E'_1 + E_2') \tag{7.6}$$

and

$$\frac{A}{ml}(E'_1\eta_1 + E_2'\eta_2) \tag{7.7}$$

By converting Equation 7.5 from the *s*-domain to the frequency-domain, multiplying the numerator and denominator by the complex conjugate of the denominator, and collecting like terms, Equation 7.8 is derived. The result is the desired equation, which

represents the frequency dependent transfer function, $T(\omega)$, between the base and center mass.

$$T(\omega) = \frac{Y_m(\omega)}{Y_t(\omega)} = \frac{-\omega^2 c_1 + c_1^2 + c_2^2}{(-\omega^2 + c_1)^2 + c_2^2} - \frac{\omega^2 c_2}{(-\omega^2 + c_1)^2 + c_2^2} j \tag{7.8}$$

As previously discussed, the experimental setup precisely records the transfer function between the input accelerometer and the output accelerometer, which due to the linearity of derivatives, has the same transfer function as the associated displacements. Specifically the phase delay, ϕ, and magnitude of the transfer function, $\|T(\omega)\|$ are determined via Equation 7.9 and 7.10.

$$\phi(\omega) = \tan^{-1}\left(\frac{\mathcal{I}(T)}{\Re(T)}\right) \tag{7.9}$$

$$\|T(\omega)\| = \sqrt{\Re(T)^2 + \mathcal{I}(T)^2} \tag{7.10}$$

Figure 7.7 provides model-based predictions of the magnitude and phase delay of the transfer function for materials with the properties shown in Table 7.1. The value of $\eta_1$is varied at four equal increments from 0.1 to 0.4 to showcase the different results obtained for different values of the loss factor. The plots are generated assuming the storage modulus and loss factor are constant as a function of frequency, which is not necessarily true.

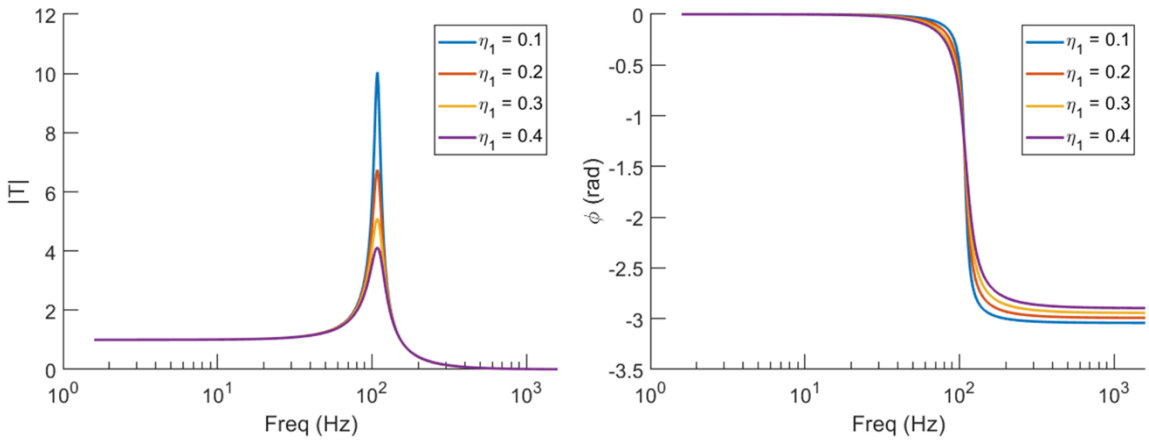

Figure 7.7: Modeled results of a characterization test with the magnitude of the transfer as a function of frequency (left) and phase delay as a function of frequency (right)

Table 7.1: Table of geometric values and material properties used to generate the example transfer function.

E'_1	1.25 MPa
E'_2	1.25 MPa
η_2	0.1
A	0.0014 m^2
l	11.2 mm
m	0.34 kg
η_1	0.1, 0.2, 0.3, and 0.4

The goal of establishing Equation 7.9 and Equation 7.10 is to invert them to obtain the material properties based on the measured values. As posed, the system of equations is underdetermined because there are two equations but four unknowns, E'_1, η_1, E'_2, and η_2. This challenge can be overcome by utilizing the measurements obtained from the first experimental configuration in which both blocks are the same polyurethane blocks. For this configuration, the two storage moduli and loss factors are equal. Once this

characterization has been performed, the values of E_2', and η_2 are known for each subsequent test, allowing E_1', and η_1 to be determined.

As discussed previously, though, there are other resonances being induced in the system so the material properties are most reliably determined close to the resonance of the central mass. While the material properties will be determined using the previously discussed approach, a secondary inversion approach is discussed that is less sensitive to the undesired resonances which is the standard half-power bandwidth method. The relevant measurements for the half-power method are given by Figure 7.8 in which $|T|$ is in normalized decibel units. The magnitude of the transfer function at the desired resonance, f_r, was normalized to 1 and then converted to decibels.

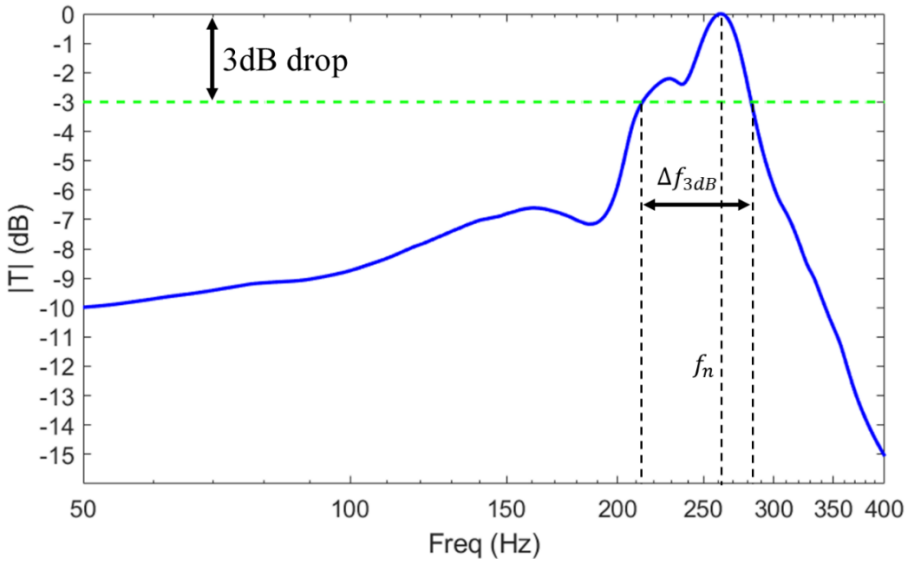

Figure 7.8: Illustration of the relevant quantities needed to utilize the half-power bandwidth method to calculate material properties.

From the normalized plot of Figure 7.8, the two frequencies corresponding to a 3 dB drop in the magnitude of the transfer function relative to the resonance magnitude can

be computed. This 3 dB drop corresponds a halving in the power present in the central mass compared to the power available at the natural frequency. The range between these two frequencies, Δf_{3dB}, can be computed which allows for the quality factor, Q, to be determined which is a measure of the energy dissipated in a loading cycle. Equation 7.11 provides the relationship between the measured quantities and the quality factor.

$$Q = \frac{\Delta f_{3dB}}{f_r} \tag{7.11}$$

The quality factor is related to the damping ratio, ξ, of a single DOF system by Equation 7.12 .

$$Q = \frac{1}{2\xi} \tag{7.12}$$

For single DOF systems in which the stiffness and damping are independent of frequency, the damping ratio can be related to the physical damping of the system easily but due to the frequency dependence of the material properties providing such a simple relationship is difficult. Rather, the quality factor, provides a more qualitative measure of the damping in the system which allows for relative comparisons of material properties but not absolute quantification. Future work could investigate a quantitative relationship between the damping ratio and material properties but that is beyond the scope of this work. The following section will discuss a strategy for embedding the inclusions in a polymer so it can be tested with the described approach and apparatus.

7.3 Embedding NS Inclusions in a Polymer Matrix

To embed the inclusions the identified matrix, Clear Flex 30, two liquid mixtures, Part A and Part B, were combined and poured into a mold where it cures forming the solid polyurethane elastomer. The simplest approach for embedding the inclusions with such a

resin would be to combine the inclusions into the resin during the mixture process and let the resin cure resulting in a fully formed metamaterial. Unfortunately this procedure would likely result in resin penetrating key areas of the inclusion that must be unobscured to perform correctly. These regions are identified by Figure 7.9.

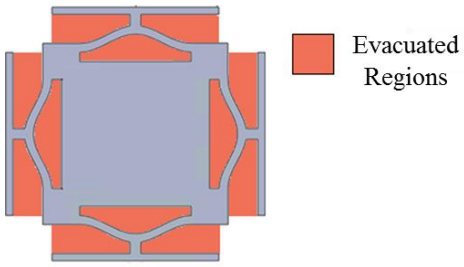

Figure 7.9: Illustration of the regions of an embedded inclusion that must be free of solids to perform correctly.

To evacuate these critical regions of the inclusion, another approach must be adopted for embedding the inclusions in the polyurethane. An initial option was to pour polyurethane around the inclusions to form sheets of a metamaterial that could then be adhered together to form the metamaterial. This method, shown in Figure 7.10, would likely lead to a metamaterial that is largely heterogeneous, and adhesion of the layers could be challenging.

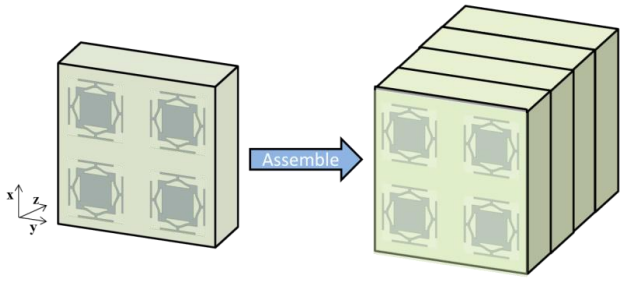

Figure 7.10: Initially proposed strategy for forming a metamaterial with sheets of inclusions embedded in polyurethane.

Therefore a new strategy for embedding was developed and Figure 7.11 provides an illustration of the proposed steps of embedding the inclusion within polyurethane.

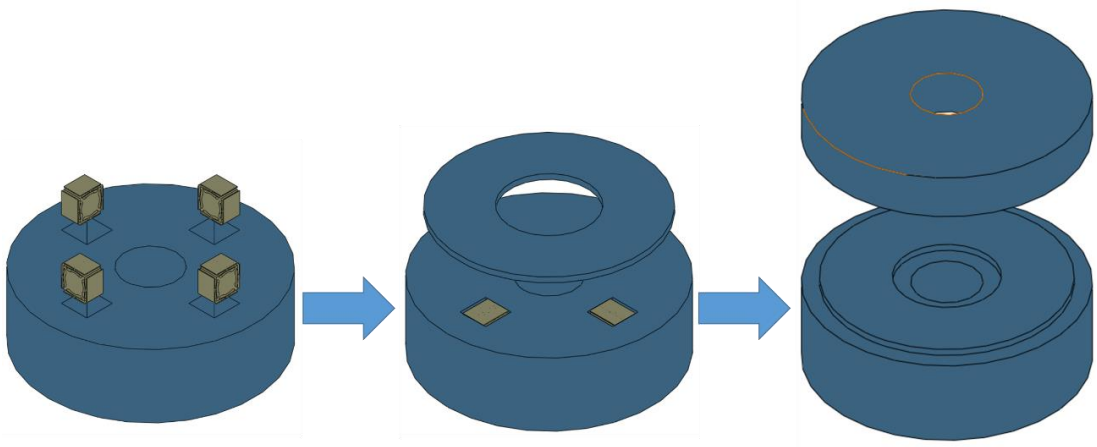

Figure 7.11: Proposed strategy for embedding inclusions (grey) in polyurethane (blue). First a mold is made with cavities just large enough for the inclusions to be embedded. Then a thin, sealing layer of polyurethane is adhered to the top which allows more resin to be poured and cured on top of the assembly without penetrating the cavity.

First, the polyurethane is molded into a circular column with cavities just large enough for the inclusions to be inserted after the polyurethane cures. After the inclusions are embedded, a second sealing layer of polyurethane is bonded with polyurethane-based glue to the top of the larger portion of polyurethane *and* the inclusions. This layer seals the inclusions and provides high traction and continuity between the thin layer and the inclusion. Finally, with the inclusions sealed, a third layer of polyurethane is poured over the assembly in a mold to achieve the desired volume fraction of 2%.

With a proposed strategy for embedding the inclusions, a procedure for molding the polyurethane had to be developed. When forming the mold, it is essential that no bubbles form in the resin because they can drastically change the material properties of the

cured polymer. Therefore, a KovyVacu 500 vacuum pump was used to pull a vacuum pressure differential of 29 mmHg along with a desiccator to degas the resin. Once the liquid polyurethane was degassed it was placed into the molds that were all coated with a nonstick aerosol provided by Smooth-On Inc.. The most critical features like the dimensions of the cavity for the inclusions were machined from aluminum and encased in FDM printed molds. Figure 7.12 provides images of a NS metamaterial being assembled.

Figure 7.12: Images of a NS Metamaterial being assembled.

A limitation of this manufacturing method, however, is that the inclusions are not prestrained so that they act in the negative stiffness regime. It is technically possible to precisely control the geometry of the cavities to prestrain the inclusions when they are

embedded. This strategy was avoided because forcing the inclusions into small cavities may damage them. Therefore, the experimental apparatus descried in Section 7.1 was developed to prestrain the inclusions for testing. The following section will describe the results of prestraining the materials for material characterization.

7.4 Experimental Characterization of NS Metamaterial

Three different specimens were manufactured to determine whether embedding NS inclusions into a polyurethane polymer leads to improvement in the loss factor. The geometry and mass of relevant components of the material characterization apparatus are documented in Table 7.2.

Table 7.2: Geometry and masses of the components of the material characterization apparatus that are dynamic.

	Outer Radius	Inner Radius	Thickness	Mass
Top Polyurethane Specimen	44.2 mm	14 mm	21.5 mm	29.5 g
Bottom Polyurethane Specimen	44.2 mm	14 mm	21.5 mm	29.5 g
NS Metamaterial Specimen	44.2 mm	14 mm	20.6 mm	29 g
Voided Material Specimen	44.2 mm	14 mm	22 mm	30 g
Central Mass	60 mm	14 mm	14 mm	126 g

Each specimen was mounted in the material characterization apparatus and excited by a frequency sweep from 30 Hz to 700 Hz logarithmically over 5 seconds. Various prestrains were prescribed to each of the specimens before the frequency sweeps, and the initial strain of the specimens and control polyurethane were recorded by measuring the distances shown in Figure 7.13.

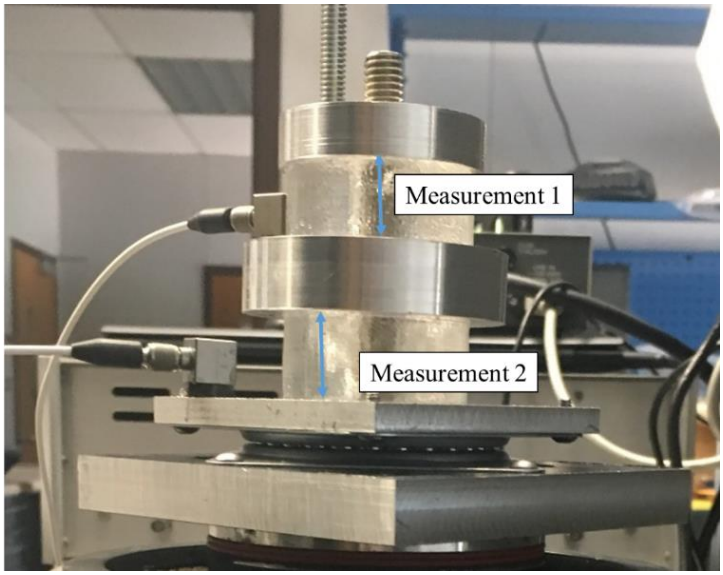

Figure 7.13: Measurements required to determine the initial strain of each specimen.

The distance between the prestrain plate and the top face of the center mass, d_1, and the distance between the bottom of the center mass and base plate number 2, d_2, was used to calculate the engineering prestrain of the respective components, ϵ_1 and ϵ_2, of a specimen by comparing it to the original thickness of the respective specimen, t_1 and t_2. Equation 7.13 provides the calculation of the engineering strain of the i^{th} specimen and Table 7.3 documents the prestrains applied to each specimen during the testing. Knowledge of the initial thicknesses of the specimens was also required for approximating k_1' and k_2' which are used to invert Equations 7.9 and 7.10 for the material properties.

$$\epsilon_i = \frac{d_i}{t_i} \tag{7.13}$$

Table 7.3: Engineering prestrains applied to each specimen during each of the frequency sweeps from 30 Hz to 700 Hz.

Polyurethane	Voided Material	NS Metamaterial
0	0	0
0.007	0.0196	0.0042
0.0114	0.0392	0.0075
0.0216	0.0647	0.034
0.0428	0.0958	0.047
0.046	0.1062	0.0625
0.0626	0.1369	0.0695
0.0851	0.1439	0.0749
0.1002	0.1728	0.0817
0.1209	0.1858	0.1013
0.1344	0.2092	0.1259
0.1572	0.2296	0.1381
0.1795	0.1833	0.148
0.204		0.1562
		0.1671
		0.1802
		0.1904

At each of the prestrains specified in Table 7.3, the frequency sweep was performed and the magnitude and phase shift of the transfer function were recorded. To obtain the nominal material properties of the polyurethane polymer, the magnitude and phase shift of the transfer function were obtained for the unstrained polyurethane. Then Equation 7.9 and 7.10 were simultaneously used to determine the frequency-dependent storage modulus and loss factor of the polyurethane at frequencies near the natural frequency. The bandwidth associated with the 3 dB drop in magnitude of the transfer function was used as the range for inversion. To compute the inversion, each block of polyurethane material was assumed to exhibit the same material properties, and a grid search method was employed that minimized the Euclidian norm between measurement and model predictions. The results

of the inversion are shown in Figure 7.14 in which the storage modulus and loss factor are shown as a function of frequency in range of the half-power bandwidth.

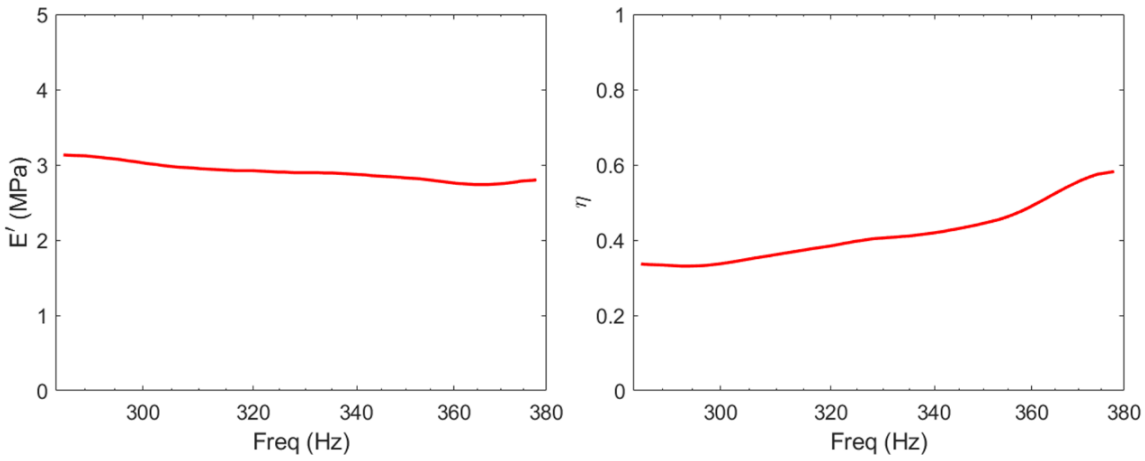

Figure 7.14: Frequency-dependent storage modulus (left) and loss factor (right) determined by inverting the forward model via the measurements obtained from the unstrained polyurethane specimens.

The material properties were determined only from 285 Hz to 380 Hz due to the range of the half-power bandwidth which helps to ensure the most accurate results. The results are quite promising for validating the material characterization apparatus. The storage modulus of the polyurethane was speculated to be approximately 1.25 MPa based on previous work [144], so the approximately constant storage modulus of 3 MPa in Figure 7.12 is reasonable. The loss factor is higher than the cited values of approximately 0.1-0.2 for Clear Flex 75, but other work has shown the loss factor of polyurethanes can be quite high and approach a value of 1 [147], so the average value of 0.42 determined from the loss factors in Figure 7.14 also seem reasonable.

After determining the dynamic material properties of the polyurethane, the material properties of the other materials could be determined. The same inversion procedure was

applied to each of the specimens to obtain the prestrain- and frequency- dependent material properties in which the properties were only obtained in the frequency range associated with the half-power bandwidth. It was assumed that by comparing the material properties of the specimens at similar prestrains, any differences would be apparent in the loss factor and material properties. For the majority of the prestrains the results were similar to those shown in Figure 7.15 in which the magnitude and phase shift of the transfer functions are similar for a prestrain approximately equal to 0.1 for each specimen. The resulting material properties at the same prestrain for each material are shown in Figure 7.16, as well, to demonstrate the similarities in material properties.

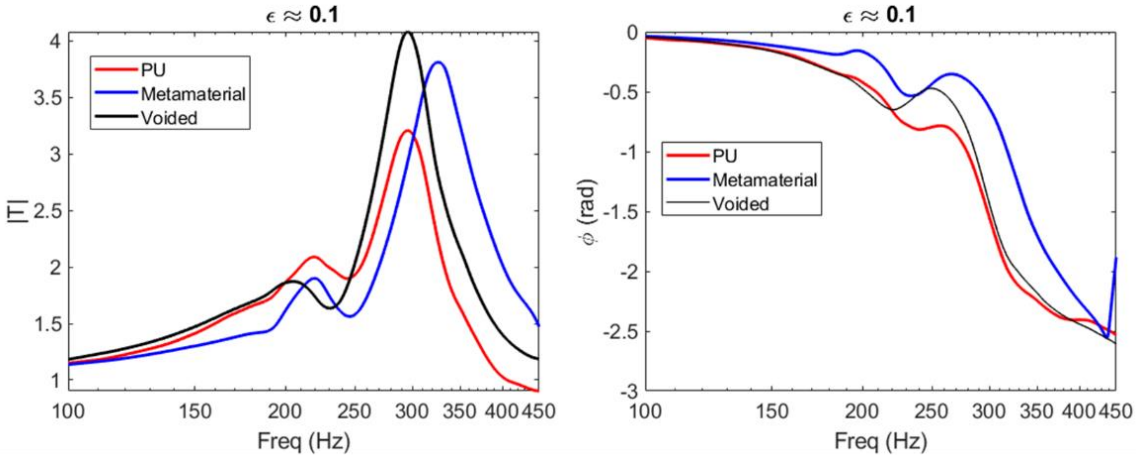

Figure 7.15: Magnitude and phase shift of the transfer obtained after exciting a polyurethane (red), NS metamaterial (blue), and voided material (black) at a prestrain of approximately 0.1.

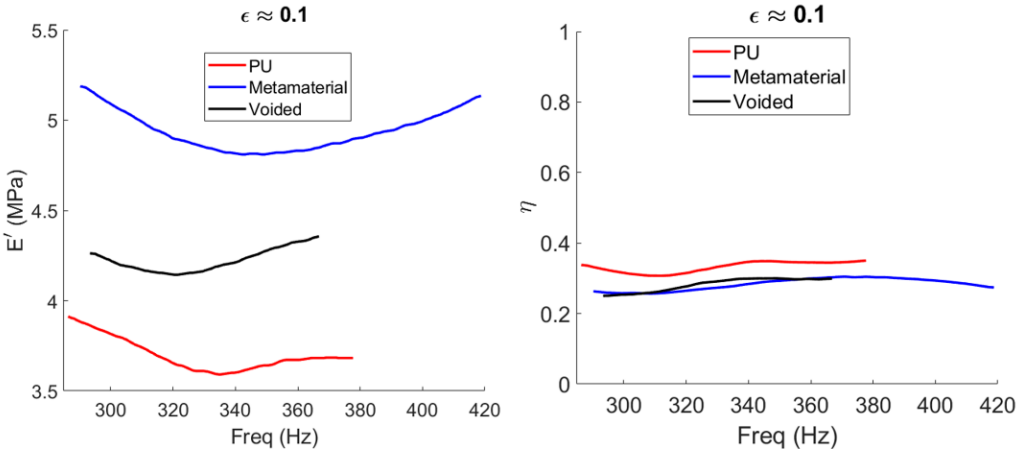

Figure 7.16: Storage modulus and loss factor determined after exciting a polyurethane (red), NS metamaterial (blue), and voided material (black) at a prestrain of approximately 0.1.

When the materials were prestrained to approximately 0.15, however, the results diverged for the metamaterial in a manner indicative of a NS metamaterial. Figure 7.17 presents the magnitude and phase shift of the transfer functions for each specimen at a prestrain of 0.15. The resulting material properties at the same prestrain for each material are shown in Figure 7.18 to highlight the difference in loss factors.

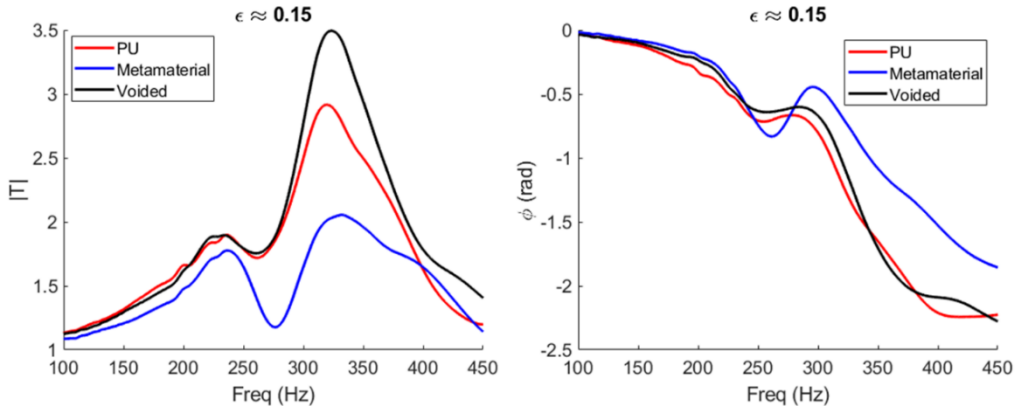

Figure 7.17: Magnitude and phase shift of the transfer obtained after exciting a polyurethane (red), NS metamaterial (blue), and voided material (black) at a prestrain of approximately 0.15.

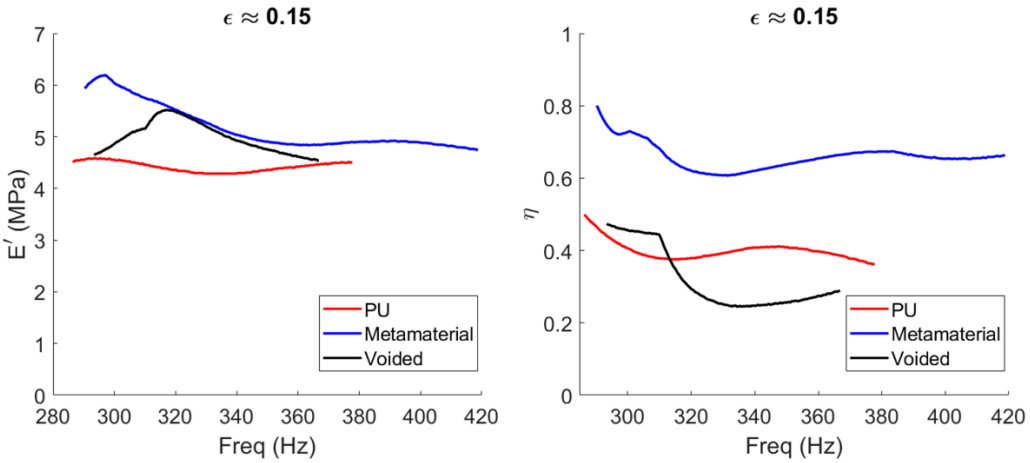

Figure 7.18: Storage modulus and loss factor determined after exciting a polyurethane (red), NS metamaterial (blue), and voided material (black) at a prestrain of approximately 0.15.

The magnitude of the transfer function shown in Figure 7.17 indicates that the amplitude of the movement of the center mass is being greatly diminished in the presence of the prestrained metamaterial. By inverting for the material properties, it becomes apparent that the loss factor of the metamaterial in the 285H Hz to 420 Hz frequency range is about twice as high as the original polymer. It also appears that the increased loss factor is due to the inclusions because the voided material behaves similarly to the original polyurethane. The storage modulus of the metamaterial appears to be slightly higher at the lower range of the frequencies, which may be due to the nonlinear effects of the inclusions that are not captured by the single DOF model but it still maintains the same order of magnitude of the other materials.

It appears that prestraining the metamatetial enabled the inclusions to enter the NS regime, which allowed the local strains to be amplified and energy attenuated by the inclusions. To visualize the effect of prestrain on the performance of the metamaterial Figure 7.19 is provided which shows the measured magnitude of the transfer function as a

function of frequency and prestrain. The blue lines indicate the exact measurements while the meshed surface is a cubic interpolation of the results to assist in visualizing the topology.

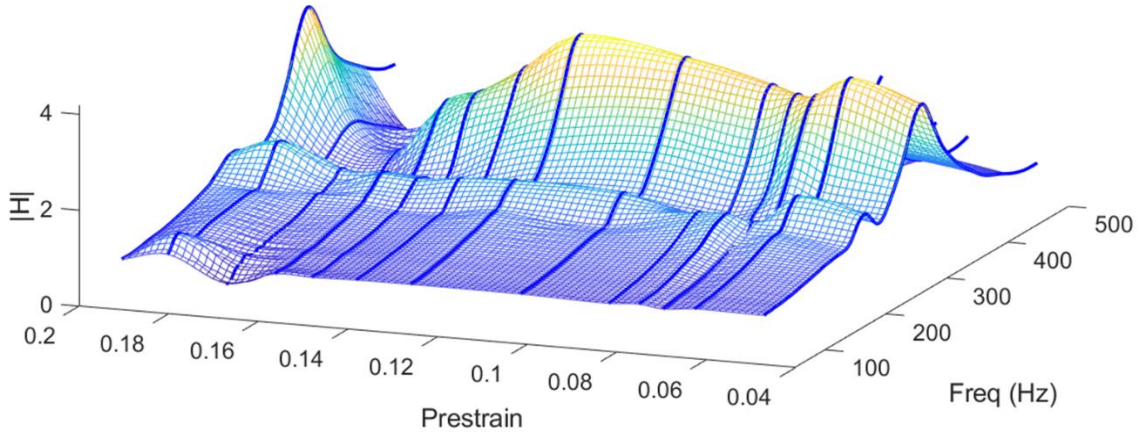

Figure 7.19: Magnitude of the transfer function for the metamaterial as a function of prestrain and frequency in which the exact measurements (solid blue) have been cubically interpolated (mesh) to clarify the topology.

Figure 7.19 strongly indicates that the prestrain is responsible for the variation in the transfer function and as the strain approaches approximately 0.15-0.16 the magnitude greatly decreases. Eventually, the strain is too large and the magnitude increases once again which is likely due to the beams of the inclusion bottoming out.

To confirm that the results were not anomalous, the NS metamaterial was freed from prestrain and once again prestrained to 0.15. The same behavior was observed, even after moving the accelerometers to multiple positions and performing the tests again. These results indicate that the augmented BNC approach was able to identify a reliably manufacturable NS metamaterial. One such retesting is shown in Figure 7.20 where the same procedure was as before to determine the material properties in the frequency associated with the half-power bandwidth of the metamaterial.

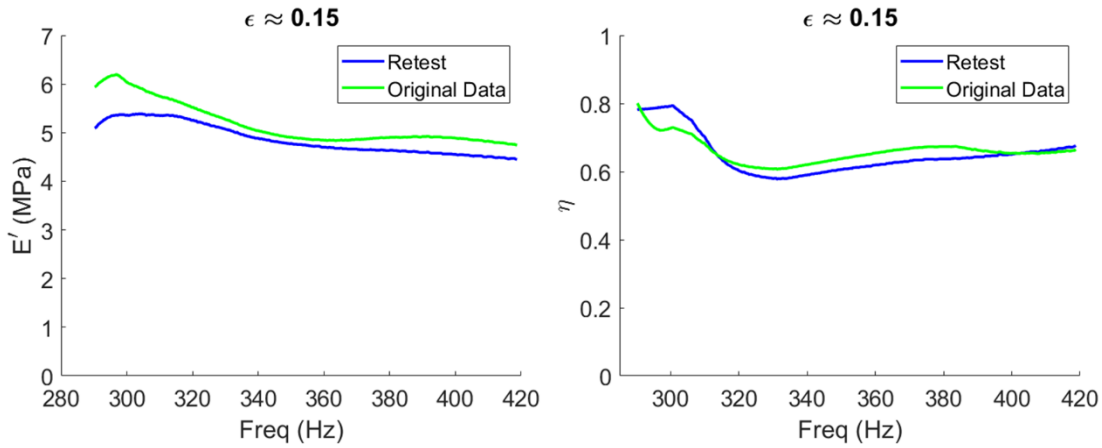

Figure 7.20: Results after relieving then prestraining the inclusions (blue) to the same prestrain of 0.15 compared to the original results (green) that demonstrated the improved storage modulus (left) and loss factor (right).

As stated before, at lower frequencies, around 200 Hz, there appears to be a second resonance in all of the experiments that is likely due to a component of the experimental apparatus resonating such as an off center mass or different mode being excited. To diagnose these vibrations a scanning laser Doppler vibrometer could be used to obtain high resolution information regarding the vibration of the system. It also could potentially allow for more material properties, such as the Poisson ratio, to be calculated. The presence of these undesired resonances, though, motivated the previous discussion of the quality factor of the materials. Therefore the quality factor for each of the materials was calculated and presented in Table 7.4.

Table 7.4: Quality factor obtained for each of the materials using the half-power bandwidth method.

Polyurethane	Voided Material	NS Metamaterial
3.5	4.4	2.5

Table 7.4 indicates that, qualitatively, the results of the complete inversion and quality factor inversion provide similar relative loss relationships. The lower the quality factor, the higher the damping in the system. The NS metamaterial has a substantially smaller quality factor than the other materials, although, relating this value to an exact material property is much more difficult and should be investigated in the future.

7.5 DISCUSSION

In this section the final inclusion design identified by the BNC approach was manufactured and embedded within a polyurethane elastomer. A specific prototype fabrication and testing procedure was developed to evaluate the material properties of the polymer, metamaterial, and voided material. While much of the higher frequency and lower frequency results were obscured by noise, the frequency range ofapproximately 280 Hz to 420 Hz provided clear and relatively conclusive results. For most prestrains, all three materials performed similarly with no appreciable distances, but once a critical displacement was achieved, the metamaterial demonstrated a dramatically increased loss factor.

While it is tempting to confirm that a successful metamaterial has been developed, there are still some unanswered questions that should be explored in future work to confirm the quality of the metamaterial. For example, the material properties of the polyurethane do not match the nominal values used in the design process, so it is surprising to observe an increase in damping. The effective medium theory model was rerun using the identified inclusion and a matrix with a loss factor of 0.4 and storage modulus of 4.0 MPa to reflect the obtained results. The improvement in loss factor modeled with the EMT model was negligible, so further work could investigate the accuracy of these models. Also during manufacturing, it was observed that the adhesive used to seal the inclusion left unwanted

residue within the metamaterial which could be leading to misleading results. Furthermore, the modeling of the experiment should be improved to ensure the proper physical phenomena are being modeled. However, it appears that the results of this initial dynamic experimentation indicate that a NS metamaterial can be developed and tested with the proposed approach. The following chapter expands on the future work associated with this research and provides some closing remarks.

Chapter 8: Conclusions and Future Work

The previous chapters described, validated, and applied an augmented BNC approach to identify and visualize reliably manufacturable sets of designs for a NS metamaterials design problem. The intent of introducing such an approach was to facilitate the design of complex multilevel systems in the presence of manufacturing variation. Metamaterial development is particularly well-suited for the approach because of its hierarchical nature, complex models with large numbers of design variables, and reliance on emerging and highly variable manufacturing processes. While the BNC approach was applied specifically to a metamaterials design problem, various contributions were made to the fields of simulation-based design and materials design through the completion of the central tasks of this work.

8.1 Summary of Research Contributions

As shown in Table 2.1, which is reprinted as Table 8.1, four tasks were proposed for the development of the augmented BNC approach.

Table 8.1: Research tasks of this work.

1	Incorporate manufacturing variation inherent to production into the BNC approach.
2	Provide the designer with an effective and appropriate clustering method for identification of design regions of interest in a high dimensional design space.
3	Provide the designer with an effective and appropriate visualization technique to visualize each cluster/region in a high dimensional design space.
4	Apply the new design tool to manufacture and evaluate a NS metamaterial.

The first task was to incorporate manufacturing variation into the BNC approach, which was accomplished by introducing a dual classification strategy that efficiently identified designs that not only performed satisfactorily but were reliably manufacturable. The strategy supplies a statistical confidence in the reliability of a candidate design when manufactured. The ability to narrow the design space to the most reliable designs reduces the expected time to produce a functional and reliable product. In particular, the approach is well-suited for materials design problems that rely on integrating emerging technology to manufacture structures and systems that are difficult to efficiently model, such as the NS metamaterials example. The manufacturing processes used to develop these complex systems can be highly variable in regards to material properties or geometric resolution so this work introduced a strategy for modeling such uncharacterized systems through the use of KDEs.

Manufacturing variation data was leveraged to generate nonparametric distributions that described the manufacturing variation even if a parametric form could not be assumed. With the manufacturing variation modeled, a Monte Carlo-based approach that samples designs from manufacturing variation distributions was performed. For each sampled design, its performance was then classified as either satisfactory or unsatisfactory with the original BNC approach. The percentage of randomly sampled designs that still perform satisfactorily was compared to a reliability threshold, which allows designs with satisfactory performance to be further classified as reliably manufacturable or not. By predicting the performance of manufactured designs with the BNC approach, the computational expense is greatly reduced compared to approaches that require modeling the performance of each randomly sampled point.

This work also introduced a strategy for integrating the design process with the characterization of manufacturing variation. Rather than perform these processes serially,

in which a selected design is manufactured to determine the reliability of its performance, manufacturing characterization and design can be performed in parallel to identify a reliable design. Such an approach was demonstrated for a NS metamaterial design problem which required development of two metrology parts for characterization of a microstereolithography system. Manufacturing variation was collected for the metrology parts prior to selection of a final design which was then successfully implemented to identify a reliably manufacturable design. Therefore, not only did this work contribute a strategy for incorporating manufacturing variation, it also provided a practical procedure for collecting manufacturing variation data for incorporation into the approach. While this work required the fabrication of metrology parts for manufacturing variation, future work could collect and disseminate manufacturing data for various systems.

The second task of identifying the regions of interest to visualize introduced a computationally efficient strategy for accurately determining the number of clusters in a high-dimensional design space that will eventually be visualized. The approach utilized spectral clustering, which has been implemented previously for engineering design applications, but by exploiting the Nyström method, the clustering approach was reduced from cubic computationally complexity to linear complexity. While the approach did sometimes misrepresent the clustering of design regions, in general, it partitioned the design regions into the correct groupings. The linearly scaling computation time needed to implement the clustering approach allowed it to be executed multiple times to determine the most likely number of clusters. For high-dimensional spaces, computational expense becomes even more critical because exponential increases in the number of data points are required to maintain equivalent sample density as dimensionality increases. The Nyström modified STSC approach was shown to be well suited for such a task.

Furthermore, the work established a guide for designers to select the most appropriate of three different spectral clustering- based technique for specific applications. The three techniques were: 1) ϵ-neighborhood spectral clustering, 2) Self-tuning spectral clustering, and 3) Nyström modified STSC. To compare the techniques, the guide provided four criteria for the designer to consider during the selection process. The first three criteria—computational complexity, accuracy, and degree of automation—were objectively compared for the three proposed variations of spectral clustering. The final criterion, ease of implementation, was a more subjective metric evaluated based on the experience of the author. Through these comparisons, the relative strengths and weaknesses of each clustering method were illuminated, so designers can be informed when selecting a clustering technique for a design exploration application.

The second task of identifying the number of design regions in a high dimensional space was largely motivated by the third task of visualizing the design regions. By developing a procedure for visualizing design spaces, two contributions were made: 1) development and validation of a new metric, preservation, for measuring the quality of a visualization and 2) introduction of t-SNE visualization to design exploration

The new metric, preservation, was developed as a tool for designers to determine which visualization is most appropriate for the design space of interest. Knowing which visualization approach to use *a priori* is quite difficult for designers who may be unfamiliar with visualization techniques in general or the specific design space of interest. Therefore, preservation was proposed as a metric that balances the positive aspects of previous visualization metrics without the negatives, so a single value can inform the designer if the visualization scheme of interest was successful. The metric was also implemented into a Bayesian optimization framework which allowed automatic identification of the appropriate heuristic values to optimize the quality of the visualization.

The second contribution with respect to visualization was the introduction of t-SNE. The approach has shown significant promise in the machine learning community for not only visualizing high dimensional regions but naturally separating clusters. The major limitation of the approach for design, however, is the nonlinear nature of the visualizations. While structure is retained from the mappings, it is unclear how to interpret the axes of the mappings. Therefore, a preliminary tool was developed that allowed the physical embodiment of a selected design to be shown to compliment the visualization approach. While the tool assisted in clarifying the interpretation of the topology of the visualized design regions, it did not provide sufficient detail regarding design variable relationships, which is an opportunity for future work.

Finally, by accomplishing Task 4, a negative stiffness metamaterial was manufactured and tested. The manufacturing and testing of the inclusion is one of the most significant contributions of this work because it required the culmination of all other contributions to achieve. This is the first demonstration of a systematic design process being utilized to design, fabricate, and test such a metamaterial. Rather than iterate through different designs and experiments to arrive at a final part, a set-based approach was implemented, manufacturing variation considered, and the feasible designs were visualized.

The results of the metamaterial testing provides an advancement in the applicability of embedding NS inclusions within a matrix to attain higher loss factors. In particular, this work furthered the results of Cortes *et al.* [148] in which a cm scale NS structure was embedded within a polyurethane matrix to determine the quasistatic material properties. The method demonstrated an improvement in energy dissipation in quasistatic loading conditions but did not prestrain the inclusions independently from any dynamic excitation to measure dynamic material properties. This work was able to develop such an

experimental apparatus for material characterization. Other work on embedding inclusions that exhibit NS, such as the work of Lakes *et al.* [29], achieved exceptional damping through thermal loading rather than prestraining. For the intended applications of the NS metamaterials, such as aerospace applications, it is appears more feasible to mechanically prestrain a material to attain high loss factors rather than to thermally load it. Therefore, by demonstrating the ability to prestrain the materials to tune the loss factor, progress has been made to implement NS metamaterials in a mechanical system.

8.2 FUTURE WORK

Several opportunities for future work are motivated by the four tasks accomplished in this work. The first opportunity is to incorporate more sophisticated models of manufacturing-induced variation into the BNC approach. For example, the joint probability distributions were assumed to be either constant or scalable in this research, but this assumption is not always valid. To investigate the hypothesis that manufacturing variations are consistent across changes in inclusion dimensions, a preliminary study was performed. A second set of metrology parts with the geometry shown in Table 8.1 was fabricated and measured.

Table 8.2: Geometry of second metrology part manufactured to determine if manufacturing variation changes with the scale of a design.

Apex Height, h	140 μm
Beam Thickness, t	100 μm
Beam Length, L	2.15 mm
Beam Separation, W	2.51 mm

The design provided in Table 8.2 is nearly an order of magnitude larger in terms of volume than the inclusion geometry described in Section 6.5. Ten inclusions with the new geometry were produced and measured using the same approach described previously,

which resulted in the KDE plot of Figure 8.1. The previous distribution is also shown for comparison.

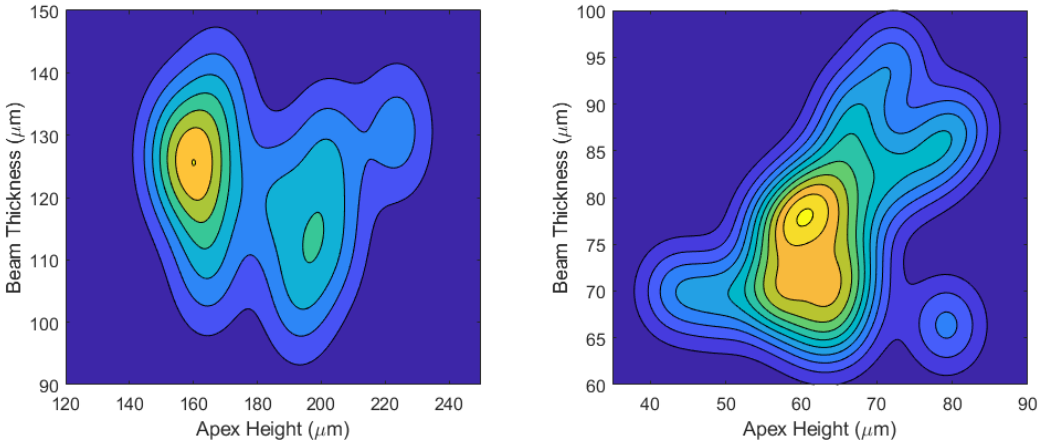

Figure 8.1: KDE generated from beam thickness measurements of new design (left) compared to original distribution (right)

These distributions are relatively dissimilar, which indicates that specific distributions should be considered for each size scale. The larger geometry demonstrated a larger spread in the apex height, which is unexpected. It was thought that the variation in geometry should be constant with scale, but the KDEs indicate otherwise. Also, there appears to be less dependency between variation in apex height and beam thickness for the larger geometry. This difference is likely due to the different post processing procedures the inclusions received. The smaller inclusions were cleaned with IPA while the larger inclusions were not. The post processing has been shown to distort the beams, so eliminating the process removed any dependencies related to warping.

The results further indicate that manufacturing variation is scale-dependent, which motivates the need for building statistical databases of measurements from metrology parts that span length scales and geometric features of interest to designers. Furthermore, designers may be interested in comparing capabilities across AM processes, if more than

one AM process is potentially suitable for their application, motivating the need for metrology-backed statistical databases for a wide variety of AM processes.

The second and third tasks of clustering and visualizing motivate the further expansion of the metamaterials design problem to include even more design variables at both the micro and meso levels. Additional geometric parameters could be varied, such as beam length and separation, which would likely lead to more interesting and nonlinear design regions in a high-dimensional space. More material types and volume fractions could be included in the meso-scale as well, which could motivate work in using the BNC approach for mixed variable problems if specific materials are selected.

One of the challenges associated with adding more variables is generating sufficient training points, which requires extensive computational resources. Rather than relying on random or space-filling sampling strategies, a sequential sampling technique could be leveraged, such as Bayesian optimization, to focus additional samples on regions of interest, such as creating higher fidelity representations of the decision boundaries between design spaces. The approach could utilize the underlying classifiers to specifically sample training points that are likely to be on the decision boundary to refine the decision boundary itself or to sample training points within the satisfactory region to identify candidate designs with even better performance. Even with a sequential sampling-based technique, the classification accuracy of the BNC approach has been shown to decrease for high dimensional spaces. This classification inaccuracy could also drive research in developing a more dynamic prior distribution that could incorporate expert knowledge or update itself as performance information becomes more available.

To further increase the dimensionality of the design space, a topology optimization strategy could be used to generate structures that exhibit negative stiffness, rather than starting with a fixed topology. If these designs are pixelated based on mass density, the t-

SNE algorithm could theoretically be used to cluster the discovered designs into regions of similar geometries. For an example of such an approach of clustering images see the application of t-SNE on the MNIST dataset [108]. By increasing the dimensionality of the design space, the intuition regarding axes representation becomes more obscured. Even with a relatively small number of design variables, it can be difficult to comprehend what each axis represents for nonlinear mappings. Future work could attempt to clarify what each axis represents or embed more information in the mappings that help orient the designer's visual interpretation of the design space.

The departure from a specific topology is also motivated by what is likely the largest obstacle for developing a metamaterial with applicability as a structural component. Currently, the NS metamaterials discussed in the work have been made of polymers and soft elastomers, which are typically not used as structural components. The selection of these materials is due to the required balancing of positive and negative stiffness of the matrix and inclusion as well as manufacturing limitations for the micron-scale structure. In the future these metamaterials need to be formed from even stiffer materials that will allow them to be implemented as structural components rather than from highly damped elastomers. Investigation of other mechanisms that exhibit negative stiffness as well as manufacturing methods for producing NS inclusions from metals with the same resolution as microstereolithography should be investigated.

Finally, improving the manufacturing of the metamaterials is an interesting area of focus. To be able to scale the metamaterials to large scale production, the most viable approach would be to embed the inclusions while mixing the resins. This motivates the investigation of methods to prevent penetration of the polymer into interior regions of the inclusions. It is possible that the capillary effect will prevent thicker resins from infiltrating the inclusions, but future work should investigate possible avenues for embedding. Also,

other matrix materials with different material properties should be investigated. For example, PDMS, a clear polymer may also be feasible for embedding inclusions because of its advantageous material properties.

Another opportunity for future work is identifying specifically when the proposed design strategy should be implemented. The NS metamaterials design problem is well-suited for the approach because it satisfies some implicit assumptions. Specifically, it has been assumed that, while the forward models are computationally expensive, sufficient training data can be collected to train the classifiers. If the data is not available, confidence in the BNC approach is reduced due to the higher likelihood of misclassifying design spaces, which by extension reduces the confidence in the visualizations and topology of the reliably manufacturable regions. Furthermore, if the design space is exceptionally high dimensional, it may be infeasible to sufficiently sample the design space to train the classifier, or the required number of sampled points needed to describe the high dimensional space may lead to computational efficiency issues with the BNC approach. It has been shown that a KDE-based classifier struggles to classify accurately in the presence of 10D and higher datasets, so there may be a limit on the applicability of the proposed strategy for high dimensional mapping regardless of the sampling density [149].

Conversely, the augmented BNC approach should not be applied to design problems where the relationships between design and performance are simple and analytically provided. A materials design problem may have a complex hierarchical structure but if the forward models are simple, analytical functions of a relatively small number of design variable that can be instantaneously evaluated, the BNC approach should not be utilized. Rather, a grid of designs should be formed and evaluated through the forward models to generate mappings of the satisfactory design space. The lack of computational expense allows for a Monte Carlo-based strategy to be implemented that

allows for reliably manufacturable designs to be identified as well. The BNC approach and visualization approach could serve as a means to visualize the decision boundary of such a highly sampled space but there is limited applicability of the approach for such problems.

The BNC approach is most applicable to design problems for which resources such as computational and experimental expense are limited by the complexity of the design problem but are not so prohibitive that training data cannot be obtained to accurately train the classifier. Cross validation, such as the strategies applied in this work, can be used to determine if sufficient data has been collected to converge to an accurate classifier. This cross validation, though, must be performed after data has been collected, which could lead to wasted resources if the classifier is not accurate. It would be convenient to know *a priori* whether the BNC approach is applicable for a proposed design problem, but additional work is needed to generate more specific guidelines.

The BNC approach is also particularly useful for coupled design spaces for either multidisciplinary or multilevel design problems. For multidisciplinary design, each team can identify satisfactory regions that meet their respective performance requirements. By intersecting the regions, teams can identify mutually feasible regions of design that meet their sub-problem's performance requirements. For multilevel design, the BNC approach identifies sets of feasible designs in the coupled space that are likely to yield satisfactory performance. For both the multidisciplinary and multilevel design formulations, the smaller sets of feasible designs can then be optimized to identify the most successful design. Compared to multi-objective optimization of the entire design space, the set-based approach will result in fewer iterations between design teams and arrive at a final viable design more quickly.

If the BNC approach can be trained to accurately classify the design space, the other augmentations of the strategy such as incorporation of manufacturing variation and

visualization of the design regions can be confidently implemented, in general. Specifically, the incorporation of manufacturing variation can be implemented whenever an accurate classifier has been trained because the BNCs are used to evaluate the reliability of a design. The visualization strategy can be implemented whenever an accurate classifier is trained with the exception of sparse design regions. If the design region of interest is too small relative to the rest of the high-dimensional design space, it may be difficult to sample sufficient candidate designs within the region of interest. This under-sampling would lead to poor visualization and clustering, so future work could investigate sampling in these regions to increase the accuracy of the visualization approach.

8.3 CLOSURE

In closing, this work presented a strategy for identifying and visualizing sets of reliably manufacturable designs in a multilevel design space. As a result of this work, engineering designers now have a suite of tools for multi-level design exploration, including generation of reliably manufacturable regions, identification of design regions in high-dimensional design spaces, and visualization of the design regions. The approach was utilized to identify a NS metamaterial design, which was fabricated and tested to validate its performance. The metamaterial demonstrated an improved loss factor relative to the original host matrix that housed the inclusion. Beyond the scope of metamaterials, this work is intended to serve as a general design strategy for design exploration of additively manufactured parts and systems as well as multi-scale material systems.

References

[1] V. Smil, Still the Iron Age: Iron and Steel in the Modern World, Oxford, UK: Butterworth-Heinemann, 2016.

[2] J. Mokyr, "The Second Industrial Revolution, 1870-1914," in *Storia dell'economia Mondiale*, Rome, Laterza Publishing, 1999, pp. 219-245.

[3] G. B. Olson, "Designing a New Material World," *Science,* vol. 288, no. 5468, pp. 993-998, 2000.

[4] G. B. Olson, "Computational Design of Hierarchically Structured Materials," *Science,* vol. 277, no. 5330, pp. 1237-1242, 1997.

[5] M. C. Payne, D. C. Allan, T. A. Arias and A. J. Joannopoulos, "Iterative Minimization Techniques for ab initio Total-Energy Calculations: Molecular Dynamics and Conjugate Gradients," *Reviews of Modern Physics,* vol. 64, no. 4, pp. 1045-1097, 1992.

[6] D. Sánchez-Portal, P. Ordejón and E. Canadell, "Computing the Properties of Materials from First Principles with SIESTA.," in *InPrinciple and Application of Density Functional Theory in Inorganic Chemistry II*, Berlin-Heidelberg, Springer, 2004, pp. 103-170.

[7] B. Liu, H. Jiang, Y. Huang, S. Qu, M. F. Yu and K. C. Hwang, "Atomic-Scale Finite Element Method in Multiscale Computation with Applications to Carbon Nanotubes," *Physical Review B,* vol. 72, no. 3, p. 035435, 2005.

[8] O. A. Shenderova, D. W. Brenner, A. A. Nazarov, A. R. Romanov and L. H. Yang, "Multiscale Modeling Approach for Calculating Grain-Boundary Energies from First Principles," *Physical Review B,* vol. 57, no. 6, pp. R3181-3184, 1998.

[9] G. B. Olson, M. Arzin and E. S. Wright, "Innovation in Ultrahigh-Strength Steel Technology," Government Printing Office (GPO), Washington, DC, 1990.

[10] P. Voorhees, H. J. Jou and G. B. Olson, "Computer Simulations of the Prediction of Microstructure/Property Variation in Aeroturbine Disks," in *Tenth International Symposium on Superalloys*, Champion, PA, 2004.

[11] D. L. McDowell, K. Gall, M. F. Horstemeyer and J. Fan, "Microstructure-based Fatigue Modeling of Cast A356-T6 Alloy," *Engineering Fracture Mechanics ,* vol. 70, no. 1, pp. 49-80, 2003.

[12] R. Krishnamurthy, Y. G. Yoon, D. J. Srolovitz and R. Car, "Oxygen Diffusion in Yttria-Stabilized Zirconia: A New SImulation Model," *Journal of the American Ceramic SOciety,* vol. 87, no. 10, pp. 1821-1830, 2004.

[13] J. C. Mauro and A. K. Varshneya, "Multiscale Modeling of GeSe2 Glass Structure," *Journal of the American Cermaic Society,* vol. 89, no. 7, pp. 2323-2326, 2006.

[14] B. Natarajan, Y. Li, H. Deng, L. C. Brinson and L. S. Schadler, "Effect of Interfacial Energetics on Dispersion and Glass Transition Temperature of Polymer Nanocomposites," *Macromolecules,* vol. 46, no. 7, pp. 2833-2841, 2013.

[15] C. M. Breneman, L. C. Brinson, L. S. Schadler, B. Natarajan, M. Krein, K. Wu, L. Morkowchuck, Y. Li, H. Deng and H. Xu, "Stalking the Materials Genome: A Data-Driven Approach to the Virtual Design of Nanostructured Polymers," *Advanced Functional Materials,* vol. 23, no. 46, pp. 5746-5752, 2013.

[16] T. Ziegler, A. Neubrand and R. Piat, "Multiscale Homogenization Models for the Elastic Behaviour of Metal/Ceramic COmposites with Lamellar Domain," *Composites Science and Technology,* vol. 70, no. 4, pp. 664-670, 2010.

[17] C. T. Sun and R. S. Vaidya, "Prediction of Composite Properties from a Representative Volume Element," *Composites Science and Technology,* vol. 56, no. 2, pp. 171-179, 1996.

[18] X. Zhang, X. N. Jiang and C. Sun, "Micro-Stereolithography of Polymeric and Ceramic Microstructures," *Sensors and Actuators A: Physical,* vol. 77, no. 2, pp. 149-156, 1999.

[19] M. Agarwala, D. Bourell, J. Beaman, H. Marcus and J. Barlow, "Direct Selective Laser Sintering of Metals," *Rapid Prototyping Journal,* vol. 1, no. 1, pp. 26-36, 1995.

[20] X. Zheng, H. Lee, T. H. Weisgraber, M. Shusteff, J. DeOtte, E. B. Duoss, J. D. Kuntz, M. M. Biener, Q. Ge, J. A. Jackson and S. O. Kucheyev, "Ultralight, Ultrastiff mechanical Metamaterials," *Science,* vol. 344, no. 6190, pp. 1373-1377, 2014.

[21] C. S. Ha, M. E. Plesha and R. S. Lakes, "Chiral Three-Dimensional Isotropic Lattices with Negative Poisson's Ratio," *physica status solidi,* vol. 253, no. 7, pp. 1243-1251, 2016.

[22] A. Takezawa, M. Kobashi and M. Kitamura, "Porous Composite with Negative Thermal Expansion Obtained by Photopolymer Additive Manufacturing," *APL Materials,* vol. 3, no. 7, p. 076103, 2015.

[23] D. M. Correa, T. Klatt, S. Cortes, M. Haberman, D. Kovar and C. Seepersad, "Negative Stiffness Honeycombs for Recoverable Shock Isolation," *Rapid Prototyping Journal,* vol. 21, no. 2, pp. 193-200, 2015.

[24] N. Engheta and R. W. Ziolkowoski, Metamaterials: Physics and Engineering Explorations, USA: John Wiley & Sons, 2006.

[25] C. S. Wojnar and D. M. Kochmann, "A Negative-Stiffness Phase in Elastic Composities Can Produce Stable Extreme Effective Dynamic but Not Static Stiffness," *Philosophical Magazine,* vol. 94, no. 6, pp. 532-555, 2013.

[26] M. R. Haberman, Y. H. Berthelot and M. Cherkaoui, "Micromechanical Modeling of Particulate Composite for Damping of Acoustic Waves," *Journal of Engineering Materials and Technology,* vol. 128, no. 3, pp. 320-329, 2006.

[27] Y. Koutsawa, M. R. Haberman, E. M. Daya and M. Cherkaoui, "Multiscale Design of a Rectangular Sandwich Plate with Viscoelastic Core and Supported at Extents by Viscoelastic Materials," *International Journal of Mechanical Materials Design,* vol. 5, no. 1, pp. 29-44, 2008.

[28] J. Qiu, J. H. Lang and A. H. Slocum, "A Curved-Beam Bistable Mechanism," *Journal of microeletromechanical Systems,* vol. 13, no. 2, pp. 137-146, 2004.

[29] R. S. Lakes, "Extreme Damping in Composite Materials with a Negative Stiffness Phase," *Physical Review Letters,* vol. 86, no. 13, pp. 2897-2900, 2001.

[30] R. S. Lakes, T. Lee, A. Bersie and Y. C. Wang, "Extreme Damping in Composites Materials with Negative-Stiffness Inclusions," *Nature,* vol. 410, no. 6828, pp. 565-567, 2001.

[31] B. A. Fulcher, D. W. Shahan, M. R. Haberman, C. C. Seepersad and P. S. Wilson, "Analytical and Experimental Investigation of Buckled Beams as Negative Stiffness Elements for Passive Vibration and Shock Isolation Systems," *ASME Journal of Vibration and Acoustics,* vol. 136, no. 3, pp. 1-12, 2014.

[32] T. Klatt and M. R. Haberman, "A Nonlinear Negative Stiffness Metamaterial Unit Cell and Small-On-Large Multiscale Material Model," *Journal of Applied Physics,* vol. 114, no. 3, pp. 1-12, 2013.

[33] Z. Hashin, "Viscoelastic Behavior of Heterogeneous Media," *Journal of Applied Mechanics,* vol. 32, no. 3, pp. 630-635, 1965.

[34] J. Jarzynsky, "Sound and Vibration Damping with Polymers," in *Mechanisma of Sound Attenuation in Materials*, Washington, DC, ACS Symposium Series, 1990, pp. 167-207.

[35] J. Matthews, T. Klatt, C. Morris, C. C. Seepersad, M. R. Haberman and D. W. Shahan, "Hierarchical Design of Negative Stiffness Metamaterials Using a Bayesian Network Classifier," *Journal of Mechanical Design,* vol. 138, no. 4, pp. 1-12, 2016.

[36] H. M. Kim, P. Y. Papalambros and T. Jiang, "Target Cascading in Optimal System Design," *Journal of Mechanical Design,* vol. 125, no. 3, pp. 474-480, 2003.

[37] B. A. Wujek, J. E. Renaud, S. M. Batill and J. B. Brockman, "Concurrent Subspace Optimization Using Design Variable Sharing in a Distributed Computing Environment," *Concurrent Engineering,* vol. 4, no. 4, pp. 361-377, 1996.

[38] A. Ward, J. K. Liker, J. J. Cristiano and D. K. Sobek, "The Second Toyota Paradox: How Delaying Decisions can Make Better Cars Faster," *Sloan Management Review,* vol. 36, no. 3, p. 43, 1995.

[39] J. H. Panchal, M. G. Fernández, J. J. Christiaan, J. K. Paredis and F. Mistree, "An Interval-based Constraint Satisfaction (IBCS) Method for Decentralized Collaborative Multifunctional Design," *Concurrent Engineering,* vol. 15, no. 3, pp. 309-323, 2007.

[40] R. J. Malak and C. J. Paredis, "Using Support Vector Machines to Formalize the Valid Input Domain of Predictive Models in Systems Design Problems," *Journal of Mechanical Design,* vol. 132, no. 10, p. 101001, 2010.

[41] K. Zeliff, W. Bennette and S. Ferguson, "Zeliff, Kayla, Walter Bennette, and Scott Ferguson. "Benchmarking the Performance of a Machine Learning Classifier Enabled Multiobjective Genetic Algorithm on Six Standard Test Functions," in *Internation Design Engineering Technical Conferences and Computers and Information in Engineering Conference*, Cleveland, Ohio, 2017.

[42] W. Chen and M. Fuge, "Beyond the Known: Detecting Novel Feasible Domains Over an Unbounded Design Space," *Journal of Mechanical Design,* vol. 139, no. 11, p. 11405, 2017.

[43] D. W. Shahan and C. C. Seepersad, "Bayesian Network Classifiers for Set-Based Collaborative Design," *Journal of Mechanical Design,* vol. 134, no. 7, pp. 1-14, 2012.

[44] G. H. John and P. Langley, "Estimation Continuous Distribution in Bayesian Classifiers," in *Proceddings of the Eleventh Conference on Uncertainty in Artificial Interlligence*, Montreal, Canada, 1995.

[45] R. Hoffmann and V. Tresp, "Discovering Structure in Continuous Variables using Bayesian Networks," in *Advances in Neural Information Processing Systems*, Denver, CO, 1996.

[46] P. A. N. Bosman and D. Thierens, "IDEAs Based on the Normal Kernels Probability Density Function," Utrecht University Technical Report , Utrecht, The Netherlands, 2000.

[47] R. O. Dudda, P. E. Hart and D. G. Stork, Pattern Classification, New York: Wiley & Sons Inc., 2001.

[48] J. Pearl, Probabilistic Reasoning in Intelligent Systems: Networks of Plausible Inference, San Francisco: Morgan Kauffman Publishers, Inc., 1988.

[49] A. K. Jain and M. D. Ramaswami, "Classifier Design with Parzen Windowss," *Machine Intelligence and Pattern Recognition,* vol. 7, pp. 221-228, 1988.

[50] E. Parzen, "On Estimation of Probability Density Function and Mode," *Annals of Mathematical Statistics,* vol. 33, no. 3, pp. 1065-1076, 1962.

[51] D. W. Scott, Multivariate Density Estimation, New York: John Wiley & Sons, 1992.

[52] B. W. Silverman, Density Estimation, London: Chapman and Hall, 1986.

[53] C. Sharpe, C. Morris, B. Goldsberry, C. C. Seepersad and M. R. Haberman, "Bayesian Network Structure Optimization of Improved Design Space Mapping for Design Exploration with Materials Design Applications," in *International Design Engineering Technical Conferences*, Cleveland, OH, 2017.

[54] A. Perez, P. Larranaga and I. Inza, "Bayesian Classifiers Based on Kernel Density Estimation: Flexible Classifiers," *International Journal of Approximate Reasoning,* vol. 50, no. 2, pp. 341-362, 2009.

[55] P. Cox, P. Yang, S. S. Mahant-Shetti and P. Chatterjee, "Statistical Modeling for Efficient Parametric Yield Estimation of MOS VLSI Circuits," *IEEE Journal of Solid-State Circuits,* vol. 20, no. 1, pp. 391-398, 1985.

[56] J. P. Brockman and S. W. Director, "Predictive SUbset Testing: Optimizing IC Parametric Performance Testing for Quality, Cost, and Yield," *IEEE Trans. Semiconductor Manufacturing,* vol. 2, no. 3, pp. 104-113, 1989.

[57] J.-C. Yu and K. Ishii, "Design for Robustness Based on Manufacturing Variation Patterns," *Journal of Mechanical Design,* vol. 120, no. 2, pp. 196-202, 1998.

[58] D. P. Thunnissen, "Uncertainty Classification for the Design and Development of Complex Systems," in *Predictive Methods Conference*, Santa Clara, CA, 2003.

[59] G. Shafer, A Mathermatical Theory of Evidence, Princeton: Princeton University Press, 1976.

[60] D. Dubois and H. Prade, "Possibility Theory," in *Computational Complexity*, New York, Springer, 2012, pp. 2240-2252.

[61] H. Z. Huang and X. Zhang, "Design Optimization with Discrete and Continuous Variables of Aleatory and Epitemic Uncertainties," *Journal of Mechanical Design,* vol. 131, no. 3, pp. 1-8, 2009.

[62] B. D. Youn, K. K. Choi, L. Du and D. Gorsich, "Integration of Possibility-Based Optimization and Robust Design for Epistemic Uncertainty," *Journal of Mechanical Design,* vol. 129, no. 8, pp. 876-882, 2007.

[63] T. W. Simpson, T. M. Mauery, J. J. Korte and F. Mistree, "Kriging Models for Global Approximation in Simulation-Based Multidisciplinary Design Optimization," *AIAA Journal,* vol. 39, no. 12, pp. 2233-2241, 2001.

[64] P. Pandita, I. Bilionis and J. Panchal, "Extending Expected Improvement for High-Dimensional Stochastic Optimization of Expensive Black-Box Function," *Journal of Mechanical Design,* vol. 138, no. 11, pp. 1-8, 2016.

[65] J. C. Yu and K. Ishii, "Design for Robustness Based on Manufacturing Variation Patterns," *Journal of Mechanical Design,* vol. 120, no. 2, pp. 196-202, 1998.

[66] A. Ahmad, K. Andersson and U. Sellgren, "An Optimization Approach Toward a Robust Design of Six Degrees of Freedom Haptic Devices," *Journal of Mechanical Design,* vol. 137, no. 4, pp. 042301-1-14, 2015.

[67] W. Yao, X. Chen, W. Luo, M. van Tooren and J. Guo, "Review of Uncertainty-Based Multidisciplinary Design Optimization Methods for Aerospace Vehicles," *Progress in Aerospace Sciences,* vol. 47, no. 6, pp. 450-479, 2011.

[68] X. Gu and J. E. Renaud, "Implicit Uncertainty Propagation for Robust Collaborative Optimization," in *Design Engineering Technical COnferences and Computers and Information in Engineering Conference*, Pittsburgh, 2001, Paper Number: DETC2001/DAC-21118.

[69] R. S. Sellar, S. M. Batill and J. E. Renaud, "Response Surface Based Concurrent Subspace Optimization for Multi-disciplinary System Design," in *Aerospace Sciences Meeting and Exhibit*, Reno, 1996.

[70] M. Kokkolaras, J. Moulrlatos and P. Y. Papalambros, "Design Optimization of Hierarchically Decomposed Multilevel Systems Under Uncertainty," in *Design Engineering Technical COnference and Computers and Information in Engineering Conference*, Long Beach, 2005, Paper Number: DETC2004/DAC-57357.

[71] W. W. Finch and A. C. Ward, "A Set-Based System for Eliminating Infeasible Designs in Engineering Problems Dominated by Uncertainty," in *ASME Design Engineering Technical Conferences*, Sacramento, CA, 1997.

[72] S. J. Rekuc, J. M. Aughenbaugh, M. Bruns and C. J. Paredis, "Eliminating Design Alternatives Based on Imprecise Information," in *SAE World Congress & Exhibition*, Chicago, IL, 2006.

[73] R. J. Malak Jr, J. M. Aughenbaugh and C. J. Paredis, "Multi-Attribute Utility Analysis in Set-Based Conceptual Design," *Computer-Aided Design,* vol. 41, no. 3, pp. 214-227, 2009.

[74] B. Yannou, P. Yvars, C. Hoyle and W. Chen, "Set-based Design by Simulation of Usage Scenario Coverage," *Journal of Engineering Design,* vol. 24, no. 8, pp. 575-603, 2013.

[75] A. Sinha, N. Bera, J. K. Allen, J. H. Panchal and F. Mistree, "Uncertainty Management in the Design of Multiscale Systems," *Journal of Mechanical Design,* vol. 135, no. 1, pp. 011008-1-16, 2013.

[76] H.-J. Choi, J. K. Allen, D. Rosen, D. L. McDowell and F. Mistree, "An Inductive Design Exploration Method for the Integrated Design of Multi-Scale Materials and Products," in *International Design Engineering Technical Conferences and Computers and Information in Engineering Conference*, Long Beach, CA, 2005.

[77] A. Sinha, N. Bera, J. K. Allen, J. H. Panchal and F. Mistree, "Uncertainty Management in the Design of Multiscale Systems," *Journal of Mechanical Design,* vol. 135, no. 1, p. 011008, 2013.

[78] T. T. Soong, Fundamentals of Probability and Statistics for Engineers, Hoboken, NJ: John Wiley & Sons, 2004.

[79] N. Knerr and D. Selva, "Cityplot: Visualization of High-Dimensional Design Spaces with Multiple Criteria," *Journal of Mechanical Design,* vol. 138, no. 9, p. 091403, 2016.

[80] E. H. Winer and C. L. Bloebaum, "Development of Visual Design Steering as an Aid in Large-Scale Multidisciplinary Design Optimization. Part I: Method Development," *Structural Multidisciplinary Optimization,* vol. 40, no. 1, p. 97, 2010.

[81] G. Stump, M. Yukish, J. Martin and T. Simpson, "The ARL Trade Space Visualizer: An Engineering Decision-Making Tool," in *Multidisciplinary Analysis and Optimization Conference*, Albany, New York, 2004.

[82] X. Zhang, T. W. Simpson, M. Frecker and G. Lesieutre, "Supporting Trade Space Exploration of Multi-Dimensional Data with Interactive Multi-Scale Nested

Clustering Aggregation," in *International Design Engineering Technical Conference*, San Diego, CA, 2009.

[83] W. Chen, M. Fuge and J. Chazan, "Design Manifolds Capture the Intrinsic Complexity and Dimension of Design Spaces," *Journal of Mechanical Design,* vol. 139, no. 5, p. 051102, 2017.

[84] C. C. Aggarwal and C. K. Reddy, Data Clustering: Algorithms and Application, Boca Raton, FL: CRC Press, 2013.

[85] J. B. MacQuen, "Some Methods for Classification and Analysis of Multivariate Observations," in *Berkeley Symposium on Mathematical Statistics and Probability*, Berkeley, CA, 1967.

[86] J. Bezdek, E. Robert and F. William, "FCM: The Fuzzy C-means Clustering Algorithm," *Computers & Geosciences,* vol. 10, no. 2-3, pp. 191-203, 1984.

[87] K. Pearson, "Contributions to the Mathematical Theory of Evolution," *Philosophical Transactions of the Royal Society of London,* vol. 185, pp. 71-110, 1894.

[88] J. H. Ward Jr., "Hierarchical Grouping to Optimize an Objective Function," *Journalof the American Statistical Association,* vol. 58, no. 301, pp. 236-244, 1963.

[89] T. Kohonen, "Self-Organized Formation of Topologically Correct Feature Maps," *Biological Cybernetics,* vol. 43, no. 1, pp. 59-69, 1982.

[90] A. J. Richardson, C. Risien and A. Shillington, "Using Self-Organizing Maps to Identify Patterns in Satellite Imagery," *Progress in OCeanography,* vol. 59, no. 2-3, pp. 223-239, 2003.

[91] C.-I. Chang, N. P. Lin and N.-Y. Jan, "An Axis-Shifted Grid-Clustering Algorithm," *Tamkang Journal of Science and Engineering,* vol. 12, no. 2, pp. 183-192, 2009.

[92] M. Fiedler, "Algebraic Connectivity of Graphs," *Czechoslovak Mathematical Journal,* vol. 23, no. 2, pp. 298-305, 1973.

[93] F. V. Paulovich, M. F. Oliveira and R. Minghim, "The Projection Explorer: A Tool for Projection-Based Multidimensional Visualization," in *Computer Graphics and Image Processing*, Minas Gerais, Brazil, 2007.

[94] A. Kusiak and J. Wang, "Decomposition of the Design Process," *Journal of Mechanical Design,* vol. 115, no. 4, pp. 687-695, 1993.

[95] P. J. Newcomb, B. Bras and D. W. Rosen, "Implications of Modularity on Product Design for the Life Cycle," *Journal of Mechanical Design,* vol. 120, no. 3, pp. 483-490, 1998.

[96] J. Jiao and M. M. Tseng, "A Methodology of Developing Product Family Architecture for Mass Custimization," *Journal of Intelligent Manufacturing,* vol. 10, no. 1, pp. 3-20, 1999.

[97] T. Shao and S. Krishnamurty, "A Clustering-Based Surrogate Model Updating Approach to Simulation-Based Engineering Design," *Journal of Mechanical Design,* vol. 130, no. 4, pp. 041101-041114, 2008.

[98] F. Borjesson and K. Hölttä-Otto, "Improved Clustering Algorithm for Design Structure Matrix," in *International Design Engineering Technical Conference*, Chicago, 2012.

[99] L. Zelnik-Manor and P. Perona, "Self-Tuning Spectral Clustering," in *NIPS 17*, Vancouver, Canada, 2004.

[100] F. R. Bach and M. I. Jordan, "Learning Spectral Clustering," in *Advances in Neural Information Processing Systems*, Vancouver, 2004.

[101] S. White and P. Smyth, "A Spectral Clustering Approach to Finding Communities in Graphs," in *SIAM International Conference on Data Mining*, Newport Beach, CA, 2005.

[102] K. Itô, Encyclopedic Dictionary of Mathematics, Cambridge, Massachusetts: MIT Press, 1993.

[103] A. Y. Ng, M. I. Jordan and Y. Weiss, "On Spectral Clustering: Analysis and an Algorithm," in *Advances in Neural Information Processing Systems*, Vancouver, 2002.

[104] D. Yan and M. I. Jordan, "Fast Approximate Spectral Clustering," in *International Conference on Knowledge Discovery and Data Mining*, Paris, 2009.

[105] M. Ester, H. P. Kriegel, J. Sander and X. Xu, "A Density-Based Algorithm for Discovering Clusters in Large Spatial Databases with Noise," in *Proceedings of Second International COnference on Knowledge Discovery and Data Mining*, Portland, 1996.

[106] C. Fowlkes, S. Belongie, F. Chung and J. Malik, "Spectral Grouping Using the Nyström Method," *IEEE Transactions on Pattern Analysis and Machine Intelligence,* vol. 26, no. 2, pp. 214-225, 2004.

[107] C. T. Pan, "On the Existence and Computation of Rank-Revealing Lu Factorization," *Linear Algebra and its Applications,* vol. 316, no. 1-3, pp. 199-222, 200.

[108] S. B. Pope, "Algorithms for Ellipsoids," Cornell Universtity Report, Cornell, 2008.

[109] J. A. Wilson, "Volume of n-dimensional Ellipsoid," *Sciencia Acta Xaveriana,* vol. 1, no. 1, pp. 101-106, 2009.

[110] B. Schölkopf, A. Smola and K.-R. Müller, "Kernel Principal Component Analysis," in *International Conference on Artificial Neural Networks*, Berlin, 1997.

[111] L. van der Maaten and G. Hinton, "Visualizing Data Using t-SNE," *Journal of Machine Learning Research,* vol. 9, pp. 2579-2605, 2008.

[112] J. Venna and S. Kaski, "Local Multidimensional Scaling with Controlled Tradeoff Between Trustworthiness and Continuity," *Proceeding of WSOM,* vol. 5, pp. 695-702, 2005.

[113] L. van der Maaten, E. Postma and J. van den Herik, "Dimensionality Reduction: A Comparitive," *Journal of Machine Learning Research,* vol. 10, pp. 66-71, 2009.

[114] S. Liu, D. Maljovec, B. Wang, P. T. Bremer and V. Pascucci, "Visualizing High-Dimensional Data: Advances in the Past Decade," in *Eurographics Conference on Visualization*, Cagliari, Italy, 2015.

[115] K. Pearson, "On Lines and Planes of Closest Fit to Systems of Points in Space," *The London, Edinburgh, and Dublin Philosophical Magazine and Journal of Science,* vol. 2, no. 11, pp. 559-572, 1901.

[116] J. B. Tenenbaum, V. De Silva and J. C. Langford, "A Global Geometric Framework for Nonlinear Dimensionality Reduction," *Science,* vol. 290, no. 5500, pp. 2319-2323, 2000.

[117] K. Q. Weinberger and L. K. Saul, "An Introduction to Nonlinear Dimensionality Reduction by Maximum Variance Unfolding," *AAAI,* vol. 6, pp. 1683-1686, 2006.

[118] Z. Zhang and H. Zha, "Principal Manifolds and Nonlinear Dimensionality Reduction via Tangent Space Alignment," *Journal on Scientific Computing,* vol. 26, no. 1, pp. 313-338, 2004.

[119] S. Roweis and L. Saul, "Nonlinear Dimensionality Reduction by Locally Linear Embedding," *Science,* vol. 290, no. 5500, pp. 2323-2326, 2000.

[120] M. Belkin and P. Niyogi, "Laplacian Eigenmaps for Dimensionality Reduction and Data Representation," *Neural Computation,* vol. 15, no. 6, pp. 1373-1396, 2003.

[121] D. L. Donoho and C. Grimes, "Hessian Eigenmaps: Locally Linear Embedding Techniques for High-DImensional Data," *Proceedings of the National Academy of Sciences,* vol. 100, no. 10, pp. 5591-5596, 2003.

[122] J. W. Sammon, "A Nonlinear Mapping for Data Structure Analysis," *IEEE Transaction on Computers,* vol. 100, no. 5, pp. 401-409, 1969.

[123] S. T. Roweis, L. K. Saul and G. E. Hinton, "Glocal Coordination of Local Linear Modals," in *Advances in Neural Information Processing Systems*, Vancouver, 2002.

[124] M. Brand, "Charting a Manifold," in *Advanceing Neural Information Processing Systems*, Vancouver, 2003.

[125] G. E. Hinton and R. R. Salakhutdinov, "Reducting the Dimensionality of Data with Neural Networks," *Science,* vol. 313, no. 5786, pp. 504-507, 2006.

[126] S. Gerber, P. T. Bremer, V. Pascucci and R. Whitaker, "Visual Exploration of High DImensional Scalar Function," *IEEE Transaction on Visualization and Computer Graphics,* vol. 16, no. 6, pp. 1271-1280, 2010.

[127] P. Mordohai and G. G. Medioni, "Unsupervised Dimensionality Estimation and Manifold Learning in High-Dimensional Spaces by Tensor Voting," in *International Joint Conferences on Artifical Intelligences*, Edinburgh, 2005.

[128] J. Eddy and L. Kemper, "Multidimensional Design Visualization in Multiobjective Optimization," in *AIAA/ISSMO Symposium on Multidisciplinary Analysis and Optimization*, Atlanta, 2002.

[129] P.-W. Chiu and C. L. Bloebaum, "Hyper-Radial Visualization (HRV) Method with Range-Based Preferences for Multi-objective Decision Making," *Structural and Multidisciplinary Optimization,* vol. 40, no. 1, p. 97, 2010.

[130] P. Vincent, H. Larochelle, I. Lajoie, Y. Bengio and P. A. Manzagol, "Stacked Denoising Autoencoders: Learning Useful Representations in a Deep Network with a Local Denoising Criteriaon," *Journal of Machine Learning Research,* vol. 11, pp. 3371-3408, 2010.

[131] F. Esposito, D. Malerba and G. Semararo, "Multistrategy Learning fo Document Recognition," *Applied Artifical Intelligence,* vol. 8, no. 1, pp. 33-84, 1994.

[132] J. Snoek, H. Larochelle and R. P. Adams, "Practical Bayesian Optimization of Machine Learning Algorithms," in *Advances in Neural Information Processng Systems*, Lake Tahoe, 2012.

[133] G. M. Odegard, "Constituitive Modelin of Piezoelectric Polymer Composites," *Acta Materialia,* vol. 52, no. 18, pp. 5315-5330, 2004.

[134] M. R. Haberman, Y. H. Berthelot and M. Cherkaoui, "Micromechanical Modeling of Particulate Composites for Damping of Acoustic Waves," *Journal of Engineering Materials and Technology,* vol. 128, no. 3, pp. 320-329, 2006.

[135] J. Matthews, T. Klatt, C. C. Seepersad, M. R. Haberman and D. W. Shahan, "Hierarchical Design of Composite Materials with Negaive Stiffness Inclusions Using a Bayesian Network Classifier," in *ASME IDETC Design Automation Conference*, Portland, Oregon, 2013.

[136] D. S. Huh and S. L. Cooper, "Dynamic Mechanical Properties of Polyurethane Block Polymers," *Polymer Engineering & Science,* vol. 77, no. 5, pp. 369-376, 1971.

[137] D. L. Bourell, T. J. Watt, D. K. Leigh and B. Fulcher, "Performance Limitation in Polymer Laser Sintering," *Physics Procedia,* vol. 56, pp. 147-156, 2014.

[138] B. C. Salzbrenner, J. M. Rodelas, J. D. Madison, B. H. Jared, L. P. Swiler, Y. L. Shen and B. L. Boyce, "High-Throughput Stochastic Tensile Performance of Additively Manufactured Stainless Steel," *Journal of Materials Processing Technology,* vol. 241, pp. 1-12, 2017.

[139] J. Allison, C. Sharpe and C. C. Seepersad, "A Test Part for Evaluating the Accuracy and Resolution of a Polymer Powder Bed Fusion Process," *Journal of Mechanical Design,* vol. 139, no. 10, pp. 1-5, 2017.

[140] S. K. Everton, M. Hirsch, P. Stravroulakis, R. K. Leach and A. T. Clare, "Review of In-Situ Process Monitoring and In-Situ Metrology for Metal Additive Manufacturing," *Materials and Design,* vol. 95, pp. 431-445, 2016.

[141] L. Castillo, "Study About the Rapid Manufacturing of Complex Parts of Stainless Steel and Titanium," TNO Industrial Technology, Eindhoven, The Netherlands, 2005.

[142] M. Mahesh, Y. Wong, J. Y. H. Fuh and H. T. Loh, "Benchmarking for Comparative Evaluation of RP Systems and Processes," *Rapid Prototyping Journal,* vol. 10, no. 2, pp. 123-135, 2004.

[143] S. Moylan, J. Slotwinski, A. Cooke, K. Jurrens and M. A. Donmez, "An Additive Manufacturing Test Artifact," *Journal of Research of the National Institite of Standards and Technology,* vol. 119, pp. 429-459, 2014.

[144] T. Govett, K. Kim, D. Pinero and M. Lundin, "Design Rules for Selective Laser Sintering," The University of Texas at Austin, Austin, TX, 2012.

[145] W. C. Young, R. G. Budynas and A. M. Sadegh, Roark's Formulas for Stress and Strain, New York: McGraw-Hill, 2011.

[146] F. J. Massey, "The Kolmogorov-Smirnov Test for Goodness of Fit," *Journal of the American Statistical Association,* vol. 46, no. 253, pp. 68-78, 1951.

[147] P. J. Van Ekeren and E. P. Carton, "Polyurethanes for Potential Use in a Transparent Armour Investigated Using DSC and DMA," *Journal of Thermal Analysis and Calorimetry,* vol. 105, no. 2, pp. 591-598, 2011.

[148] N. G. McCrum, B. E. Read and W. Graham, Anelastic and Dielectric Effects in Polymeric Solids, Wiley,New York: Dover, 1967.

[149] M. L. Williams, R. F. Landel and J. D. Ferry, "The Temperature Dependence of Relaxation Mechanisms in Amorphous Polymers and Other Glass-forming Liquids," *Journal of the American Chemical Society,* vol. 77, no. 14, pp. 3701-3707, 1955.

[150] D. Xiao, X. Zhao, Y. Feng, P. Xiang, L. Zhang and W. Wang, "The Structure and Dynamic Properties of Thermoplastic Polyurethane Elastome/Hindered Phenol Hybrids," *Journal of Applied Polymer Science,* vol. 116, no. 4, pp. 2143-2150, 2010.

[151] S. Cortes, J. Allison, C. Morris, M. R. Haberman, C. C. Seepersad and D. Kovar, "Design, Manufacture, and Quai-static Testing of Metallic Negative Stiffness Structures within a Polymer Matrix," *Experimental Mechanics,* vol. 57, no. 8, pp. 1183-1191, 2017.

[152] C. M. van der Walt and E. Barnard, "Variable Kernel Density Estimation in High-Dimensional Feature Spaces," in *Conference on Artificial Intelligience*, San Francisco, 2017.